Towards Predictive Large-Eddy-Simulation-based Modeling of Reactive Multiphase Flows using Tabulated Chemistry

Dem Fachbereich Maschinenbau
an der Technischen Universität Darmstadt
zur
Erlangung des Grades eines Doktor-Ingenieurs (Dr.-Ing.)
genehmigte

Dissertation

vorgelegt von

Louis Jons Dreßler, M.Sc.

aus Straßburg, Frankreich

Berichterstatter:	Prof. Dr. rer. nat. A. Dreizler
Mitberichterstatter:	Prof. Dr. rer. nat. A. Sadiki
Mitberichterstatter:	Prof. Dr.-Ing. G. C. Krieger Filho
Tag der Einreichung:	18.05.2021
Tag der mündlichen Prüfung:	14.07.2021

Darmstadt 2021
D17

Louis, Dreßler: *Towards Predictive Large-Eddy-Simulation-based Modeling of Reactive Multiphase Flows using Tabulated Chemistry*
Darmstadt, Technische Universität Darmstadt,
Jahr der Veröffentlichung der Dissertation auf TUprints: 2021
URN: urn:nbn:de:tuda-tuprints-195119
Tag der mündlichen Prüfung: 14.07.2021

Erklärung

Hiermit erkläre ich, dass ich die vorliegende Arbeit, abgesehen von den in ihr ausdrücklich genannten Hilfen, selbstständig verfasst habe.

Datum, Unterschrift

Acknowledgments

This PhD thesis was carried out during my work as a doctoral candidate at the department of Energy and Power Plant Technology, and later at the department of Reactive Flows and Diagnostics at the Technical University of Darmstadt. Even though it is ultimately my name on the title page of this work, many exceptional people have contributed to the accomplishment of this thesis.

The first people in this long list are Prof. Dr.-Ing. Johannes Janicka (head of the former department of Energy and Power Plant Technology), Prof. Dr. rer. nat. Andreas Dreizler (head of the department of Reactive Flows and Diagnostics) and Prof. Dr. rer. nat. Amsini Sadiki (head of the research group on Modeling and Simulation of Technical Energy Systems at the department of Reactive Flows and Diagnostics). I would like to thank Johannes Janicka for giving me the opportunity to accomplish this fascinating PhD project, for providing me with excellent working conditions and for his encouraging attitude and his scientific input during my first three years in Darmstadt. I am also grateful to Andreas Dreizler for allowing me to finalize my work at his institute, and for his encouraging, motivating and positive attitude throughout the final phase of this project. A special thankyou is dedicated to my supervisor, Amsini Sadiki, for the numerous productive scientific discussions, his guidance, interest, and positive perspective on my work.

I am sincerely grateful to Prof. Dr.-Ing. Guenther Carlos Krieger Filho, not only for accepting to be a co-advisor on my thesis, but also for giving me the opportunity to work within his research group in São Paulo, Brazil. This exchange of ideas has been a great enrichment full of unforgettable experiences, mainly due to André, Helio, Filipi, Clayton, and Flavio who welcomed me like a family. I deeply miss the *pasteis* lunches with you! I am also extremely thankful for the support and friendship of Fernando, who patiently pulled the strings in São Paulo to make this research cooperation possible. Looking back, it is deeply satisfying to see what great work we have been able to accomplish together.

I would also like to thank my scientific co-workers at the EKT, RSM and STFS, many of whom I call friends. In particular, I would like to thank Florian, Adam, Dennis, Sebastian, Martin, Federica, Maria Angela, Li, Johannes and Hendrik. All of you have inspired me in some way or another to become a better version of myself.

I am deeply grateful to Prof. Dr.-Ing. Markus Klein, who has had a significant influence on my path so far. Thank you for introducing me to the world of computational fluid dynamics and awakening a curiosity for scientific research in me.

I am also grateful for the support, motivation and love of my mother and father, Sylvie and Felix, and of my sisters and my brother, Jeanne, Mathilde, Thérèse and François. Finally I would like to thank Kathi, for being the best partner I can imagine, for her love and for believing in me. Thank you.

Darmstadt, May 2021
Louis Dreßler

To Kathi

Abstract

Probably the strongest argument in favor of liquid fuels, compared to gaseous fuels, electrical batteries or mechanical energy storages, is their high energy density at ambient conditions. This contributed to the strong attention dedicated to combustion devices fueled with liquids in the last few decades. At present, liquid fuels are still the primary choice for transport and storage systems. However, in view of their detrimental impact on the environment, it is of the utmost importance to increase the overall efficiency of combustion-driven devices and simultaneously to minimize their environmental impact.

From a practical standpoint, the combustion of liquids includes multiple interwoven processes, such as the gradual breakup of large liquid structures into small droplets, the dispersion and evaporation of these droplets, the mixture formation and the subsequent combustion process. With respect to technical applications, all of these processes generally occur under the influence of turbulence, a chaotic, strongly unsteady process, which involves a broad spectrum of time and length scales. The better understanding of these processes is crucial to reach the goals mentioned above. Numerical simulations, beside experimental investigations, play a key role in improving this understanding.

In this work, the large eddy simulation (LES) approach is used and further developed to investigate turbulent spray combustion systems while consistently considering the turbulence-chemistry-droplets interaction processes. The LES is combined with a tabulated chemistry approach to represent the detailed kinetics of the combustion reaction.

Beside the development of an interface to efficiently apply chemistry tabulation strategies within the finite volume code OpenFOAM, the present work implements and investigates two different approaches to model the interaction of the turbulence and chemistry in the context of LES: the artificially thickened flame (ATF) model and the Eulerian stochastic field (ESF) method. The methodologies are rigorously verified and validated, first in simple test-cases and then in turbulent single phase turbulent combustion. It is shown that the modeling framework is able to reproduce experimental measurements with great accuracy. The final step in this ladder of gradually increasing complexity is to apply the respective frameworks to spray combustion. Thereby, the multiphase system is treated using a two-way coupled Euler-Lagrange approach.

For the liquid phase treatment, two novel approaches to represent the interaction of droplets with a thickened flame are proposed and evaluated. By taking into account the relative orientation of flame front and droplet movement using the proposed projection correction method, the overall consistency of the modeling framework is improved. Additionally, a novel strategy to compute turbulent spray combustion based on the ESF method coupled to the chemistry tabulation strategy is proposed. Its predictive capability is demonstrated and it is shown that this novel approach has great potential to evaluate classical turbulence-chemistry interaction models.

Therefore, the developed methodologies constitute a significant achievement towards predictive simulations of spray combustion.

Kurzfassung

Ein entscheidender Vorteil flüssiger Brennstoffe, verglichen mit gasförmigen Brennstoffen, elektrischen Batterien oder mechanischen Energiespeichern, ist ihre hohe Energiedichte bei Standardbedingungen. Aus diesem Grund wurde zuletzt der Verbrennung von flüssigen Energieträgern viel Aufmerksamkeit gewidmet. Gegenwärtig ist der Einsatz flüssiger Brennstoffe im Transportsektor oder im Bereich der Energiespeicherung unverzichtbar. Angesichts der mit einhergehenden Schadstoffaustoße ist es essenziell, nicht nur die Effizienz von Verbrennungssystemen zu steigern, sondern auch ihre Auswirkungen auf die Umwelt zu minimieren.

Aus praktischer Sicht beinhaltet die Verbrennung von Flüssigkeiten eine Vielzahl gekoppelter Prozesse, wie das Aufbrechen großer Flüssigkeitsstrukturen in kleine Tröpfchen, die Dispersion und Verdampfung jener Tröpfchen, die Gemischbildung und den anschließenden Verbrennungsprozess. Im Hinblick auf technische Anwendungen laufen diese Prozesse in der Regel unter dem Einfluss von Turbulenz ab, einem chaotischen, stark instationären Prozess, der ein breites Spektrum an Zeit- und Längenskalen umfasst. Das bessere Verständnis dieser Prozesse ist entscheidend, um die oben genannten Ziele zu erreichen. Numerische Simulationen spielen, neben experimentellen Untersuchungen, eine Schlüsselrolle bei der Verbesserung dieses Verständnisses.

In dieser Arbeit wird der *Large Eddy Simulation* (LES) Ansatz verwendet und weiterentwickelt, um die turbulente Sprayverbrennung zu untersuchen und dabei die Turbulenz-Chemie-Tropfen-Wechselwirkungsprozesse umfassend zu berücksichtigen. Die LES wird mit dem Ansatz der tabellierten Chemie kombiniert, um die detaillierte Kinetik der Verbrennungsreaktion darzustellen.

Neben der Entwicklung einer Schnittstelle zur effizienten Anwendung von Chemie-Tabellierungsstrategien innerhalb des Finite Volumen Code OpenFOAM werden zwei verschiedene Ansätze zur Modellierung der Interaktion von Turbulenz und Chemie im LES-Kontext implementiert und untersucht: Das Modell der künstlich aufgedickten Flamme (*artificially thickened flame*–ATF) und die Eulersche stochastische Feldmethode (*Eulerian stochastic fields*–ESF). Die Methoden werden systematisch verifiziert und validiert, zuerst in einfachen Testfällen und anschließend für turbulente Gasphasenverbrennung. Dabei wird gezeigt, dass das Framework in der Lage ist, experimentelle Messungen mit großer Genauigkeit zu reproduzieren. Der letzte Schritt ist die Anwendung der jeweiligen Ansätze auf die Sprayverbrennung. Die reaktive Zweiphasenströmung wird dabei durch einen Zweiwegegekoppelten Euler-Lagrange Ansatz beschrieben.

Für die Behandlung der flüssigen Phase werden zwei neuartige Ansätze zur Beschreibung der Wechselwirkung von Tropfen mit einer aufgedickten Flamme vorgeschlagen, erprobt und bewertet. Durch die Berücksichtigung der relativen Orientierung der Flammenfront und der Tropfenbewegung wird die Gesamtkonsistenz der Modellierung verbessert. Zusätzlich wird eine neue Strategie zur Berechnung der turbulenten Sprayverbrennung basierend auf der ESF-Methode in Verbindung mit der Chemietabellierung vorgeschlagen. Die Vorhersagefähigkeit des Ansatzes wird belegt und es wird gezeigt, dass diese Methode großes Potenzial aufweist, um klassische Turbulenz-Chemie-Interaktionsmodelle zu bewerten.

Daher stellen die entwickelten Methoden einen wesentlichen Schritt in Richtung prädiktiver Simulationen der Sprayverbrennung dar.

List of Publications

The content of this thesis is partly based on the following journal and conference publications which have been published during this research project.

Journal Publications

[**E1**] F. Ries, K. Nishad, L. Dressler, J. Janicka and A. Sadiki. Evaluating Large-Eddy Simulation Results based on Error Analysis. Theoretical and Computational Fluid Dynamics, 32(11), pp. 1-20, **2018**, DOI 10.1007/s00162-018-0474-0

[**E2**] L. Dressler, F. Ries, G. Kuenne, J. Janicka and A. Sadiki. Analysis of Shear Effects on Mixing and Reaction Layers in Premixed Turbulent Stratified Flames using LES coupled to Tabulated Chemistry, Combustion Science and Technology, **2019**, DOI: 10.1080/00102202.2019.1678915

[**E3**] F. L. Sacomano Filho, L. Dressler, A. Hosseinzahdeh, A. Sadiki and G. C. Krieger Filho. Investigations of Evaporative Cooling and Turbulence Flame Interaction Modeling in Ethanol Turbulent Spray Combustion Using Tabulated Chemistry. Fluids, 4(4):187, **2019**, DOI: 10.3390/fluids4040187

[**E4**] L. Dressler, F. L. Sacomano Filho, A. Sadiki and J. Janicka. Influence of Thickening Factor Treatment on Predictions of Spray Flame Properties Using the ATF Model and Tabulated Chemistry. Flow, Turbulence and Combustion, 106, pp. 419–451, **2021**, DOI: 10.1007/s10494-020-00149-7

[**E5**] L. Dressler, F. L. Sacomano Filho, F. Ries, H. Nicolai, J. Janicka and A. Sadiki. Numerical Prediction of Turbulent Spray Flame Characteristics Using the Filtered Eulerian Stochastic Field Approach Coupled to Tabulated Chemistry. Fluids, 6(2):150, **2021**, DOI: 10.3390/fluids6020050

[**E6**] F. Ries, Y. Li, K. Nishad, L. Dressler, M. Ziefuss, A. Mehdizadeh, C. Hasse and A. Sadiki. A Wall-Adapted Anisotropic Heat Flux Model for Large Eddy Simulations of Complex Turbulent Thermal Flows, Flow, Turbulence and Combustion, 106, pp. 733–352, **2021**, DOI: 10.1007/s10494-020-00201-6

[**E7**] X. Wen, L. Dressler, A. Dreizler, A. Sadiki, J. Janicka and C. Hasse. Flamelet LES of turbulent premixed/stratified flames with H2 addition, Combustion and Flame, 230(2):111428, **2021**, DOI: 10.1016/j.combustflame.2021.111428

Conference Publications

[**E8**] L. Dressler, F. Ries, G. Kuenne, J. Janicka and A. Sadiki. Characterization of the stratification process in a turbulent premixed flame using LES. 11th Mediterranean Combustion Symposium MCS-11, Tenerife, Spain, **2019**

[**E9**] L. Dressler, F. L. Sacomano Filho, A. Sadiki and J. Janicka. Influence of the mixture composition treatment on combustion characteristics in a dilute turbulent spray flame using LES coupled to tabulated chemistry. Internal Workshop on Clean Combustion IWCC, Darmstadt, Germany **2019**

Contents

List of Figures

List of Tables

Nomenclature

Bold symbols denote vectorial or tensorial quantities.

Upper case Latin letters		**Units**
A	Flame surface	m^2
A_j	Arrhenius law pre-exponential factor	–
B_M	Spalding mass transfer number	–
B_T	Spalding energy transfer number	–
C_D	Drag coefficient	–
C_M	Model parameter	–
$\mathcal{D}$	Diffusion coefficient	$\mathrm{m}^2\,\mathrm{s}^{-1}$
$\mathcal{D}_M$	Model differential operator	m^{-1}
D_{10}	Mean diameter	m
D_{32}	Sauter mean diameter	m
Da	Damköhler number	–
E_j	Arrhenius law activation energy	$\mathrm{J}\,\mathrm{mol}^{-1}$
E_k	Energy spectrum	$\mathrm{m}^3\,\mathrm{s}^{-2}$
F	Thickening factor	–
$\mathbf{F}$	Force	$\mathrm{kg}\,\mathrm{m}\,\mathrm{s}^{-2}$
F_f	Mass flux crossing S_f	$\mathrm{kg}\,\mathrm{s}^{-1}$
F_{eff}	Effective particle heat- and mass transfer correction factor	–
G	Spatial filtering operator	m^{-1}
H	Hellinger norm	–
H_M	Mass transfer driving potential	–
$\mathbf{J}^\phi$	Boundary flux of the quantity ϕ	–
K	Flame stretch rate	s^{-1}
$\mathcal{K}_j$	Reaction rate constant	–
Ka	Karlovitz number	–
$\mathcal{L}$	Characteristic length scale	m
L_2	Normalized rms global error norm	–
L_∞	Maximum error norm	–
L_d	Inter-particle spacing	m
L_K	Knudsen layer thickness	m
L_t	Turbulent length scale	m
L_v	Latent heat of vaporization	$\mathrm{J}\,\mathrm{kg}^{-1}$
L_{11}	Longitudinal length scale	m
L_{ij}	Velocity gradient tensor	s^{-1}
Le	Lewis number	–
M	Molar mass	$\mathrm{kg}\,\mathrm{kmol}^{-1}$
$\mathcal{M}$	Placeholder for a chemical specie (for instance CH_4)	–

Ma	Mach number	–
N	Neighbor control volume centroid	–
N_d	Number of real droplets in a computational parcel	–
N_r	Number of elementary reactions	–
N_s	Number of stochastic fields	–
$\mathcal{O}$	Order of magnitude	–
P	Control volume centroid	–
P	Probability density function	–
$\widehat{P}$	Kernel density estimation of the FDF	m
$\overline{PN}$	Distance between the two cell centroids P and N	m
Pr	Prandtl number	–
PV	Progress variable	–
$\dot{Q}$	External source/sink of enthalpy	$\mathrm{J\,m^{-3}\,s^{-1}}$
$\mathcal{Q}_j$	Reaction rate of the j^{th} reaction	$\mathrm{mol\,m^{-3}\,s^{-1}}$
R	Universal gas constant	$\mathrm{J\,mol^{-1}\,K^{-1}}$
$\mathcal{R}$	Right-hand-side symbol	–
R_{ij}	Two-point correlation tensor	–
Re	Reynolds number	–
S	Surface/Area	$\mathrm{m^2}$
$\mathcal{S}$	Characteristic velocity gradient scale	$\mathrm{s^{-1}}$
S_f	Control volume boundary face f	$\mathrm{m^2}$
$S_{*,l}$	Source term due to the presence of a liquid phase	–
S_{ij}	Rate of strain	$\mathrm{s^{-1}}$
Sc	Schmidt number	–
St	Stokes number	–
T	Temperature	K
$\mathcal{T}$	Characteristic time scale	s
U	Characteristic velocity scale	$\mathrm{m\,s^{-1}}$
V	Volume	$\mathrm{m^3}$
$\mathbf{V}_k$	Diffusion velocity vector of species k in the mixture	$\mathrm{m\,s^{-1}}$
We	Weber number	–
Y_k	Mass fraction of the species k	–
Z	Mixture fraction	–
Z_{Bilger}	Bilger mixture fraction	–

Lower case Latin letters		**Units**
a	Strain rate	$\mathrm{s^{-1}}$
c_k	Molar concentration	$\mathrm{mol\,m^{-3}}$
$c_{p,l}$	Liquid heat capacity	$\mathrm{J\,kg^{-1}\,K^{-1}}$
d, d_d	Particle/droplet diameter	m
$\mathrm{d}\mathbf{W}$	Increment vector of a stochastic Wiener process	–
f_2	Heat transfer correction parameter	–
f_i	Force per unit mass	$\mathrm{m\,s^{-2}}$
h	Specific enthalpy	$\mathrm{J\,kg^{-1}}$
l_d	Diffusion layer thickness	m
l_0	Characteristic flow-scale	m
m_d	Particle/droplet mass	kg
$\dot{m}_d$	Evaporation mass flux	$\mathrm{kg\,s^{-1}}$
$\mathbf{n}$	Boundary normal unit vector	–
n_s	Number of species in a mixture	–

n_{CV}	Number of control volumes to resolve the flame front	–
p	Pressure	$\mathrm{kg\,m^{-1}\,s^{-2}}$
$\mathbf{q}$	Heat flux vector	$\mathrm{J\,m^{-2}\,s^{-1}}$
$\mathbf{r}$	Distance vector	m
s	Arbitrary spatial coordinate	m
s_l	Laminar flame speed	$\mathrm{m\,s^{-1}}$
s_t	Turbulent flame speed	$\mathrm{m\,s^{-1}}$
t	Time	s
$\mathbf{u}$	Velocity vector	$\mathrm{m\,s^{-1}}$
u'	Velocity fluctuation	$\mathrm{m\,s^{-1}}$
$\mathbf{u}_d$	Droplet velocity vector	$\mathrm{m\,s^{-1}}$
u_η	Kolmogorov velocity scale	$\mathrm{m\,s^{-1}}$
$\mathbf{u}_\infty$	Carrier phase velocity vector	$\mathrm{m\,s^{-1}}$
$\mathrm{var}(\cdot)$	Variance	–
$w_\perp$	Flame orthogonal weighting factor	–
x, y, z	Cartesian coordinates	m
x_i	Cartesian coordinates	m

Upper case Greek letters		**Units**
Δt	Time step	s
Δ,Δx	Filter width or grid width	m
$\Delta_R H$	Heat of reaction	$\mathrm{J\,mol^{-1}}$
Γ	Γ-function	–
Γ	Effective straining function	–
Γ_ϕ	Diffusion coefficient of the generic quantity ϕ	$\mathrm{m^2\,s^{-1}}$
Ω	Flame sensor	–
Φ	Arbitrary extensive quantity	–
Ξ	Wrinkling factor	–
$\mathbf{\Sigma}^\phi$	Rate of production or destruction of ϕ	–

Lower case Greek letters		**Units**
α	Flux limiter function	–
α_d	Liquid volume fraction	–
α_e	Molecular accommodation coefficient	–
β^*	Non-dimensional evaporation parameter	–
β^j	Arrhenius law temperature exponent	–
χ	Scalar dissipation rate	m
δ	Delta distribution δ	–
δ_l	Laminar flame thickness	m
δ_{ij}	Kronecker delta	–
η	Kolmogorov length scale	m
η_d	Mass loading	–
γ	Blending factor for spatial discretization of convective terms	–
γ	Droplet motion angle defined through radial to axial momentum ratio	°
$\boldsymbol{\kappa}$	Wave number vector	$\mathrm{m^{-1}}$
λ	Thermal conductivity	$\mathrm{J\,s^{-1}\,m^{-1}\,K^{-1}}$
μ	Dynamic viscosity	$\mathrm{kg\,m^{-1}\,s^{-1}}$
μ_{sgs}	Subgrid-scale dynamic viscosity	$\mathrm{kg\,m^{-1}\,s^{-1}}$
∇	Nabla-operator	$\mathrm{m^{-1}}$
ν	Kinematic viscosity	$\mathrm{m^2\,s^{-1}}$

$\nu''_{k,j}$	Stoichiometric coefficients on the product side	–
$\nu'_{k,j}$	Stoichiometric coefficients on the reactant side	–
ν_{sgs}	Subgrid-scale kinematic viscosity	$\mathrm{m^2\,s^{-1}}$
ϕ	Equivalence ratio	–
ϕ	Specific value of an arbitrary extensive quantity	–
ρ	Mass density	$\mathrm{kg\,m^{-3}}$
σ_{ij}	Cauchy stress tensor	$\mathrm{m^2\,s^{-2}}$
τ	Integral time scale	s
τ_c	Characteristic combustion time scale	s
τ_d	Diffusion time scale	s
τ_d	Particle response time	s
τ_f	Carrier flow time scale	s
τ_p	Particle relaxation time	s
τ_t	Turbulent time scale	s
τ_η	Kolmogorov time scale	s
τ_{ij}	Deviatoric part of the Cauchy stress tensor	$\mathrm{m^2\,s^{-2}}$
θ	Particle-flame interaction angle	$^\circ$
ε_k	Dissipation rate of turbulent kinetic energy	$\mathrm{m^2\,s^{-3}}$
ξ	Flame index	–
ξ_Z^i	i^{th} mixture fraction stochastic field	–
$\dot{\omega}_k$	Chemical source term of species k	$\mathrm{s^{-1}}$

Abbreviations

β-PDF	Beta Probability Density Function
δ-PDF	Delta Probability Density Function
σ-model	Sigma model
ATF	Artificially Thickened Flame
BD	Blended Differencing
CD	Central Differencing
CFD	Computational Fluid Dynamics
CV	Control Volume
DNS	Direct Numerical Simulation
EGR	Exhaust Gas Recirculation
EMC	Eulerian Monte Carlo
EMST	Euclidean Minimum Spanning Tree
ESF	Eulerian Stochastic Fields
FDF	Favre-filtered Density Function
FGM	Flamelet Generated Manifold
FP	Fokker-Planck
FPI	Flame Prolongation of ILDM
FPV	Flamelet Progress Variable
FVM	Finite Volume Method
GA	Grid-Adaptive
IEM	Interaction by Exchange with the Mean
KDE	Kernel Density Estimation
LDV/LDA	Laser Doppler Velocimetry/Anemometry
LES	Large Eddy Simulation
LFA	Laminar Flamelet Assumption
LIF	Laser Induced Fluorescence
LMSE	Linear Mean Square Estimation

MA	Mixture-Adaptive
MES	Method of Exact Solutions
MILD	Moderate or Intense Low oxygen Dilution
MMS	Method of Manufactured Solutions
NASA	National Aeronautics and Space Administration
NDF	Number Density Function
ODE	Ordinary Differential Equation
OoA	Order of Accuracy
OpenFOAM	OPEN source Field Operation And Manipulation
PDA	Phase Doppler Anemometry
PDE	Partial Differential Equation
PDF	Probability Density Function
PISO	Pressure-Implicit with Splitting of Operators
PIV	Particle Image Velocimetry
PLIF	Planar LIF
PPM	Point-Particle-Method
PSIC	Particle-Source-In-Cell
QMOM	Quadrature-based Method Of Moments
RANS	Reynolds-Averaged Navier-Stokes
REDIM	REaction-DIffusion Manifold
RHS	Right-Hand-Side
rms	root mean square
SF	Stochastic Field
sgs	subgrid-scale
SIMPLE	Semi-Implicit Method for Pressure Linked Equations
SMD	Sauter Mean Diameter
TCI	Turbulence Chemistry Interaction
TCS	Turbulent Combustion of Sprays
TH	Top Hat
TKE	Turbulent Kinetic Energy
UD	Upwind Differencing
VOF	Volume of Fluid

PART I: FUNDAMENTALS AND MODELING

Chapter 1

Introduction

Approximately at the time this research project started, the diesel emission scandal [24, 178], the biggest scandal in the car manufacturing industry to this day, was made public. A multitude of manufacturers admitted that in some way or another, there had been irregularities with their declarations concerning exhaust emissions, resulting in extensive internal (and external) investigations to resolve these potential cases of frauds. This is when the public aversion towards combustion related technologies began to intensify, mainly because of their detrimental impact on the environment. In view of the almost incalculable multidimensional impact of climate change, it therefore appears reasonable to reconsider the application of combustion-based technologies in the future, and to evaluate their possible replacement with cleaner alternatives. The European Green Deal, which sets the ambitious goal of climate neutrality in the European Union by 2050 [48], attests that from a political and sociocultural perspective, combustion-based applications will likely not be part of the envisioned future. It is therefore justified to raise the question of whether combustion-related scientific research has a raison d'être in the long term. The answer to this question is tightly interwoven with the understanding of the role of scientific research in a modern society. The commonly accepted opinion is that scientific research should provide potential solutions to current (and future) problems as well as guidance on their application. In the context of climate change, the problem is complex and it is very likely that its solution will rely on multiple technologies. The key to achieving this feat is to let the scientific community explore different paths, each one related to a specific aspect or technology, to help realize the target of a climate-friendly future. Combustion is one possible foundation on which to build such a future [41], as it has the following advantages compared to other technologies: (1) From the perspective of storage, the chemical energy sources used for combustion are superior to thermal, mechanical or electrical storage as they can store energy for much longer. (2) The second benefit is the high energy density of the chemical energy carriers used. The advantage is even more pronounced when considering liquid fuels as done in this work. (3) The release of energy from chemical sources through combustion can easily be scaled from small applications (as in the transport sector) to large power plants. These benefits are the main reason why this technology has been dominating the energy and transport sector for the last few decades. However, for combustion to prevail in the future, it is of the uttermost importance not only to increase the overall efficiency of combustion-driven devices, but also to minimize their environmental impact. Beside relying on carbon-capture and storage (CCS)—a method which is currently restricted to large scale facilities—the latter can be achieved by replacing fossil fuels with bio- or e-fuels, yielding a carbon-neutral or even zero-carbon combustion.

This thesis deals with the topic of turbulent and multiphase combustion, and more precisely its accurate representation in numerical simulations. Alongside experimental measurements, this is one of the key tools to improve the understanding of complex thermo-fluid multiphase flows. With respect to numerical simulations, often referred to as computational fluid dynamics (CFD), direct numerical simulation (DNS) can help researchers and engineers to better characterize and understand complex flow processes. However, DNS generally involves prohibitive computational costs, which makes the development of computationally affordable models a key desideratum. In this regard, large eddy simulation (LES) has proven its capability to accurately handle unsteady flow phenomena [90, 146] in both, single- and multiphase flow system. In this work, the LES approach is used and further developed to investigate turbulent spray combustion cases while consistently considering the turbulence-chemistry-droplets interaction processes. The current state of research regarding the modeling of reactive turbulent multiphase flows is summarized next.

1.1 State of Research

Note that in this work, multiphase combustion denotes a reactive process involving the simultaneous flow of materials with two or more thermodynamic phases, here with a gaseous and liquid (spray) component. Before the current state of the research is examined, an overview of the main phenomena occurring in turbulent combustion is provided based on the comprehensive review article by Jenny et al. [93]. The key phenomena and their mutual influence are presented in Figure 1.1. Unsurprisingly, one of the key factors in turbulent combustion is turbulence itself, which can be seen as an agglomeration of so-called eddies—each representing a coherent turbulent structure—of multiple sizes and velocities [161]. As pictured by arrows ❶ and ❸ in Figure 1.1, turbulence influences the mixing not only at macroscopic scales (driven by convection) but also at the smallest scales (due to its influence on local scalar gradients). The mixture and temperature resulting from the mixing process are determining parameters for the combustion reaction, which in turn alters scalar gradients (arrow ❹). Additionally, the change of the thermochemical state and the thermal expansion accompanying the combustion reaction may also significantly impact the turbulence itself (arrow ❺).

Further dependencies arise when an additional liquid phase is considered (red area in Figure 1.1). In this case, both phases interact through momentum exchange at their common interface (arrow ❻). This may, for instance, influence the spatial dispersion of the spray droplets, and eventually actuate, enhance or damp the turbulence in the gaseous phase. A central aspect in the chart shown in Figure 1.1 is the local distribution of liquid. For instance, the dispersion of droplets may impact their evaporation due to concentration variations (arrow ❽). On the other hand, the sheer presence of droplets may also affect the micro-mixing process (arrow ❿). Additionally, it should not be forgotten that the evaporation is also strongly influenced by the turbulence as well as the distribution of species and temperature emerging from the macro- and micro-mixing process within the carrier phase (arrows ❼, ❾ and ⓫). Lastly, the heat released due to the combustion reaction will undoubtedly affect the evaporation process. This is represented by arrow ⓬. Note that this schematic representation can by no means be deemed complete. Consider, for example, the complexities arising in the evaporation process of multicomponent mixtures, the liquid breakup preceding droplet formation, droplet-droplet collisions, or droplet-wall interaction. Each of these effects represents a field of research in itself; they are beyond the scope of this research project.

The parts of this work dedicated to multiphase combustion deal with so-called dilute sprays, which facilitate the representation of the liquid phase by neglecting any dense spray effects as liquid breakup or inter-droplet collisions. Additionally, by using a single component liquid fuel (ethanol), it is possible to circumvent the complexities of multi-species evaporation.

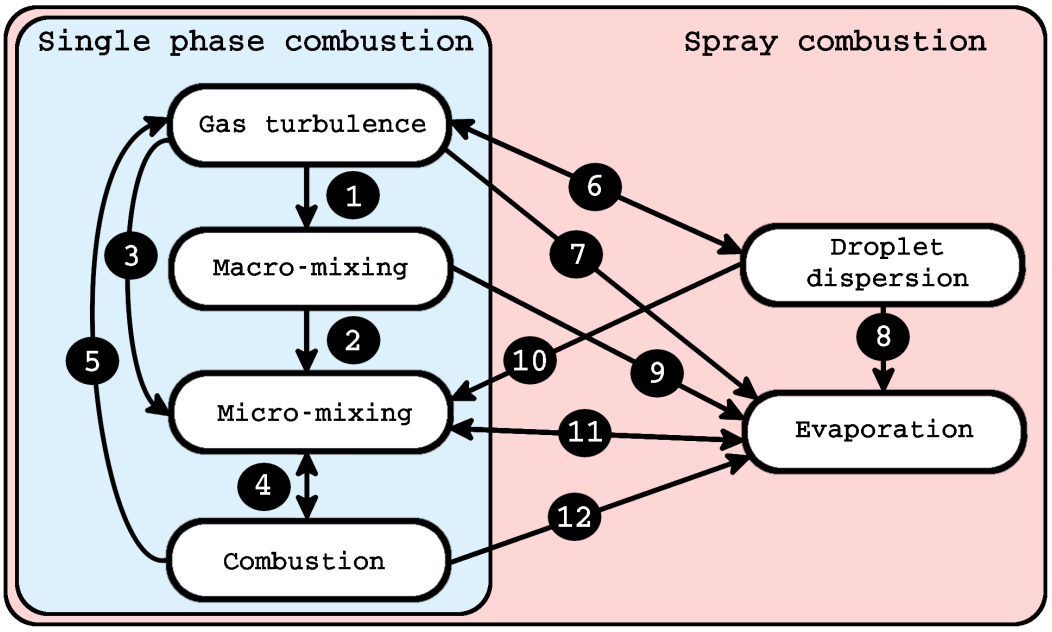

Figure 1.1: Overview of the main phenomena occurring in gaseous and spray combustion and their interactions, inspired by [93] and [170].

The high number of factors influencing the turbulent combustion and the combustion of sprays also explains the multiplicity of approaches to model such processes within CFD. The first question arising is related to the representation of the flow field. How much detail and instationarity should be resolved by the simulation? And at what computational costs? This problem is a consequence of the broad spectrum of scales present in a turbulent flow. On one hand, there is the DNS, which, in contrast to the other approaches subsequently discussed, does not require the modeling of any unresolved scales (everything is resolved). This type of simulation is currently not feasible in complex configurations due to the excessive computational costs it entails. The other extreme is the Reynolds-averaged Navier-Stokes (RANS) ansatz, which describes the turbulence in terms of temporal averages. While this type of simulation is computationally inexpensive, it strongly relies on the approach to model the unresolved turbulence. Accordingly, the quality of the data that can be extracted from such type of simulations is fairly low. This is different for LES, where the larger turbulent structures are resolved and only the smaller scales are modeled. This allows the main features of the flow to be reproduced at moderate computational costs and at the same time reduces the impact of the so-called subgrid model. For these reasons and due to the fact that LES has proven its capability to accurately handle unsteady reactive flow phenomena [90, 146], the LES approach is used in this work. An overview of the different approaches, i.e. DNS, LES and RANS, can be found in [49].

Regarding turbulent combustion simulations, it is essential to connect the fuel chemistry and the feasible computational costs of LES. In fact, the combustion of already simple fuels yields the production and consumption of numerous species $\mathcal{O}(100)$ which

are described by an even larger set of reactions $\mathcal{O}(1000)$. The solution of transport equations for each of these species is unfeasible for large-scale application due to the stiff coupling of the equations being solved. To avoid the intensive computational requirements of the detailed kinetics, various chemical reduction mechanisms [189] and chemistry tabulation approaches were suggested and successfully applied [107, 42, 44, 30, 172]. In this regard, various methods were proposed, including the intrinsic low dimensional manifold (ILDM) by Maas and Pope [114], the reaction-diffusion manifold (REDIM) [23], the flamelet progress variable approach (FPV) [144], the flame prolongation of ILDM (FPI) [67, 50] or the flamelet generated manifold (FGM) [196], among others. Flamelet-based methods allow detailed kinetics to be efficiently included in LES at feasible computational costs [90, 146]. As the turbulent flame is represented by an ensemble of one-dimensional flames, the chemistry can be preprocessed and stored in a thermochemical lookup-table. These approaches map the thermochemical state onto a reduced number of scalars, for which respective transport equations are solved. For a n-dimensional tabulation strategy, this allows the thermochemical state to be retrieved for any given combination of the n scalars used to access this state.

The above discussion of Figure 1.1, described how turbulence and combustion are tightly interwoven. In the context of combustion LES, one additional problem arises, which is due to the fact that the small scales are not resolved. This necessitates the usage of models to represent the interaction of the chemistry and turbulence at the unresolved scales. Many approaches exist to represent the turbulence-chemistry interaction in the context of LES; these are well summarized in the review papers by Janicka and Sadiki [90] and Pitsch [146]. Among these are flame front tracking methods [101, 147], flame front thickening approaches [22, 111], and statistical approaches, that are methods based on probability density functions (PDFs) [153]. These so-called PDF methods can be subdivided into either presumed or transported PDF approaches [153]. In the former, the shape of the subgrid PDF is presumed (*a-priori*) [160] and reconstructed through transport (or algebraic) equations for lower order moments of the PDF, while the latter consists in approximating the transport of the (joint) PDF at runtime using either a Lagrangian particle based Monte Carlo approach [152, 153], a Quadrature-based Moment method (QMOM, see for instance [150]) or the Eulerian Stochastic Field (ESF), also known as Eulerian Monte Carlo (EMC) method [194, 195].

The ESF method was originally proposed by Valiño [194] and later improved in [195] based on an Îto interpretation of the stochastic integral. An alternative formulation was derived and successfully applied by Sabel'nikov and Soulard [169] based on a Stratonovich interpretation of the stochastic term. A comprehensive comparison of both approaches may be found in [168, 64]. The ESF approach was applied to a multitude of reactive flow problems, for instance in computations of the Sandia flames D-F [98, 116], to stratified premixed combustion [5], to a partially premixed swirled flame [59], to oxy-fuel combustion [116], to a mixed-mode flame [75], and was recently extended in [74] to include the effects of differential diffusion, thus demonstrating the method's good prediction ability.

Another promising approach to model turbulent combustion in LES is the Artificially Thickened Flame (ATF) model, which consists in thickening the flame front in order to resolve it at coarser resolutions, a matter of special importance in premixed combustion. The ATF model was first applied to single-phase, laminar combustion [22], and later extended to turbulent combustion [26, 32], to stratified combustion using a grid-adaptive dynamic thickening strategy [107] and later to multiphase combustion [175, 170, 29].

In the case of simulations involving an additional liquid component beside the gaseous phase, the approaches can be divided into two subcategories: Euler-Euler and Euler-

Lagrange. In both cases, the gaseous medium is treated as a continuum phase, while the liquid can either be treated as a continuum too (Euler-Euler) or as set of discrete particles (Euler-Lagrange). As well summarized by Sommerfeld et al. [191] Euler-Euler methods generally represent both phases as two inter-penetrating fluids. A prominent example is the volume of fluid (VOF) approach [79], where the volumetric fraction of liquid is itself a transported quantity. Beside necessitating very fine numerical resolutions, this method usually requires a special treatment to counteract the numerical diffusion at the liquid-gas interface. On the other hand, Euler-Lagrange methods represent the liquid phase through a finite number of particles, each evolving through Lagrangian equations of motion. The interaction between the gaseous and liquid phase is realized by introducing source terms in the Eulerian carrier phase equations, while the opposite is achieved by interpolating the carrier phase quantities onto the particle positions. One advantage is that Euler-Lagrange approaches do not require any special treatment of the liquid-gas interface, as it is not resolved. Moreover, this formulation is simple to implement and enables the main aspects of spray combustion to be represented more easily than with the Euler-Euler approach, which makes it the method of choice for most applications in this field.

With respect to the application of the ESF approach to LES of multiphase combustion, some initial promising results have been attained. More specifically, the approach has been validated for multiphase combustion in a gas turbine combustor [95], a methanol spray flame [94], as well as for spray auto-ignition under EGR conditions [61], and MILD spray combustion [62]. All these modeling frameworks rely on a Lagrangian description of the liquid phase, including an additional stochastic component to model the influence of the subgrid as applied in [16]. However, all these works rely on a reduced kinetic mechanism to take into account combustion chemistry.

When it comes to the application of the ATF model in LES of turbulent spray combustion, there are few contributions. Work in this field was notably carried out by Cheneau [28] and Cheneau et al. [29], who applied this method in a swirled combustor. These works are based on the preparatory work by Boileau [21] and Paulhiac [139]. The contribution by Sacomano Filho et al. [175] is also of importance; this involves a numerical investigation of a lean partially prevaporized spray flame. Further applications of this approach can be found in [166, 170, 171, 171, 172]. However, the contributions generally differ in their strategy for representing the interaction of the droplets with the thickened flame.

1.2 Objectives of this Work

The previous section demonstrates that the numerical description of spray combustion is a challenging task, and even though the latest research has contributed to its better understanding, there is still the need for a more complete representation of the turbulent combustion of sprays. With respect to LES, this is mainly achieved by providing improved modeling frameworks with high predictive capabilities. Developing a reliable framework of this kind is the main objective of this work. From a practical point of view, this goal cannot be reached without the development of a robust, extensible and efficient software to perform the simulations. Consequently, a large part of this work has been dedicated to the implementation, verification and validation of libraries to apply chemistry tabulation, the ATF model and the stochastic field formalism within the OpenFOAM [92, 202] codebase.

In the context of ATF and tabulated chemistry, the focus is on the following questions: What potential issues and uncertainties are related to the description of the interaction of droplets with a thickened flame? Are the numerical predictions sensitive to the representation of the interaction? How should the interaction of evaporating droplets with a

thickened flame be represented? Much of this work is devoted to answering these questions.

Additionally, this research project evaluates a novel strategy to simulate spray combustion by combining the recent progress made in tabulated chemistry approaches for spray combustion with the advanced subgrid closure for the turbulence-chemistry interaction provided by the ESF method. Furthermore, the ESF approach is also used to evaluate the scalar subgrid dynamics and to compare the obtained scalar distributions with common shapes used in the context of presumed PDF methods.

1.3 Thesis Outline

The rest of this dissertation consists of nine chapters, which are organized in five parts. **Part I** familiarizes the reader with the topic of reactive multiphase flows and the modeling strategy used to perform simulations of such systems. Beside this introductory chapter, this part consists of a two additional chapters. Chapter 2 introduces the fundamentals of turbulent reactive flows on which this work is grounded, with brief summaries of the most relevant aspects, namely the balance laws and constitutive relations adopted, the basics of turbulence, combustion, and two-phase flows. Thereafter, the modeling framework is presented in Chapter 3. On the one hand, this chapter introduces the applied core modeling concepts related to the carrier phase, such as turbulence modeling in the context of LES, chemistry tabulation, and turbulence-chemistry-interaction modeling. This includes a detailed description of the ATF and ESF strategy. On the other hand, the Lagrangian formalism adopted for the liquid phase is introduced and the evolution equations for point particles are presented. In this context, special attention is given to the interaction of droplets with a thickened flame and two novel approaches are proposed to potentially improve the consistency of the modeling strategy. **Part II** consists of two chapters and focuses on the numerical treatment, the implementation, and its verification and validation. Chapter 4 is dedicated to the numerical methods, the solution procedure and the implementation in the open-source code OpenFOAM. Thereafter, a series of simple test-cases to verify and validate the implementation are presented in Chapter 5. The complexity is further increased in **Part III**, where the previously verified and validated modeling framework is applied to single-phase combustion. In Chapter 6, the prediction ability of the tabulated-chemistry approach coupled to ATF is demonstrated in the context of gaseous combustion for two operating conditions of the Darmstadt Stratified Burner [183]. The results are also used to analyze and characterize the investigated flames. In a similar manner, Chapter 7 attests the predictive capability of the implementation of the tabulated-chemistry approach coupled to the ESF method. The investigation is performed for the well-known Sandia Flame D configuration [182, 10]. The research activities culminate in **Part IV**, where the approaches are applied to a turbulent spray flame, namely the operating condition EtF6 of the Sydney Spray Burner. Chapter 8 applies the ATF-based modeling framework to this configuration. Herein, the proposed strategies to represent the interaction of droplets with a thickened flame are set aside with state-of-the-art approaches. The ESF-based framework is then applied to the same configuration in Chapter 9 and the predictive capabilities of the novel approach are evaluated. Additionally, the information obtained with the Eulerian stochastic fields are used to assess common presumed PDF shapes. Finally, **Part V** summarizes the main outcomes, reflects upon the achieved objectives and provides a potential outlook for future research.

Chapter 2

Fundamentals of Reactive Thermo-Fluid Systems

In this chapter, the governing equations to describe reactive thermo-fluid systems are first introduced. Thereafter, a summary of the integral aspects relevant to this work is given, i.e. turbulence, combustion, multiphase flows and their characterization. Regarding multiphase flows at subcritical conditions, the respective phases are generally separated by an interface. Nonetheless, both of these phases evolve according to the same set of transport equations. The only peculiarity is the common interface, where both phases exchange mass, momentum and energy.

2.1 Basic Equations of Reactive Thermo-Fluid Systems

In thermo-continuum mechanics, any extensive scalar quantity Φ occupying a volume V with the boundaries S is defined as

$$\Phi = \int_V \rho\phi dV, \tag{2.1}$$

that is the volume integral of its specific value ϕ times the mass density ρ. The balance equation for the scalar ϕ takes the form [99]

$$\int_V \frac{\partial}{\partial t}(\rho\phi)dV = -\int_S \mathbf{J}^\phi \mathbf{n} dS + \int_V \mathbf{\Sigma}^\phi dV, \tag{2.2}$$

where $\partial/\partial t$ represents the (Eulerian) temporal derivative, $\mathbf{J}^\phi$ denotes the convective and non-convective fluxes of the quantity ϕ across S, $\mathbf{n}$ is the boundary-normal unit vector, and $\mathbf{\Sigma}^\phi$ is the rate of production or destruction of ϕ within V. Using Gauss's divergence theorem and through integration over V, Equation 2.2 is reformulated to

$$\frac{\partial}{\partial t}(\rho\phi) = -\nabla \cdot \mathbf{J}^\phi + \mathbf{\Sigma}^\phi. \tag{2.3}$$

Here, ∇ represents the nabla operator, subsequently represented through $\partial/\partial x_i$ following the Einstein summation convention.

With respect to spray combustion, the presence of a liquid-gas interface within V is not unexpected. This yields discontinuous fields at their common interface S^*, which is expressed by the jump condition [99]

$$\left[\rho u_n \phi\right] + \left[\mathbf{n} \cdot \mathbf{J}^\phi\right] = \mathbf{\Sigma}^\phi_{S^*}, \tag{2.4}$$

where $[\,\cdot\,]$ stands for the jump of the quantities across the discontinuity and u_n the normal displacement velocity of S^* relative to the material phase.

Subsequently, the transport equations for reacting single phase flows are presented. This facilitates the discussion of turbulence and combustion that follow this section. The effect of a second phase in the transport equations, represented via source terms, is for now omitted and will be introduced in Chapter 3.

The transport of the fundamental properties of mass, momentum, species mass fractions and enthalpy all follow the basic formulation introduced in Equation 2.3, with specific expressions for $\mathbf{J}^\phi$ and $\mathbf{\Sigma}^\phi$. The transport equations for mass and momentum read

$$\frac{\partial \rho}{\partial t} + \frac{\partial}{\partial x_i}\big(\rho u_i\big) = 0, \tag{2.5}$$

$$\frac{\partial \rho u_i}{\partial t} + \frac{\partial}{\partial x_j}\big(\rho u_i u_j\big) = \frac{\partial}{\partial x_i}\sigma_{ij} + \rho f_i, \tag{2.6}$$

where u_i denotes the i^{th} Cartesian velocity component, f_i any external or body force per unit mass in i^{th} direction and σ_{ij} the Cauchy stress tensor.

With respect to reacting systems, it is common to represent the mixture composition through species mass fractions Y. In that context, the mass fraction of species k, Y_k, is subject to changes caused by convective and diffusive transport, and chemical reaction

$$\frac{\partial \rho Y_k}{\partial t} + \frac{\partial}{\partial x_i}\Big[\rho\big(u_i + V_{k,i}\big)Y_k\Big] = \rho\dot{\omega}_k. \tag{2.7}$$

The expression $\dot{\omega}_k$ denotes the rate of production or destruction of species k through chemical reaction and $V_{k,i}$ represents the i^{th} velocity component of species k relative to the mixture. The transport of the enthalpy h is given by

$$\frac{\partial \rho h}{\partial t} + \frac{\partial}{\partial x_i}\big(\rho h u_i\big) = \frac{Dp}{Dt} + \tau_{ij}L_{ij} + \frac{\partial q_i}{\partial x_i} + \frac{\partial}{\partial x_i}\Big(\rho \sum_{k=1}^{n_s} h_k Y_k V_{k,i}\Big) + \rho\dot{Q}, \tag{2.8}$$

where p is the pressure, q_i the heat flux vector component in i^{th} direction, τ_{ij} the deviatoric part of the Cauchy stress tensor σ_{ij}, L_{ij} the velocity gradient matrix, and $\dot{Q}$ any heat source/sink.

2.2 Constitutive Relations and Simplifications

In the case of Navier-Stokes-Fourier fluids, as assumed in this work, the following expressions for the stress tensor

$$\sigma_{ij} = -p\delta_{ij} + 2\mu\left[\frac{1}{2}\left(\frac{\partial u_i}{\partial x_j} + \frac{\partial u_j}{\partial x_i}\right) - \frac{1}{3}\frac{\partial u_k}{\partial x_k}\delta_{ij}\right], \tag{2.9}$$

and the heat flux vector

$$q_i = -\lambda\frac{\partial T}{\partial x_i}, \tag{2.10}$$

are obtained. Here, μ denotes the dynamic viscosity and λ the thermal conductivity of the mixture, respectively. Note that the term $\frac{1}{2}\big(\frac{\partial u_i}{\partial x_j} + \frac{\partial u_j}{\partial x_i}\big)$ in Equation 2.9 is often referred to as the rate of strain S_{ij}.

The above set of equations is supplemented by so-called constitutive equations. For a pure fluid under the ideal gas assumption, the thermodynamic properties are related through the following equation of state:

$$p = \frac{\rho R T}{M}, \tag{2.11}$$

with the universal gas constant R and the fluids molar mass M. In this work, it is assumed that the mixture properties can be represented by a mixture of n_s ideal gases, so that

$$M = \left(\sum_{k=1}^{n_s} \frac{Y_k}{M_k} \right)^{-1}. \tag{2.12}$$

Furthermore, all reacting flows in this work are characterized by low Mach numbers ($Ma < 0.3$), where the effects of compressibility are insignificant. Following Williams [205] and Poinsot and Veynante [148], this permits the density to be decoupled from the pressure, thus simplifying Equation 2.11 to

$$\rho = \frac{p_{th} M}{R T}, \tag{2.13}$$

where p_{th} is the (constant) thermodynamic pressure.

Finally, a definition is required for the species diffusion velocity $\mathbf{V}_k$ in Equations 2.7 and 2.8. This velocity is decomposed into two parts, one related to the temperature gradient (based on the Soret effect), and one that is purely diffusive (driven by species gradients). In this work, the Soret effect is neglected. Under this assumption, the diffusion velocities can be obtained by solving a system of equations of size n_s^2 [205], which is a computationally challenging undertaking. In this work, the Lewis number is assumed to be unity for all species, which yields the following expression [148]

$$V_{k,i} = \frac{\mathcal{D}}{Y_k} \frac{\partial Y_k}{\partial x_i} = \frac{\lambda}{\rho c_p} \frac{1}{Y_k} \frac{\partial Y_k}{\partial x_i}, \tag{2.14}$$

with the Lewis number

$$Le = \frac{\lambda}{\rho c_p \mathcal{D}} = 1. \tag{2.15}$$

Here, $\mathcal{D}$ and c_p denote the diffusion coefficient (equal for all species) and heat capacity at constant pressure of the mixture, respectively. The diffusion coefficient can also be expressed by relating the diffusive species and momentum transport through the Schmidt number

$$Sc = \frac{\mu}{\rho \mathcal{D}}. \tag{2.16}$$

By inserting Equations 2.14, 2.15 and 2.16 in Equation 2.7, one obtains

$$\frac{\partial \rho Y_k}{\partial t} + \frac{\partial}{\partial x_i} \Big(\rho u_i Y_k \Big) = \frac{\partial}{\partial x_i} \left(\frac{\mu}{Sc} \frac{\partial Y_k}{\partial x_i} \right) + \rho \dot{\omega}_k. \tag{2.17}$$

Combining the approximation of the diffusion velocity using the Fickian Equation 2.14 and the $Le = 1$ assumption with the expression for the heat flux vector in Equation 2.10 permits to considerably simplify the enthalpy transport [142]. Additionally, by omitting any enthalpy variations due to changes in the pressure, neglecting viscous heating and in the absence of any external sources of enthalpy, Equation 2.8 reduces to

$$\frac{\partial \rho h}{\partial t} + \frac{\partial}{\partial x_i} \big(\rho h u_i \big) = \frac{\partial}{\partial x_i} \left(\frac{\mu}{Pr} \frac{\partial h}{\partial x_i} \right), \tag{2.18}$$

where the enthalpy diffusion is expressed in terms of the Prandtl number

$$Pr = \frac{\mu c_p}{\lambda}. \tag{2.19}$$

Note that the unity Lewis number assumption results in $Sc = Pr$, as can be deduced from Equations 2.15 and 2.16.

2.3 Turbulence

The flow regime is an important attribute in many fluid-flow relevant applications. It can be categorized as either laminar, turbulent, or in a transition state between the two. Note that whichever regime occurs, the fluid flow is fully described by the balance equations introduced above. However, the characteristics of the flow in the laminar or turbulent regimes are very different. While laminar flows appear almost deterministic and regular, their turbulent counterparts are mainly characterized as chaotic, quasi-stochastic, unsteady, rotational and highly diffusive [154, 102]. In the former, the flow is characterized by a dominant momentum diffusion compared to momentum convection. In turbulent flows, by contrast, this balance is shifted towards higher momentum convection and lower diffusion. Consequently, small perturbations are able to evolve into large structures, which eventually influence the flow behavior at large scales. The balance between convective and diffusive terms is represented by the Reynolds number Re, which is in turn used to categorize the fluid flow as either laminar or turbulent

$$Re = \frac{\rho U L}{\mu}. \tag{2.20}$$

Here, U and L denote characteristic (or representative) velocity and length quantities for a given flow configuration. Considering a flow through a round pipe, the transition from laminar to turbulent flow happens at a Reynolds number of approximately 2000 [138].

Turbulence plays a crucial role in many reacting fluid-flow-related technical applications, for instance internal combustion systems, rockets or gas turbines [148]. In such flows, the diffusive effects of the turbulence are often used to enhance mixing. On the other hand, turbulence yield higher pressure losses. The impact of turbulence on combustion is depicted in Figure 2.1, which presents a turbulent diffusion flame with a jet Reynolds number of 22400. A detailed introduction to the configuration is provided in Chapter 7. The velocity magnitude contours shown in the upper part illustrates the chaotic nature typical for a turbulent flow. The impact of the turbulence on the reaction process becomes apparent when considering the temperature contours shown in the lower part of Figure 2.1. The turbulent eddies interact with the reaction zone, thus increasing the flame surface and the fuel burning rates. Likewise, the combustion reaction influences the turbulence as it alters the previously mentioned balance between the momentum convection and diffusion. This may either enhance or weaken the turbulent character of the flow [148]. From Figure 2.1, it can be inferred that the behavior of a turbulent reacting flow cannot be deterministically predicted. This holds true temporally and spatially due to its quasi-stochastic, three-dimensional, unsteady and dissipative character.

The random nature of turbulence makes statistical methods necessary to characterize such flows. For instance, the temperature and velocity at a specific position may vary substantially in time and some states will be more probable than others. Generally, instead of studying the probability density distribution directly, the turbulent flow is characterized by the statistical moments of that distribution. The statistical concepts required to

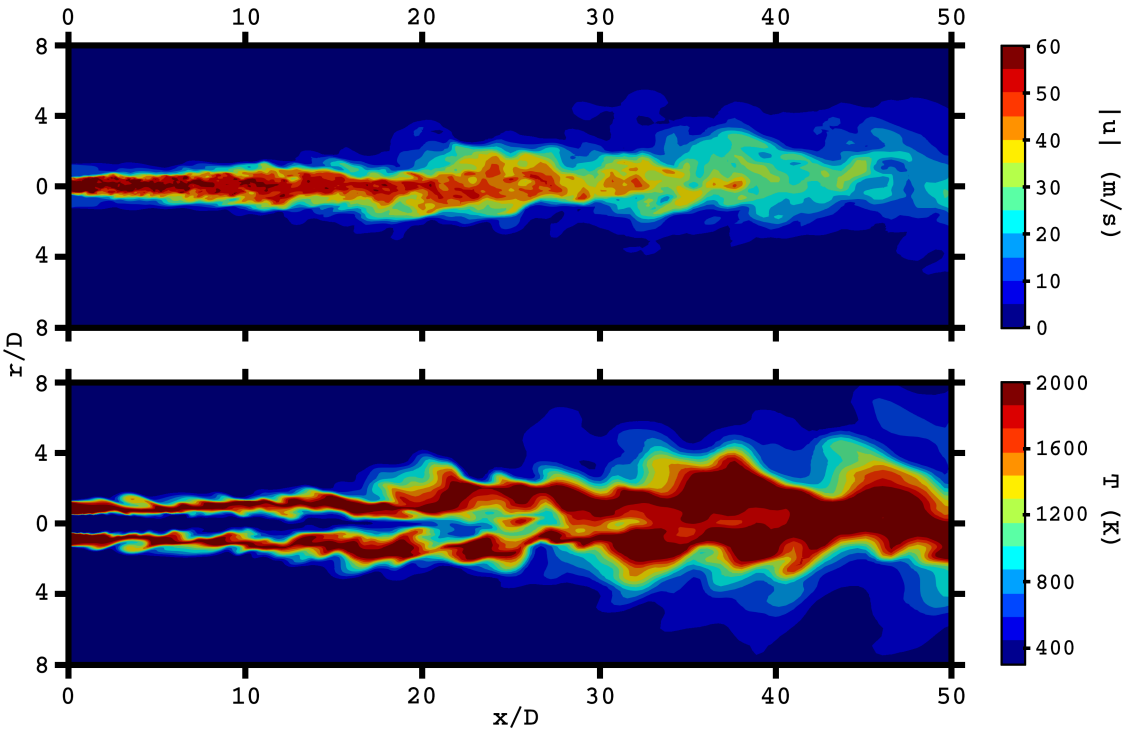

Figure 2.1: Instantaneous contours of velocity magnitude (top) and temperature (bottom) for large eddy simulation of a turbulent methane diffusion flame (Sandia Flame D) with a central jet Reynolds number $Re = 22400$.

describe turbulence are introduced in the next section. A more detailed introduction to this topic can be found in [154, 112].

2.3.1 Statistical Description of Turbulence

An examination of Figure 2.2 reveals why statistical methods are required to describe turbulence and its resulting scalar fluctuations. The left-hand-side of the figure depicts the temporal evolution of a generic scalar quantity ϕ at a specific position x_0 in a statistically stationary turbulent flow. Here, ϕ could be any property of interest, such as the velocity magnitude, the temperature, or a species mass fraction. On the right, the corresponding one-point probability density function (PDF) for the time interval and position considered is depicted. From the temporal profile of ϕ, it can be inferred that the quantity ϕ cannot be predicted. This is why ϕ is generally characterized by using time-averaged quantities, such as the mean $\langle\phi\rangle$, variance $\mathrm{var}(\phi)$, and standard deviation ϕ_{rms}:

$$\langle\phi\rangle = \frac{1}{\Delta t}\int_{t_0}^{t_0+\Delta t} \phi(t')dt', \tag{2.21}$$

$$\mathrm{var}(\phi) = \frac{1}{\Delta t}\int_{t_0}^{t_0+\Delta t} \big(\phi(t') - \langle\phi\rangle\big)^2 dt' = \Big\langle \big(\phi - \langle\phi\rangle\big)^2 \Big\rangle, \tag{2.22}$$

$$\phi_{rms} = \sqrt{\mathrm{var}(\phi)}. \tag{2.23}$$

In this context, the expression

$$\phi' = \phi - \langle\phi\rangle \tag{2.24}$$

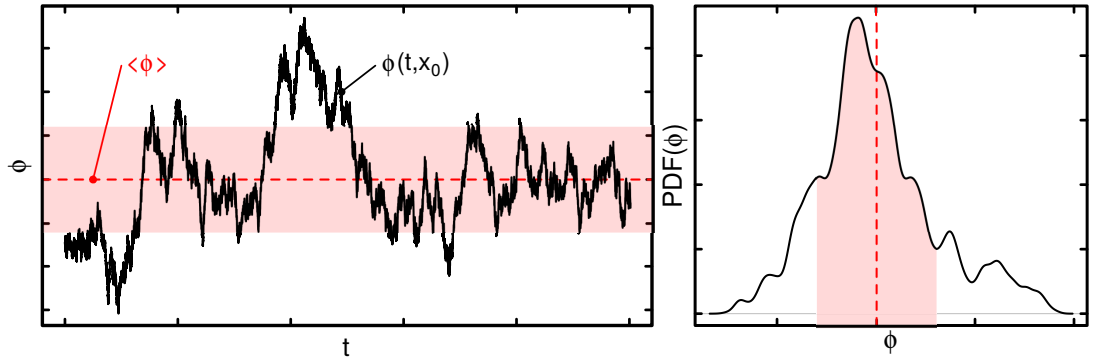

Figure 2.2: Temporal evolution of a generic scalar quantity ϕ probed in a turbulent flow (left) and the corresponding probability density distribution (right). The dashed red line indicates the mean value, whereas the shaded area indicates a region within one standard deviation of the mean.

is often referred to as fluctuation and represents the random deviation of ϕ with respect to its mean.

In view of the investigations presented in subsequent parts of this work, it is worth considering a different approach, which characterizes the process in terms of probabilities. For example, the probability can be evaluated that at a specific time, the value of ϕ at the position x_0 is between two values $\{\phi_{low} \leq \phi \leq \phi_{up}\}$. That probability $\mathcal{P}$ can be evaluated if the PDF of ϕ, $P(\phi)$ is known. In this case, the probability for such event can be evaluated through

$$\mathcal{P}\{\phi_{low} \leq \phi \leq \phi_{up}\} = \int_{\phi_{low}}^{\phi_{up}} P(\phi^*) d\phi^*, \tag{2.25}$$

where ϕ^* denotes the sample space variable. Similarly, the moments of the PDF can be evaluated through integration in sample space, shown here for the mean (or expectation) $\langle\phi\rangle$ and the variance

$$\langle\phi\rangle = \int_{-\infty}^{\infty} \phi^* P(\phi^*) d\phi^*, \tag{2.26}$$

$$\mathrm{var}(\phi) = \int_{-\infty}^{\infty} \Big(\phi^* - \langle\phi\rangle\Big)^2 P(\phi^*) d\phi^*, \tag{2.27}$$

which yield identical results as the Equations 2.21 and 2.22. In Figure 2.2, the expectation is depicted with dashed red lines, whereas the red-shaded area corresponds to the region within one standard deviation of the mean, i.e. $\{\big(\langle\phi\rangle - \phi_{rms}\big) \leq \phi \leq \big(\langle\phi\rangle + \phi_{rms}\big)\}$.

2.3.2 Scales of Turbulent Motion

Turbulence is a multi-scale phenomenon, occurring at a large variety of time and length scales. As will be outlined in a later section of this work, these scales are a central aspect in the modeling of turbulent fluid flows and are therefore briefly discussed. Note that the introduced relations are only valid in a fully developed turbulent flow, which implies a sufficiently high Reynolds number. Following the concept introduced by Richardson [161], turbulence can be seen as an agglomeration of so-called eddies of multiple sizes and

velocities, each representing a coherent turbulent structure. The energy in these structures is referred to as turbulent kinetic energy (TKE)

$$k = \frac{1}{2}\langle u_i' u_i' \rangle = \int_0^\infty E_k(\kappa) d\kappa, \tag{2.28}$$

where $E_k(\kappa)$ denotes the turbulent kinetic energy spectrum in wavenumber space κ. Richardson postulated that the TKE stored in the turbulent structures flows from large to smaller eddies, until the turbulent motion finally reaches a critical scale where the energy is fully dissipated. This concept is commonly described as energy cascade, with large eddies of roughly the characteristic size of the flow configuration l_0 (for instance the jet diameter of a pipe) on one side, and the Kolmogorov scales, the smallest scales of turbulent motion, on the other. In [105], Kolmogorov postulates that at a sufficiently high Reynolds number, all directional information is lost in the energy cascade, yielding an universal, homogeneous and isotropic distribution of the small scales of turbulence, which are characterized by the length scale η, the velocity u_η and the time scale τ_η, known as the Kolmogorov scales

$$\eta \equiv \left(\frac{\nu^3}{\varepsilon}\right)^{\frac{1}{4}}, \quad u_\eta \equiv \left(\nu\varepsilon\right)^{\frac{1}{4}}, \quad \tau_\eta \equiv \left(\frac{\nu}{\varepsilon}\right)^{\frac{1}{2}}. \tag{2.29}$$

These scales solely depend on two parameters, the viscosity ν, and the turbulent kinetic energy dissipation rate ε. The latter describes the rate of energy transfer from large to small scales. From dimensional analysis, the scaling of the turbulent dissipation rate $\varepsilon \sim u^3/l_0$ can be used to derive the following expression for the ratio of the smallest to largest turbulent scales

$$\frac{l_0}{\eta} \sim Re^{\frac{3}{4}}, \tag{2.30}$$

which turns to $\sim Re^{\frac{9}{4}}$ for a three-dimensional flow, suggesting an exponential behavior between the spectrum width and the Reynolds number.

In addition, so-called integral time and length scales of the turbulence can be obtained by correlating the signal of a quantity either temporally or spatially. The integral time scale τ of a turbulent signal at position $\mathbf{x}$ is estimated by means of the autocovariance of the temporal profile of its fluctuation ϕ', normalized by its variance

$$\tau = \int_0^\infty \frac{\langle \phi'(\mathbf{x}, t)\, \phi'(\mathbf{x}, t+s) \rangle}{\mathrm{var}(\phi)(\mathbf{x})} ds. \tag{2.31}$$

Likewise, the integral length scales of the turbulence can be estimated by means of the two-point correlation $\mathbf{R}$, a tensorial quantity expressed by [154]

$$R_{ij}(\mathbf{r}) = \langle \phi_i'(\mathbf{x}, t)\, \phi_j'(\mathbf{x}+\mathbf{r}, t) \rangle. \tag{2.32}$$

For instance, considering the unit vector in the x-direction $\mathbf{e}_1$ yields the following expression for the integral length scale in x- direction

$$L_{11} = \frac{1}{R_{11}(0)} \int_0^\infty R_{11}(\mathbf{e}_1 r) dr. \tag{2.33}$$

Considering homogeneous turbulence, that is a turbulent flow where the respective averages do not vary spatially, the distribution of turbulent scales can be represented by the spectrum tensor of the quantity ϕ

$$\Phi_{ij}(\kappa) = \frac{1}{8\pi^3} \int_{-\infty}^\infty e^{-i\boldsymbol{\kappa}\mathbf{r}} R_{ij}(\mathbf{r}) d\mathbf{r}. \tag{2.34}$$

Accordingly, substituting ϕ_i with u_i in Equation 2.32 yields the velocity spectrum tensor. The integration of the velocity spectrum tensor over a sphere with surface S in wave number space ($\kappa = 2\pi/l$) and contraction yields the energy spectrum [102]

$$E(\kappa) = \frac{1}{2} \int \Phi_{ij}(\boldsymbol{\kappa}) dS(\kappa), \tag{2.35}$$

which is schematically shown in Figure 2.3. The energy spectrum describes how the kinetic energy is distributed across the wavenumber space. The spectrum can be divided into three characteristic subranges: the *energy-containing*, the *inertial*, and the *dissipative* range [154]. Unsurprisingly, the energy-containing range includes the majority of the turbulent kinetic energy. This energy is mainly stored in the largest turbulent structures and originates from the mean flow field. At the other end of the spectrum, i.e. at scales around the Kolmogorov scales, the energy is transformed into heat in the dissipative range. Between these two subranges lies the inertial range. Kolmogorov postulated that in this range, the viscous effects are negligible and that the energy transfer from larger to smaller eddies only depends on the dissipation rate ε. As can be deduced from Equation 2.28, the integration of $E(\kappa)$ across wavenumber space defines the turbulent kinetic energy.

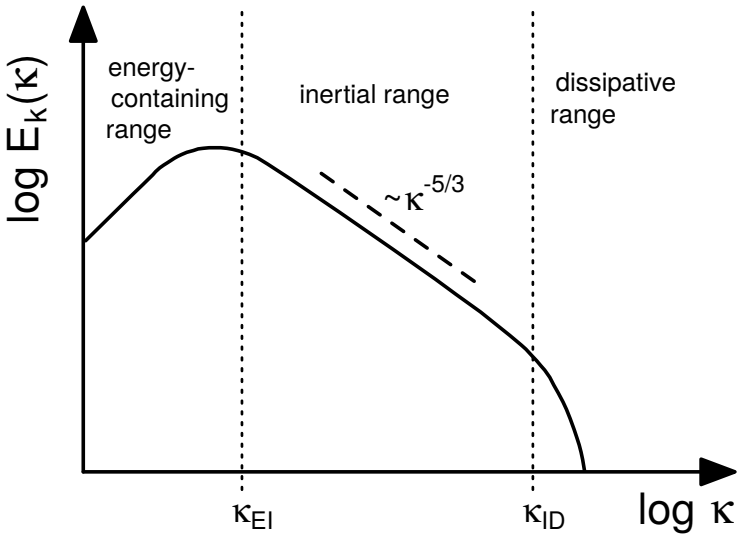

Figure 2.3: Schematic representation of the turbulent energy spectrum $E(\kappa)$. The dashed vertical lines at $\kappa_{EI} \approx 12\pi/l_0$ and $\kappa_{ID} \approx \pi/30\eta$ separate the different subranges generally used to describe the turbulent energy cascade [154].

2.4 Combustion

The goal of this work is to deepen the knowledge on combustion and spray combustion and to improve the current modeling state-of-the-art to simulate such problems. But what is combustion, exactly? Here, a rather narrow definition of combustion is used: it is an exothermic chemical reaction with the presence of a flame front. Combustion generally involves the reaction of a fuel and an oxidizer. Note that in this work, it is assumed that all chemical reactions take place in the gaseous phase. The simplest perspective is that of the thermodynamics, where a chemistry is reduced to a single global reaction with one

initial and one end state. Let us consider the combustion of methane, for which the global reaction can be written as

$$\mathrm{CH_4} + 2\,\mathrm{O_2} \longrightarrow 2\,\mathrm{H_2O} + \mathrm{CO_2} \qquad \Delta_R H = -802.3\,\mathrm{kJ\,mol^{-1}} \tag{2.36}$$

This equation is stoichiometric, because all the fuel (CH_4) and oxidator (O_2) are converted to products ($CO_2 + H_2O$). The reaction is exothermic, as can be deduced from the negative sign for the heat of reaction $\Delta_R H$. The problem with this representation is that it lacks information on how the reactants react to the products. In reality, a global reaction is decomposed into a multitude of so-called elementary reactions, all happening simultaneously and at different rates. This involves the production and destruction of a multitude of species, which are left aside if one only considers the two states, i.e. unburnt and burnt. The representation of the course of the reaction, that is its temporal evolution, is a matter of reaction kinetics. Subsequently, the main concepts of reaction kinetics are briefly introduced.

2.4.1 Reaction Kinetics

As previously mentioned, reaction kinetics deals with the temporal evolution of the various chemical species involved in the combustion process. The accurate representation of reaction kinetics is still an ongoing research topic. This is because novel reaction pathways are still discovered. The representation of methane combustion kinetics is often treated using the GRI-3.0 mechanism [188], which includes a total of 53 species, for which the evolution is described by 325 elementary reactions. In general, these elementary reactions all take the form

$$\sum_{k=1}^{N} \nu'_{k,j} \mathcal{M}_k \rightleftharpoons \sum_{k=1}^{N} \nu''_{k,j} \mathcal{M}_k \quad j = (1, 2, ..., N_r) \tag{2.37}$$

where $\mathcal{M}_k$ denotes the k^{th} chemical specie and the subscript j the j^{th} of N_r elementary reaction. The variables $\nu'_{k,j}$ and $\nu''_{k,j}$ respectively represent the stoichiometric coefficients on the reactant and product side. This system of reactions is directly coupled to the species transport equation for the species k (Equation 2.7) via the rate of production or destruction term $\dot{\omega}_k$, which corresponds to the sum of the production and destruction terms of the species in all elementary reactions

$$\dot{\omega}_k = \sum_{j}^{N_r} \dot{\omega}_{k,j} = M_k \sum_{J}^{N_r} \left(\nu''_{k,j} - \nu'_{k,j}\right) \mathcal{Q}_j, \tag{2.38}$$

with the reaction rate of the j^{th} reaction, $\mathcal{Q}_j$, which depends on the molar concentration of species k, c_k and on the reaction rate constants for the forward and backward reactions $\mathcal{K}_{j,f}$ and $\mathcal{K}_{j,b}$, and reads

$$\mathcal{Q}_j = \mathcal{K}_{j,f} \prod_{k}^{N_s} c_k^{\nu'_{k,j}} - \mathcal{K}_{j,b} \prod_{k}^{N_s} c_k^{\nu''_{k,j}}. \tag{2.39}$$

The reaction rate constants are calculated using an Arrhenius-type equation, exemplary shown for the forward reaction rate constant

$$\mathcal{K}_{j,f} = A_{j,f} T^{\beta_{j,f}} e^{-\frac{E_{j,f}}{RT}}, \tag{2.40}$$

with the pre-exponential factor $A_{j,f}$, the temperature exponent $\beta_{j,f}$ and the activation energy for the forward reaction $E_{j,f}$. The reaction rate constant for the backward reaction $\mathcal{K}_{j,b}$ is obtained in an analogous manner.

2.4.2 Combustion Regimes

As outlined previously, fluid transport and chemical reaction are two interwoven processes. To take into account their interaction, it is helpful to introduce two canonical flame types: the premixed flame and the diffusion flame. For the premixed flame type, fuel and oxidizer are mixed prior to the combustion process, while the diffusion flame archetype is characterized by fuel and oxidizer entering the reaction zone via separate paths or streams. As a consequence, mixing and reaction take place in direct proximity. It should be noted that even though these two generic types are helpful to classify flames, the presence of a purely premixed or diffusion flame in technical applications is relatively rare. Often, both flame regimes are encountered in the same configuration, which is commonly referred to as partially premixed combustion.

2.4.2.1 Premixed Flame

If the fuel and oxidizer are mixed before entering the reaction zone or prior to ignition, one speaks of premixed combustion or of a premixed flame. This process is schematically illustrated in Figure 2.4a, where a mixture of fuel and oxidizer approaches the flame (red line). In this context it is helpful to introduce a measure to describe this mixture. For this purpose, the equivalence ϕ is introduced

$$\phi = \left(\frac{Y_{fuel}}{Y_{ox}}\right) \Big/ \left(\frac{Y_{fuel}}{Y_{ox}}\right)_{st}, \tag{2.41}$$

which describes the ratio of the fuel and oxidizer mass fractions compared to the ratio present at stoichiometry (subscript $(\cdot)_{st}$). Here, $\phi < 1$ denotes a sub-stoichiometric (lean) mixture, and $\phi > 1$ represents an over-stoichiometric (fuel-rich) composition. The equivalence ratio is a helpful measure to quantify premixed mixtures. In view of the restrictions related to the definition of the equivalence ratio on the burnt side of the flame, it is better to use a measure which is conserved across the reaction zone. Such properties can be obtained by defining a suitable mixture fraction Z, which is generally based on the element mass fractions found in the fuel [14]. Depending on the elementary composition of the fuel, an additional normalization may be required to to ensure that Z ranges from 0 to 1. For the conserved quantity Z, it is then possible to introduce a transport equation, which, under the assumption of equal diffusivity for all species, takes the following form

$$\frac{\partial \rho Z}{\partial t} + \frac{\partial}{\partial x_i}(\rho Z u_i) = \frac{\partial}{\partial x_i}\left(\frac{\mu}{Sc}\frac{\partial Z}{\partial x_i}\right). \tag{2.42}$$

Accordingly, the mixture fraction does not change across a premixed flame front. Note that from the mixture fraction, it is also possible to reconstruct the equivalence ratio by using the relationship

$$\phi = \frac{1 - Z_{st}}{Z_{st}}\frac{Z}{1 - Z}, \tag{2.43}$$

where Z_{st} denotes the stoichiometric mixture fraction.

To get a better understanding of the premixed flame, the profiles of some characteristic quantities which change across the flame front are shown in Figure 2.4b. These profiles describe the evolution of the respective quantities along the spatial coordinate s displayed in Figure 2.4a. The process can be described as follows: (1) far away from the flame front, the mixture is in a cold state; even though the mixture may be within the flammability limit, there is not enough energy to ignite it. (2) As the mixture approaches the flame,

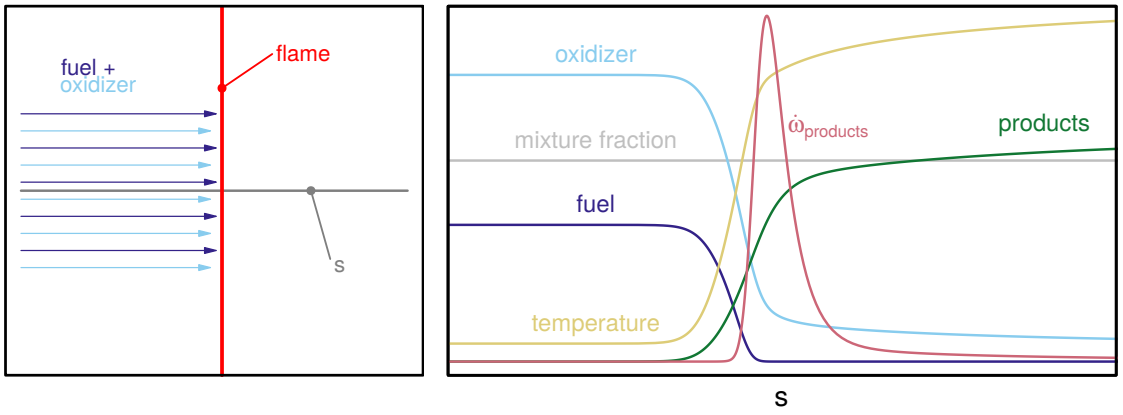

(a) (b)

Figure 2.4: (a) Schematic representation of a generic premixed flame where oxidizer and fuel are mixed prior to entering the reaction zone. (b) Profiles of oxidizer, fuel, product concentration and source term, and temperature along the coordinate s defined in (a).

the fuel and oxidizer are preheated by thermal diffusion from the flame front and the temperature starts to rise. At some point, the activation energy for the reaction onset is reached (3), which is where the zone of reaction begins and is characterized by large chemical source terms for the reaction products. As previously stated, this process involves the production and consumption of numerous species. As can be observed in Figure 2.4b, the zone of strong chemical reactions is narrow. However, after the peak in the chemical reaction source term, the product concentration and temperature still continue to increase. In this region, generally referred to as oxidation zone, the combustion reaction slowly converges towards chemical equilibrium. This zone is dominated by chemical reactions occurring at larger time-scales. These are sufficient to sustain the further increase in temperature. In view of the investigations presented later in this work, it is essential to introduce the notions of the flame thickness and the flame speed. Both are quantities used to characterize premixed flames. The flame thickness can be defined with respect to any suitable quantity, such as the temperature or product mass fraction, and relates unburnt values (subscript $(\cdot)_u$) and burnt values (subscript $(\cdot)_b$) to the maximum gradient of the considered quantity ϕ

$$\delta_l = \frac{\phi_b - \phi_u}{\max\left(|\frac{\partial \phi}{\partial s}|\right)}. \tag{2.44}$$

For instance, the flame thickness can be defined based on the mass fraction of CO_2. The second quantity of interest is the laminar flame speed, which stands for the speed at which the premixed flame would propagate into a resting mixture of fuel and oxidizer. Generally, there are many possible ways to determine the laminar flame speed, an overview of which is given in [148, 108]. In this work, the definition based on the chemical source term of the k-th species is used

$$s_l = \frac{1}{\rho_u (Y_{k,b} - Y_{k,u})} \int_{-\infty}^{\infty} \rho \dot{\omega}_k ds. \tag{2.45}$$

2.4.2.2 Diffusion flame

Unlike their premixed counterpart, diffusion (or non-premixed) flames are characterized by oxidizer and fuel entering the reaction via separate streams. This is a fundamental

difference as the flame cannot propagate into a burnable mixture, but is spatially constrained by the local composition. This implies a combustion process taking place in the presence of mixture fraction gradients, which is fundamentally different from premixed combustion. One prominent example of this non-premixed flame type is the counterflow diffusion flame, which is schematically shown in Figure 2.5a. In this flame, the fuel enters the domain from the left, while the oxidizer flows from the right towards the reaction zone. Both move with their respective velocities u_{fuel} and $u_{oxidizer}$ towards the reaction zone, which is located close to the stagnation plane. In this counterflow situation, the strain rate a can be defined as

$$a = \frac{u_{fuel} + u_{oxidizer}}{L_{domain}}, \tag{2.46}$$

where L_{domain} denotes the distance between the fuel and oxidizer inlets. The strain rate

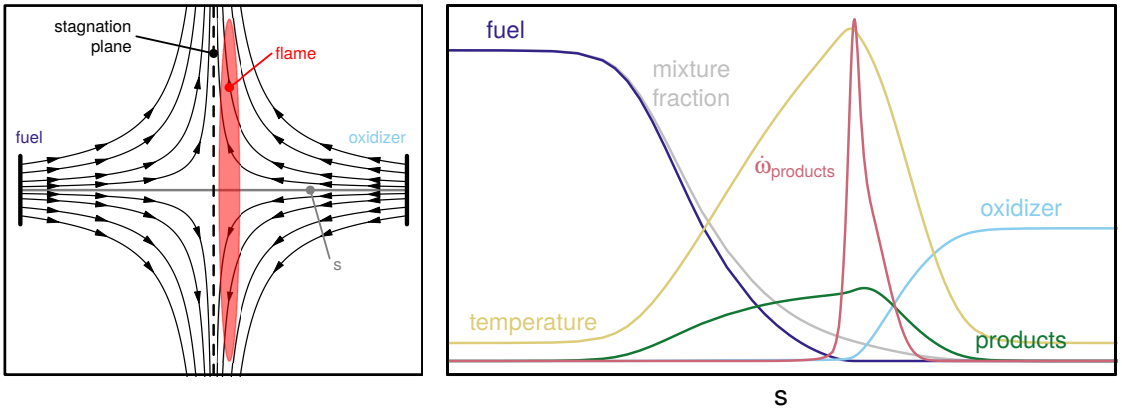

(a) (b)

Figure 2.5: (a) Schematic representation of a counterflow flame, a typical configuration where the oxidizer and fuel enter the reaction zone via separate paths. (b) Profiles of oxidizer, fuel and product concentration and source term, and temperature along the coordinate s shown in (a).

is an important measure as it determines the spatial structure of the flame. The strain rate also determines another important quantity: the scalar dissipation rate χ, which is defined as

$$\chi_Z = 2\mathcal{D}\left(\frac{\partial Z}{\partial s}\frac{\partial Z}{\partial s}\right). \tag{2.47}$$

The strain rate and the dissipation rate are directly connected. An increase in a results in an increase in χ. In analogy to the premixed flame, Figure 2.5b presents the spatial profiles of several quantities along the flame orthogonal coordinate s. The reaction zone is characterized by the strong peak in the chemical source term of the products $\dot{\omega}_{products}$. In this region, the chemical time scales are small compared with the mixing or diffusion time scales of the reactants. This yields a combustion process dominated by diffusion, where the chemical reaction takes place as soon as fuel and oxidizer are brought together. In consequence, diffusion flames cannot be characterized by any flame speed, as the flame position is spatially fixed. Neither can the flame structure be described in terms of a flame thickness, since the structure of the reaction zone is mainly determined by the strain rate.

2.4.3 Flame-Turbulence Interaction

Up to this point, turbulence and flame have been introduced and treated separately. However, in technical applications, the two phenomena are strongly connected. On one hand,

turbulence influences the flame through wrinkling, thus potentially increasing the flame surface and the chemical reaction. On the other hand, the changing balance of inertial and viscous forces across the flame front may alter the turbulence itself. The impact of turbulence on a premixed and a diffusion flame is schematically illustrated in Figure 2.6. In both cases, the turbulent eddies yield a perturbation of the flame.

In the case of premixed combustion, the turbulent eddies wrinkle the flame, which increases the flame surface. This in turn enhances the consumption rate of the reactants and results in a higher flame speed. In fact, the turbulent flame speed s_t is directly related to the flame surface area of the turbulent premixed flame A_t through the relation

$$\frac{A_t}{A} = \frac{s_t}{s_l}, \tag{2.48}$$

where A denotes the laminar flame surface area.

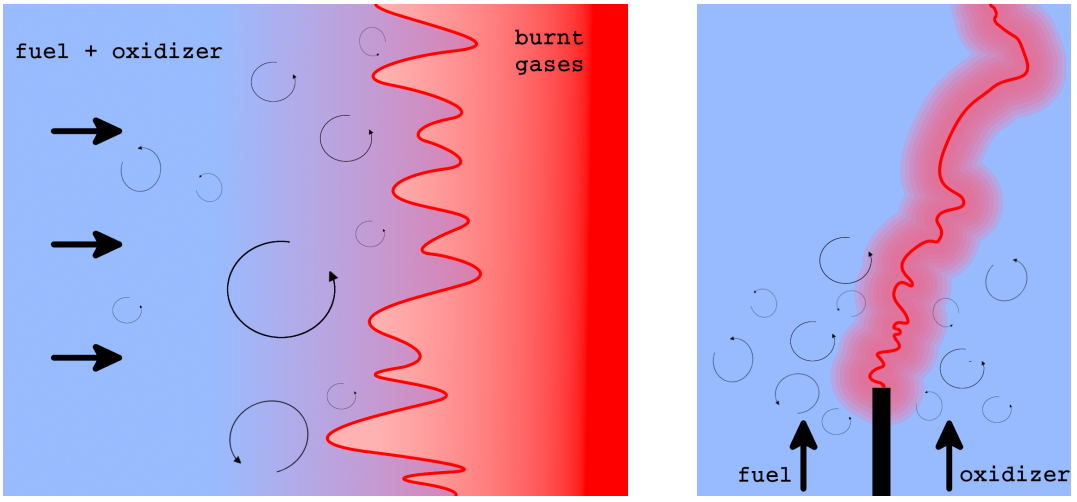

(a) (b)

Figure 2.6: Schematic illustration of the flame turbulence interaction, for (a) a premixed, and (b) a diffusion flame.

In the case of non-premixed flames, the reaction depends on the diffusion of fresh gases towards the reaction zone. This process involves longer timescales than in premixed combustion, where the mixing has already occurred. As a result, the diffusion flame is more likely to be influenced by the turbulent motion, which is due to the high impact of the turbulence on the diffusion speed of the species [148].

2.4.4 Characterization of Turbulent Combustion

The previous section describes only vaguely the interaction of turbulence and combustion. In reality, it is possible to subdivide each of the two flame archetypes into several regimes, depending on the characteristics of the turbulence and of the combustion process. The aim of this section is to introduce these different subregimes. In order to perform this differentiation, the turbulence is characterized by the two parameters u' and L_t. Both are integral quantities and can be used to define a characteristic time scale τ_t and a turbulence Reynolds number Re_t

$$\tau_t = \frac{L_t}{u'}, \qquad Re_t = \frac{L_t u'}{\nu}. \tag{2.49}$$

Similarly, a characteristic time scale can be defined for the premixed flame as

$$\tau_c = \frac{\delta_l}{s_l}, \tag{2.50}$$

where the flame thickness is here approximated by $\delta_l = \nu / s_l$. The characteristic time scales are used to define the Damköhler number

$$Da = \frac{\tau_t}{\tau_c}, \tag{2.51}$$

which relates the characteristic turbulent time scale and the combustion time scale. At large Damköhler numbers, the scales of the chemistry are much smaller than the turbulent time scale and the turbulence is therefore not able to significantly alter the structure of the flame. This is different for the case $Da << 1$, where the chemical time scale is significantly larger than the turbulence time scale. In this scenario, the turbulence is able to affect the combustion process. An additional dimensionless parameter is the Karlovitz number Ka, which is used to characterize the interaction of the smallest turbulent structures with the flame

$$Ka = \frac{\tau_c}{\tau_\eta}. \tag{2.52}$$

Here, τ_η refers to the Kolmogorov time, defined in Equation 2.29. Using the previously introduced dimensionless parameters, Peters [141] proposed the well-known regime diagram for premixed combustion shown in Figure 2.7a. The diagram is split into four different sectors. The first region, represented by the grey area in the bottom left of the diagram is denoted as *laminar combustion regime*. This region is demarcated by the line $Re_t = 1$, where the perturbation of the flow field are so small that there is no perceivable interaction between them and the flame. This is different for the so-called *flamelet region*, which contains the *wrinkled flamelet* and *corrugated flamelet* regimes. Both zones are found above the $Re_t = 1$ line, but below the $Ka = 1$ line, indicating that even though the turbulence influences the flame, no turbulent scale is able to modify the inner structure of the flame. The differentiation between the *wrinkled flamelet* and the *corrugated flamelet* regime is based on the ratio between the turbulent fluctuation of the velocity field and the laminar flame speed. In the corrugated case, i.e. $u' > s_l$, the turbulence is able to distort the flame front until pockets of fresh reactants and burnt products form. Below that limit, the turbulence is not strong enough to yield such effects. In between the $Ka = 1$ and $Ka = 100$ is the *thickened-wrinkled flame* zone. If the condition $Da > 1$ is met, the integral time scale of the turbulence is still larger than the chemical time scale. However, the smallest scales of the turbulence are able to enter the flame and modify its structure. However, as pointed out in [148], it seems that below the $Ka = 100$ limit, the influence of the Kolmogorov scales on the premixed flame is limited to the preheating zone while the reaction zone remains mostly unaffected. The region above this limit is called the *thickened flame regime*. In this region, the chemical scales are long compared to the time scales of the turbulence. Hence, the inner structure of the flame is strongly modified by the turbulence.

Going over to the non-premixed counterpart, some additional quantities must be introduced. As previously outlined, diffusion flames cannot be characterized by the typical quantities of flame thickness and flame speed, as used for premixed flames. Therefore, the diffusion layer thickness l_d is introduced. Picturing a flame where pure fuel, corresponding to a mixture fraction $Z = 1$ and oxidizer ($Z = 0$) mix and react, the diffusion layer thickness defines the width of the region where the mixture fraction changes. The second property of interest is the reaction zone thickness l_r, which describes the region of the

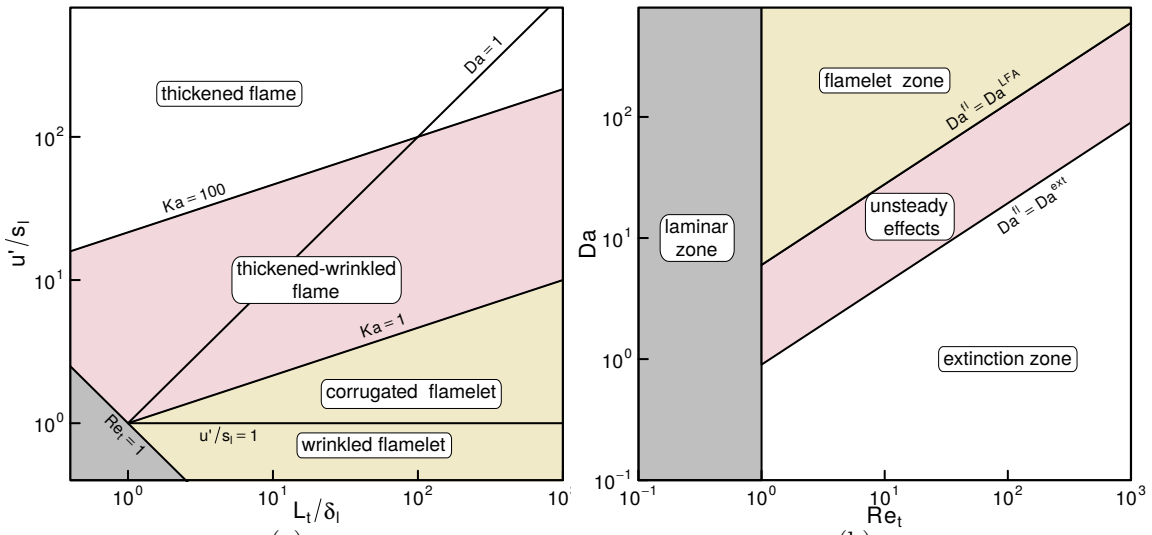

Figure 2.7: Proposed diagrams to characterize (a) turbulent premixed combustion [141] and (b) turbulent non-premixed combustion [148].

flame where chemical reaction occurs. Even though both properties depend on the local strain rate, it is possible to state that the reaction zone thickness is much smaller than the diffusion layer thickness. This is shown in Figure 2.5b, where the zone of reaction (represented by the chemical source term of the products) is significantly narrower than the region where gradients of fuel and oxidizer are perceived. In a turbulent non-premixed flame, the thickness of the diffusion layer can be approximated via

$$l_d \approx \sqrt{\frac{\mathcal{D}_{st}}{\widetilde{\chi}_{st}}}, \tag{2.53}$$

where $\widetilde{\chi}_{st} = \langle \rho\chi | Z_{st} \rangle / \langle \rho | Z_{st} \rangle$ denotes the Favre mean dissipation rate conditioned on the stoichiometric mixture fraction. Additionally, $\widetilde{\chi}_{st}$ can be used to estimate the diffusion time scale

$$\tau_d \approx (\widetilde{\chi}_{st})^{-1}, \tag{2.54}$$

which in turn is used to define the flame Damköhler number

$$Da^{fl} = \frac{\tau_d}{\tau_c}. \tag{2.55}$$

With this definition, it is possible to sketch the regime diagram shown in Figure 2.7b, which is divided into four regions [148]. Similarly to its premixed counterpart, the region $Re_t < 1$ denotes the *laminar zone*. The next region is termed the *flamelet zone*. In this case, Da^{fl} is sufficiently high to assume a thin flame, which is often connected to a Laminar Flamelet Assumption (LFA). The other extreme is the so-called *extinction zone*, which is delimited by the condition $Da^{fl} < Da^{ext}$. Between the two previously mentioned regions lies the *unsteady effects* zone. In this region, the reaction layer thickness is of the order of the Kolmogorov scale η and the reaction is disturbed by the smallest scales of the turbulence. Note that, as pointed out by Poinsot and Veynante [148], the diagrams shown above are both derived based on several assumptions so that the combustion can be characterized by a reduced set of parameters. As a consequence, they cannot deliver a complete perspective on the different scenarios occurring in turbulent combustion. The

discussion above is, however, sufficient to make sense of the assumptions presented in later parts of this work.

2.5 Two-Phase Flows

The topic of turbulent spray combustion is a key element of this work. This involves, beside the previously treated topics, the interaction of the gaseous carrier phase with an additional liquid phase, which means that the flow considered is a two-phase system. This section introduces further relations that inherently accompany the treatment of two-phase flows.

2.5.1 Characterization of Two-Phase Flows

The characterization of two-phase flows is most effectively performed using integral quantities. The first of these is the liquid volume fraction α_l, which represents the ratio of the volume occupied by the liquid phase to the total volume. Considering a dispersed liquid phase consisting of N entities (droplets, ligaments etc.), the liquid volume fraction reads

$$\alpha_d = \frac{V_d}{V_{total}} = \frac{\sum_i^N V_i}{V_{total}}. \tag{2.56}$$

Here, V_i is the volume of the i^{th} liquid structure. Assuming that all liquid structures are spherical yields $V_i = \frac{1}{6}\pi d_i^3$, where d_i denotes the equivalent diameter to obtain V_i. Other quantities used to describe a disperse phase within a volume V are the number density n_d and the mass loading η_d

$$n_d = \frac{N_d}{V}, \tag{2.57}$$

$$\eta_d = \frac{\dot{m}_d}{\dot{m}_c} = \frac{\alpha_d \rho_d |\mathbf{u}_d|}{(1-\alpha_d)\rho|\mathbf{u}|}, \tag{2.58}$$

with the liquid phase density ρ_d and the liquid phase velocity magnitude $|\mathbf{u}_d|$. Another important integral quantity is the mean distance between the liquid particles, often denoted as inter-particle spacing L_d. If the particles are regularly arranged within a cubic volume V, the inter-particle spacing can be estimated using [191]

$$\frac{L_d}{d_d} = \left(\frac{\pi}{6\alpha_l}\right)^{\frac{1}{3}}. \tag{2.59}$$

At this point it is important to note that the quantities introduced here are used when the liquid phase is in a dispersed state. This presumes that the liquid phase has already undergone all processes, i.e. primary and secondary breakup, which lead to that dispersed condition. Whether or not the atomization process is ongoing can be assessed by relating the surface tension σ_d and the inertial forces acting on a liquid structure. This dimensionless ratio is defined as the Weber number

$$We = \frac{\rho d |\mathbf{u}_d - \mathbf{u}|}{\sigma_d}. \tag{2.60}$$

The term $\mathbf{u}_d - \mathbf{u}$ represents the velocity difference between particle and carrier, often termed the slip velocity $\mathbf{u}_{slip}$. Note that the Weber number is not an integral property

of the disperse phase, but varies from droplet to droplet. The integral Weber number can be obtained through integration over all liquid structure in a volume. At high Weber numbers, the aerodynamic forces outweigh the surface tension. This causes the droplets to distort and eventually disintegrate. For $We < 5$, the surface tension dominates, implying that no breakup effects prevail. As stated by Kuo and Acharya [109], a spherical shape can be assumed under such conditions. More details on the topic of liquid atomization can be found in [110].

The interaction of the disperse phase with the carrier phase can be quantified by comparing the two characteristic time scales τ_d and τ_f, which denote a suitable time scale for a droplet and its carrier medium, respectively. This interaction is expressed by the Stokes number

$$St = \frac{\tau_d}{\tau_f}. \tag{2.61}$$

Thereby, a small Stokes number indicates a droplet following the changes in the carrier motion. In contrast, when St is large, the time scale of the particle are larger than τ_f and the droplet can only slowly respond to changes in the carrier phase. Usually, τ_d is referred to as the particle relaxation time, or particle response time

$$\tau_d = \left(\frac{3}{4}\frac{\mu}{\rho_d d_d^2} C_D Re_d\right)^{-1}. \tag{2.62}$$

Here, C_D denotes the drag coefficient and Re_d the particle Reynolds number

$$Re_d = \frac{\rho d_d |\mathbf{u}_{slip}|}{\mu}. \tag{2.63}$$

Similarly to the previously introduced combustion regime diagrams, it is possible to define different spray regimes as a function of the various spray-defining parameters. From a modeling perspective, the classification into different spray regimes helps to determine the best strategy to adequately represent such flows. Such categorization has been performed by Elghobashi [47] and is shown in Figure 2.8. The subdivision of the diagram is based on the expected interaction mechanisms within the disperse phase, and on the interaction of the particles with the carrier phase turbulence. These aspects are estimated by means of the dispersed phase volumetric fraction α_d, and using a turbulent Stokes number, which can either be defined based on the integral scale of the turbulence τ_t (Equation 2.49), or on the Kolmogorov time scale τ_η (Equation 2.29).

The diagram is divided horizontally into two zones, namely the dilute and dense zone. The dilute zone is characterized by low values for the volumetric fraction of the dispersed phase ($\alpha_d < 10^{-3}$). In this region, the particle loading is so low that the mutual interaction of the liquid particles can be neglected. The dilute zone is further split into two segments. The first of these is termed the *one-way coupling* zone. In this region, the disperse phase is very sparse and can be assumed to have no influence on the carrier phase, hence the term "one-way coupled". As α_d increases, the impact of the dispersed phase on the carrier increases. At some point, this aspect cannot be neglected any longer, and the system is referred to as *two-way coupled*. The term "two-way coupled" indicates the mutual interaction of the carrier and liquid phase. Note that, depending on the turbulent Stokes number, the impact of the dispersed phase may result in a production of turbulence in the carrier phase (for instance through vortex shedding for large droplet Reynolds numbers) or lead to a damping of the turbulence. As pointed out in [47], keeping the volumetric fraction α_d constant, while decreasing the particle relaxation time τ_d by reducing the diameter,

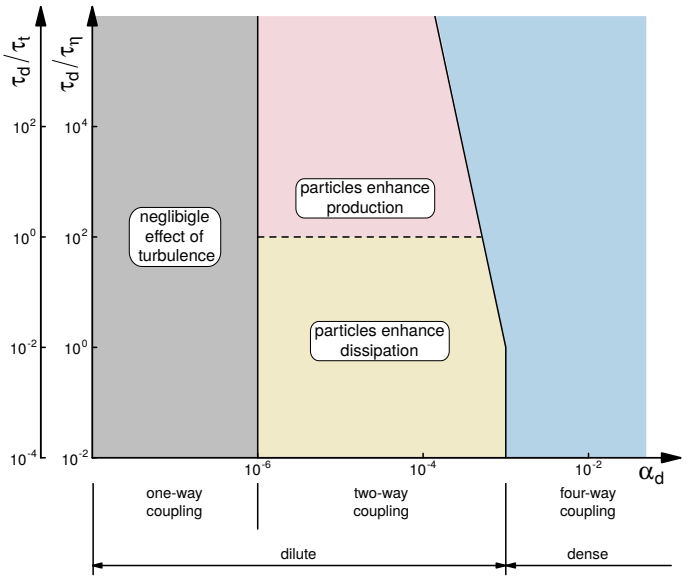

Figure 2.8: Classification of spray regimes based on the dispersed volumetric fraction and turbulent Stokes number, as proposed by Elghobashi [47].

increases the surface area of the dispersed phase. This also increases the turbulent energy dissipation rate.

In the dense suspension zone (blue colored region in Figure 2.8), the inter-particle spacing becomes of the order of magnitude of the diameter itself. This results in additional effects within the disperse phase. In this region, droplet-droplet collisions, coalescence and secondary breakup effects take place. In other words, the disperse phase interacts not only with the carrier phase, but also with itself. This regime is therefore referred to as the *four-way coupling* zone. The two-phase system evolves into a granular flow as α_d further approaches unity.

Chapter 3

Modeling of Turbulent Spray Combustion

In this chapter, the modeling strategy used in this work is introduced. The chapter is divided into two parts: The first section covers the methods related to the carrier phase, which includes on the one hand the treatment of the turbulence within LES and on the other hand the representation of the combustion chemistry, performed by means of chemistry tabulation. Additionally, as will become clear throughout this chapter, the interaction of the chemistry and turbulence within LES necessitates further attention. The different approaches to model this interaction are therefore also included. This part is followed by a section dedicated to the representation of the dispersed liquid phase. In this context, the point-particle-method is introduced, which is used to describe the liquid spray. For the sake of clarity, the full set of transport equations is summarized at the end of this chapter.

3.1 Carrier Phase Modeling

3.1.1 Turbulence Modeling

The treatment of turbulence in numerical simulations of turbulent non-reactive, reactive, and reactive multiphase flows has a crucial impact on the level of details available in later analyses. Three main approaches exist to address the turbulence: the direct numerical simulation (DNS), the large eddy simulation (LES) and the Reynolds-averaged Navier-Stokes (RANS) method. The amount of resolved quantities is used to differ between these approaches. The classification is highly relevant, as it results in a different mathematical treatment of the previously introduced transport equations for mass, momentum, enthalpy and species.

In the case of DNS, the whole range of turbulent scales is resolved. Therefore, no additional model to account for unresolved quantities is required. This implies a fine resolution of the domain of interest, as all length scales, from l_0 to η, and time scales of the order of τ_η must be captured (see Section 2.3.2). Extending Equation 2.30 to three-dimensional flows and assuming a linear relationship between spacial and temporal resolution yields computational requirements $\equiv Re^3$ for the DNS [176]. Consequently, DNS is currently restricted to moderate Reynolds numbers flows. Nonetheless, the two other strategies, i.e. LES and RANS, strongly rely on the reference data that DNS computations provide. The data obtained from DNS does not only contribute to a holistic insight into the phenomena occurring in a reactive flow, but also help derive adequate models to reproduce these phenomena at moderate computational costs.

The second approach is the RANS strategy and is diametrically opposed to DNS. Here, the so-called Reynolds-decomposition is applied to derive transport equation for the mean

quantities of the flow. In this context, the whole spectrum of turbulent scales is modeled and the approach necessitates the usage of models to close the additional terms that are introduced in the Reynolds-averaged transport equations. This approach is extensively adopted in engineering applications due to its low computational cost. The main deficiency of this approach is that it inhibits any fundamental analysis of the flow. Furthermore, since all turbulent scales have to be modeled, the results obtained from RANS computations may heavily depend on the model employed to represent these scales.

The disadvantages of the previous methods are bypassed in LES. The concept is, as the name suggests, to resolve the large turbulent structures, and to model only the small scales. This allows to resolve the majority of the turbulent kinetic energy of the spectrum, as can be deduced from Figure 2.3. The small scales are then modeled using a turbulence closure model, often labeled as subgrid-scale model. The benefits of the LES compared to RANS and DNS can be summarized as follows: (1) Since only small scales are modeled, the turbulence closure model carries less weight than in RANS simulations, thus reducing the turbulence model related uncertainties. (2) Another benefit compared to the RANS approach is the ability of LES to investigate the dominant phenomena in complex, unsteady flows. (3) At the same time, these fundamental characteristics of the fluid-flow can be captured at moderate computational cost, a major advantage compared to DNS.

In this work, all performed reacting flows and reactive multiphase simulations rely on the LES strategy. Therefore, the basic idea of LES is introduced subsequently as well as the mathematical formalism required to derive the used transport equations. Thereafter, the adopted closures to take the unresolved scales into account are presented.

Concept of Large Eddy Simulation

The idea behind LES is quite intuitive and can be grasped with the help of the turbulent energy spectrum shown in Figure 2.3. This spectrum involves a large range of time and length scales and resolving all these scales in a simulation would result in prohibitive computational costs. In order to minimize the computational expense and to bypass the need to resolve this whole range of scales, LES makes uses of a filtering operation to separate the small scales from the large scales. Thereby it is assumed that the main characteristics of the flow are determined by the large structures. The separation of scales can be though of as cut-off or low-pass filtering operation of the energy spectrum, which then necessitated the introduction of a model to represent the influence of the scales that have been cut off. This separation of the small scales is justified by the universal, isotropic character of the smallest scales of turbulence. From a mathematical perspective, the filtering operation of a turbulent field $\psi(\mathbf{x})$ can be expressed by the convolution

$$\overline{\psi}(\mathbf{x}) = \int_{-\infty}^{\infty} G(\mathbf{r}, \mathbf{x}) \psi(\mathbf{x} - \mathbf{r}) d\mathbf{r}, \tag{3.1}$$

where $G(\mathbf{r}, \mathbf{x})$ denotes the filter kernel, with the attribute $\int G(\mathbf{r}, \mathbf{x}) d\mathbf{r} = 1$, and a filter width Δ, which is defined as the second moment of the filter kernel. The notion of the filter width can be envisioned as follows: a larger Δ increases the spatial smoothening of $\psi(\mathbf{x})$. Note that in order to obtain the transport equations in filtered form, the kernel function must fulfill the following conditions [176]:

- Conservation of constants, that is $\overline{a} = a$.
- Linearity: $\overline{\phi + \psi} = \overline{\phi} + \overline{\psi}$.

- Commutation with derivations: $\overline{\frac{\partial \psi}{\partial x}} = \frac{\partial \overline{\psi}}{\partial x}$.

The turbulent field can then be decomposed into its filtered part $\overline{\psi}(\mathbf{x})$, which stands for the resolved part in LES, and a residual, or sub-filter part $\psi'(\mathbf{x})$

$$\psi(\mathbf{x}) = \overline{\psi}(\mathbf{x}) + \psi'(\mathbf{x}). \tag{3.2}$$

Generally, the filtering procedure can be applied either explicitly or implicitly. In the case of explicit filtering, the resolution of the turbulent field ψ is finer than Δ and the small scale motions are then removed by explicitly filtering the field. In this work, the equations are implicitly filtered, since any scales of ψ smaller than the spatial resolution are inevitably ignored.

Going over to flows with variable density, the notion of the Favre-filtering is introduced, which denotes a density weighted filtering operation, expressed as

$$\widetilde{\psi} = \frac{\overline{\rho\psi}}{\overline{\rho}}. \tag{3.3}$$

Similarly to Equation 3.2, the quantity ψ can be decomposed into a Favre-filtered and residual part

$$\psi(\mathbf{x}) = \widetilde{\psi}(\mathbf{x}) + \psi''(\mathbf{x}). \tag{3.4}$$

With the previously introduced relations, the filtered transport equations for mass, momentum, species and enthalpy read

$$\frac{\partial \overline{\rho}}{\partial t} + \frac{\partial}{\partial x_i}(\overline{\rho}\tilde{u}_i) = 0, \tag{3.5}$$

$$\frac{\partial \overline{\rho}\tilde{u}_i}{\partial t} + \frac{\partial}{\partial x_j}\left(\overline{\rho u_i u_j}\right) = -\frac{\partial \overline{p}}{\partial x_i} + \frac{\partial}{\partial x_j}\overline{\tau}_{ij} + \overline{\rho} f_i, \tag{3.6}$$

$$\frac{\partial \overline{\rho}\widetilde{Y}_k}{\partial t} + \frac{\partial}{\partial x_i}\left(\overline{\rho Y_k u_i}\right) = \frac{\partial}{\partial x_i}\left(\frac{\overline{\mu}}{Sc}\frac{\partial \widetilde{Y}_k}{\partial x_i}\right) + \overline{\rho}\widetilde{\dot{\omega}}_k, \tag{3.7}$$

$$\frac{\partial \overline{\rho}\widetilde{h}}{\partial t} + \frac{\partial}{\partial x_i}\left(\overline{\rho h u_i}\right) = \frac{\partial}{\partial x_i}\left(\frac{\overline{\mu}}{Pr}\frac{\partial \widetilde{h}}{\partial x_i}\right). \tag{3.8}$$

With exception of the mass transport equation, all equations contain unknown (convective) terms, which cannot be directly evaluated using the Favre-filtered quantities, because of the inequality $\widetilde{\psi\psi} \neq \widetilde{\psi}\widetilde{\psi}$. In order to solve this system of equations, closures are required. For this purpose, Equations 3.5-3.8 are usually reformulated to

$$\frac{\partial \overline{\rho}}{\partial t} + \frac{\partial}{\partial x_i}(\overline{\rho}\tilde{u}_i) = 0, \tag{3.9}$$

$$\frac{\partial \overline{\rho}\widetilde{u}_i}{\partial t} + \frac{\partial}{\partial x_j}\left(\overline{\rho}\widetilde{u}_i\widetilde{u}_j\right) = -\frac{\partial \overline{p}}{\partial x_i} + \frac{\partial}{\partial x_j}\left(\overline{\tau}_{ij} - \overline{\rho}\tau_{ij}^{sgs}\right) + \overline{\rho} f_i, \tag{3.10}$$

$$\frac{\partial \overline{\rho}\widetilde{Y}_k}{\partial t} + \frac{\partial}{\partial x_i}\left(\overline{\rho}\widetilde{Y}_k\widetilde{u}_i\right) = \frac{\partial}{\partial x_i}\left(\frac{\overline{\mu}}{Sc}\frac{\partial \widetilde{Y}_k}{\partial x_i} - \overline{\rho}\tau_{Y_k}^{sgs}\right) + \overline{\rho}\widetilde{\dot{\omega}}_k, \tag{3.11}$$

$$\frac{\partial \overline{\rho}\widetilde{h}}{\partial t} + \frac{\partial}{\partial x_i}\left(\overline{\rho}\widetilde{h}\widetilde{u}_i\right) = \frac{\partial}{\partial x_i}\left(\frac{\overline{\mu}}{Pr}\frac{\partial \widetilde{h}}{\partial x_i} - \overline{\rho}\tau_h^{sgs}\right). \tag{3.12}$$

Herein, the three subgrid parts $\tau_{ij}^{sgs} = \left(\widetilde{u_i u_j} - \widetilde{u_i}\widetilde{u_j}\right)$, $\tau_{Y_k}^{sgs} = \left(\widetilde{u_i Y_k} - \widetilde{u_i}\widetilde{Y_k}\right)$ and $\tau_h^{sgs} = \left(\widetilde{u_i h} - \widetilde{u_i}\widetilde{h}\right)$ have been introduced. These terms have to be modeled. which is the topic of the next section.

LES Subgrid-Scale Modeling

The modeling of the subgrid-scales (sgs) is of central importance in LES. As has been outlined in the previous chapter, the turbulent kinetic energy flows from larger to smaller structures until fully dissipated. In LES, however, the small scales are not resolved and their dissipative effect has to be correctly described. In order to relate resolved and subgrid parts, τ_{ij}^{sgs}, $\tau_{Y_k}^{sgs}$ and τ_h^{sgs} must be expressed in terms of known, i.e. resolved, quantities. In this work, a so-called eddy-viscosity approach is followed, which considers the effect of the subgrid part through the introduction of an additional subgrid-scale viscosity ν_{sgs} in the transport equations. In this context, it is useful to formally decompose τ_{ij}^{sgs} into an isotropic and anisotropic part. Herein, the isotropic part is added to the pressure, yielding the modified filtered pressure

$$\overline{P} = \overline{p} + \frac{1}{3}\overline{\rho}\tau_{kk}^{sgs}, \tag{3.13}$$

while the anisotropic part is expressed through the Boussinesq approximation based on the subgrid-scale viscosity ν_{sgs}

$$\tau_{ij}^{sgs} - \frac{1}{3}\tau_{kk}^{sgs}\delta_{ij} = -2\nu_{sgs}\Big(\widetilde{S}_{ij} - \frac{1}{3}\widetilde{S}_{kk}\delta_{ij}\Big). \tag{3.14}$$

The remaining unknown is the subgrid-scale viscosity, which, from dimensional analysis, can be described via the mixing-length hypothesis [155]

$$\nu_{sgs} \propto \mathcal{L}^2/\mathcal{T} = \mathcal{L}^2 \cdot \mathcal{S} \tag{3.15}$$

where $\mathcal{L}$ stands for a characteristic length scale and $\mathcal{T}$ a characteristic time scale. $1/\mathcal{T}$ can also be substituted by a characteristic velocity gradient scale $\mathcal{S}$. This concept is used in numerous subgrid-scale models [187, 129, 128]. In the LES context, Equation 3.15 can be reformulated to

$$\nu_{sgs} = (C_M\Delta)^2\mathcal{D}_M(\widetilde{\mathbf{u}}), \tag{3.16}$$

where C_M denotes a model parameter, which can either be determined dynamically [66] or kept constant, Δ the LES specific filter width and $\mathcal{D}_M(\widetilde{\mathbf{u}})$ a model related differential operator. The probably most popular model is the Smagorinsky model, where $C_M = 0.18$ and $\mathcal{D}_M(\widetilde{\mathbf{u}}) = \sqrt{2S_{ij}S_{ij}}$.

In this work, the $\sigma(sigma)$-model is used [129], where the differential operator D_M is based on the singular values of the velocity gradient tensor. ν_{sgs} is calculated via

$$\nu_{sgs} = (C_\sigma\Delta)^2\frac{\sigma_3(\sigma_1-\sigma_2)(\sigma_2-\sigma_3)}{\sigma_1^2}, \tag{3.17}$$

with the model constant $C_\sigma = 1.7$, and σ_i the i^{th} singular value ($i = \{1,2,3\}$) of the resolved velocity gradient

$$\overline{L}_{ij} = \begin{bmatrix} \partial\widetilde{u}_1/\partial x_1 & \partial\widetilde{u}_2/\partial x_1 & \partial\widetilde{u}_3/\partial x_1 \\ \partial\widetilde{u}_1/\partial x_2 & \partial\widetilde{u}_2/\partial x_2 & \partial\widetilde{u}_3/\partial x_2 \\ \partial\widetilde{u}_1/\partial x_3 & \partial\widetilde{u}_2/\partial x_3 & \partial\widetilde{u}_3/\partial x_3 \end{bmatrix}. \tag{3.18}$$

More precisely, the singular value corresponds to the square root of the eigenvalues of the tensor $\overline{L}_{ki}\overline{L}_{kj}$. The properties of the σ-model are subsequently listed [129]:

- Positiveness of ν_{sgs} by construction, since $\sigma_1 \geq \sigma_2 \geq \sigma_3$.
- ν_{sgs} decays with the third power in the vicinity of walls.

- ν_{sgs} is zero in one- and two-dimensional flows.
- ν_{sgs} is zero for axisymmetric or isotropic expansion.

Regarding the scalar subgrid-scale fluxes of species and enthalpy $\tau_{Y_k}^{sgs}$ and τ_h^{sgs}, a gradient approach is adopted. The rationale behind this is that the subgrid fluxes should be aligned with their respective filtered gradient. In this context, a constant turbulent (or subgrid-scale) Schmidt and Prandtl number Sc_{sgs} and Pr_{sgs} are introduced. This concept is better known as Reynolds analogy. The subgrid-scale fluxes read

$$\tau_{Y_k}^{sgs} = -\frac{\nu_{sgs}}{Sc_{sgs}} \frac{\partial \widetilde{Y}_k}{\partial x_i} \qquad \text{and} \qquad \tau_h^{sgs} = -\frac{\nu_{sgs}}{Pr_{sgs}} \frac{\partial \widetilde{h}}{\partial x_i}. \tag{3.19}$$

3.1.2 Concept of Chemistry Tabulation

As outlined in the previous chapter, the combustion reaction involves a multitude of chemical species. In fact, the combustion of simple fuels can involve the production and destruction of hundreds of species, which is described by even more chemical reactions. Evidently, this imposes a computational constrain, if the goal is to perform at the same time a well resolved LES. If this is desired, one transport equations must be solved for each species. In addition, the multiplicity of time scales related to the chemical reaction—some species may react much faster than others—result in a very stiff system [201]. To avoid the expensive consideration of the detailed kinetics, various chemical reduction mechanisms [189] were suggested. These approaches generally strongly reduce the number of chemical species and reactions considered in order to be computationally affordable and are generally tuned to match the area of interest (for instance, ignition delay time in an internal combustion engine, or pollutant formation). In general, these mechanism are only valid in a narrow range of scenarios. Another strategy is the chemistry tabulation. The method can be summarized as follows: (1) Compute the chemistry in a preprocessing step. (2) Map the thermochemical state onto a reduced set of variables to create a lookup-table. (3) Within the LES, solve a transport equation for each of the mapping variables and retrieve the tabulated thermochemical state using these variable at runtime. In this regard, various methods were proposed, including the intrinsic low dimensional manifold (ILDM) by Maas and Pope [114], the reaction-diffusion manifold (REDIM) [23], the flamelet progress variable approach (FPV) [144], the flame prolongation of ILDM (FPI) [67, 50] or the flamelet generated manifold (FGM) [196], among others. In this work, the FGM and FPV tabulation strategies are adopted. Here, the thermochemical state is mapped on the two table controlling variables of mixture fraction Z and progress variable PV. Both approaches make use of the flamelet assumption and are presented subsequently. The chemistry can be solved using the following set of one-dimensional equations [200]:

$$\frac{\partial}{\partial x}(\rho u) = -\rho K, \tag{3.20}$$

$$\frac{\partial}{\partial x}(\rho u Y_k) - \frac{\partial}{\partial x}\big(\frac{\mu}{Sc}\frac{\partial Y_k}{\partial x}\big) = -\rho K Y_k + \rho \dot{\omega}_k, \tag{3.21}$$

$$\frac{\partial}{\partial x}(\rho u h) - \frac{\partial}{\partial x}\big(\frac{\mu}{Pr}\frac{\partial h}{\partial x}\big) = -\rho K h, \tag{3.22}$$

$$\frac{\partial}{\partial x}(\rho u K) - \frac{\partial}{\partial x}\big(\mu\frac{\partial K}{\partial x}\big) = -2\rho K^2 + \rho a^2, \tag{3.23}$$

where K denotes the flame stretch rate. The density is computed using Equations 2.11 and 2.12. Note that the unity Lewis number assumption yields $Pr = Sc$.

Independently of the approach used, the species transport equations are then replaced with the transport equations for mixture fraction and progress variable, subsequently written in the context of LES with the subgrid-flux closure presented in Equation 3.19

$$\frac{\partial \overline{\rho}\widetilde{Z}}{\partial t} + \frac{\partial}{\partial x_i}\left(\overline{\rho}\widetilde{Z}\widetilde{u}_i\right) = \frac{\partial}{\partial x_i}\left(\left(\frac{\overline{\mu}}{Sc} + \frac{\mu_{sgs}}{Sc_{sgs}}\right)\frac{\partial \widetilde{Z}}{\partial x_i}\right) \tag{3.24}$$

$$\frac{\partial \overline{\rho}\widetilde{PV}}{\partial t} + \frac{\partial}{\partial x_i}\left(\overline{\rho}\widetilde{PV}\widetilde{u}_i\right) = \frac{\partial}{\partial x_i}\left(\left(\frac{\overline{\mu}}{Sc} + \frac{\mu_{sgs}}{Sc_{sgs}}\right)\frac{\partial \widetilde{PV}}{\partial x_i}\right) + \overline{\rho}\widetilde{\dot{\omega}}_{PV}. \tag{3.25}$$

Note that within this work, an adiabatic tabulation strategy is employed. This assumption inherently neglects any heat losses to walls or, as will be pointed out later, due to evaporative cooling of the liquid spray. Accordingly, the system of equations solved does not include any enthalpy equation.

3.1.2.1 Flamelet Generated Manifold Method

The FGM approach relies on the description of the thermochemical state via one-dimensional premixed flamelets, which are then assembled to a lookup-table. It is noteworthy that this approach was proposed by Van Oijen and De Goey [196] around the same time as Gicquel et al. [67] introduced the FPI approach. Both methods can be considered identical. In this work, the term FGM is used, which is by no means intended to diminish the FPI approach.

Before a lookup-table can be generated, the one dimensional flames must be computed in a preprocessing step. This computation requires the usage of a solver which is able to solve the detailed chemistry in a one-dimensional domain. For this purpose, either the detailed chemistry code CHEM1D, developed at the University of Eindhoven [190], or the Cantera chemical kinetics toolkit [68] are used. The chemical mechanisms used in this work are GRI-3.0 for methane combustion [188] and the mechanism by Marinov for ethanol combustion [118]. Both codes are solving the chemistry in physical space x, which consists in finding the solution to the system of Equations 3.20-3.23, with the following constrains [200]:

$$\begin{aligned}
&Y_k(-\infty) = ZY_k^{fuel} + (1-Z)Y_k^{oxidizer}, && \frac{\partial Y_k}{\partial x}(\infty) = 0,\\
&h(-\infty) = Zh^{fuel} + (1-Z)h^{oxidizer}, && \frac{\partial h}{\partial x}(\infty) = 0,\\
&K(-\infty) = 0, && \frac{\partial K}{\partial x}(\infty) = 0,\\
&Z(x) = Z, && \rho u = \rho_u s_l.
\end{aligned}$$

Such conditions yield a stationary premixed flame solely determined by the mixture fraction Z (since $K(x) = 0$ and $s_l = s_l(Z)$). This property allows to vary the mixture fraction and to obtain a one dimensional flame solution, a flamelet, for each mixture fraction considered. The next step is to map these flamelets solution onto a suitable reaction progress variable, which should fulfill the following conditions: (1) In order to allow a unique relation between thermochemical state and progress variable, the latter must monotonically increase or decrease throughout the one-dimensional solution. (2) Cover the whole physical solution range. This is important to describe species that may be produced outside of the reaction zone. (3) Well resolvable, in order to capture the flame at the highest resolution possible. In the context of premixed combustion, it is often assumed that the thickness of

the reaction progress variable source term is the determining scale. All conditions can be satisfied by defining the reaction progress variable as linear combination of several species mass fractions

$$PV = \sum_i w_i Y_i, \tag{3.26}$$

where w_i denotes the weighting factor of the i-th species. In analogy, the source term of the progress variable is defined as

$$\dot{\omega}_{PV} = \sum_i w_i \dot{\omega}_i. \tag{3.27}$$

For retrieval purposes, it is also beneficial to define the normalized progress variable

$$c = \frac{PV - \min(PV(Z))}{\max(PV(Z)) - \min(PV(Z))}. \tag{3.28}$$

Consequently, a value $c = 0$ denotes pure reactants and $c = 1$ a fully burnt mixture. In this work, combustion simulations are performed for the two fuels methane and ethanol. The respective progress variables $PV_{\mathrm{CH_4}}$[108] and $PV_{\mathrm{C_2H_5OH}}$[170] read

$$PV_{\mathrm{CH_4}} = Y_{\mathrm{CO_2}}, \qquad \text{and} \qquad PV_{\mathrm{C_2H_5OH}} = \frac{Y_{\mathrm{CO_2}}}{M_{\mathrm{CO_2}}} + \frac{Y_{\mathrm{CO}}}{2M_{\mathrm{CO}}} + \frac{Y_{\mathrm{H_2O}}}{2M_{\mathrm{H_2O}}}. \tag{3.29}$$

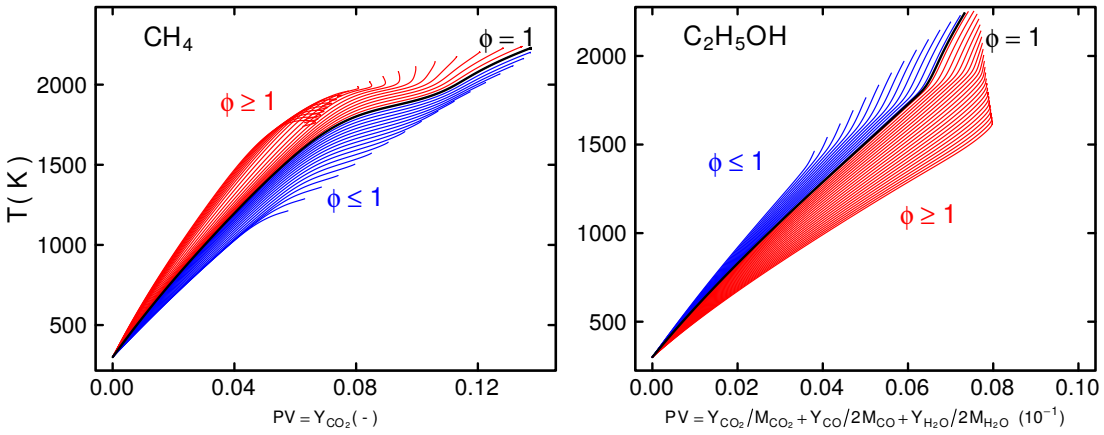

Figure 3.1: Monotonicity of the progress variables employed in this work. Rich mixtures are colored red, while lean mixture are shown in blue. The thickened black line represents the stoichiometric flamelet.

Both definitions have been widely used and delivered descent results [107, 108, 170]. This is confirmed by investigating the monotonicity of the temperature in progress variable space shown in Figure 3.1. The plot is subdivided into a lean (blue lines) and rich zone (red lines). The black line represents the stoichiometric condition. In the case of methane, it can be observed that at higher equivalence ratios, the monotonicity criterion is not fulfilled. However, in this work, this lookup-table is only applied to lean combustion, which makes its usage justifiable, as the monotonic behavior is given in that region. With these definitions, it is possible to span a two-dimensional space, a manifold, which can be used to retrieve the thermochemical state at runtime when solving the transport equations for the table controlling variable. This is shown in Figure 3.2 in normalized space for the

progress variable source term and the temperature. For ethanol, the mixture fraction is defined similarly to [170], whereas for methane, the mixture fraction definition used in [107, 108] is adopted.

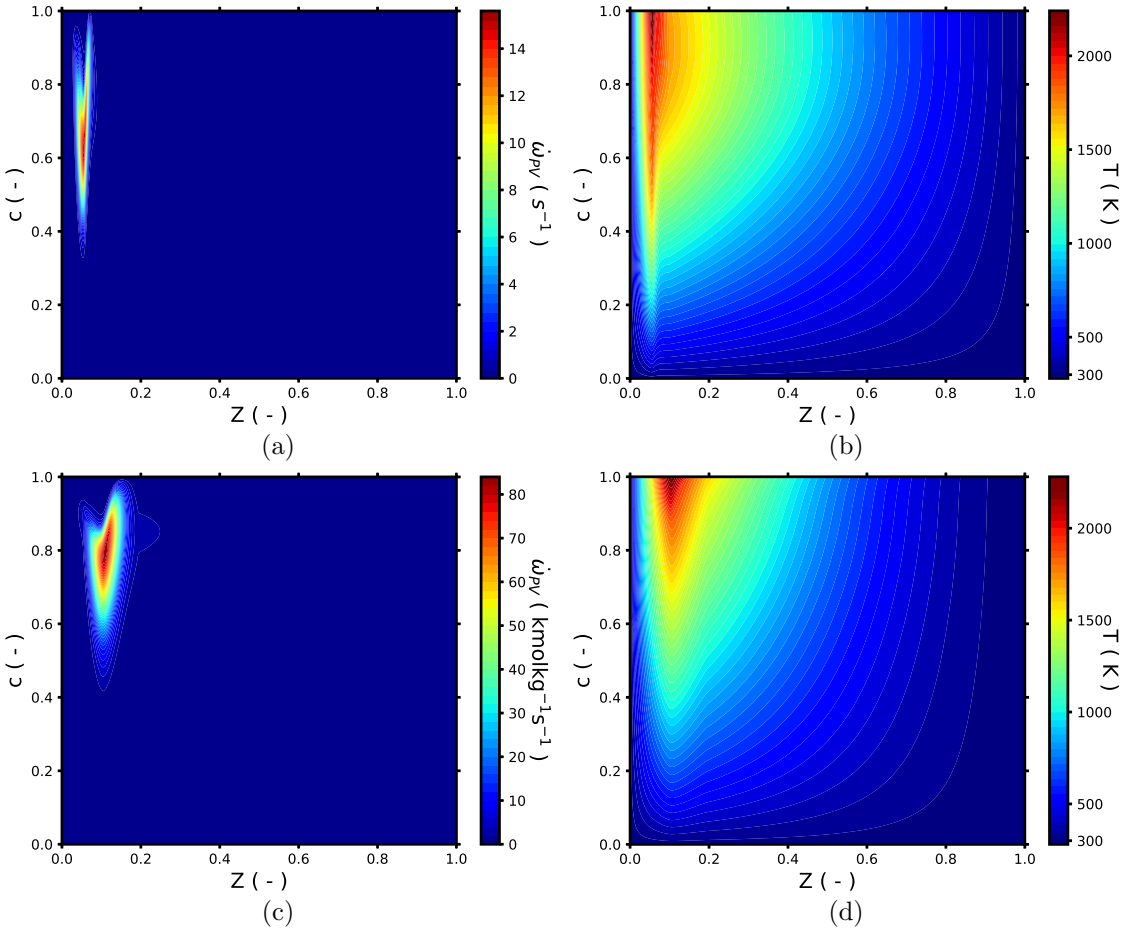

Figure 3.2: Flamelet generated manifolds employed in this work (both shown in normalized space). (a) and (b): CH_4 manifold colored by (a) the progress variable source term and (b) temperature. (c) and (d): C_2H_5OH manifold colored by (c) the progress variable source term and (d) temperature.

3.1.2.2 Flamelet Progress Variable Method

The flamelet progress variable approach was initially proposed by Pierce and Moin [144]. The idea is very similar to the FGM strategy with the exception that, instead of creating a manifold from premixed flamelets, the FPV method is based on one-dimensional diffusion flames. Similarly to its premixed flamelet counterpart, the solution for the diffusion flamelet can be obtained by solving the same system of Equations 3.20-3.23 with a different

set of boundary conditions, which reads [200]:

$$
\begin{aligned}
Y_k(-\infty) &= Y_k^{fuel}, & Y_k(\infty) &= Y_k^{oxidizer},\\
h(-\infty) &= h^{fuel}, & h(\infty) &= h^{oxidizer},\\
\frac{\partial K}{\partial x}(-\infty) &= 0, & K(\infty) &= a,\\
Z(-\infty) &= 1, & Z(\infty) &= 0.
\end{aligned}
$$

As pointed out by Vreman et al. [200], and differently from the premixed setup, the determining parameter is now the strain rate a applied to the flame. This means that, in analogy to the FGM lookup-table, it is possible to construct a two dimensional space based on a set of diffusion flamelets computed at varying strain rates. Such manifold is shown in Figure 3.3 for the progress variable source term and temperature. Note that to construct the thermochemical lookup-table, the Bilger mixture fraction [14], is used to ensure a mixture fraction space spanning from 0 to 1. The relation between Z_{Bilger} and the mixture fraction Z is given by

$$
Z_{Bilger} = \frac{Z - Z^{min}}{Z^{max} - Z^{min}}, \tag{3.30}
$$

where Z_{max} and Z_{min} refer to the expected maximum and minimum value of the mixture fraction for a given configuration. The progress variable definition employed for the diffusion CH_4 flamelet manifold follows the suggestion of [200]

$$
PV = \frac{Y_{\mathrm{CO_2}}}{M_{\mathrm{CO_2}}} + \frac{Y_{\mathrm{H_2}}}{M_{\mathrm{H_2}}} + \frac{Y_{\mathrm{H_2O}}}{M_{\mathrm{H_2O}}}. \tag{3.31}
$$

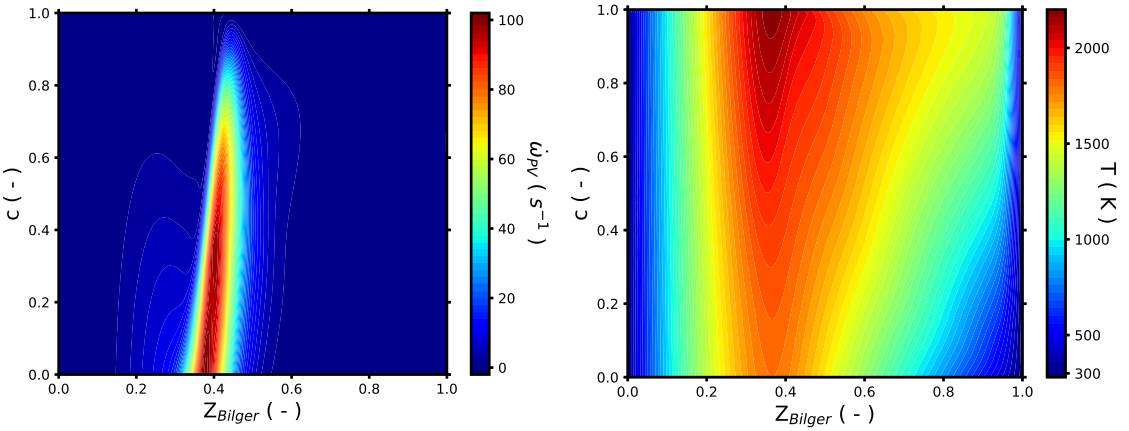

Figure 3.3: CH_4-FPV manifold employed in this work shown for (a) the progress variable source term and (b) the temperature.

3.1.3 Modeling of the Turbulence Chemistry Interaction

One open point remains in the context of LES: how should the interaction of the chemistry with the turbulent structures (resolved and subgrid) be represented? A lot of attention has been given to this topic in the last years, resulting in a broad spectrum of approaches to account for the turbulence-chemistry interaction within LES [90, 146]. A popular approach

originates from the idea that the flame front can be perceived as thin surface [205, 101]. In this context, the position of the flame-front is represented by a level-set function G, of which the evolution is determined by its convective transport, its flame speed and curvature. Accordingly closures are required to account for the unresolved flame speed and curvature [145, 86]. Differently, flame front thickening approaches [22, 111] do not consider the flame as thin surface but aim at resolving the reaction zone by artificially increasing its dimensions. Not so different is the filtered tabulated chemistry for large eddy simulation (F-TACLES) strategy, where the reaction zone [51] is explicitly filtered a-priori to the LES to obtain a filtered thermochemical lookup-table. Both approaches necessitate further modeling for the unresolved flame wrinkling [32, 26]. A fundamentally different way is to consider the combustion reaction in a statistical manner via probability density function (PDF) based methods. The closure for the filtered chemical reaction rates is then directly obtained from the (joint scalar) subgrid probability distribution. The approaches can be subdivided into either presumed or transported PDF approaches [153]. While in the former, the shape of the subgrid PDF is presumed (a-priori) [160] and reconstructed through transport (or algebraic) equations for lower order moments of the PDF, the latter consists in approximating the transport of the PDF at runtime using either a Lagrangian particle based Monte Carlo approach [152, 153], a Quadrature-based Moment method (QMOM, see for instance [150]) or the Eulerian Stochastic Field, also known as Eulerian Monte Carlo (EMC) method. A detailed overview of the various turbulence-chemistry interaction models in the LES context can be found in [146, 142, 90, 148].

The next section is dedicated to the two approaches adopted in this work, the artificially thickened flame (ATF) approach, and transported probability density function methods. The first approach has been mostly applied to turbulent premixed or stratified flames [106, 6, 5, 42], while PDF methods are usually applied to flames predominantly burning in a diffusion mode, see for instance [116, 115]. Nonetheless, PDF based method have also been applied to premixed combustion and delivered good result [5].

3.1.3.1 Artificial Thickening of the Flame Front

The main difficulty arising in the context of LES of premixed combustion is related to the small length scales at which the combustion process takes place. Indeed, the thickness of the flame can be significantly smaller than the resolution of the numerical grid. However, in premixed flames, a determining factor is the resolution of the chemical source terms. This is because the source term determines the laminar flame speed, as can be reasoned from Equation 2.45. The idea behind ATF is to artificially thicken the flame front in order to resolve the chemical source term and obtain the correct flame propagation speed. Such procedure has been proposed by Butler and O'Rourke [22] and O'Rourke and Bracco [135] and successfully applied to laminar flames. From a mathematical perspective, the thickened scalar equations are obtained through coordinate transformation. The coordinate transformation yields an altered diffusion and reaction term in the transformed scalar transport equations. This new transport equation is then solved with respect to the original coordinate system. In [135], it is shown that this procedure conserves the flame propagation. This is because the flame speed scales with both, the reaction and diffusion term. All other terms are left unchanged, which implies that the physics inside the flame are modified. On one hand, this is because the gradients are smoothed out across the flame front. On the other hand, solving with respect to the original coordinate system instead of the new one is equivalent to relaxing the time inside the flame front [108]. In the tabulated chemistry context adopted in this work, the thickened progress variable equation

(in a laminar flame) reads

$$\frac{\partial \rho PV}{\partial t} + \frac{\partial}{\partial x_i}\left(\rho PV u_i\right) = \frac{\partial}{\partial x_i}\left(F\frac{\mu}{Sc}\frac{\partial PV}{\partial x_i}\right) + \frac{\rho\dot{\omega}_{PV}}{F}, \tag{3.32}$$

where the flame thickening factor F has been introduced, which relates the new to the original coordinate system. The thickened flame has the following properties:

$$\delta_l^F = F\delta_l, \qquad \text{and} \qquad s_l^F = s_l \tag{3.33}$$

Thereby, the superscript $(\cdot)^F$ denotes properties of the thickened flame. Accordingly, the thickening procedure is broadening the reaction zone while keeping the laminar flame speed unaltered. The thickening factor F can be specified through an adequate criterion, for instance by defining a maximum resolution scale at which the laminar flame speed is retrieved Δ_{max}. With such limit, one can formulate the following criterion:

$$F \geq \frac{\Delta}{\Delta_{max}}. \tag{3.34}$$

If this condition is fulfilled, the thickening procedure conserves the laminar propagation speed at any desired resolution. However, the simulations presented in this work feature turbulent combustion, and the focus is on retrieving the turbulent flame speed. The major drawback of the ATF method is that the flame-thickening reduces the wrinkling caused by the turbulent eddies interacting with it. At the same time, the flame becomes more sensitive to stretch effects. In order to take these effects into account, an efficiency function E is introduced to obtain the correct turbulent flame propagation speed

$$s_t = E \cdot s_l. \tag{3.35}$$

Usually, this efficiency function would take into accout the effect of unresolved flame wrinkling onto the flame propagation speed. Not so within ATF. In fact the efficiency function should ideally correct the loss of wrinkling with the resolved and unresolved scales [32]. The increase of the flame propagation speed is incorporated into Equation 3.32 by multiplying the diffusion and reaction terms with the efficiency function, yielding

$$\frac{\partial \rho PV}{\partial t} + \frac{\partial}{\partial x_i}\left(\rho PV u_i\right) = \frac{\partial}{\partial x_i}\left(EF\frac{\mu}{Pr}\frac{\partial PV}{\partial x_i}\right) + \frac{E}{F}\rho\dot{\omega}_{PV}. \tag{3.36}$$

In this work, the popular formulation by Charlette et al. [26] is adopted to model the efficiency function. This model describes the unresolved flame surface using an inner scale η_c, and an outer scale Δ_O to characterize the range of scales which must be taken into account by the model. These scales are used to define the winkling factor

$$\Xi = \left(1 + \frac{\Delta_O}{\eta_c}\right)^{\beta}, \tag{3.37}$$

where β denotes an exponential factor, which can be either computed dynamically [27] or kept constant [26]. In this work, the standard formulation is employed using a model exponent $\beta = 0.5$. The efficiency function is then expressed through the wrinkling factor Ξ, which is approximated by

$$E = \Xi = \left(1 + \min\left[\frac{\Delta_O}{\delta_l}, \Gamma\frac{u'_\Delta}{s_l}\right]\right)^{\beta}. \tag{3.38}$$

Γ is the effective straining function, which describes the distortion of the flame front at scales below Δ_O. Within [26], Δ_O is defined as product of the thickening factor F and laminar flame thickness δ_l. For practical purposes, a polynomial fit for Γ is proposed in [26]

$$\Gamma = \Gamma\Big(\frac{\Delta_O}{\delta_l}, \frac{u'_\Delta}{s_l}, Re_\Delta\Big) = \Big[\big((f_u^{-a} + f_\Delta^{-a})^{-1/a}\big)^{-b} + f_{Re}^{-b}\Big]^{-1/b}, \tag{3.39}$$

with the following definitions for f_u, f_Δ and f_{Re}:

$$f_u = 4\bigg(\frac{27C_k}{110}\bigg)^{1/2}\bigg(\frac{18C_k}{55}\bigg)\bigg(\frac{u'_{\Delta_O}}{s_l}\bigg)^2, \tag{3.40}$$

$$f_\Delta = \bigg[\frac{27C_k\pi^{4/3}}{110}\bigg(\bigg(\frac{\Delta_O}{\delta_l}\bigg)^{4/3} - 1\bigg)\bigg]^{1/2}, \tag{3.41}$$

$$f_{Re} = \bigg[\frac{9}{55}\exp\bigg(-\frac{3}{2}C_k\pi^{4/3}Re_{\Delta_O}^{-1}\bigg)\bigg]^{1/2} Re_{\Delta_O}^{1/2}. \tag{3.42}$$

Here, C_k represents the Kolmogorov constant with a value of 1.5, and $Re_{\Delta_O} = 4(\Delta_O/\delta_l)(u'_{\Delta_O}/s_l)$ the subgrid scale Reynolds number below the scale Δ_O. The velocity fluctuation u'_{Δ_O} is computed using the expression proposed by Colin et al. [32]:

$$u'_{\Delta_O} = 2\Delta^3\Big|\nabla\times\big(\nabla^2\mathbf{u}\big)\Big|. \tag{3.43}$$

The exponents a and b in Equation 3.39 are computed as

$$a = 0.6 + 0.2\exp\bigg(-0.1\bigg(\frac{u'_{\Delta_O}}{s_l}\bigg)\bigg) - 0.2\exp\bigg[-0.01\bigg(\frac{\Delta}{\delta_l}\bigg)\bigg], \qquad \text{and} \qquad b = 1.4. \tag{3.44}$$

Equation 3.36 provides a straight forward approach to model a thickened flame wrinkled by turbulent eddies. However in view of the LES performed in this work, the problem of the non-locality of the thickening factor arises. Indeed, the region where chemical reaction occurs is in general small compared to the dimensions of the computational domain. This is problematic, as the current formulation performs a global thickening which is not considering where the combustion is taking place. Applying Equation 3.36 globally yields (unfortunately) an overestimation of the diffusive term outside of the reaction zone. This issue is solved by using dynamic procedures for the thickening factor, as initially proposed by Legier et al. [111]. Ideally, this dynamic thickening produces a factor F using Equation 3.34 within the flame, and 1 otherwise. This is achieved by introducing a flame sensor Ω which detects the zone of reaction. The flame sensor evaluates to 1 near the flame and to 0 elsewhere. To incorporate these properties, Equation 3.34 is reformulated to

$$F = 1 + \Omega\Big(\frac{\Delta}{\Delta_{max}} - 1\Big). \tag{3.45}$$

The most popular formulation for the flame sensor is the one proposed by Durand and Polifke [46]

$$\Omega = 16\Big[c\big(1-c\big)^2\Big]^2, \tag{3.46}$$

where the normalized progress variable c is computed using Equation 3.28. Ideally, the flame sensor should only be active in regions where high reaction source terms occur. However, the formulation above has its peak at $c = 0.5$, which imposes an unnecessary

constrain on the progress variable definition. To overcome this deficit, other formulations have been proposed [181, 4], which are based on the progress variable source term directly. In this work, a similar formulation to [181, 81] is adopted. The flame sensor is then defined as

$$\Omega = \max\left(0, \frac{1}{3}\left(4 \cdot \tanh\left(5\frac{\dot{\omega}_{PV}}{\max(\dot{\omega}_{PV})}\right) - 1\right)\right). \tag{3.47}$$

This expression guarantees that the flame thickening is performed only in regions characterized by strong chemical reactions.

Finally, the notion of grid-adaptive (GA) and mixture-adaptive (MA) thickening is introduced. These have been proposed alongside the dynamic thickening procedure in order to further reduce unnecessary thickening and its related uncertainties. The grid-adaptive thickening [108] can be obtained by introducing a spatial dependence in the resolving scale of the simulation $\Delta = \Delta(\mathbf{x})$. For this, Δ_{max} is estimated prior to the computation based on the thinnest flame thickness expected in the simulation δ_l^{exp} as well as the number of control volumes n_{CV} needed to reproduce the correct laminar flame speed

$$\Delta_{max}^{GA} = \frac{\delta_l^{exp}}{n_{CV}}. \tag{3.48}$$

In contrast, the mixture-adaptive version [175, 170] extends the grid-adaptive thickening by introducing the dependency of the local flame thickness (based on the mixture) in the equation. This is especially relevant in spray or stratified flames, where the mixture composition is expected to vary strongly. Additionally, the method has the benefit that no a-priori estimation of Δ_{max} must be performed, since the flame thickness is directly evaluated at runtime as function of the mixture fraction Z. Δ_{max} is therefore expressed as

$$\Delta_{max}^{MA} = \frac{\delta_l(Z)}{n_{CV}}. \tag{3.49}$$

In regard of the simulations preformed in this work, the ratio Δ/Δ_{max} in Equation 3.34 and 3.45 appears oversimplifying as it assumes that Δ_{max} is always smaller then the resolving scale. However, in LES, the resolution may significantly vary within the computational domain and the previously mentioned assumption cannot be guaranteed. Therefore the thickening factor is re-expressed as

$$F = 1 + \Omega\left[\max\left(1, \frac{\Delta}{\Delta_{max}}\right) - 1\right]. \tag{3.50}$$

3.1.3.2 Probability Density Function based Methods

Beside the ATF model, a probability density function (PDF) based approach, i.e. the Eulerian stochastic field (ESF) method, is adopted in this work. Therefore, the core concepts of PDF methods are introduced. These are, as done previously for the ATF model, formulated within the tabulated chemistry context. For this purpose, the so-called filtered- and Favre-filtered subgrid PDF, $\overline{P}$ and $\widetilde{P}$, are introduced. In LES, these PDFs represent the probability distribution of a quantity in the subgrid. This idea is pictured in Figure 3.4 for a generic configuration. In this example, the aim is to obtain a valuable approximation for the filtered Temperature field $\overline{T}$ in the LES cell shown in Figure 3.4a. The two-dimensional LES cell, delimited by the red line, consists of 9 DNS cells. Considering a reactive thermo-fluid flow, the temperature is a function depending on multiple parameters, here represented through the quantity $\boldsymbol{\phi}$. In the case of tabulated

chemistry, $\boldsymbol{\phi} = \{Z, PV\}$. However, for the sake of simplicity, in this example, $\boldsymbol{\phi}$ is reduced to one single variable ϕ. In the case of the DNS, obtaining the temperature is straightforward since no subgrid contribution exists. This is different in the case of LES, where only filtered quantities are available, i.e. $\overline{\phi}$. A rather naive approach is to assume that the temperature can be obtained through $\overline{T} = T(\overline{\phi})$. This simplification is only valid in the case of a linear relationship between T and ϕ, and cannot be justified in the LES performed in this work due to the non-linearity of the thermochemical state and the table lookup variables. For the sake of simplicity, the LES filter operator is reduced to a simple averaging filter, such that $\overline{T} = \langle T \rangle$. The unknown filtered temperature can then be obtained by averaging over the DNS cells. Similarly, one can use the DNS-data to construct the LES subgrid probability density function of ϕ and T. An example of such PDFs is shown in 3.4b. For this concrete example, ϕ represents the mixture fraction and the relation between ϕ (or Z) and T is taken from a one-dimensional counterflow diffusion flamelet. As can be observed, the Gaussian subgrid PDF of mixture fraction yields a completely different temperature PDF shape. More important is however the difference between $\overline{T}$ and $T(\overline{\phi})$, which highlights the non-linear behavior of mixture fraction and temperature. This example motivates the usage of PDF-based methods, due to their capability to approximate the scalar subgrid distribution at runtime. Thereby, the filtered or Favre-filtered quantities can be computed using

$$\overline{T} = \int_{-\infty}^{\infty} T(\boldsymbol{\phi}) \overline{P}(\boldsymbol{\phi}) d\boldsymbol{\phi} \qquad \text{and} \qquad \widetilde{T} = \int_{-\infty}^{\infty} T(\boldsymbol{\phi}) \widetilde{P}(\boldsymbol{\phi}) d\boldsymbol{\phi}. \tag{3.51}$$

In analogy, the integration of the subgrid PDF can be performed to obtain any quantity of interest.

PDF methods can be subdivided into either presumed or transported PDF approaches [153]. In the former, the shape of the subgrid PDF is presumed (*a priori*) [160] and reconstructed through transport (or algebraic) equations for lower order moments of the PDF, while the latter consists in approximating the transport of the (joint) Favre-filtered PDF at runtime [152, 153, 150, 194, 195]. In this research project, the PDF is approximated at runtime using the ESF method. Additionally, various points of contact with the presumed PDF approach can be found in Chapter 9 of this work. In the context of the tabulated chemistry approach applied combined with LES, both methods aim at representing the joint Favre-filtered scalar subgrid PDF of progress variable and mixture fraction $\widetilde{P}(Z, PV)$. The presumed PDF and the ESF strategy are subsequently introduced.

Presumed PDF method In order to retrieve $\widetilde{P}(Z, PV)$ at runtime, presumed PDF approaches rely on the prior assumption of a shape function for the scalar probability density distribution. The shape function has then to be parametrized by the moments of the distribution and it is often assumed that the PDF can be represented by its first two moments $\widetilde{\boldsymbol{\phi}}$ and $\widetilde{\text{var}(\boldsymbol{\phi})}$. However, in the case of a multidimensional probability distributions $\widetilde{P}(\boldsymbol{\phi})$, prescribing a feasible presumed shape turns out to be a difficult endeavor. This problem leads to the simplifying assumption of statistical independence between the scalar dimensions of the PDF, thus substantially facilitating its description to the product of its marginal PDFs $\widetilde{P}(\boldsymbol{\phi}) \approx \prod \widetilde{P}(\phi_\alpha)$. Therefore, if the moments of the marginal PDFs are known, it is possible to evaluate any quantity under consideration of the non-resolved scales. This is exemplarily shown for the reaction progress variable source term and a two dimensional PDF of mixture fraction and progress variable

$$\widetilde{\dot{\omega}}_{PV} = \int\int \dot{\omega}_{PV}(Z, PV) \widetilde{P}\big(Z, \widetilde{Z}, \widetilde{\text{var}(Z)}\big) \widetilde{P}\big(PV, \widetilde{PV}, \widetilde{\text{var}(PV)}\big) \mathrm{d}Z \mathrm{d}PV, \tag{3.52}$$

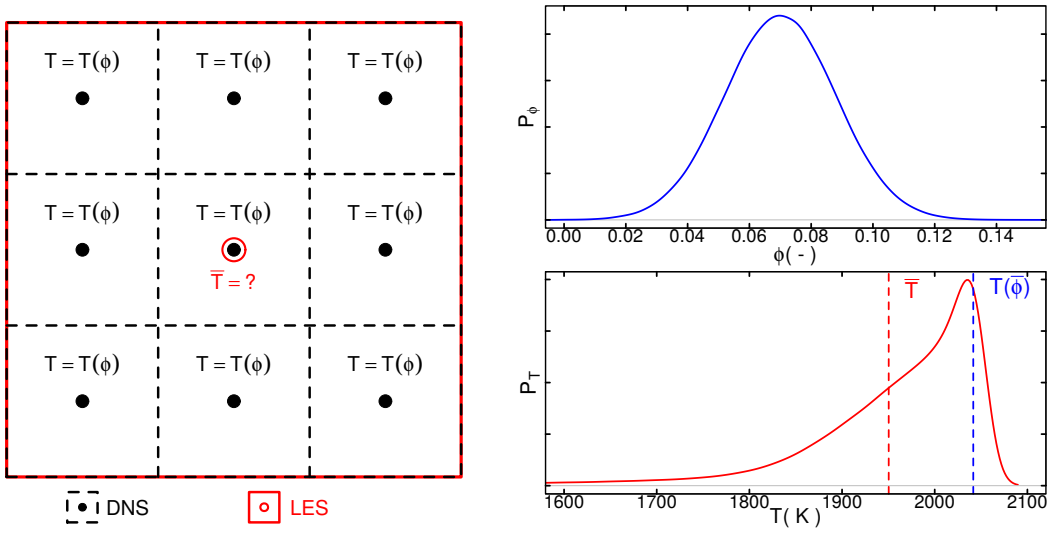

(a) (b)

Figure 3.4: (a) Schematic representation of a LES-cell consisting of 9 DNS-cells. (b) Illustration of the non-linear relation between temperature and mixture fraction ($\phi = Z$) by means of their respective scalar subgrid PDFs. The relation between $\phi = Z$ and T is taken from a one-dimensional counterflow diffusion flamelet.

where $\widetilde{PV}$, $\widetilde{Z}$, $\widetilde{\mathrm{var}(PV)}$ and $\widetilde{\mathrm{var}(Z)}$ are required input parameters. In order to avoid the expensive PDF integration at runtime, the thermochemical lookup-table is preintegrated with the moments of the distribution, which in turn become additional table controlling variables (thus increasing the dimensionality of the lookup-table). Herein, depending on the presumed shape of the subgrid PDF, the variance terms $\widetilde{\mathrm{var}(PV)}$ and $\widetilde{\mathrm{var}(Z)}$ are obtained via additional transport equations or algebraic closures.

With respect to the application of the presumed PDF approach for reactive flow problems, the β-, top-hat-, and δ-shape are most widely spread. The β-shape [160] is a combination of Γ functions

$$P(x, \widetilde{x}, \widetilde{\mathrm{var}(x)}) = \frac{\Gamma(a+b)}{\Gamma(a)\Gamma(b)} x^{a-1}(1-x)^{b-1} \tag{3.53}$$

for which the parameter a and b are computed from the first two moments of the probability density function as

$$a = \tilde{x}\Big(\frac{\tilde{x}(1-\tilde{x})}{\widetilde{\mathrm{var}(x)}} - 1\Big); \qquad b = \frac{1-\tilde{x}}{\tilde{x}}\Big(\frac{\tilde{x}(1-\tilde{x})}{\widetilde{\mathrm{var}(x)}} - 1\Big). \tag{3.54}$$

Similarly, the top-hat-shape relies on the first two moments of the PDF [53]

$$P(x, \widetilde{x}, \widetilde{\mathrm{var}(x)}) = \begin{cases} x_0 & \text{if}(x_a \leq x \leq x_b) \\ 0 & \text{else} \end{cases} \tag{3.55}$$

with the parameters

$$x_0 = \frac{1}{x_b - x_a}; \qquad x_a = \tilde{x} - \sqrt{12\widetilde{\mathrm{var}(x)}}; \qquad x_b = \tilde{x} + \sqrt{12\widetilde{\mathrm{var}(x)}}. \tag{3.56}$$

Each of these presumed shapes has a different physical interpretation. For instance, presuming a δ-shape for the subgrid PDF for both, mixture fraction and reaction progress variable is equivalent to assuming that $\widetilde{\dot{\omega}}_{PV} = \dot{\omega}_{PV}(\widetilde{Z}, \widetilde{PV})$.

Eulerian Stochastic Fields Method The Eulerian Stochastic Fields method is directly based on the transport equation of the joint scalar Favre-filtered PDF (FDF)

$$\widetilde{P}(\boldsymbol{\phi}, \mathbf{x}, t) = \frac{\overline{\rho P(\boldsymbol{\phi}, \mathbf{x}, t)}}{\overline{\rho}}, \tag{3.57}$$

subsequently abbreviated as $\widetilde{P}_\phi$. The transport equation is based on the integration of the joint velocity-composition FDF and reads [76, 151, 54]

$$\begin{aligned} &\underbrace{\frac{\partial}{\partial t}\left(\overline{\rho}\widetilde{P}_\phi\right)}_{\text{accumulation}} + \underbrace{\frac{\partial}{\partial x_i}\left(\overline{\rho}\widetilde{u}_i\widetilde{P}_\phi\right)}_{\text{macro-mixing}} + \underbrace{\frac{\partial}{\partial \psi_\alpha}\left(\overline{\rho}\dot{\omega}_\alpha(\boldsymbol{\psi})\widetilde{P}_\phi\right)}_{\text{chemical reaction}} = -\underbrace{\frac{\partial}{\partial x_i}\left[\overline{\rho}(u_i''|\boldsymbol{\phi}=\boldsymbol{\psi})\widetilde{P}_\phi\right]}_{\text{meso-mixing}} \\ &\underbrace{-\frac{\partial^2}{\partial \psi_\alpha^2}\left[\left(\overline{\rho\frac{\nu}{Sc}\frac{\partial \psi_\alpha}{\partial x_i}\frac{\partial \psi_\alpha}{\partial x_i}\middle|\boldsymbol{\phi}=\boldsymbol{\psi}}\right)\widetilde{P}_\phi\right]}_{\text{micro-mixing}} + \underbrace{\frac{\partial}{\partial x_i}\left(\overline{\rho}\frac{\overline{\nu}}{Sc}\frac{\partial \widetilde{P}_\phi}{\partial x_i}\right)}_{\text{diffusion}}. \end{aligned} \tag{3.58}$$

As outlined in [54], the FDF-evolution is described by its convection in space (macro-mixing), by subgrid-scale fluxes arising from the scalar-conditioned residual velocity $(u_i''|\boldsymbol{\phi} = \boldsymbol{\psi})$ (meso-mixing), by transport in composition space due to molecular mixing (micro-mixing), by its diffusion in space, and chemical reaction. More details on the derivation of the transport equation can be found in [151] and [76]. Similarly to the previously introduced LES Favre-filtered equations, Equation 3.58 includes unknown terms: (1) the meso-mixing term and (2) the micro-mixing term. Both terms require modeling. On the other side, the FDF transport equation features a chemical reaction term in closed form. Usually, the meso-mixing term is modeled using a gradient-ansatz similar to Equation 3.19 and reads

$$(u_i''|\boldsymbol{\phi} = \boldsymbol{\psi})\widetilde{P}_\phi = -\frac{\nu_{sgs}}{Sc_{sgs}}\frac{\partial \widetilde{P}_\phi}{\partial x_i}. \tag{3.59}$$

In regard of the micro-mixing, many suggestions have been made to close this term, as the Euclidean minimum spanning tree (EMST) [193], the interaction by exchange with the mean (IEM) [199], also known as linear mean square estimation closure (LMSE) [60, 39, 133], or the Fokker-Planck (FP) model [55]. In this work, the IEM model is adopted, not only because of its simplicity, but also because of its proven performance in LES [88, 116, 59, 58, 75]. Note that in order to fully unveil the advantages of more sophisticated models, the modeling share should be more significant, as for instance in RANS simulations. The IEM model expresses the micro-mixing term in Equation 3.58 as

$$\frac{\partial^2}{\partial \psi_\alpha^2}\left[\left(\overline{\rho\frac{\nu}{Sc}\frac{\partial \psi_\alpha}{\partial x_i}\frac{\partial \psi_\alpha}{\partial x_i}\middle|\boldsymbol{\phi}=\boldsymbol{\psi}}\right)\widetilde{P}_\phi\right] = \frac{\overline{\rho}}{2\tau_{MM}}\frac{\partial}{\partial \psi_\alpha}\left[\left(\widetilde{\psi}_\alpha - \psi_\alpha\right)\widetilde{P}_\phi\right]. \tag{3.60}$$

Here, $\widetilde{\boldsymbol{\psi}}$ represents the mean of the FDF and τ_{MM} a suitable time scale at which micro-mixing occurs. The formulation implies a linear relaxation of the $\widetilde{P}_\phi$ towards its mean. In the context of LES, the micro-mixing time scale is often expressed in terms of a micro-mixing frequency ω_{MM}, which is approximated by the following expression [97]

$$\omega_{MM} = \frac{1}{\tau_{MM}} = C\frac{\overline{\nu} + \nu_{sgs}}{\Delta^2}, \tag{3.61}$$

with the constant $C = 2$ [5, 116, 143, 96]. Using Equations 3.59, 3.60 and 3.61 provides a closed equation for the FDF. Still, it remains to be determined how $\widetilde{P}_\phi$ shall be represented in the simulation. For this purpose, the Eulerian stochastic fields method is used. The concept of the ESF method, originally proposed by Valiño [194] and later improved in [195], is to approximate the joint scalar FDF as ensemble of N_s Eulerian stochastic fields ξ_α^n for each of the PDF dimensions $\{Z, PV\}$ and to solve a stochastic differential equation (SDE) for each of these fields. This implies that the PDF can be approximated by a set of Dirac delta peaks in joint scalar space $\boldsymbol{\psi}$

$$P_\phi(\boldsymbol{\psi}, \mathbf{x}, t) \approx \frac{1}{N_s} \sum_n^{N_s} \delta(\boldsymbol{\psi} - \boldsymbol{\xi}_n(\mathbf{x}, t)). \tag{3.62}$$

Following an Itô interpretation of the stochastic integral arising in the SDEs, the evolution of the n^{th} stochastic field in dimension space ψ_α is expressed as [194, 195]

$$\mathrm{d}(\bar{\rho}\xi_\alpha^n) = -\frac{\partial}{\partial x_j}(\bar{\rho}\xi_\alpha^n \widetilde{u}_j)\mathrm{d}t + \frac{\partial}{\partial x_i}\left[\left(\frac{\bar{\mu}}{Sc} + \frac{\mu_{sgs}}{Sc_{sgs}}\right)\frac{\partial \xi_\alpha^n}{\partial x_i}\right]\mathrm{d}t \tag{3.63}$$

$$+ \bar{\rho}\dot{\omega}_\alpha^n(\boldsymbol{\phi}^n)\mathrm{d}t + \frac{1}{2}\bar{\rho}\omega_{MM}\left(\xi_\alpha^n - \tilde{\phi}_\alpha\right)\mathrm{d}t + \bar{\rho}\sqrt{\frac{2}{\bar{\rho}}\frac{\mu_{sgs}}{Sc_{sgs}}}\frac{\partial \xi_\alpha^n}{\partial x_j}\mathrm{d}W_j^n. \tag{3.64}$$

The last term on the right-hand side is the stochastic contribution, which represents the random advection caused by the unresolved turbulence in the presence of scalar gradients for the individual fields. In this context, $\mathrm{d}\mathbf{W}^n = \boldsymbol{\eta}^n\sqrt{\Delta t}$ denotes an increment-vector of a stochastic Wiener process, which is constant in space but different for each field. Accordingly, $\mathrm{d}W_j^n$ represents its j^{th} component. The Wiener process is a random walk, normally distributed with a mean value of zero and a variance equal the time step size Δt. More details regarding the treatment of this term is given in the implementation section of this work. From the solution of the stochastic fields, it is then possible to obtain the moments of the respective marginal subgrid FDF, shown exemplarily for its expectation $\widetilde{\phi}_\alpha$ and variance $\widetilde{\mathrm{var}(\phi_\alpha)}$:

$$\tilde{\phi}_\alpha = \frac{1}{N_s}\sum_{n=1}^{N_s} \xi_\alpha^n \tag{3.65}$$

$$\widetilde{\mathrm{var}(\phi_\alpha)} = \frac{1}{N_s}\sum_{n=1}^{N_s}\left(\xi_\alpha^n - \bar{\phi}_\alpha\right)^2. \tag{3.66}$$

3.2 Disperse Phase Modeling

This section is dedicated to the treatment of the liquid phase. Before outlining the adopted approach, a brief summary of the common modeling strategies employed to compute multiphase flows is given. Note that when subsequently referring to a multiphase or two-phase flow, a gaseous-liquid flow—a spray—is implied.

3.2.1 Euler-Euler vs. Euler-Lagrange

Numerous approaches exist to describe two-phase flows. The differentiation between the strategies is often based on the representation for the carrier phase and the liquid phase,

which is categorized as either Euler-Euler, or Euler-Lagrange. In the former, the two fluids are treated using the same set of Eulerian equations (similar to the previously introduced one, but phase-averaged), while the latter represents the liquid phase as discrete particles for which Lagrangian equations of motion are solved. Among Euler-Euler approaches, the volume of fluid (VOF) method [79] or the level-set method [184] are widespread. However, their usage is generally limited to DNS due to their high resolution constrains [191]. Other Euler-Euler approaches rely on the description of the liquid phase as number density functions (NDFs) for each of the phase properties (for instance, size, velocity, composition), which are transported in physical space using a suitable method, for example the quadrature based method of moments (QMoM) [117]. On the other hand, Euler-Lagrange methods represent the liquid phase as set of discrete particles tracked in a Lagrangian manner. The interaction between both phases is realized by introducing source terms in the carrier phase PDEs, while the evolution of the particles is determined by the carrier phase properties interpolated onto their position. The idea is sketched in [35] and is also known as particle-source-in-cell (PSIC) approach.

3.2.2 Evolution of Lagrange Point-Particles

In this work, an Euler-Lagrange method is adopted, where the liquid phase is represented by means of point-wise computational parcels, each representing a heap of real droplets sharing the same properties. This strategy allows to significantly reduce the computational effort linked to the evolution of the disperse phase. The point-wise assumption is better known as point-particle-method (PPM). The overall approach includes the following assumptions or simplifications: (1) The liquid phase is considered to be in a diluted state. Therefore, no interactions between droplets are considered. (2) The Weber number in Equation 2.60 is presumed to be below the critical value where breakup processes are relevant. Thus, no breakup effects are considered. Additionally, the droplets are assumed spherical. (3) The temperature is uniformly distributed within the droplets, which is equivalent to presuming a droplet Biot number much smaller than unity. Additionally (4), the droplets considered in this work consist of only one species (ethanol). Lastly (4), it is assumed that the interaction of droplets and carrier phase occurs predominantly at the resolved scales. Therefore, no dispersion or additional subgrid scale droplet interaction model is employed.

The particle or droplet evolution (subscript $(\cdot)_d$) is expressed by the equations for the position $\mathbf{x}_d$, velocity $\mathbf{u}_d$, mass m_d and temperature T_d. Starting with the equations of motion, the position and velocity ordinary differential equations (ODE) read

$$\frac{d\mathbf{x}_d}{dt} = \mathbf{u}_d, \tag{3.67}$$

$$\frac{d\mathbf{u}_d}{d_t} = \frac{1}{m_d}\sum_i \mathbf{F}_i. \tag{3.68}$$

Here, $\sum_i \mathbf{F}_i$ denotes the forces acting on the parcels considered in the present investigations, that is drag [180, 208] and gravity. The gravitational force acting on the particle is computed as

$$\mathbf{F}_g = m_d\mathbf{g}\left(1-\frac{\rho}{\rho_d}\right) = \rho_d\frac{\pi d_d^3}{6}\mathbf{g}\left(1-\frac{\rho}{\rho_d}\right), \tag{3.69}$$

where $\mathbf{g}$ denotes the gravitational acceleration, m_p the particle mass, and ρ and ρ_d the carrier and particle density respectively. In the case of liquid droplets, the counteracting lift force caused by the displacement of the surrounding carrier mass is small compared

to the gravitational force acting on the liquid. This can be deduced from the small gas to liquid density ratio ρ/ρ_d in Equation 3.69. The drag force is expressed by

$$\mathbf{F}_D = \frac{3}{4}\frac{\rho}{\rho_d}\frac{m_d}{d_d}C_D\Big(\mathbf{u}_\infty - \mathbf{u}_d\Big)\Big|\mathbf{u}_\infty - \mathbf{u}_d\Big|. \tag{3.70}$$

Herein, $\mathbf{u}_\infty$ represents the carrier phase velocity. Equation 3.70 can also be reformulated using the droplet Reynolds number as defined in Equation 2.63 to

$$\mathbf{F}_D = \frac{3}{4}\frac{m_d\mu}{\rho_d d_d^2}Re_d C_D\Big(\mathbf{u}_\infty - \mathbf{u}_d\Big). \tag{3.71}$$

The drag coefficient C_D is computed as proposed by Nordin [130], a minor modification of the original formulation by Schiller and Naumann [179]

$$C_D = \begin{cases} \frac{24}{Re_d}\left(1 + \frac{1}{6}Re_d^{2/3}\right) & Re_d \leq 1000 \\ 0.424 & Re_d > 1000 \end{cases}. \tag{3.72}$$

In the context of spray combustion, droplets may heat up and release vapor, eventually fueling the combustion reaction. In order to represent such effects, the two additional equations describing the droplet temperature and mass evolution are required. In this work, the notation introduced by Miller et al. [123] is adopted. Herein, the droplet mass m_d and temperature T_d are described by the following ODEs

$$\frac{dm_d}{dt} = -\frac{1}{3}\frac{Sh}{Sc}\left(\frac{m_d}{\tau_p}\right)H_M, \tag{3.73}$$

$$\frac{dT_d}{dt} = f_2\frac{Nu}{3Pr}\left(\frac{c_p}{c_{p,l}\tau_p}\right)(T_\infty - T_d) + \left(\frac{L_v}{c_{p,l}}\right)\frac{\dot{m}_d}{m_d}. \tag{3.74}$$

Sh, Sc, Pr and Nu denote the Sherwood, Schmidt, Prandtl and Nusselt number, respectively. $\tau_p = \rho_d d_d^2/18\mu$ has the dimensions of a timescale and is therefore termed as particle relaxation time. Additionally, a heat transfer correction parameter due to evaporation f_2 is introduced [123]. H_M corresponds to the mass transfer driving potential. The quantities L_v, c_p and $c_{p,l}$ stand for the latent heat of vaporization of the liquid, the heat capacity of the surrounding gas, and the liquid heat capacity, respectively. In this work, two different evaporation models are implemented and thoroughly compared. Both models are subsequently briefly introduced.

Abramzon-Sirignano Model The model proposed by Abramzon and Sirignano [3], termed M2-approach in [123], can be interpreted as modified d^2-law under consideration of the Stefan flow. This effect is describing the flow from droplet to carrier caused by the liquid evaporation at the droplet surface. In this model, the correction factor f_2 is expressed as

$$f_2 = -\frac{\dot{m}_d}{m_d B_T'}\left(\frac{3\tau_d Pr}{Nu}\right), \tag{3.75}$$

and the mass transfer potential as

$$H_M = \ln\big(1 + B_{M,eq}\big). \tag{3.76}$$

The quantities B_T' and $B_{M,eq}$ denote the Spalding energy and mass transfer numbers. In this model, the Spalding transfer numbers are related via

$$B_T' = \big(1 + B_{M,eq}\big)^\phi - 1 \qquad \text{with} \qquad \phi = \frac{c_{p,v}}{c_{p,l}}\frac{Sh^*}{Nu^*}\frac{1}{Le}, \tag{3.77}$$

and the mass transfer number is defined as

$$B_{M,eq} = \frac{Y_{s,eq} - Y_\infty}{1 - Y_{s,eq}}, \tag{3.78}$$

where $Y_{s,eq}$ and Y_∞ represent the vapor mass fraction at the droplet surface and in the carrier, respectively. $Y_{s,eq}$ can be obtained from the vapor molar fraction at the surface $X_{s,eq}$, which is generally estimated by correlating the vapor pressure of the liquid p_v to its temperature through a suitable equation. An overview of the possible strategies to approximate the vapor pressure is given in [149]. In this work, the vapor pressure correlation is given by [36]

$$\ln(p_v) = A + \frac{B}{T} + C\ln(T) + DT^E, \tag{3.79}$$

with the species-specific coefficients, A, B, C, D and E. With exception of the variable exponent E in the last term, this equation is equivalent to the method proposed by Riedel [162]. The effect of the Stefan flow is taken into account by using modified formulations for the Nusselt and Sherwood number in Equations 3.73 and 3.74

$$Nu^* = 2 + \frac{Nu - 2}{F_T}, \qquad F_T = \frac{\left(1 + B'_T\right)^{0.7}}{B'_T}\ln(1 + B'_t) \tag{3.80}$$

$$Sh^* = 2 + \frac{Sh - 2}{F_M}, \qquad F_M = \frac{\left(1 + B_{M,eq}\right)^{0.7}}{B_{M,eq}}\ln(1 + B_{M,eq}) \tag{3.81}$$

instead of the formulation proposed by Ranz and Marshall [159]

$$Nu = 2 + 0.552 Re_d^{1/2} Pr^{1/3} \tag{3.82}$$

$$Sh = 2 + 0.552 Re_d^{1/2} Sc^{1/3}. \tag{3.83}$$

In order to derive the introduced Equations 3.73 and 3.74 for droplet heat and mass transfer, constant thermodynamic properties across the droplet boundary layer are assumed [12] and it is therefore crucial to estimate these quantities as accurately as possible. This is important for the evaluation of the dimensionless numbers, as Schmidt, Prandtl or Reynolds number. If not explicitly stated otherwise, the reference properties are evaluated using the well-established "1/3" - rule [104, 123, 3] proposed by Yuen and Chen [208]. In this context, the reference temperature and composition are obtained using

$$T_r = T_s + \frac{1}{3}\left(T_\infty - T_s\right), \tag{3.84}$$

$$Y_r = Y_s + \frac{1}{3}\left(Y_\infty - Y_s\right). \tag{3.85}$$

Once the composition and temperature at the reference state are known, the Wilke rule [204] is used to obtain the dynamic viscosity μ and thermal conductivity λ while the heat capacity is mass averaged. In the context of tabulated chemistry, the procedure can be summarized as follows: first, the composition and temperature are retrieved from the thermochemical lookup-table and interpolated at the parcel position. Secondly, reference conditions are determined according to Yuen and Chen [208]. Subsequently, all properties of interest are evaluated through NASA polynomials [122]. Finally, the mixing rules are applied, and mass and heat exchange computed.

Miller Model The model subsequently referred to as Miller model corresponds to the model M7 investigated in [123]. As advertised by the authors, this model features non-equilibrium assumptions in the evaporation process and is therefore expected to yield better results under a wider range of conditions. The incorporation of non-equilibrium effects is considered via the Langmuir-Knudsen law. The mass transfer potential shown in Equation 3.76 is therefore reformulated using the non-equilibrium Spalding mass transfer number $B_{M,neq}$ instead of $B_{M,eq}$

$$B_{M,neq} = \frac{Y_{s,neq} - Y_\infty}{1 - Y_{s,neq}}. \tag{3.86}$$

The correction factor f_2 reads

$$f_2 = \frac{\beta^*}{e^{\beta^*} - 1}, \tag{3.87}$$

with the non-dimensional evaporation parameter β^*, expressed by

$$\beta^* = -\left(\frac{3\tau_p Pr}{2}\right)\frac{\dot{m}_d}{m_d}. \tag{3.88}$$

The mass fraction at the surface $Y_{s,neq}$ is obtained from its molar counterpart $X_{s,neq}$, which represents a corrected version of the equilibrium molar fraction obtained from the vapor pressure

$$X_{s,neq} = X_{s,eq} - \frac{2L_K}{D}\beta^*. \tag{3.89}$$

L_K is the Knudsen layer thickness, defined as

$$L_K = \frac{\mu\sqrt{2\pi T_d R/M_v}}{p_{th}\alpha_e Sc}. \tag{3.90}$$

In this context, R denotes the universal gas constant, M_v the vapor molar mass, p_{th} the thermodynamic pressure and α_e the molecular accommodation coefficient. Similarly to [123], α_e is assumed to be one. Note that all reference properties are evaluated similarly to the Abramzon-Sirignano model.

3.2.3 Coupling with the Carrier Phase

As is outlined above, the evolution of a droplet (or parcel) position, velocity, mass and temperature is mainly determined by the carrier phase properties. Undoubtedly, the acceleration of a particle due to drag, i.e. its momentum increase, should in reverse cause a decrease of the carrier phase momentum. This is realized by introducing source terms in the Eulerian equations of the carrier phase and mimics the dynamics of a two-way coupled system. Within LES, the amount of mass and momentum exchange is depending on the number of real droplets within a computational parcel as well as the interaction time of the parcel in a specific LES control volume. With respect to the two-dimensional tabulation strategy adopted in this work, the effect of the liquid phase must taken into account in the mass, momentum, mixture fraction and progress variable transport equations. These source terms are respectively denoted as $\overline{S}_{m,l}$, $\overline{\mathbf{S}}_{u,l}$, $\overline{S}_{Z,l}$ and $\overline{S}_{PV,l}$. Describing the mass contribution of the disperse phase is straight forward and consists in summing up all time integrated evaporation rates of the parcels, each multiplied by the number of real droplets N_d represented by the parcel. This yields the following expression for $\overline{S}_{m,l}$ in a volume V populated with N_p parcels:

$$\overline{S}_{m,l} = \frac{1}{V\Delta t}\sum_j^{N_t}\sum_i^{N_p} N_{d,i}\dot{m}_{d,i,j}\Delta t_{i,j}, \qquad \text{with} \qquad \Delta t = \sum_j^{N_t}\Delta t_j. \tag{3.91}$$

The parcel specific time step $\Delta t_{i,j}$ has been introduced, which represents a fraction of the Eulerian time step Δt. The momentum source term is composed of a term grounded on Newton's third law, i.e. that the force resulting from the carrier-particle interaction is inversely exercised by the parcel on the carrier phase, and a term issuing from the evaporated parcel mass

$$\overline{\mathbf{S}}_{u,l} = \frac{1}{V\Delta t}\sum_{j}^{N_t}\sum_{i}^{N_p} N_{d,i}\Big(- \mathbf{F}_{D,i,j} + \dot{m}_{d,i,j}\mathbf{u}_{d,i,j}\Big)\Delta t_{i,j}. \tag{3.92}$$

In this work, the spray-droplets studied consist of pure fuel. Under consideration of the mixture fraction and progress variables definitions adopted in this work (see Equations 3.29 and 3.31), the source terms of mixture fraction and progress variable are expressed as

$$\overline{S}_{Z,l} = \overline{S}_{m,l}, \qquad \text{and} \qquad \overline{S}_{PV,l} = 0. \tag{3.93}$$

3.2.4 Interaction of Droplets with a Thickened Flame

A significant interest of this work is the representation of the interaction of droplets with a flame that has been thickened using the ATF approach. This is relevant since the interaction of a droplet with a thickened flame will definitely differ from the one where no thickening is applied. Differences are expected to be high for heat and mass exchange. In literature, this impact is either neglected (e.g. [166]) or the correction procedure, initially proposed by Sacomano Filho et al. [175] is employed. Usually, the correction procedure consists in defining a correction factor for droplet heat and mass transfer in order to retrieve a correct flame exit diameter for droplets crossing the thickened flame. In the present work, the correction is expressed in terms of an effective factor F_{eff}. Taking this factor into account, Equations 3.73 and 3.74 are reformulated to

$$\frac{dm_d}{dt} = -\frac{1}{F_{\mathit{eff}}}\left[\frac{1}{3}\frac{Sh}{Sc}\left(\frac{m_d}{\tau_d}\right)H_M\right], \tag{3.94}$$

$$\frac{dT_d}{dt} = \frac{1}{F_{\mathit{eff}}}\left[f_2\frac{Nu}{3Pr}\left(\frac{c_p}{c_{p,l}\tau_d}\right)(T_\infty - T_d)\right] + \left(\frac{L_v}{c_{p,l}}\right)\frac{\dot{m}_d}{m_d}. \tag{3.95}$$

In this context, the uncorrected and corrected approaches result in a different effective thickening factor $F_{\mathit{eff}} = 1$ and $F_{\mathit{eff}} = F$. The validity of the second method is shown in [175, 170], where flame front and droplet are moving orthogonally to each other. The definition is consistent with the initial idea of the thickened flame approach as both, movement of droplet relative to the flame front and the direction in which thickening is applied (flame orthogonal) are equivalent. However, this procedure is expected to introduce distorted heat and mass transfer for droplets moving with a substantial velocity component parallel to the flame front, as is often the case in spray jet flames.

This is outlined in Figure 3.5, which shows a droplet traveling with a velocity $\mathbf{u}_p$ across a non thickened flame with thickness δ_l or a thickened flame with thickness $F\delta_l$. The non-thickened and thickened flame front are represented in Figure 3.5 through vertical black and thickened red lines, respectively. The path of a particle (blue line in Figure 3.5) traveling with the velocity $\mathbf{u}_p$ across the flame front for an unthickened flame can be described by the states (a) (before the flame), (b) (flame front entry) and (c) (flame front exit). Taking advantage of the monotonic increase of the reaction progress variable, it is possible to assess the flame front orientation using the reaction progress variable gradient ∇PV, which is used to define the flame front orthogonal direction (i.e. $\frac{\nabla PV}{|\nabla PV|}$)

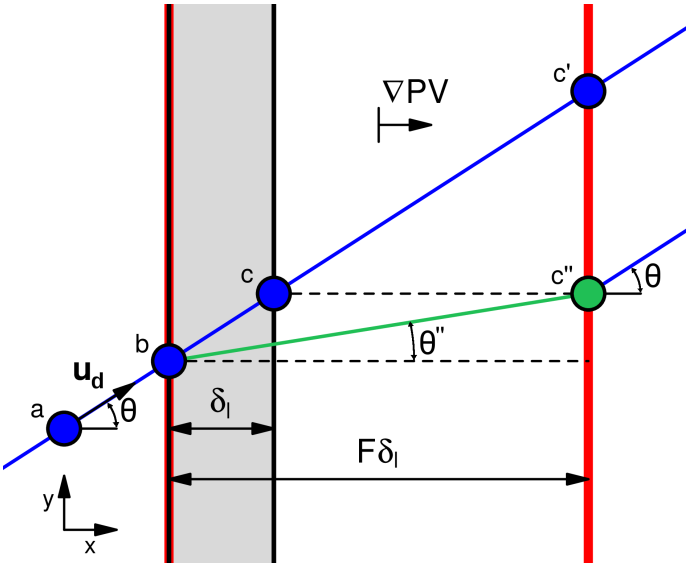

Figure 3.5: Schematic representation of a particle interacting with a (thickened) flame. The shaded area delimited by the vertical black line corresponds to the unthickened flame front. Thick red lines delimit the thickened flame front. (Blue line: Normal droplet trajectory; green line: Modified droplet trajectory (refraction correction).

and the flame front parallel direction. While the length of the droplet path in flame front orthogonal direction is defined by the actual flame thickness, its parallel component is determined by its flame parallel velocity. The relation of both components is specified through the particle-flame interaction angle θ. When the droplet enters the flame, its temperature rises quickly, yielding strong evaporation rates which are distributed along the droplet movement path and thus influencing mixture evolution in both flame front normal and parallel direction. This is an important point that must be kept in mind when going over to the analogous scenario with a thickened flame. In this case, the droplet follows an elongated path and the flame front exit position is shifted to (c') in Figure 3.5. As stated in [22], the idea of thickening is to expand the coordinate normal to a discontinuity in order to resolve it, which is a one-dimensional transformation. However, a particle interacting with a flame in a specific angle θ can no longer be perceived as such problem. If the flame is thickened in one direction, the path of the droplet within the flame is not only elongated in flame normal, but also in flame parallel direction, which will alter the mixture evolution in flame parallel direction. It is likely that such a constellation will influence flame dynamics.

In view of the issues related to the droplet displacement along the parallel direction of a thickened flame, two approaches are introduced, which aim at reducing the stretching of the vapor release in flame front parallel direction [44]. The first formulation is obtained by limiting the correction of heat and mass transfer through the parameter F_{eff} to the flame orthogonal direction of droplet movement. The strategy is derived by considering the limiting conditions of a droplet moving (1) orthogonally or (2) parallel to the flame front. While for the first scenario, the original formulation found in [175] or [28] should be recovered, the second scenario would yield no correction at all. Such properties are achieved by weighting the thickening factor F with the projection of droplet movement onto the flame propagation direction. Accordingly, the correction factor F_{eff} takes the

following form [44]:

$$F_{\mathit{eff}} = 1 + \left| \frac{(\nabla PV)}{|\nabla PV|} \cdot \frac{\mathbf{u}_d}{|\mathbf{u}_d|} \right| (F - 1) \tag{3.96}$$

As previously pointed out, the quantity ∇PV refers to the gradient of the progress variable, which is interpolated onto the parcel position. This quantity describes the flame front orientation perceived by the parcel. The quantity $\frac{\mathbf{u}_d}{|\mathbf{u}_d|}$ denotes the normal unity vector defining the parcel movement direction. Various limiting conditions shall be considered from Equation 3.96: (1) far away from the flame, i.e. where no thickening is applied, the term $(F - 1)$ is zero and no correction of heat and mass transfer is applied (see Equation 3.50); (2) supposing ∇PV and $\mathbf{u}_d$ are orthogonal to each other, corresponding to a parcel moving parallel to the flame front (while thickening is applied, in other words $F \neq 1$), the last term of the right-hand-side of Equation 3.96 also vanishes, yielding $F_{\mathit{eff}} = 1$; (3) in the case of a droplet moving orthogonal to the flame front while thickening is performed, the factor initially proposed by Sacomano Filho et al. [175] is retrieved. Subsequently, this method will be referred to as *projection correction*.

A different manner to approach such a problem is the second strategy, which will be referenced in the rest of this work as *refraction correction*, because of its geometrical resemblance with the phenomenon of light refraction. Here, the same formulation for F_{eff} as used in [175, 29], i.e. $F_{\mathit{eff}} = F$, is employed. However, the trajectory of the droplet in flame parallel direction is limited to the unthickened flame front parallel displacement. Such a tracking correction yields the green path and the corrected exit position and state (c'') in Figure 3.5. The correction is equivalent to reducing the particle flame interaction angle to $\theta'' = \theta/F$. From a practical point of view, such path correction requires a passive transformation of particle movement in a flame front orthogonal coordinate system, of which the axes can be defined by evaluating $\frac{\nabla PV}{|\nabla PV|}$ and its orthogonal vectors at the droplet position. Once the transformed velocity is obtained, the flame parallel components are scaled by the thickening factor F, while the flame orthogonal component is left unchanged. Subsequently, the corrected velocity is re-transformed into the original reference coordinate system. This corrected velocity is then employed to track the particle along the thickened flame. It should be noticed that this velocity correction does not change the particle velocity $\mathbf{u}_d$. In fact, this correction is only applied to update the droplet position during the droplet-flame interaction time. Thus, no change on momentum exchange or convective heat and mass transfer is explicitly applied here.

The difference between refraction and projection correction can be summarized as follows: The former modifies the distribution of vapor release in flame front parallel direction and at the same time keeps the droplet-flame interaction time equal to the formulation found in [175]. Differently, the projection approach avoids any trajectory correction but changes the vapor release along the droplet path, which causes a reduction of its lifetime compared with the refraction correction and the approach found in [175]. An evaluation of the various approaches to treat the droplet heat and mass transfer is first shown for a simple configuration in Chapter 5 and later in a complex turbulent spray flame in Chapter 8.

3.2.5 Interaction of Droplets and Carrier in the Context of ESF

So far, the transport equation for the Favre-filtered PDF has only been introduced for single-phase flows. In analogy to the the transport equations for mass, momentum, mixture fraction and reaction progress variable, an additional term arises on the right-hand-side of

Equation 3.58 due to the presence of the liquid phase

$$\begin{aligned}&\frac{\partial}{\partial t}\left(\overline{\rho}\widetilde{P}_\phi\right)+\frac{\partial}{\partial x_i}\left(\overline{\rho}\widetilde{u}_i\widetilde{P}_\phi\right)+\frac{\partial}{\partial \psi_\alpha}\left(\overline{\rho}\dot{\omega}_\alpha(\boldsymbol{\psi})\widetilde{P}_\phi\right)=-\frac{\partial}{\partial x_i}\left[\overline{\rho}(u_i''|\boldsymbol{\phi}=\boldsymbol{\psi})\widetilde{P}_\phi\right]\\&-\frac{\partial^2}{\partial \psi_\alpha^2}\left[\left(\overline{\rho\frac{\nu}{Sc}\frac{\partial\psi_\alpha}{\partial x_i}\frac{\partial\psi_\alpha}{\partial x_i}\middle|\boldsymbol{\phi}=\boldsymbol{\psi}}\right)\widetilde{P}_\phi\right]+\frac{\partial}{\partial x_i}\left(\overline{\rho}\frac{\overline{\nu}}{Sc}\frac{\partial\widetilde{P}_\phi}{\partial x_i}\right)+\frac{\partial}{\partial \psi_\alpha}\left(\overline{S}_{\alpha,l}\widetilde{P}_\phi\right).\end{aligned}\tag{3.97}$$

Consequently, this source term is also present in the stochastic field equations, which are presented in the next section. Within the PSIC-formalim, the Lagrangian source terms are uniformly distributed within the control volumes. This implies equal source terms for all stochastic fields, which is equivalent to presuming that the droplets do not produce any scalar subgrid variance (the source term is uniformly shifting the scalar FDF in scalar space). This procedure is similar to previous works [95, 94, 61, 62]. Even though models have been proposed in the RANS [80] and LES [140] context, it remains difficult to evaluate the impact of the liquid source terms on the subgrid PDF. Here a DNS of carrier and liquid phase could help to gain a better understanding of the effect and help develop suitable models for LES.

In addition, it should be noted that since for the ESF method, no thickening is applied, no explicit correction of the droplet/parcel evolution is performed. Accordingly, the droplet evolution is described by the unmodified equations for particle position, momentum, mass and temperature (Equations 3.67, 3.68, 3.73 and 3.74). Thereby any effects connected to the subgrid scalar or velocity fluctuations are not considered. Still, it should be noted that the temperature perceived by the droplet is obtained from the FDF integration. The subgrid-scale information is therefore not completely left aside.

In fact, the consideration of the subgrid-scale velocity fluctuations is not strictly related to the ESF method, but could also be included when the artificial flame-front-thickening is performed. The idea is based on the closure for the subgrid turbulent kinetic energy k_{sgs}, which allows to add random fluctuation based on k_{sgs} to the velocity perceived by the droplet (this is suggested in [170]). Another strategy is to take the influence of the subgrid velocity in the particle momentum equation into account through a stochastic Markov model [15]. This idea has later been extended by Bini and Jones [16] to model the effect on the convective droplet mass transfer through the introduction of a subgrid Sherwood number. The main justification for not considering these effects is that the LES resolves the vast majority of the turbulent kinetic energy. Consequently, it is assumed that the remaining subgrid part has a negligible influence on the droplet evolution.

The influence of the subgrid scalar fluctuations on the disperse phase in the context of transported PDFs is still an untouched research topic. Different strategies may be adopted to take the subgrid scalar fluctuation into account. One possibility might be to add a random component to the resolved part of the scalars based on their respective subgrid variances (similar to the k_{sgs}-based approach for the velocity). This could be performed in the context of presumed PDFs as well as for the ESF method. Another feasible procedure could be to directly sample the carrier state perceived by the droplets from the joint subgrid scalar distribution provided by the stochastic fields. However, none of these strategies are applied in this work. The carrier phase properties perceived by the droplets are thereby solely represented through resolved carrier quantities, which is similar to other contributions [15, 16, 95, 94, 61, 62, 170]. The implementation and the investigation of the impact of more advanced methods is left for future research.

3.3 Summary of the Solved Equations

To conclude this chapter, the final set of equations solved in this work are presented in the context of ATF and the ESF method. For the sake of brevity, the introduced equation for Lagrangian droplets are not rewritten. The reader is much more referred to the preceding sections of this chapter. Both ATF and ESF approaches rely on the transport equation for mass and momentum

$$\frac{\partial \overline{\rho}}{\partial t} + \frac{\partial}{\partial x_i}(\overline{\rho}\widetilde{u}_i) = \overline{S}_{m,l}, \tag{3.98}$$

$$\frac{\partial \overline{\rho}\widetilde{u}_i}{\partial t} + \frac{\partial}{\partial x_j}(\overline{\rho}\widetilde{u}_i\widetilde{u}_j) = -\frac{\partial \overline{P}}{\partial x_i} + \frac{\partial}{\partial x_j}\left(\mu_{eff}\left(2\widetilde{S}_{ij} - \frac{1}{3}\widetilde{S}_{kk}\delta_{ij}\right)\right) + \overline{\rho}g_i + \overline{S}_{u_i,l}, \tag{3.99}$$

where an effective viscosity has been introduced $\mu_{eff} = \overline{\mu} + \mu_{sgs}$.

ATF model Regarding the coupling of LES with the ATF approach, Equations 3.98 and 3.99 are complemented by the thickened scalar equations for the progress variable and mixture fraction

$$\frac{\partial \overline{\rho}\widetilde{PV}}{\partial t} + \frac{\partial}{\partial x_i}\left(\overline{\rho}\widetilde{u}_i\widetilde{PV}\right) = \frac{\partial}{\partial x_j}\left(\left[FE\frac{\overline{\mu}}{Sc} + (1-\Omega)\frac{\mu_{sgs}}{Sc_{sgs}})\right]\frac{\partial \widetilde{PV}}{\partial x_j}\right) + \frac{E}{F}\overline{\rho}\dot{\omega}_{PV} \tag{3.100}$$

$$\frac{\partial \overline{\rho}\widetilde{Z}}{\partial t} + \frac{\partial}{\partial x_i}\left(\overline{\rho}\widetilde{u}_i\widetilde{Z}\right) = \frac{\partial}{\partial x_j}\left(\left[FE\frac{\overline{\mu}}{Sc} + (1-\Omega)\frac{\mu_{sgs}}{Sc_{sgs}})\right]\frac{\partial \widetilde{Z}}{\partial x_j}\right) + \overline{S}_{Z,l} \tag{3.101}$$

Note that the liquid phase source term in the progress variable transport equation has been explicitly omitted due to the progress variable definition (see Section 3.2.3).

ESF method For the ESF approach, the stochastic field equations for the progress variable read

$$\begin{aligned}\mathrm{d}(\bar{\rho}\xi^n_{PV}) = &-\frac{\partial}{\partial x_j}(\bar{\rho}\xi^n_{PV}\widetilde{u}_j)\mathrm{d}t + \frac{\partial}{\partial x_i}\left[\left(\frac{\bar{\mu}}{Sc} + \frac{\mu_{sgs}}{Sc_{sgs}}\right)\frac{\partial \xi^n_{PV}}{\partial x_i}\right]\mathrm{d}t \\ &+ \bar{\rho}\dot{\omega}^n_{PV}(\xi^n_{PV}, \xi^n_Z)\mathrm{d}t + \frac{1}{2}\bar{\rho}\omega_{MM}\left(\xi^n_{PV} - \widetilde{PV}\right)\mathrm{d}t + \bar{\rho}\sqrt{\frac{2}{\bar{\rho}}\frac{\mu_{sgs}}{Sc_{sgs}}}\frac{\partial \xi^n_{PV}}{\partial x_j}\mathrm{d}W^n_j,\end{aligned} \tag{3.102}$$

while the mixture fraction stochastic fields evolve according to

$$\begin{aligned}\mathrm{d}(\bar{\rho}\xi^n_Z) = &-\frac{\partial}{\partial x_j}(\bar{\rho}\xi^n_Z\widetilde{u}_j)\mathrm{d}t + \frac{\partial}{\partial x_i}\left[\left(\frac{\bar{\mu}}{Sc} + \frac{\mu_{sgs}}{Sc_{sgs}}\right)\frac{\partial \xi^n_Z}{\partial x_i}\right]\mathrm{d}t \\ &+ \frac{1}{2}\bar{\rho}\omega_{MM}\left(\xi^n_Z - \widetilde{Z}\right)\mathrm{d}t + \bar{\rho}\sqrt{\frac{2}{\bar{\rho}}\frac{\mu_{sgs}}{Sc_{sgs}}}\frac{\partial \xi^n_Z}{\partial x_j}\mathrm{d}W^n_j + \overline{S}_{Z,l}\mathrm{d}t.\end{aligned} \tag{3.103}$$

PART II: IMPLEMENTATION, VERIFICATION AND VALIDATION

Chapter 4

Numerical Methods and Implementations

The lack of analytical solution to the previously introduced set of partial different equations makes the application of numerical methods necessary to obtain an approximate solution of the system considered. In this context, a spatial and temporal discretization is performed, which allows to transform the PDE system into a set of algebraic equations that can be solved numerically. The solution of this set of algebraic equations represents an approximation of the solution and is obtained at discrete points in space and time. The difference between the exact solution and the discretized one is referred to as discretization error and depends on the numerical schemes adopted for the discretization. In this work, the finite volume method (FVM) is applied. The FVM discretization divides the spatial domain into discrete subvolumes, subsequently referred to as control volumes (CVs).

This chapter is introducing the FVM discretization in the context of the open-source C++ library OpenFOAM [92, 202]. The temporal and spatial discretization schemes used are presented and the pressure-velocity coupling algorithm adopted to solve the emerging algebraic system of equations is introduced. In a next step the tabulated-chemistry-based solution procedure is outlined in the context of ATF and ESF.

4.1 Discretization Procedure

As for other discretization strategies as the finite difference method, FVM relies on the spatial and temporal discretization of the system of PDEs to be solved. Before the various terms in the PDEs can be written in discretized form, the discretization of the solution domain is required. As previously outlined, this work relies on the OpenFOAM library to (1) discretize the domain into finite volumes and (2) solve the discretized set of PDEs in the CVs. A brief summary of the discretization strategy is given subsequently. More information on this matter can be found in [91, 71].

4.1.1 Spatial Discretization

In FVM, the domain of interest is divided in a finite number of control volumes or cells. One advantage of this method is its implicit conservativeness. Specifically, FVM is able to conserve the quantities of the original PDEs at the discrete level. In the OpenFOAM implementation of the finite volume method, the computational domain is subdivided into polyhedral cells and the solution variables, for instance mixture fraction, velocity or pressure are all stored at the cell centroids of these volumes, which is also known as collocated or non-staggered arrangement [91]. A typical OpenFOAM cell is illustrated in Figure 4.1. The CV is characterized by (1) a cell centroid P and (2) cell vertex points, the

latter of which are used to define (3) cell faces. The cell faces can either separate different CVs (so-called internal faces) or belong to a boundary (boundary faces). The quantity $\mathbf{S}_f$ in Figure 4.1 denotes the face normal vector with magnitude equal to the face area.

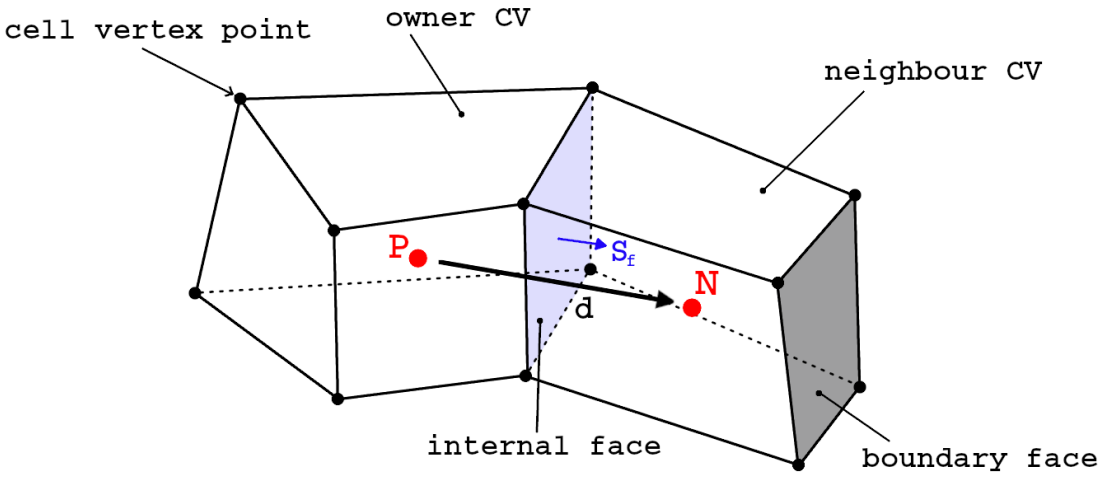

Figure 4.1: Illustration of a control volume and its neighboring cell alongside the quantities used to define such CV.

The discretization of the various terms is described by means of the transport equation in integral form for a representative scalar ϕ within a volume V_P, as introduced in Equation 2.2

$$\frac{\partial}{\partial t}\int_{V_P}(\rho\phi)dV_P + \int_S \mathbf{J}^{\phi}_{conv}\mathbf{n}dS + \int_S \mathbf{J}^{\phi}_{diff}\mathbf{n}dS = \int_V \mathbf{\Sigma}^{\phi}dV_P. \tag{4.1}$$

Here, the flux across the control volume faces has been split into a convective $\mathbf{J}^{\phi}_{conv}$, and a diffusive component $\mathbf{J}^{\phi}_{diff}$. To solve Equation 4.1, numerical integration across V_P and its boundary faces must be applied. For the volume integrals, the second-order midpoint rule is adopted. Assuming that the value of density and ϕ at the cell centroid ρ_P and ϕ_P denote suitable averages across V_P, the approximation is expressed by

$$\int_{V_P}(\rho\phi)dV_P \approx \rho_P\phi_P V_P. \tag{4.2}$$

For the convective and diffusive fluxes, the surface integral is re-expressed as sum over all internal and boundary faces of the CV. Using the midpoint rule to approximate the surface integrals, the fluxes can be written as

$$\int_S \mathbf{J}^{\phi}_{conv}\mathbf{n}dS = \sum_f \left(\int_{S_f}\mathbf{J}^{\phi}\mathbf{n}_f dS_f\right) \approx \sum_f \mathbf{J}^{\phi}_f\mathbf{S}_f. \tag{4.3}$$

In this context, $\mathbf{J}^{\phi}_f$ denotes the value of $\mathbf{J}^{\phi}$ at the center of the face S_f. These are generally not available and must be approximated. So far, the symbolic fluxes $\mathbf{J}^{\phi}_{conv}$ and $\mathbf{J}^{\phi}_{diff}$ have been used. In the PDEs considered, these fluxes do not only include values of ϕ at the face center, but also spatial derivatives of ϕ. The approximations adopted for both, the convective and diffusive fluxes, are discussed next.

Convective Fluxes In the transport equations presented in this work the convective fluxes of ϕ are approximated by

$$\int_S \mathbf{J}^{\phi}_{conv}\mathbf{n}dS = \int_S \rho\phi\mathbf{u}\mathbf{n}dS \approx \sum_f \phi_f \underbrace{(\rho\mathbf{u})_f\mathbf{S}_f}_{F_f}, \tag{4.4}$$

where the quantity F_f represents the mass flux crossing the surface f. In this work, this mass flux is approximated through linear interpolation between the cell centroids (for instance P and N in Figure 4.1). The remaining unknown is ϕ_f, which is either computed using a central differencing (CD) schemes, or a blending between upwind and central differencing scheme. In the case of central differencing, ϕ_f is obtained through linear interpolation between the cell centroids of the cell P and its neighbor N [71, 198]

$$\phi_f^{CD} = \frac{\overline{fN}}{\overline{PN}}\phi_P + (1 - \frac{\overline{fN}}{\overline{PN}})\phi_N, \tag{4.5}$$

where the distance between the cell centroid of P and face center f is denoted as $\overline{fP}$. In analogy, $\overline{PN}$ is the distance between the two centroids of P and N. The blending differencing (BD) is achieved by combining the central differencing with the first order upwind differencing (UD) scheme

$$\phi_f^{UD} = \begin{cases} \phi_P & F_f \geq 0 \\ \phi_N & F_f < 0 \end{cases}, \tag{4.6}$$

yielding the following expression for ϕ_f:

$$\phi_f = \phi_f^{UD} + \gamma\big(\phi_f^{CD} - \phi_f^{UD}\big). \tag{4.7}$$

Here, the blending factor γ has been introduced, which can either be kept constant or determined dynamically. In this work, the so-called filteredLinear scheme [71] is adopted for the convective term found in the momentum transport equation. The aim of this scheme is to remove high-frequency modes in order to improve the numerical stability of the overall solution procedure. The blending factor is defined such that the upwind portion does not exceed 20%

$$\gamma = \max(\min(\alpha, 1), 0.8), \tag{4.8}$$

with

$$\alpha = 2 - 0.5\frac{\min\left[\left|(\phi_N - \phi_P) - d_i\frac{\partial\phi}{\partial x_i}\Big|_P\right|, \left|(\phi_N - \phi_P) - d_i\frac{\partial\phi}{\partial x_i}\Big|_N\right|\right]}{\max\left[\left|d_i\frac{\partial\phi}{\partial x_i}\Big|_P\right|, \left|d_i\frac{\partial\phi}{\partial x_i}\Big|_N\right|\right]}. \tag{4.9}$$

For the convective terms in the scalar transport equation, i.e. progress variable and mixture fraction, the Minmod flux-limiter scheme is used [167]. In this case, the blending factor is defined by

$$\gamma = \max(\min(\alpha, 1), 0), \tag{4.10}$$

where the flux limiter function α is expressed as

$$\alpha = 2\frac{d_i\frac{\partial\phi}{\partial x_i}}{\phi_N - \phi_P} - 1. \tag{4.11}$$

In this equation, the gradient term is computed based on the mass flux across the surface f as

$$\frac{\partial\phi}{\partial x_i} = \begin{cases} \frac{\partial\phi}{\partial x_i}\big|_P & F_f \geq 0 \\ \frac{\partial\phi}{\partial x_i}\big|_N & F_f < 0 \end{cases}. \tag{4.12}$$

Diffusive Fluxes The diffusive fluxes found in the transport equations to be solved all take the same form and are approximated similarly to the convective fluxes

$$\int_S \mathbf{J}^{\phi}_{diff} \mathbf{n} dS = \int_S \rho \Gamma_\phi \frac{\partial \phi}{\partial x_i} \mathbf{n} dS \approx \sum_f (\rho \Gamma_\phi)_f \frac{\partial \phi}{\partial x_i}\Big|_f \mathbf{S}_f, \tag{4.13}$$

where the diffusion coefficient of ϕ, Γ_ϕ has been introduced. In contrast to the convective fluxes, the diffusive term contains a first order derivative, which must be evaluated at the face center. In an equidistant and Cartesian arrangement of the control volumes, the derivative at the cell center can be approximated through linear interpolation

$$\frac{\partial \phi}{\partial x_i}\Big|_f \mathbf{S}_f = |\mathbf{S}_f| \frac{\phi_N - \phi_P}{|\mathbf{d}|}, \tag{4.14}$$

which represents a second-order approximation. Even though the numerical meshes adopted in this work strive for high orthogonality, the ideal behavior is only rarely fulfilled. In this case, two problem arise: the first is an error related to the face-center position. This is the case when $\mathbf{d}$ does not intersect the shared face at its center. In many FVM implementations as well as in this work, this error is usually neglected, as the standard procedure represents the best compromise between computational costs and numerical accuracy. The second error results from a misalignment of $\mathbf{d}$ and $\mathbf{S}_f$. Within OpenFOAM, this problem is taken into account through an additional correction term. For more information on the correction strategy, the interested reader is referred to [91].

Source Terms Finally, the remaining term in Equation 4.1 takes any sources or sinks of ϕ into account and is approximated by

$$\int_{V_P} \mathbf{\Sigma}^{\phi} dV_P \approx \mathbf{\Sigma}^{\phi}_P V_P. \tag{4.15}$$

Note that in general, OpenFOAM offers the possibility to linearize the source terms in order to improve the stability of the solution procedure [71, 91]. Such linearization is not adopted in this work due to the strong non-linearity of the emerging source terms in the context of tabulated chemistry. As will become clear in the course of this chapter, any non-linearities arising in the source terms of the PDEs are taken into account through an iterative procedure. The only exception is the source terms caused by the presence of the liquid phase.

4.1.2 Temporal Discretization

In addition to the spatial derivatives, the transient character of the transport equations asks for a discretization of the time into discrete time-steps. Leaving any stochastic component out of the equations, the solution of the PDEs at an unknown time t_j can be obtained by extrapolating the current state at the previous time t_i. The solution is therefore depending on the initial state and on the time step used $\Delta t = t_j - t_i$. In general, the time step cannot be chosen arbitrarily but needs to fulfill various criteria in order to yield a numerically stable procedure [33, 136]. Incorporating the previously introduced numerical approximations yields the following semi-discretized form of the generic transport equation

$$\frac{\partial (\rho \phi)}{\partial t}\Big|_P = \underbrace{\frac{1}{V_P}\Big[- \sum_f F_f \phi_f + \sum_f (\rho \Gamma_\phi)_f \frac{\partial \phi}{\partial x_i}\Big|_f \mathbf{S}_f + \mathbf{\Sigma}^{\phi}_P V_P \Big]}_{\mathcal{R}(\phi)} \tag{4.16}$$

In this context, the right-hand-side (RHS) $\mathcal{R}(\phi)$ has been introduced, which symbolizes all spatial discretization. Note that it is assumed that the control volumes do not change in time. In order to obtain the fully discretized version of Equation 4.16, the temporal derivative on the left hand side must also be replaced with a suitable numerical approximation. As previously mentioned, the discretization in time yields a solution at discrete time levels. In addition, it remains to be determined how $\mathcal{R}(\phi)$ should be expressed. This treatment is categorized as either explicit or implicit. In the former, the right-hand-side is approximated by means of known quantities (i.e. previous time levels), while the latter features unknown quantities of the new time level in $\mathcal{R}$. Explicit and implicit treatment yield a fundamentally different solution procedure. In the case of explicit time stepping schemes, the new quantity ϕ_P can be directly evaluated, whereas the implicit case involves the solution of an algebraic system of equations. The schemes adopted are briefly introduced next, where the time level n of the quantity $\psi = \rho\phi$ is expressed as

$$\psi(t = t_n) = \psi^n. \tag{4.17}$$

Euler Implicit Scheme The implicit Euler scheme is the most simple scheme adopted in this work. The method is first-order accurate and reads

$$\frac{\partial(\rho\phi)}{\partial t} = \frac{\partial\psi}{\partial t} \approx \frac{\psi^{n+1} - \psi^n}{\Delta t}, \tag{4.18}$$

which results in the fully discretized version of Equation 4.16

$$\psi^{n+1} = \psi^n + \Delta t\mathcal{R}(\psi^{n+1}). \tag{4.19}$$

Second-order Implicit Backward Scheme In order to decrease the numerical error of the temporal discretization, higher order schemes can be formulated which take into account multiple time levels in the approximation of the temporal derivative. The second-order backward scheme make use of the two previous time levels and reads

$$\frac{\partial(\rho\phi)}{\partial t} = \frac{\partial\psi}{\partial t} \approx \frac{3\psi^{n+1} - 4\psi^n + \psi^{n-1}}{2\Delta t}, \tag{4.20}$$

yielding

$$\psi^{n+1} = \frac{1}{3}\big(- \psi^{n-1} + 4\psi^n + 2\Delta t\mathcal{R}(\psi^{n+1})\big). \tag{4.21}$$

Crank-Nicolson Scheme Differently from the two previous methods, the Crank-Nicholson Scheme uses old and new time level to express the RHS

$$\psi^{n+1} = \psi^n + \frac{\Delta t}{2}\big(\mathcal{R}(\psi^n) + \mathcal{R}(\psi^{n+1})\big). \tag{4.22}$$

This discretization procedure can be thought of as the application of the trapezoidal rule in time and is second-order accurate.

4.1.3 Lagrange Phase Treatment

The multiphase problems considered in this work do not only require proper numerical treatment of the carrier phase, which is taken into account through the FVM strategy, but also a description of the evolution of the disperse phase. Differently from the carrier phase, the droplet/parcel evolution is determined by a set of ordinary differential equations.

For these equations, no spatial derivatives are required and only temporal integration is performed. Assuming a generic property of a spray droplet ψ_d (for instance position or momentum), the ODE is expressed as

$$\frac{\partial \psi_d}{\partial t} = f(\psi_d, \psi). \tag{4.23}$$

This equation induces that the evolution of ψ_d is not only depending on its current state, but also on the state of the carrier phase ψ. In this work, the temporal integration is performed using the Euler method in an either explicit or semi-implicit form. Introducing a Lagrangian specific time step Δt_d, the evolution of ψ_d then reads

$$\psi_d^{n+1} = \psi_d^n + f(\psi_d^n, \psi^n)\Delta t_d. \tag{4.24}$$

This equation represents the pure explicit version. In the semi-implicit treatment, f is expressed as $f(\psi_d^{n+1}, \psi^n)$ [65]. More details regarding the Lagrangian discretization and the particle tracking can be found in [130] as well as in [65].

4.2 Solution Procedure

The following section presents the solution procedure applied in order to solve the complex system of coupled PDEs. The solution procedure is outlined in the context of multiphase flows considered in this work. The single phase equivalent is obtained by omitting the evolution of the disperse phase and setting all liquid source terms in the PDEs to zero. Since the two different approaches to represent the turbulence-chemistry interaction strongly affect the solution procedure, this section is split based on the turbulence-chemistry interaction model applied. Both approaches are grounded on a low-Mach assumption adapted to the merged PISO[87]-SIMPLE[137] standard OpenFOAM pressure-velocity coupling [91].

4.2.1 Pressure-Velocity Coupling

In computational fluid dynamics, the coupling of the pressure and velocity deserves special attention. In this work, regardless of the TCI treatment, this problem is solved using the standard OpenFOAM procedure [91] adapted to low-Mach number flows [165, 163]. The idea is to decompose the pressure p into a thermodynamic p_{th} and a mechanical component p_{dyn}. By omitting any compressibility or acoustic effects ($\rho \neq \rho(p_{dyn})$) and keeping the thermodynamic part unchanged, a pressure-independent equation is obtained for the density ($\rho = \rho(p_{th}, T, Y) = \rho(T, Y)$) [7]. Since momentum transport is only affected through pressure gradients, p can be replaced by p_{dyn} in Equation 3.99. In the context of chemistry tabulation, this pressure-density-decoupling is especially beneficial, as the density is reduced to a function of Z and PV. A further benefit is the superior numerical stability of the low-Mach approach compared to a fully compressible method [163]. Nonetheless, the pressure-velocity coupling remains to be addressed. For this purpose, the discretized momentum equation is written as [91]

$$A_P \widetilde{\mathbf{u}}_P^{n+1} = H_u - \frac{\partial \overline{p}_{dyn}^{n+1}}{\partial x_i}\bigg|_P \qquad \text{with} \qquad H_u = -\sum_N A_N \widetilde{\mathbf{u}}_{Ni}^{n+1} + \overline{S}_{l,u} + S_u. \tag{4.25}$$

Here, A_P denote the coefficient of $\widetilde{\mathbf{u}}_P$ resulting from the discretization procedure, whereas H_u represents all contributions from the neighbour cells as well as the liquid phase momentum source term $\overline{S}_{l,u}$ and all remaining terms in the momentum equation S_u. The

pressure is obtained through a Poisson-type equation by substituting the mass conservation equation into the momentum equation

$$\frac{\partial}{\partial x_i}\Big(\frac{\overline{\rho}^{n+1}}{A_P}\frac{\partial \overline{p}_{dyn}^{n+1}}{\partial x_i}\Big) = \frac{\partial \overline{\rho}^{n+1}}{\partial t} + \frac{\partial}{\partial x_i}\Big(\frac{\overline{\rho}^{n+1}}{A_P}H_u\Big) - \overline{S}_{l,m}. \tag{4.26}$$

Spatial discretization of the divergence terms yields

$$\sum_f \left(\frac{\overline{\rho}^{n+1}}{A_P}\Big|_f \frac{\partial \overline{p}_{dyn}^{n+1}}{\partial x_i}\Big|_f\right)\mathbf{S}_f = \frac{\partial \overline{\rho}^{n+1}}{\partial t} + \sum_f \left(\frac{\overline{\rho}^{n+1}}{A_P}\Big|_f H_u\right)\mathbf{S}_f - \overline{S}_{l,m}. \tag{4.27}$$

This equation is solved to obtain the pressure. Once the pressure is known, the velocity can be updated by reformulating Equation 4.25 to

$$\widetilde{\mathbf{u}}_P^{n+1} = \frac{H_u}{A_P} - \frac{1}{A_P}\frac{\partial \overline{p}_{dyn}^{n+1}}{\partial x_i}\Big|_P. \tag{4.28}$$

As previously mentioned, the merged PISO-SIMPLE is adopted to solve pressure and velocity, which is described next in the context of the TCI approaches applied.

4.2.2 Artificial Flame Thickening

In the case of the ATF approach, Equations 3.98, 3.99, 3.100, and 3.101 form the PDE system that has to be solved alongside the dispersed Lagrangian phase. A flowchart of the solution algorithm is presented in Figure 4.2 and can be summarized as follows:

(1) Each time-step begins by evolving the disperse Lagrangian phase. All droplet properties, i.e. position, velocity, mass and temperature, are updated and the source terms $\overline{S}_{l,m}$ $\overline{S}_{l,u}$ $\overline{S}_{l,Z}$ computed.

(2) The evolution of the Lagrangian phase is followed by a density predictor, which consists in solving the mass transport equation to obtain an initial guess of the density at the new time level.

(3) Subsequently, the momentum equation is solved using the latest approximates of pressure and density, which can either originate from the density predictor and last time level, or from the previous iteration. Consequently, an approximate velocity at the new time level is obtained.

(4) The next step is the solution of the table access variables equations, that is mixture fraction and progress variable, which are then used to update all thermodynamic properties of interest, as the density, viscosity, progress variable source term, composition or temperature.

(5) Then, the pressure equation (Equation 4.27) is solved and the velocity updated.

(6) Finally, the turbulent viscosity, the thickening factor, and the efficiency function are updated.

The procedure is iterative, which means that the solution steps are repeated until a suitable convergence criterion is satisfied. Thereby, the solution at the new time level is obtained through a combination of SIMPLE- and PISO-loops. As well summarized in [163], the SIMPLE-loop takes the non-linearity of the momentum equation into account, while the

PISO-loop includes any changes of the thermochemical state and its impact onto the pressure.

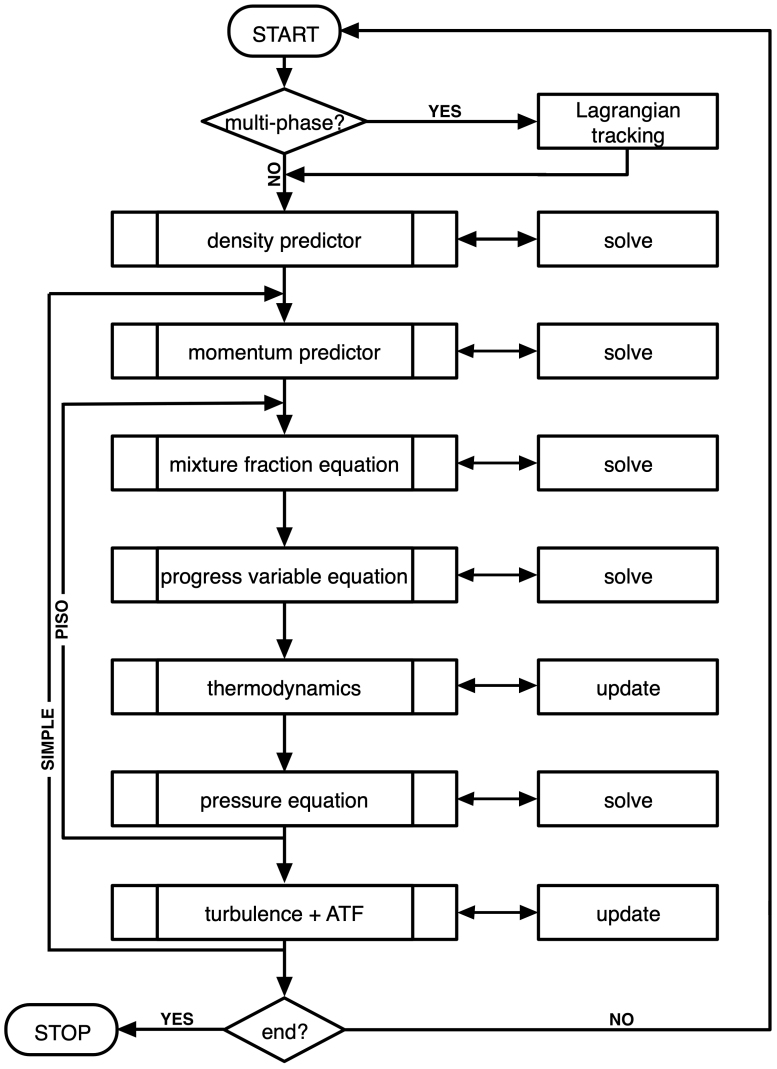

Figure 4.2: Flowchart of the merged PISO-SIMPLE algorithm in the context of tabulated chemistry and ATF.

4.2.3 Eulerian Stochastic Fields

Before introducing the solution algorithm in the context of the ESF approach, a description of the stochastic term treatment as well the introduction of auxiliary moment to improve the numerical stability of the method are briefly explained.

4.2.3.1 Stochastic Term Treatment

As outlined in Section 3.1.3, the stochastic increments found in the stochastic field (SF) equations should be normally distributed with a mean value of zero and a variance equal to the time step size Δt. However, for a low number of stochastic fields, sampling the components of the vector $\boldsymbol{\eta}^n$ of a normal distribution will rarely match these constraints.

Therefore, a weak first-order approximation is applied where the increments are sampled from a dichotomic distribution $\{-1, 1\}$ [103]. The correct mean and variance are ensured by introducing a complementary increment $\eta_i^{j+N_s/2} = -\eta_i^j$ for the second half of the stochastic increments before randomly shuffling the set to avoid any correlation between η_i^j and $\eta_i^{j+N_s/2}$ [143]. Therefore, an even number of stochastic fields is used.

4.2.3.2 Auxiliary Moments

Currently, the solution procedure for coupled partial differential equation systems involving stochastic components is still a big challenge. The main problem is related to the tight coupling of the solved equations, more precisely to the density derivatives found in the equation for the pressure, which directly impacts the momentum transport. The stochastic fluctuations of the density and its derivative make the solution procedure prone to numerical instabilities [125], especially for a low number of stochastic fields. Therefore, stabilization procedures have been developed and successfully applied to bypass this issue. In the context of particle-based methods, this is usually treated through an additional Eulerian enthalpy equation, for which the source term is obtained from the stochastic particles [158, 157, 89], which is in turn used to obtain the density.

In the context of ESF, similar approaches are used and so-called auxiliary moments are introduced, which are less susceptible to stochastic fluctuations [156, 5, 116, 143]. In this work, the procedure proposed by Prasad [156] is adopted, which has been modified to fit the tabulated chemistry framework employed. Additional auxiliary moments are solved, for which the source terms are obtained from the transported FDF. This yields the following transport equation for the Favre filtered auxiliary first moment of the mixture fraction $\widetilde{Z}^*$ and progress variable $\widetilde{PV}^*$:

$$\frac{\partial \bar{\rho}\widetilde{Z}^*}{\partial t} + \frac{\partial}{\partial x_j}\left(\bar{\rho}\widetilde{Z}^*\tilde{u}_j\right) = \frac{\partial}{\partial x_j}\left[\left(\frac{\bar{\mu}}{Sc} + \frac{\mu_{sgs}}{Sc_{sgs}}\right)\frac{\partial \widetilde{Z}^*}{\partial x_j}\right] + \bar{S}_{Z,l}, \tag{4.29}$$

$$\frac{\partial \bar{\rho}\widetilde{PV}^*}{\partial t} + \frac{\partial}{\partial x_j}\left(\bar{\rho}\widetilde{PV}^*\tilde{u}_j\right) = \frac{\partial}{\partial x_j}\left[\left(\frac{\bar{\mu}}{Sc} + \frac{\mu_{sgs}}{Sc_{sgs}}\right)\frac{\partial \widetilde{PV}^*}{\partial x_j}\right] + \frac{1}{N_s}\sum_{n=1}^{N_s}\bar{\rho}\dot{\omega}_{PV}^n. \tag{4.30}$$

The chemical source term in the progress variable equation is obtained by averaging the source terms of the individual stochastic fields, and is therefore in its closed form. These auxiliary control variables are then employed to obtain the filtered density $\bar{\rho}^*$ and viscosity $\bar{\mu}^*$, which are used consistently in all equations solved.

4.2.3.3 Solution Algorithm

Similarly to the solution procedure adopted in the context of ATF, the ESF solution algorithm is implemented using the merged PISO-SIMPLE pressure-velocity coupling strategy. The solution flowchart illustrated in Figure 4.3 is, as for the ATF approach, summarized subsequently in key-points:

(1) The solution of the carrier phase is preceded by solving the Lagrangian phase and computing the liquid source terms for the carrier phase equations. This implies an explicit treatment for all source terms in the mass, momentum, and all scalar transport equations.

(2) Thereafter, the Wiener vector increments are initialized as described in Section 4.2.3.1. These increment are left unchanged throughout the time step and are later used in the computation of the stochastic terms.

(3) Next, the density predictor is performed in order to obtain an initial guess of the density at the new time level.

(4) The density predictor is followed by the momentum predictor, which updates the velocity and additionally initializes the fields H_u and A_p required for the solution of the pressure equation.

(5) Next, the stochastic fields are solved, which also updates the source term of the individual progress variable stochastic fields (one table lookup for each field). In addition, the first moments of the mixture fraction and progress variable FDF are updated. It is important to notice that at this stage, only the drift term, that is the deterministic part, of the stochastic fields is computed. From this solution of the stochastic fields, one also obtains the closed-form source terms needed to calculate the evolution of the auxiliary moments.

(6) The closed progress variable source term is used in the auxiliary moment equations, which are in turn used to update the density $\bar{\rho}^*$ and viscosity $\bar{\mu}^*$ (see previous section).

(7) The next step is to solve the pressure equation and to update the velocity field.

(8) Thereafter, the turbulent quantities are updated

(9) Finally, the stochastic terms are added to the mixture fraction and progress variable fields. This also involves an update of the first and second moments of the FDFs.

The procedure to first solve the stochastic fields without any stochastic contribution and, once all fields have reached convergence, to add the stochastic terms is similar to the strategy proposed by Garmory [64]. As can be noticed by comparing this flowchart with the one shown in Figure 4.2, no scalar equations are solved within the PISO-loop for this approach. The reason is that the present implementation showed a good convergence behavior at moderate computational costs. This point becomes highly relevant as the number of stochastic fields increases.

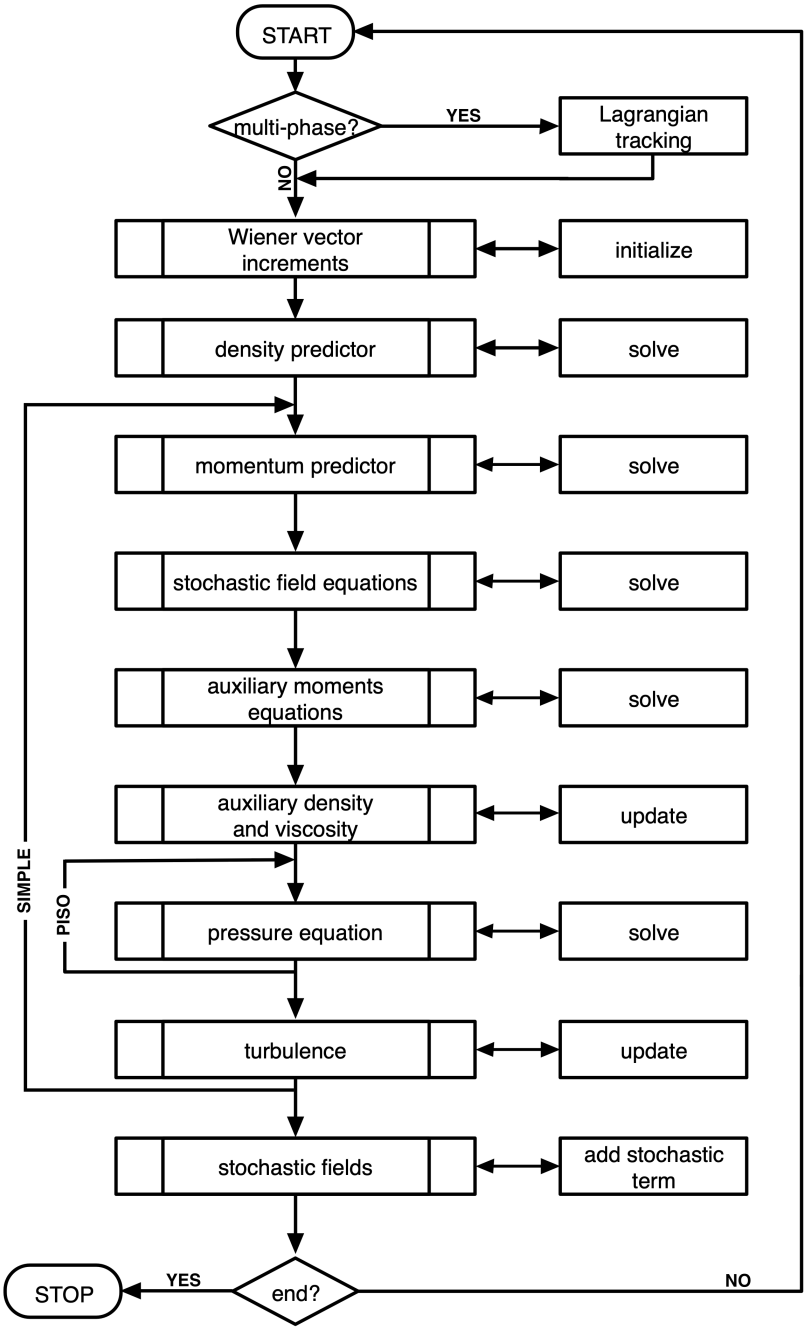

Figure 4.3: Flowchart of the merged PISO-SIMPLE algorithm in the context of tabulated chemistry coupled to the ESF method.

Chapter 5

Verification and Validation

In this chapter, a selection of simple test-cases to verify and validate the implementation is presented. These tests aim at identifying and removing potential implementation and modeling flaws before applying the framework to complex flow problems. The goal is to exercise the different parts of the code, as the artificial thickening of the flame, the stochastic field implementation, or the evaporation modeling of liquid droplets. The first part is dealing with the gas phase, whereas the second section is focused on the dispersed liquid phase.

5.1 Carrier Phase

The majority of this section is addressing the topic of verification on the carrier phase side. The procedure is based on the method of manufactured solutions (MMS), code-to-code comparison, and comparison with other approaches.

5.1.1 Method of Manufactured Solution

Before investigating the performance of any implemented model, the first question that should be raised in the context of computational fluid dynamics is whether the set of coupled partial differential equations is solved correctly. This question is of utmost importance and must be answered before starting with any model validation, independent of the complexity of the investigated case. It has been outlined in the previous chapter that the discretization of the PDE system in space and time yields an approximation of the exact solution. The difference between the two is denoted as numerical or discretization error [177]. In this work, the method of manufactured solution [131] is applied to demonstrate that the order of accuracy (OoA) resulting from the numerical schemes matches their theoretical OoA. At the same time, the MMS should prove that the adopted discretization methods are consistent. This means that as the spatial and temporal discretization become smaller, the discretization error should converge to zero. The MMS method can be perceived as opposite to the method of exact solution (MES), where an exact solution to a set of coupled set of PDEs is derived. The exact solution can then be compared to the numerical approximation obtained from the code. However, the derivation of an exact solution in the context of the Navier-Stokes equations often implies strong simplifications, which are not justifiable in view of the complex LES performed in this work. This problem is bypassed when using MMS. The idea is not to derive an exact solution to the coupled system of PDEs, but to simply define the solution a-priori—the manufactured solution

(MS). To grasp the concept, the following simple differential equation is introduced

$$\mathcal{D}(\phi) = S, \tag{5.1}$$

where a differential operator $\mathcal{D}$ is applied on a generic field ϕ. On the right-hand-side the source term S is introduced. In the PDE system considered in this work, $\mathcal{D}$ represents a series of differential operators, including temporal and spatial derivatives.

In MMS, the solution of ϕ is first manufactured. In a next step, the differential operator is applied to ϕ, which yields the source term S. This means that by reversely applying the source term S to the equation, ϕ is obtained. This is performed at the discrete level. The discretized solution can then be compared to the manufactured solution. In this work the MS proposed by Shunn et al. [185] is applied. The case mimics a one-dimensional binary diffusive mixing process with a large density ratio. The system of equations to be solved consists in the continuity, momentum, and a scalar (ϕ) transport equation. The manufactured solution reads

$$\begin{aligned}
u(x,t) &= 2k_2 \exp(-k_1 t)\frac{\rho_0 - \rho_1}{\rho(x,t)}\left[\frac{\hat{u}x}{\hat{u}^2+1}\frac{\left(\frac{k_1}{k_2}-1\right)\left(\arctan(\hat{u})-\frac{\pi}{2}\right)}{w_0\exp(-k_2 t)}\right], \\
\phi(x,t) &= \frac{\exp(-k_1 t) - \cosh(w_0 x \exp(-k_2 t))}{\exp(-k_1 t)\left(1-\frac{\rho_0}{\rho_1}\right) - \cosh(w_0 x \exp(-k_2 t))}, \\
\rho(x,t) &= \left[\frac{\phi(x,t)}{\rho_1} + \frac{1-\phi(x,t)}{\rho_0}\right]^{-1},
\end{aligned} \tag{5.2}$$

where $\hat{u} = \exp(w_0 x \exp(-k_2 t))$. The other parameters $w_0 = 50$, $k_1 = 4$, $k_2 = 2$, $\rho_0 = 10$ and $\rho_1 = 1$ are constant throughout the simulation. The spatial and temporal evolution of the solution is illustrated in Figure 5.1.

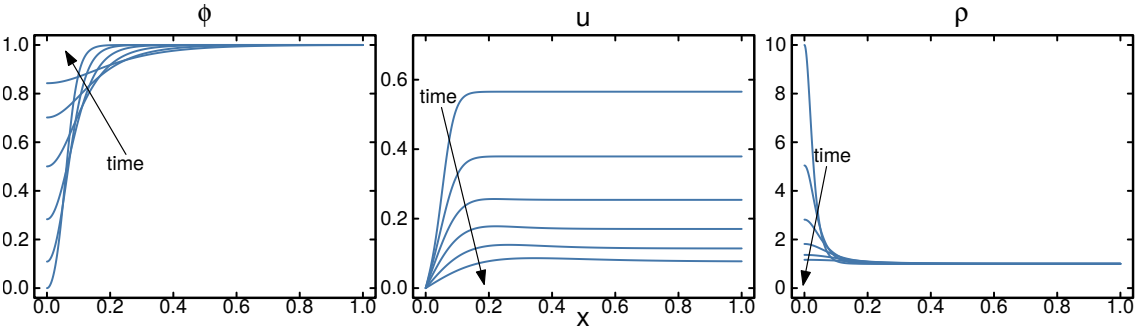

Figure 5.1: Spatial and temporal evolution of the manufactured solution proposed by Shunn et al. [185] for the three quantities ϕ, u and ρ (see Equation 5.2).

In order to investigate the consistency and determine the OoA of the spatial discretization, the numerical approximation is computed on equidistant meshes with varying cell number of 16, 32, 64, 128, 256, 512 and 1024, while the time step Δt is kept constant to prevent any variation of the temporal discretization error. Similarly, to determine the temporal OoA, the time step size is changed from 50 ms to 3.125 ms, while keeping the spatial resolution constant. The error metrics applied to define the discretization error are: (1) the L_2-norm, which represents the square-root of the average of the squared difference between discretized ($(\cdot)^{num}$) and exact ($(\cdot)^{ref}$) solution; (2) the L_∞-norm, which is defined as the maximum of the absolute difference between discretized and exact solution. Both

metrics are expressed as

$$L_2 = \sqrt{\frac{\sum_i^{N_{CV}} (\phi_i^{num} - \phi_i^{ref})^2}{N_{CV}}} \qquad \text{and} \qquad L_\infty = \max\left(|\phi_i^{num} - \phi_i^{ref}|\right). \tag{5.3}$$

Here, N_{CV} is the number of control volumes in the computational domain.

The evolution of the spatial and temporal discretization error for the scalar ϕ is shown on a logarithmic scale in Figure 5.2. The added dot-dashed line represents the theoretical second-order decrease of the discretization error prescribed by the numerical schemes. Starting with the spatial discretization error shown on the left of Figure 5.2, it becomes clear that the expected second-order decrease is well reproduced by the code. The similar profiles for L_2 and L_∞ also indicate the absence of numerical artifacts in the solution domain. A similar behavior is observed on the right of Figure 5.2 for the temporal discretization error. For these computations, the second-order Crank-Nicholson time-stepping scheme is used. As for the spatial discretization the quadratic decrease of both error-norms confirm the second-order of the implementation. Similar results are obtained for the discretization error of the velocity u.

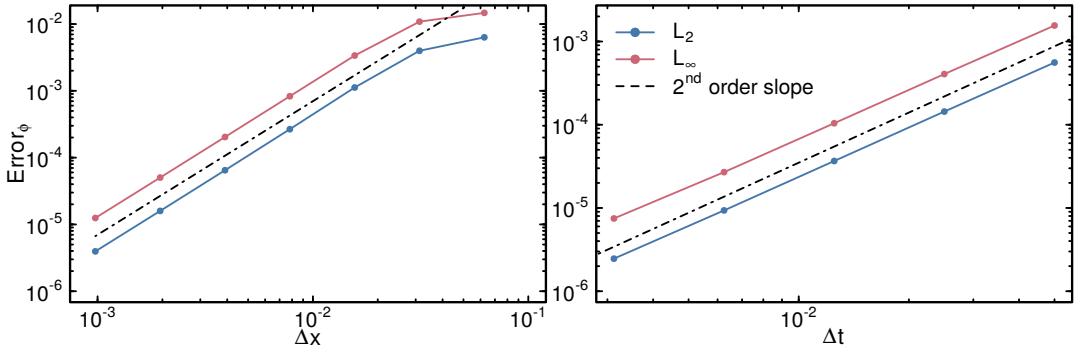

Figure 5.2: Spatial (left) and temporal (right) discretization error for the scalar ϕ along the spatial or temporal resolution. The error is shown by means of the L_2- and L_∞-norms.

The results shown above confirm that the discretization procedure functions as expected and is free of any programming errors. This builds the foundation stone for all subsequent verifications and applications. More general information on the topic of verification and MMS can be found in [177, 132], whereas specifics regarding the verification of OpenFOAM are described in [163].

5.1.2 Coupling of Tabulated Chemistry and OpenFOAM

In order to apply the chemistry tabulation strategy in a complex, turbulent spray flame, it must be shown that the coupling of CFD solver and chemistry-lookup-table is working properly. This is shown in this section by means of a code-to-code comparison, first for a one-dimensional lookup-table (keeping the mixture fraction constant), and later for a two-dimensional table. The reference solution is obtained from the detailed chemistry simulations used to construct the lookup-table, which are performed using the code CHEM1D [190].

First, a premixed flame propagating into an unburnt stoichiometric hydrogen-air mixture in a one-dimensional domain is considered ($Z = 2.79 \cdot 10^{-2}$). This yields a laminar flame thickness $\delta_l \approx 184\,\mu\text{m}$ (based on the progress variable) and a flame speed

$s_l = 1.52\,\mathrm{m\,s^{-1}}$ (see Equations 2.44 and 2.45). Since for this test-case, the one-dimensional lookup-table is directly constructed from a flamelet, the profiles obtained from the simulation can directly be compared to the flamelet solution. The flamelet itself is generated assuming a unity Lewis number. Note that the neglect of differential diffusion effects in a premixed hydrogen flame may severely alter the flame speed. However, the correct prediction of the laminar flame speed under consideration of all underlying physics is not the goal here. The aim of this section is to show that the fully coupled set of PDEs is able to reproduce the physics incorporated in the flamelet(s) used for the construction of the lookup-table.

The one-dimensional computational domain has a length of 0.064 m. The flame is initialized by imposing the following initial conditions onto the progress variable field, which is defined as the H_2O mass fraction:

$$\begin{cases} x < 0.01 & PV = \min(PV) = 0, \\ x \geq 0.01 & PV = \max(PV) = 0.2369. \end{cases} \tag{5.4}$$

The inflow velocity is set to $1.54\,\mathrm{m\,s^{-1}}$, which is slightly higher than the laminar flame speed in order to ensure that the flame does not travel towards the inlet. To investigate the effect of the spatial resolution, the computational domain is subdivided into meshes ranging from 400 (coarsest mesh) to 25600 (finest mesh) cells, which respectively correspond to a resolution $\Delta x = 160\,\mu\mathrm{m}$ and $\Delta x = 2.5\,\mu\mathrm{m}$. All simulations are run 10 ms after initialization in order to allow the laminar flame structure to develop. Thereafter, the solution is computed for 40 ms in order to obtain fully converged averages of the flame thickness and speed. The results are shown in Figure 5.3. On the left side, the profiles of the progress variable and progress variable source term obtained from the simulations are compared with the flamelet solution. It can clearly be seen that at the lowest resolution of 160 µm, the simulation can barely reproduce the reference profiles. However, as Δx decreases, the solution converges towards the detailed chemistry solution. This is confirmed by comparing the averages of flame speed and flame thickness obtained from the simulation with the flamelet solution shown on the RHS of Figure 5.3. The ratio $s_l/s_{l,ref}$ and $\delta_l/s_{l,ref}$ are plotted as function of the spatial resolution. The grey area represents the region where the difference between the OpenFOAM simulations and detailed chemistry is less than 10%. It can be observed that for high values of Δx, the simulation is neither able to reproduce the laminar flame speed nor the flame thickness. Nonetheless, as for the profiles shown on the right side, both, flame speed and flame thickness, converge towards the reference solution. This verifies the retrieval procedure implemented in this work—at least in the case of a one-dimensional table.

The second part demonstrates that the retrieval of the thermochemical state is also working for a two-dimensional thermochemical lookup-table, which spans a mixture fraction-progress variable space. The test-case consists in performing a series of one-dimensional simulations at varying mixture fraction. Since the two-dimensional table is constructed from one-dimensional flamelets at fixed mixture fraction values, performing a simulation with a mixture fraction unequal any of these reference flamelets should reveal if the two-dimensional lookup is working as expected. For this purpose, a series of one-dimensional premixed ethanol flames is computed at varying mixture fractions $Z = \{0.055, 0.057, \ldots, 0.183, 0.185\}$. All these mixture fractions are located within the flammability range of ethanol ($0.052 \leq Z \leq 0.27$) [170]. The length of the computational L_{domain} is equal to the one used for the one-dimensional premixed hydrogen flame. For

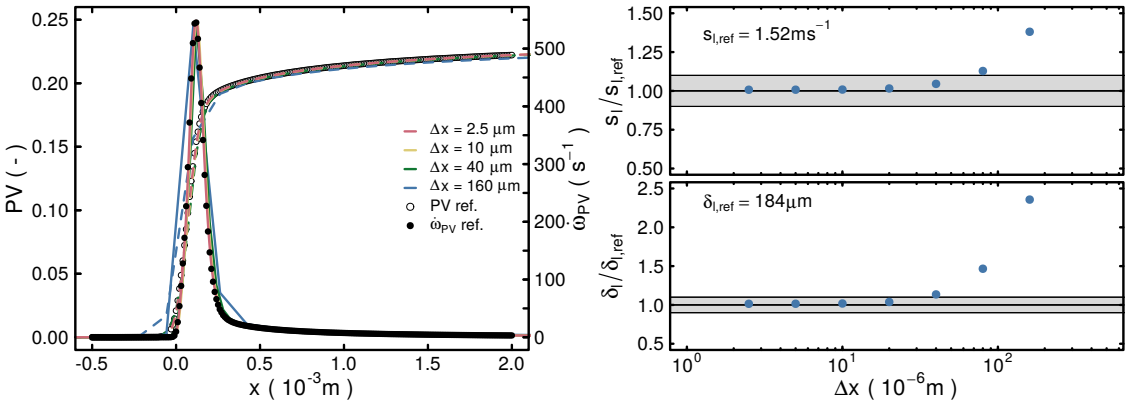

Figure 5.3: Spatial profiles of the progress variable (dashed lines) and progress variable source term (solid lines) at various resolutions alongside CHEM1D reference data (left) and evolution of laminar flame speed and flame thickness as function of the grid spacing Δx (right).

each computation, the progress variable is initialized as follows:

$$\begin{cases} x < \frac{L_{domain}}{2} & PV = \min(PV)(Z) \\ x \geq \frac{L_{domain}}{2} & PV = \max(PV)(Z) \end{cases}. \tag{5.5}$$

For all cases, the inflow velocity of the unburnt mixture is set to $0.2\,\mathrm{m\,s^{-1}}$. Additionally, the simulations are performed at two different spatial resolutions. In this regard, a coarse and a fine resolution are defined for each computation

$$\Delta x_{coarse} = \frac{\delta_{l,ref}}{4} \qquad \text{and} \qquad \Delta x_{fine} = \frac{\delta_{l,ref}}{15}. \tag{5.6}$$

The results are presented in terms of laminar flame speed and flame thickness in Figure 5.4. As for the one dimensional test-case, the grey area represents the region where the difference between the OpenFOAM simulations and the detailed chemistry is less than 10%. Considering the flame thickness shown on the right side of Figure 5.4, it can be observed that the OpenFOAM profiles match the reference detailed chemistry data well. In particular, the trends between the reference flamelets (black points) are as expected. It can also be observed that at the coarse resolution, the simulation is not able to resolve the original gradients, yielding higher flame thicknesses. The deviations between coarse and fine resolution are significantly lower in the case of the flame speed. The results suggest that in order to reproduce the laminar flame-dynamics, the flame should be resolved with at least 4 cells. This information is important, as it determines to which extent the grid- and mixture-adaptive thickening are performed in the context of ATF. Accordingly, the minimum number of cells to resolve the flame n_{CV} in Equations 3.48 and 3.49 is set to 4.

5.1.3 Flame Sensor Formulation

This investigation is performed to evaluate the implementation of the proposed flame sensor (see Equation 3.45) and to compare it with other formulations. Analogously to the verification of the coupling of OpenFOAM with tabulated chemistry, a one-dimensional stoichiometric premixed ethanol-air flame ($Z = 0.1$) is computed. Three different formulations for Ω are compared. These are summarized in Table 5.1.

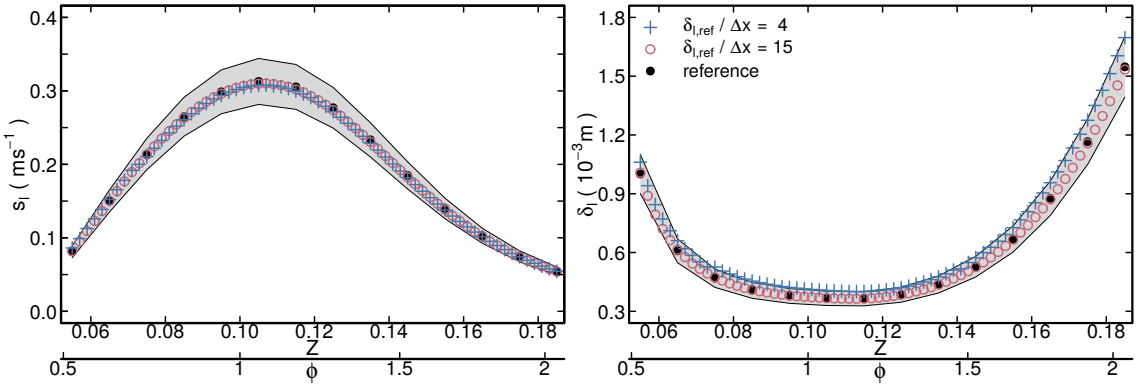

Figure 5.4: Results for the Flame speed (left) and flame thickness (right) obtained using OpenFOAM coupled to tabulated-chemistry approach at the two spatial resolutions Δx_{coarse} and Δx_{fine} alongside reference data from the detailed chemistry code CHEM1D.

Approach	Flame Sensor formulation	Reference
Hosseinzadeh	$\Omega = \max\left(0, \frac{\tanh\left(100\frac{\dot{\omega}_{PV}}{\max(\dot{\omega}_{PV})}\right)-0.25}{0.75}\right)$	[81, 170]
Durand	Equation 3.46	[46]
Present	Equation 3.47	[42, 44]

Table 5.1: Comparison of the applied flame sensor formulations.

The expressions are set aside in normalized progress variable space and in physical space in Figure 5.5. Large differences between the different approaches become apparent by considering the profiles of the flame sensor in normalized progress variable space shown on the left of Figure 5.5. The formulation by Durand [46] is symmetric by definition and therefore reaches its peak at $c = 0.5$. Differently, the one by Hosseinzadeh [81] and the one used in this work are able to adapt to the shape, i.e. to the location, of the progress variable source term. The two latter approaches also feature higher values of Ω across a broader progress variable range than the formulation by Durand. The main difference between the proposed expression and the one by Hosseinzadeh is the later onset of the flame-thickening for the former approach. Reason for this is the narrower region of high Ω-values. As previously outlined in Chapter 3, the flame sensor should evaluate to zero outside of the flame in order to prevent any artificially increased diffusion within the scalar equations outside of the flame. The present analysis suggests that the proposed formulation satisfies this criterion. However, solely considering the formulation in progress variable space is not enough. In order fully evaluate the performance of the flame sensor, it should also be considered how it behaves in physical space. This is shown on the right side of Figure 5.5. A constant thickening factor $F = 4$ is coupled to the dynamic formulation. The flame front is visualized by means of the progress variable. The profiles of the flame sensor confirm that the approaches by Durand and Hosseinzadeh are unnecessarily thickening the flame in regions behind the reaction zone. This yields an erroneous diffusion process in that region. Moreover, the usage of these expressions will—in the presence of a dispersed liquid phase—needlessly stretch the correction of heat and mass transfer for droplets crossing the thickened flame. These negative effects are notably reduced when using Equation 3.47 to compute the flame sensor.

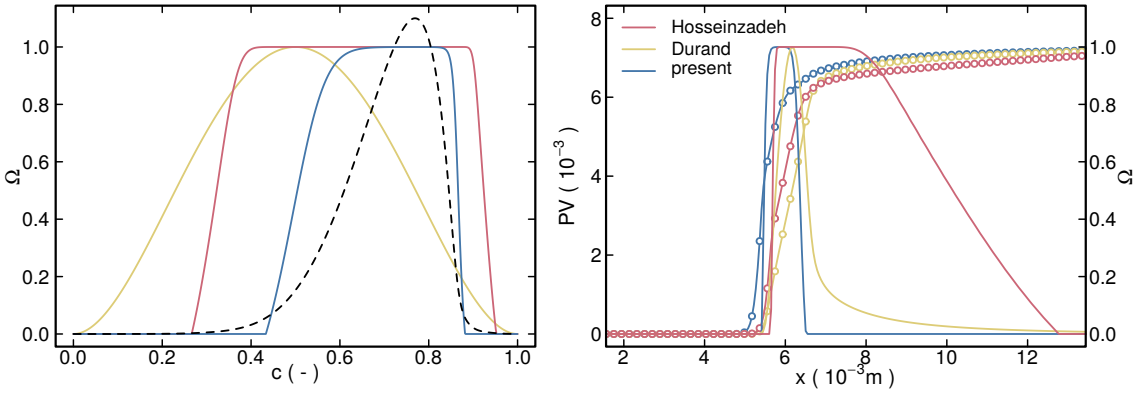

Figure 5.5: Comparison of the different flame sensor formulations shown in Table 5.1 for a stoichiometric premixed ethanol-air flame in normalized progress variable space (left) and physical space (right). The flame sensors are characterized by solid lines. The dashed line in the left plot represents the progress variable source term. The lines with points on the RHS are the progress variable profiles resulting from the different formulations.

The impact of the different definitions on the laminar flame speed is presented in Figure 5.6. The first observation is that all results using a thickening procedure converge towards the reference laminar flame speed faster than the non-thickened counterpart. This is expected, as the thickened flame can be resolved at coarser resolutions. Apparently, the convergence is reached at an approximately four times coarser resolution than the non-thickened simulation, which agrees well with the constant thickening factor value $F = 4$ applied. However, it can be perceived that the definition by Hosseinzadeh [81] and the present one approach the reference flame speed earlier than the formulation by Durand. Considering that the source term resolution is the crucial factor in order to obtain the correct laminar flame speed, it is likely that the separation of progress variable source term and flame sensor maxima are causing this behavior. The present analysis not only demonstrates the good performance of the proposed expression, but also reveals its advantages compared to previous formulations.

5.1.4 Eulerian Stochastic Fields

To show the ability of the ESF method to solve the transport equation of the PDF of a reactive scalar, two test cases are considered. Both are extensively described in [152] and [194]. The test cases are performed in a one-dimensional computational domain of non-dimensional length $x = 1$ and consist in approximating the solution of the PDF-transport equation for a reactive scalar θ. The domain is decomposed into 100 equidistant control volumes. The cases mimic a plug-flow reactor with imperfect mixing where the source term is either defined as

$$\dot{\omega}_\theta = A_1(1-\theta) \tag{5.7}$$

for the first test case (linear relation between θ and $\dot{\omega}_\theta$), or

$$\dot{\omega}_\theta = A_2\theta(1-\theta)\exp\left(\frac{-B_2}{1+C_2\theta}\right), \tag{5.8}$$

with the case specific parameters $A_1 = 3$, $A_2 = 21830$, $B_2 = 20$ and $C_2 = 3$. The second formulation is an Arrhenius-type expression similar to Equation 2.40. The equation for

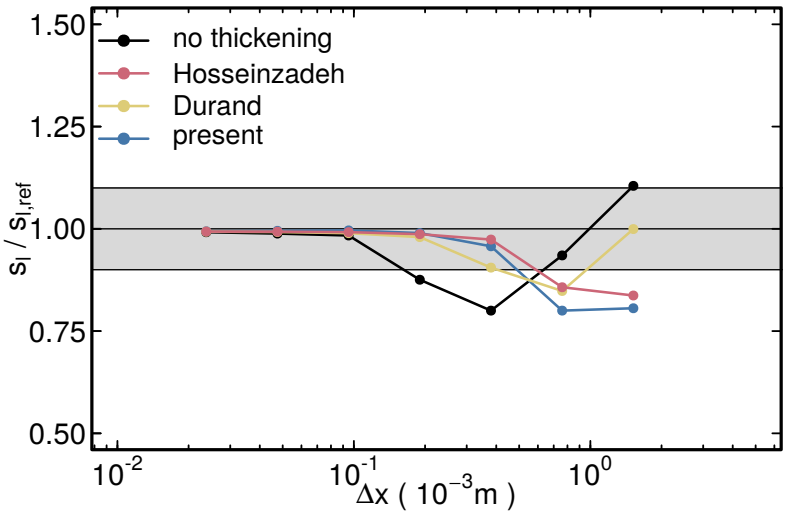

Figure 5.6: Evolution of the laminar flame speed as function of the spatial resolution for the different flame sensor formulations (see Table 5.1) in a stoichiometric premixed ethanol-air flame with a constant thickening factor of 4.

the stochastic fields reads [194]

$$\mathrm{d}(\xi_\theta^n) = -\frac{\partial}{\partial x_j}(\xi_\theta^n u_j)\mathrm{d}t + \frac{\partial}{\partial x_i}\left(\Gamma'\frac{\partial \xi_\theta^n}{\partial x_i}\right)\mathrm{d}t \tag{5.9}$$

$$+\dot{\omega}_\theta^n \mathrm{d}t + \frac{1}{2}\omega_{MM}\left(\xi_\theta^n - \theta_{mean}\right)\mathrm{d}t + \sqrt{2\Gamma'}\frac{\partial \xi_\theta^n}{\partial x_j}\mathrm{d}W_j^n, \tag{5.10}$$

where a representative diffusivity $\Gamma' = 0.1$ is introduced. The micro-mixing frequency ω_{MM} is set to a constant value of 20. As outlined by Pope [152], the constants are chosen such that the processes of convection, diffusion, reaction and mixing are evenly balanced. Both cases are computed with 40 as well as 400 stochastic fields. The results for the linear source term formulation are compared at statistical stationarity with the results of [152] in Figure 5.7. The comparison metrics are the expectation θ_{mean} and standard deviation θ_{rms} of the PDF. Note that for this case, only one simulation has been performed while the results presented in [152] represent an average of 25 Lagrangian particle Monte Carlo simulations (with 800 particles per CV). Nonetheless, it can be observed that the present results for mean and standard deviation match the reference data well.

Next, the result using the Arrhenius-type formulation for the source term are discussed. In contrast to the first test case, three time instants $t = 0.5, 1, 1.5$ are considered before the steady state solution is reached. The results are compared with the particle based Monte Carlo method proposed by Pope [152] and with the results of Valiño [194], where the ESF method was initially proposed.

It can be observed that the results agree well with the ones obtained by Valiño using 800 SF. However, similarly to Valiño [194], some differences can be observed between the present results and the results of Pope [152]. As pointed out in [194], this difference is mainly caused by the jump condition at $x = 0$, combined with a strongly non-linear source term formulation. Nonetheless, the good agreement with the results presented in [194] attests the proper functioning of the implementation.

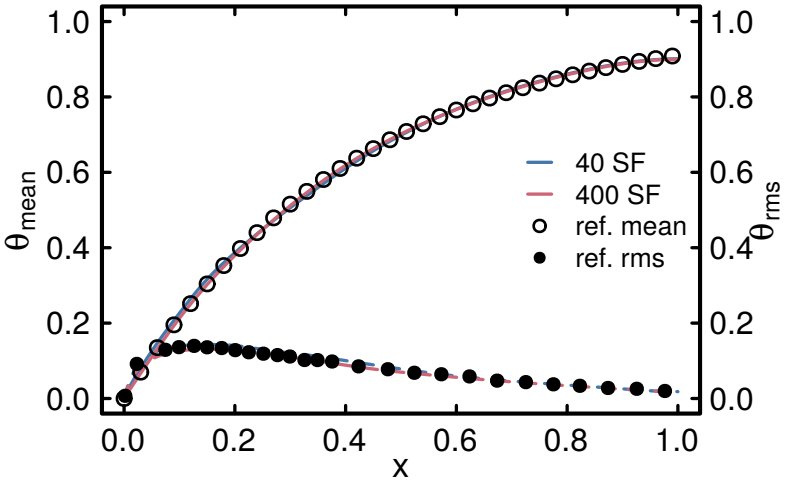

Figure 5.7: Profiles of the mean and standard deviation over the non-dimensional length x for the linear source term case (Equation 5.7) computed with 40 and 400 stochastic fields. Comparison with reference data taken from [152].

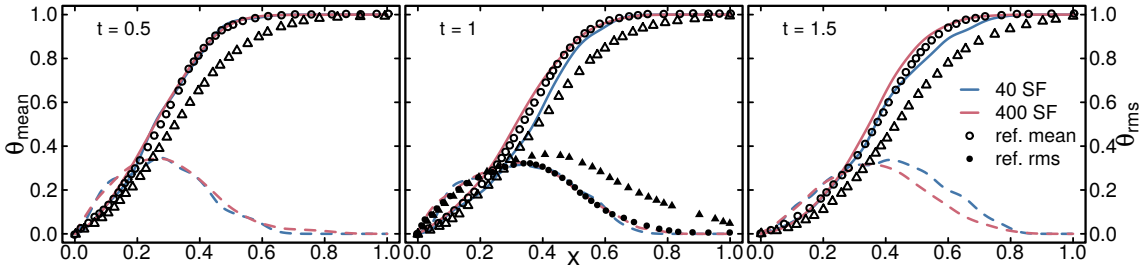

Figure 5.8: Profiles of the mean and standard deviation at the three time instants $t = 0.5, 1, 1.5$ (from left to right) for the Arrhenius type source term case (Equation 5.8) computed with 40 and 400 stochastic fields. The circles represent the ESF results obtained by Valiño [194]. Triangles correspond to the results of Pope [152] using a particle based Monte Carlo method. Note that reference data for the standard deviation are only available for time instant $t = 1$.

5.2 Dispersed Phase

In this section, the behavior of the Lagrangian phase is investigated through simple test-cases. Each of these shall reveal whether the Lagrangian parcels are evolving as expected. The first test case aims at showing that the kinematic coupling of the carrier and liquid phase is represented appropriately. Thereafter, extensive investigations of the performance of the evaporation models introduced in Chapter 3 are presented. Finally, the different approaches to represent the interaction of liquid droplets with a thickened flame discussed in Section 3.2.4 are evaluated in a simplified configuration.

5.2.1 Droplet Movement

Before investigating more complex phenomena as droplet heat and mass transfer, it is demonstrated that the liquid droplets are able to follow the carrier phase motion. The test is simple: a droplet at an initial position $\mathbf{x}_{d_0}$, with a diameter d_0, density ρ_d, drag coefficient C_D and initial velocity $\mathbf{u}_{d,0}$ positioned in a carrier with the properties ρ and ve-

locity $\mathbf{u}$ should follow a predefined trajectory, which is determined by Equations 3.67 and 3.68. Note that no gravitational force is acting on the particle. As performed in [72, 170, 100], the solution obtained from a suitable reference is used to validate the OpenFOAM implementation. The case parameters are summarized in Table 5.2. The x- and y-trajectories are shown in Figure 5.9 and set aside the reference solution, which has been computed using an Euler explicit time-stepping scheme. The evolution of the particle position is reproducing the expected trajectory, which indicates a flawless update of velocity and position within the particle-tracking-libraries of OpenFOAM.

Parameter	Value	Unit
C_D	1	(-)
ρ_d	1000	$\mathrm{kg\,m^{-3}}$
d_0	60	µm
$\mathbf{u}_{d,0}$	$(\,5,\ 0,\ 0\,)$	$\mathrm{m\,s^{-1}}$
$\mathbf{x}_{d,0}$	$(\,1,\ -9,\ 0\,)$	mm
ρ	1.167	$\mathrm{kg\,m^{-3}}$
$\mathbf{u}$	$(\,0,\ 8,\ 0\,)$	$\mathrm{m\,s^{-1}}$

Table 5.2: Summary of the parameters used for the droplet movement validation case.

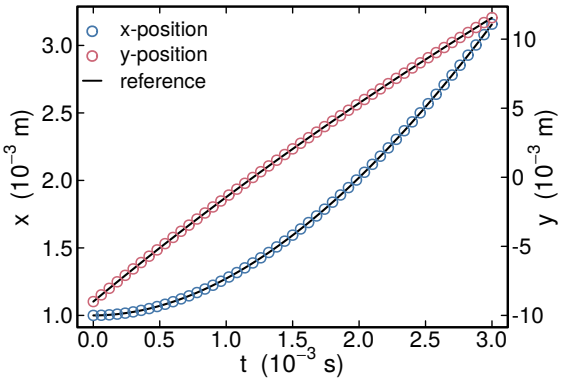

Figure 5.9: x- and y-trajectories of the droplet as computed in OpenFOAM alongside reference.

5.2.2 Droplet Evaporation

The aim of this section is not only to validate the present implementation of the evaporation models introduced in Section 3.2.2, but to compare them and to evaluate their applicability in view of the turbulent reacting ethanol spray flames that are presented in **part IV** of this work. The investigation is performed by means of four test cases, which aim at reproducing four different single droplet evaporation experiments. The operating conditions are summarized in Table 5.3. Note that all experiments were performed at atmospheric pressures.

Liquid	Carrier	d_0 (µm)	$T_d(t=0)$ (K)	T_∞ (K)	u_∞ ($\mathrm{m\,s^{-1}}$)	Reference
water	air	1049	282	298	0	[159]
hexane	air	1760	281	437	1	[40]
decane	hot gases	2000	315	1000	1	[206]
ethanol	nitrogen	430, 602, 609, 628, 651	300	673, 313, 473, 353, 298	0	[17, 18]

Table 5.3: Summary of the single droplet experiments investigated.

The first test case is based on the experimental measurements performed by Ranz and Marshall [159], who investigated the diameter evolution of a water droplet at ambient conditions. The results are shown by means of the droplet surface evolution in Figure 5.10a. The linear decrease of the droplet surface observed in the experiment is well re-

produced by both models. At these conditions, no difference between the formulation by Miller and the Abramzon-Sirignano model can be perceived. This is not unexpected, since the consideration of non-equilibrium effects, which is the main difference between both models, is supposed to be small at ambient conditions. Even though the droplet lifetime is slightly underestimated, both models are able to reproduce the experimental measurements reasonably well.

The second case is more representative of the conditions expected in a turbulent spray flame. The setup consists of a hexane droplet positioned in a heated air flow, which is moving with a constant velocity of $1\,\mathrm{m\,s^{-1}}$ [40]. In difference to the previous case, this allows to evaluate the effect of convective heat and mass transfer on the evaporation process. The simulation results are presented in Figure 5.10b in a similar manner as for the water-droplet-case. Here, it is observed that the model by Miller is better approximating the experimental data, whereas the Abramzon-Sirignano model considerably underestimates the droplet lifetime. The results are in agreement with the studies presented in [170] and [100].

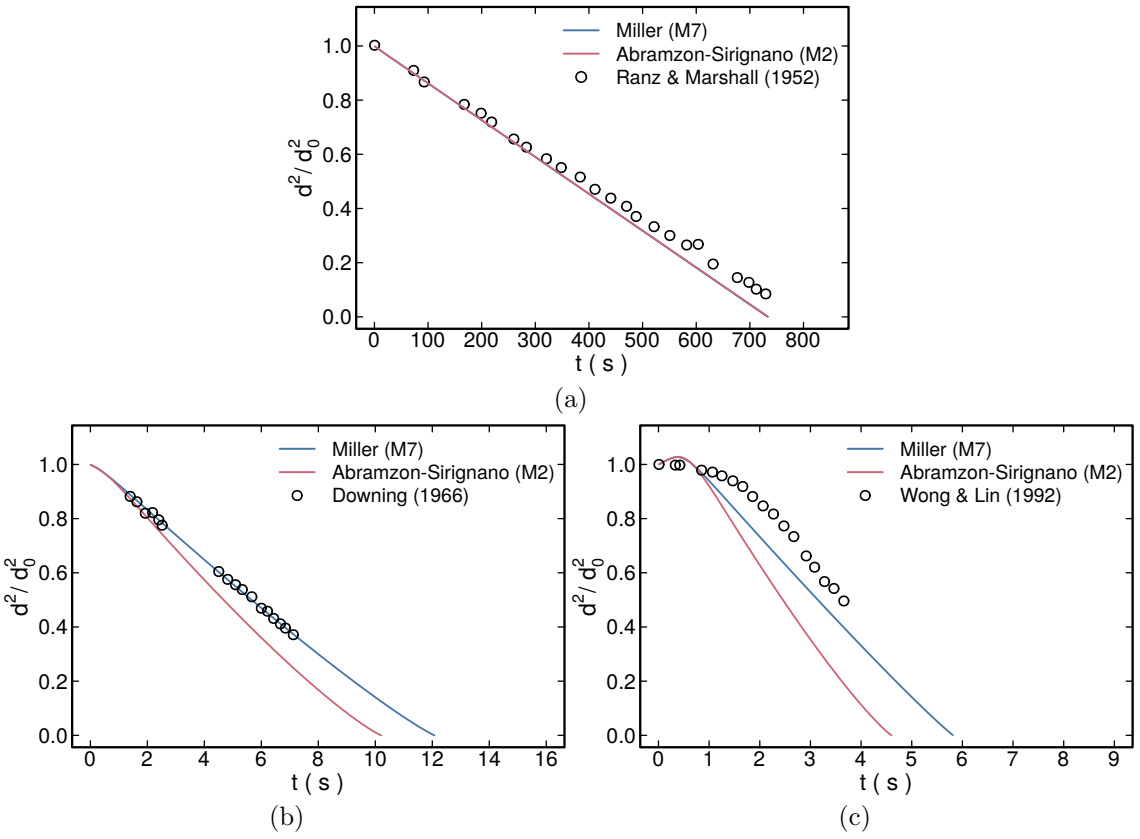

Figure 5.10: Temporal evolution of the computed droplet surface alongside the reference measurements for the respective experimental cases of (a) Ranz and Marshall [159], (b) Downing [40], and (c) Wong and Lin [206].

Differently from the first two cases, the experimental setup by Wong and Lin [206] is characterized by more extreme conditions: a decane droplet with an initial diameter of $2\,\mathrm{mm}$ is placed into a stream of hot gases with a temperature $T_\infty = 1000\,\mathrm{K}$. As for the case investigated by Downing, the gases surrounding the droplet are moving with a velocity $u_\infty = 1\,\mathrm{m\,s^{-1}}$. Since the exact composition of the surrounding gases is unknown, air is presumed in the simulations. The evolution of the droplet surface-area is shown in Figure

5.10c. In these conditions, both models seem to produce a faster diameter decrease than the experiment. This is more pronounced for the Abramzon-Sirignano model. Possible reasons for the deviations is the unknown composition of the surroundings and uncertainties in the carrier flow velocity. For instance, Sacomano Filho [170], and Kadavelil [100] obtained good agreements when using a reduced value for $u_\infty = 0.3\,\mathrm{m\,s^{-1}}$.

The last case is of special relevance as it features the same liquid as used later in the turbulent spray flame computations, i.e. ethanol. The measurement campaign was performed by Binti Saharin [18, 17], yielding a series of setups with varying initial droplet diameters and carrier temperatures (see Table 5.3). In order to prevent any chemical reaction, the evaporation measurements are performed in a pure nitrogen atmosphere. A comparison of simulated and experimentally measured data is presented in Figure 5.11. It can be observed that both models reproduce the trends correctly and matches the experimentally determined droplet surface evolution quite well. The discrepancies between simulations and experiments, which can be observed at lower diameters are caused by the presence of a second species in the liquid. This is discussed in detail in [18, 17].

In summary, it can be stated that both model are decently reproducing the experimentally measured droplet lifetimes. However, in cases where convective heat and mass transfer plays a role, the model proposed by Miller delivers better results. Therefore, this model is chosen for all further investigations which involve the evaporation of a liquid phase.

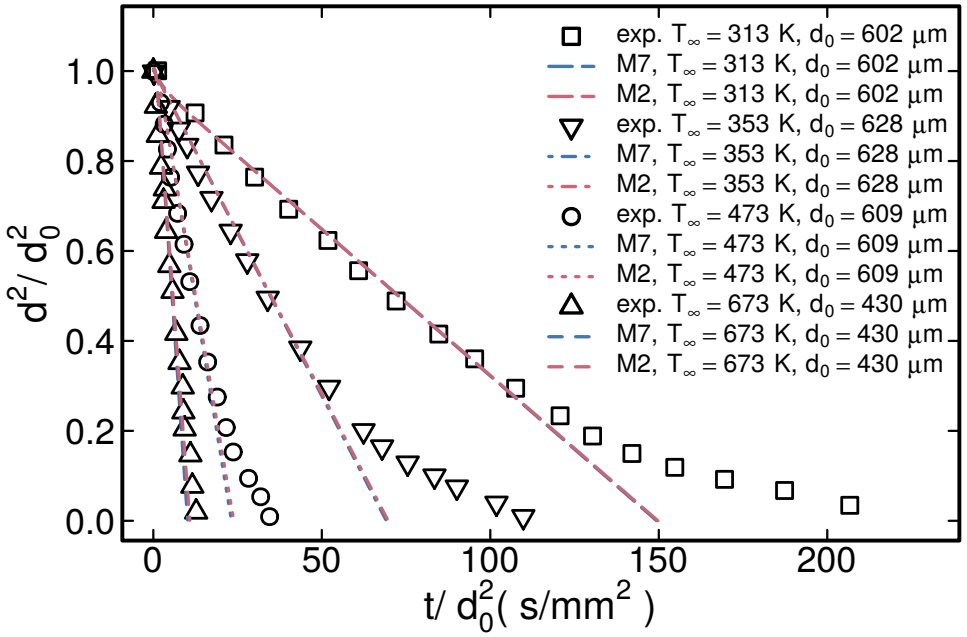

Figure 5.11: Temporal evolution of ethanol droplet surfaces alongside the reference measurements of Binti Saharin [17, 18].

5.2.3 Interaction of Droplets with a Thickened Flame

The goal of this section is to demonstrate and clarify the impact of the various approaches to consider heat and mass transfer for a droplet crossing a thickened flame. The test setup is simple and similar to the one-dimensional test configuration presented in [175] and [28]. The main difference is that the computational domain is extended to a second

spatial dimension to allow for two-dimensional droplet trajectories. The main objective is to evaluate the flame diameter after a flame crossing when compared to a reference case and—no less important—to assess the droplet diameter evolution in flame front parallel direction.

Modeling approach	Effective thickening factor calculation	color coding
no correction	$F_{eff}^{none} = 1$	–
standard correction	$F_{eff}^{std} = F$	–
refraction correction	$F_{eff}^{refr} = F$ (+ tracking modification)	–
projection correction	F_{eff}^{proj} = Equation 3.96	–

Table 5.4: Overview of the investigated modeling approaches to represent the interaction of droplets with a thickened flame.

The rectangular computational domain employed is sketched in Figure 5.12. It extends 0.02 m in x-direction and 0.01 m in y-direction and consists of 1000 x 500 control volumes, thus ensuring that the flame is well resolved in the reference case, i.e. where no artificial thickening is applied. The premixed ethanol-air flame ($Z = 0.1$), sketched as red line in Figure 5.12, is considered stationary, which is also different from the validation cases employed in [175, 28]. For all investigated cases, a droplet, represented as blue circle in Figure 5.12, travels through the domain with a constant velocity $|\mathbf{u}_d| = 0.3\,\mathrm{m\,s^{-1}}$. In this context, the angle θ describes the relation between flame orthogonal and flame parallel velocity component and can, in this case, also be used to quantify the angle of interaction between droplet and flame. As the droplet travels along its path, it crosses the flame, which, depending on the approach used (see Table 5.4), produces different heat and mass transfer rates along the droplet trajectory. To make all approaches more comparable and following [175], heat and mass transfer is only activated in regions where thickening is performed. This is achieved reasonably well by the flame sensor criterion $\Omega > 0.01$ (evaluated at the droplet position). The evaporation model by Miller is used to represent heat and mass transfer. The fuel considered is ethanol. Note that, similarly to [175], no coupling between carrier and liquid phase is performed. Besides, the impact of different flame thickening factors F, namely 1 (the reference scenario), 2, 5 and 10, is also investigated. Four different case setups are considered, each referring to a specific flame interaction angle θ. Beyond the two edge cases $\theta = 0°$ (droplet moves orthogonal to the flame front) and $\theta = 90°$ (droplet moves parallel to the flame front), the setups with the angles $\theta = 30°$ and $60°$ are studied. For the case where a droplet moves parallel to the flame front, the droplet is inserted directly into the flame.

The results for the first two cases are shown in Figure 5.13, which shows the diameter evolution of the droplet over its distance within the flame. These two edge cases can be reduced to one dimension, either flame orthogonal or flame parallel direction. First, considering the flame orthogonal case $\theta = 0°$, the diameter evolution along the trajectory is shown in Figure 5.13a. As previously stated, the heat and mass transfer is turned off outside of the flame, explaining the regions prior to (and succeeding) the flame, where the droplet diameter is assumed to remain constant. The reference solution, that is the unthickened flame case, is exhibited by the solid black line. Here, as expected, all correction approaches reproduce the reference solution for $F = 1$ (all solid lines are superimposed). However, it becomes obvious that the droplet evaporation is overpredicted when thickening is applied but the correction of droplet heat and mass transfer omitted (dashed and dotted

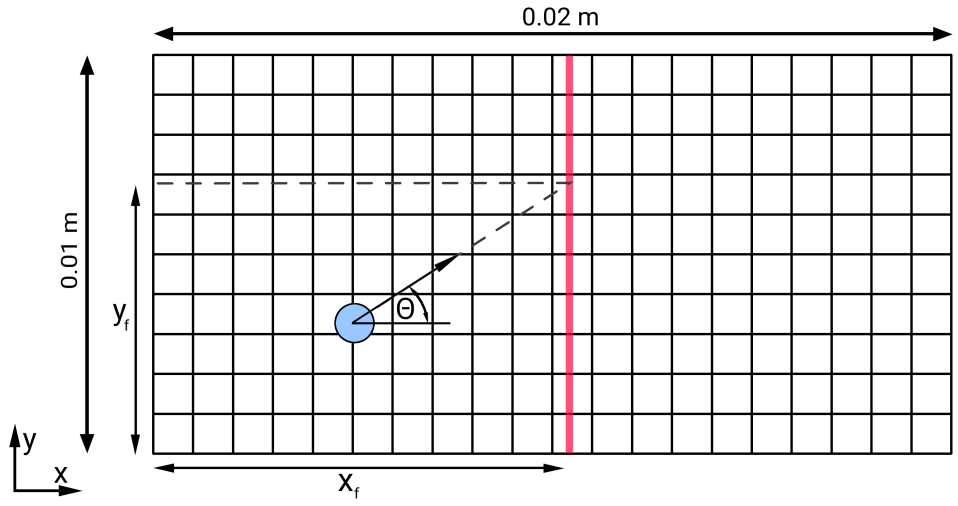

Figure 5.12: Sketch of the two-dimensional computational domain with particle (blue) and stationary flame (red).

black lines in Figure 5.13a). As a result, the approach without correction is not able to reproduce the correct flame front exit diameter. For this case, the other approaches, namely the standard, refraction and projection methods are all evenly capable to reproduce the reference flame exit diameter.

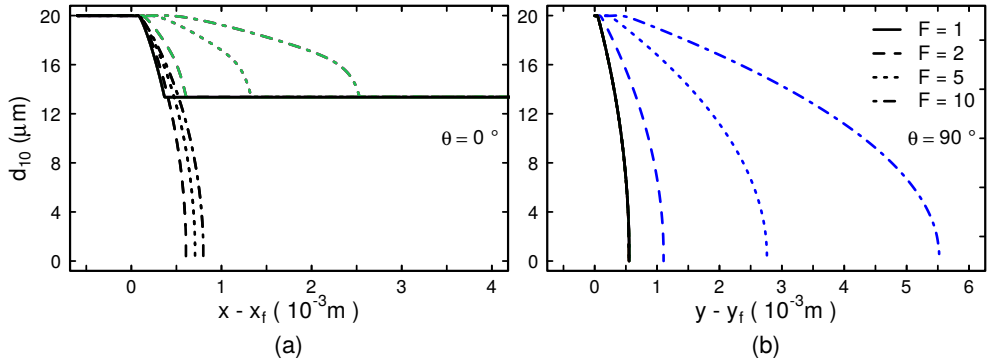

Figure 5.13: Diameter evolution of a droplet interacting with a flame for the two edge cases (a) $\theta = 0°$ and (b) $\theta = 90°$ for various thickening factors F. $x \equiv$ flame front orthogonal direction; $y \equiv$ flame front parallel direction. (—): no correction; (—): standard correction; (—): refraction correction; (—): projection correction.

Going over to droplet parallel movement case ($\theta = 90°$) exhibited in Figure 5.13b, the behavior is different. Here, all approaches, independent of the thickening factor are reproducing the same diameter evolution as the reference solution, except the standard approach (blue lines). The deficiency of the standard thickening correction becomes evident considering that the diameter evolution (and the droplet vapor source term) is elongated by the thickening factor F. This happens despite the flame being not thickened in that direction. In difference, the projection and refraction approaches are both able to reproduce the reference solution. Nonetheless, while these approaches are reproducing equal results, they are grounded on two different procedures. At a closer look, they are in fact, very different. The projection method attains the correct behavior by reducing the effective thickening correction factor F_{eff} to unity, while the refraction method does so by perform-

ing the previously explained trajectory correction. In Section 3.2.4, it is outlined that F_{eff} is the same for the refraction approach and the standard one (see Table 5.4). It can therefore be reasoned that both approaches must at least reproduce equal droplet-flame interaction times (or lifetimes in this specific flame parallel movement case). This emphasizes that, while the diameter evolves along the same path for the refraction and projection correction, they do it at different times. In the case of droplet movement parallel to the flame front, the refraction approach is, differently from the projection correction and the method without correction, elongating the droplet lifetime by the factor F.

For the two-dimensional cases $\theta = 30°$ and $60°$, the differences between the approaches are more distinct. For these cases, it is no longer enough to take a look at one direction. Both, flame parallel, and orthogonal direction, must be considered. The results are displayed in Figure 5.14, showing the flame orthogonal coordinate (left) and the flame parallel one (right). First, considering the case where $\theta = 30°$ in the top of Figure 5.14, one can already observe differences for the flame orthogonal direction. Here, the standard and refraction approaches produce equal results and are able to reproduce the reference flame exit diameter. This is a remarkable point, since, under the condition that a droplet exits the flame, i.e. that it has a flame front exit diameter, the standard approach already fulfills the exit-diameter criterion. This is independent of the droplet flame front parallel movement. However, it should be kept in mind that comparing the flame exit diameter of a droplet crossing a thickened flame front with the exit diameter of its non-thickened pendant does not reveal the potential impact of the evaporation through the flame parallel direction. This is a crucial aspect in view of the complex spray combustion simulations presented later in this work. When comparing simulations with experiments, it is not only important to observe similar effects, but also at similar positions. If flame front orthogonal effects dominate, the displacement resulting from the thickening procedure is expected to not surpass several flame thicknesses, which is in most cases insignificant compared to the geometric dimensions of the configuration. However, as flame front parallel effects become relevant, such a dislocation is expected to grow quickly. This is due to the elongation of the trajectory parallel to the flame front, which is portrayed best in Figure 5.13b and also visible in the top right of Figure 5.14. For this direction, the refraction correction yields a similar distribution of vapor release as the reference solution, which is caused by the trajectory correction. This is very different from the standard approach. As for the orthogonal scenario, the approach without correction yields much faster evaporation rates and the droplet quickly disappears. In between the other methods lies the projection approach, for which slightly smaller exit diameters than for the standard or refraction approach can be observed. It is worth noticing that for this approach, the diameter at the flame front exit is depending on the thickening factor. Both previously mentioned effects are not unexpected since the projection can be reformulated as combination of the standard approach (i.e. $F_{\mathit{eff}} = F_{\mathit{eff}}^{std} \neq$) and the one without correction ($F_{\mathit{eff}} = F_{\mathit{eff}}^{none} = 1$), which becomes more obvious by reformulating Equation 3.96 to

$$F_{\mathit{eff}}^{proj} = F_{\mathit{eff}}^{none}(1 - w_{\perp}) + w_{\perp} F_{\mathit{eff}}^{std}, \tag{5.11}$$

with the flame orthogonal weighting factor $w_{\perp} = \left| \frac{\nabla PV}{|\nabla PV|} \cdot \frac{\mathbf{u}_d}{|\mathbf{u}_d|} \right|$. The visible but small differences between the projection approach exit diameter and the one resulting from the standard or refraction approach are attributed to the minor flame parallel movement compared to its flame orthogonal component, yielding values of $w_{\perp}$ close to unity. Evidently, this is also connected to a similar expansion of vapor release in flame parallel direction in both, the projection and standard correction.

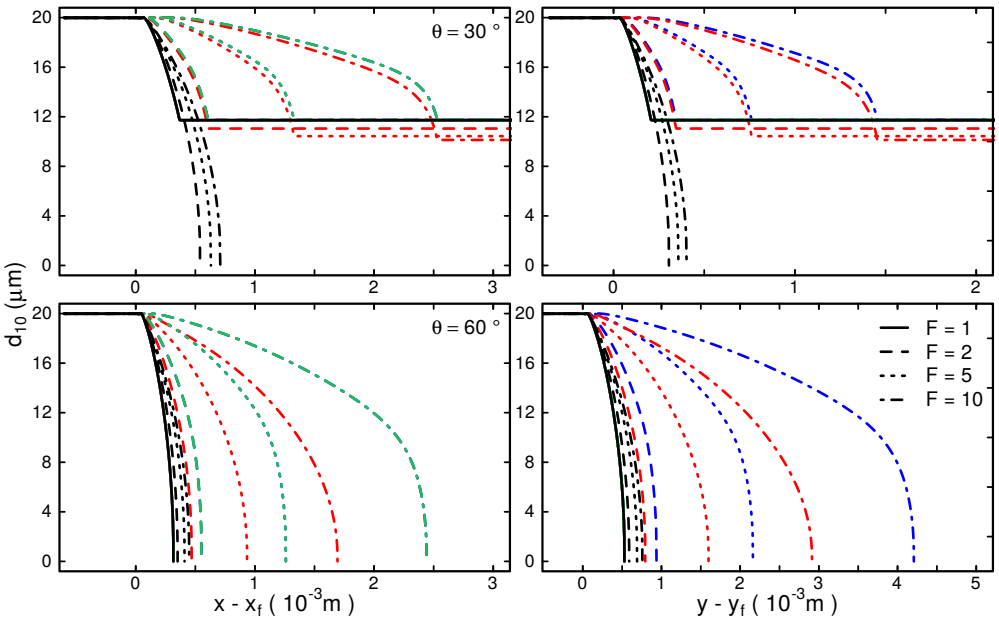

Figure 5.14: Diameter evolution along droplet flame normal (left) and flame parallel (right) direction for cases $\theta = 30°$ (top) and 60° (bottom) for various thickening factors F. $x \equiv$ flame front orthogonal direction; $y \equiv$ flame front parallel direction. (—): no correction; (—): standard correction; (—): refraction correction; (—): projection correction.

For the configuration $\theta = 60°$ in the bottom of Figure 5.14, it turns out that the low flame-orthogonal velocity yields a complete evaporation of the droplet before the flame front exit. As expected, the diameter evolution for the projection method is shifted towards the solution obtained without correction due to the decreasing ratio between the flame orthogonal and flame parallel velocity. This results in a stronger concentration of the vapor release in both, flame parallel and orthogonal direction. In the flame normal direction, as for the previous case, the vapor release is distributed equally along the thickened flame for the standard and refraction correction while similar deviations are obtained in the flame parallel direction.

To summarize, the diameter evolution of a droplet crossing a thickened flame along its flame normal and flame parallel trajectory is strongly depending on the manner heat and mass transfer is addressed. At present, the refraction correction shows the most promising results as it conserves the flame front exit droplet diameter of a given non-thickened flame and at the same time keeps the droplet evolution across the flame parallel direction unaltered. It now remains to investigate how the approaches perform in a complex spray jet flame. This is performed in Chapter 8.

PART III: VALIDATION IN TURBULENT REACTIVE SINGLE PHASE FLOWS

Chapter 6

Analysis of Shear Effects on Mixing and Reaction Layers in Turbulent Stratified Flames using the ATF-Approach

In this chapter, which is to a great extent based on the work by Dressler et al. [42], the effect of shear on turbulent lean premixed flames under stratified burning conditions is numerically investigated. The flames considered are the TSF-A-r and TSF-D-r operating conditions of the Darmstadt Stratified Burner [183]. The objectives of this chapter are twofold. The first consists in demonstrating the validity of the previously introduced and implemented ATF modeling framework in the context of purely gaseous reactive flows. This is achieved by comparing the numerical predictions of time averaged LES with available experimental data in order to determine the prediction capability of the numerical approach. Moreover, the simulation results are used to analyze and characterize the investigated turbulent stratified flames. In particular, coherent patterns in the mixing layers and their influence on the flame are identified. The onset and intensity of stratification of the two test cases are evaluated and compared in terms of equivalence ratio gradient, strength of the mixing and reaction layers, and scalar dissipation rates.

This chapter is organized as follows: first, the configuration, the numerical setup and the adopted modeling approaches are depicted. Thereafter, numerical predictions of time averaged data are compared with experimental data in the results section. The results are complemented by a characterization of the stratified mixing layers and their interaction with the flame. Finally, conclusions are presented.

6.1 Experimental Configuration

The Darmstadt stratified burner consists of three concentric tubes, therefore allowing for variations of the mixture composition and of the flow condition in the radial slots resulting in different levels of stratification or shear. The naming of the slots is chosen alike Seffrin et al. [183], where slot-1 and slot-2 stand for the two annular slots surrounding the pilot. The pilot itself has an inner diameter of 14.8 mm. The methane fueled flame is stabilized by a flameholder placed 40 mm upsteam of the pilot exit (see Figure 6.1). The burner is centered in a 600 mm coflow of pure air. In order to reduce heat losses within the pilot the centering tube is made of sintered ceramic. Experimental analysis' included laser doppler velocimetry (LDV) and particle image velocimetry (PIV) for the flow statistics [183], planar laser-induced fluorescence (PLIF) for the qualitative visualization of the mixing and reaction layer as well as Rayleigh scattering for the temperature fields

[20]. Additional measurements of temperature and main species were performed using 1D Raman/Rayleigh scattering in [107]. An extensive description of the burner is provided in the work of Seffrin et al. [183].

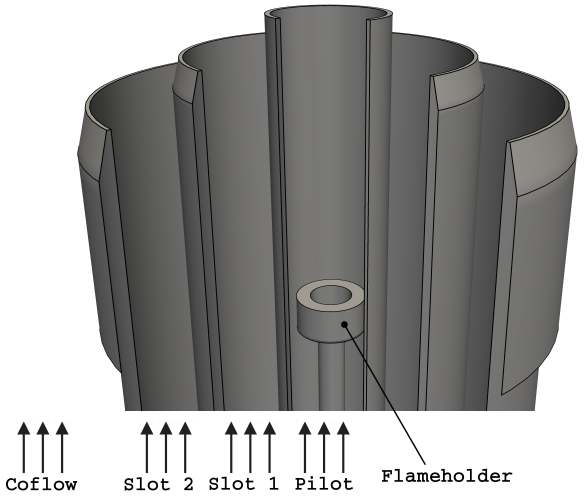

Figure 6.1: Schematics of the burner geometry of the Darmstadt Stratified Burner.

Within the scope of this work, two different cases are compared to validate the implemented framework and to gain a better understanding of the phenomena induced by shear in a stratified atmosphere. Their operating conditions are summarized in Table 6.1. Both cases, namely TSF-A-r and TSF-D-r, exhibit the same level of stratification. However, the velocity in slot-2 is twice as high in the case D, leading to increased shear effects downstream of the burner.

	ϕ_{pilot} (-)	ϕ_{slot1} (-)	ϕ_{slot2} (-)	u_{pilot} ($\mathrm{m\,s^{-1}}$)	u_{slot1} ($\mathrm{m\,s^{-1}}$)	Re_{slot1} (-)	u_{slot2} ($\mathrm{m\,s^{-1}}$)	Re_{slot2} (-)
TSF-A-r	0.9	0.9	0.6	1	10	13800	10	13300
TSF-D-r	0.9	0.9	0.6	1	10	13800	20	26600

Table 6.1: TSF-configurations investigated.

6.2 Numerical Setup

The employed computational domain is illustrated in Figure 6.2. Downstream of the burner exit, the cylindrical grid ranges approximately 20 pilot diameters (300 mm) in the axial and 100 mm in the radial direction. Additionally, in order to be able to generate valuable inflow conditions, a considerable section of the burners upstream geometry has been included in the domain resulting in an inlet 120 mm upstream of the burner exit. Assuming a fully developed turbulent flow at the burner exit, a recycling method is applied in order to generate turbulent conditions within slot-1 and slot-2. This assumption is justified by a minimum tube length of 25 hydraulic diameters for both slots, as described in [183]. Considering its low Reynolds number of approximately 900, a laminar flow is prescribed for the pilot. Other than the coflow-inflow, all outer boundaries are set to total pressure boundary conditions to enable the entrainment of the surrounding flow. To

reduce the computational effort of the LES, the near wall region is modeled using the wall function formulation of Spalding [192]. Considering the substantial parts of the burner included in the computational domain, the σ-eddy-viscosity model [129] is employed for turbulence modeling, primarily due to its ability to treat the flow in the near wall regions correctly. Combustion modeling is realized using the ATF model combined with chemistry

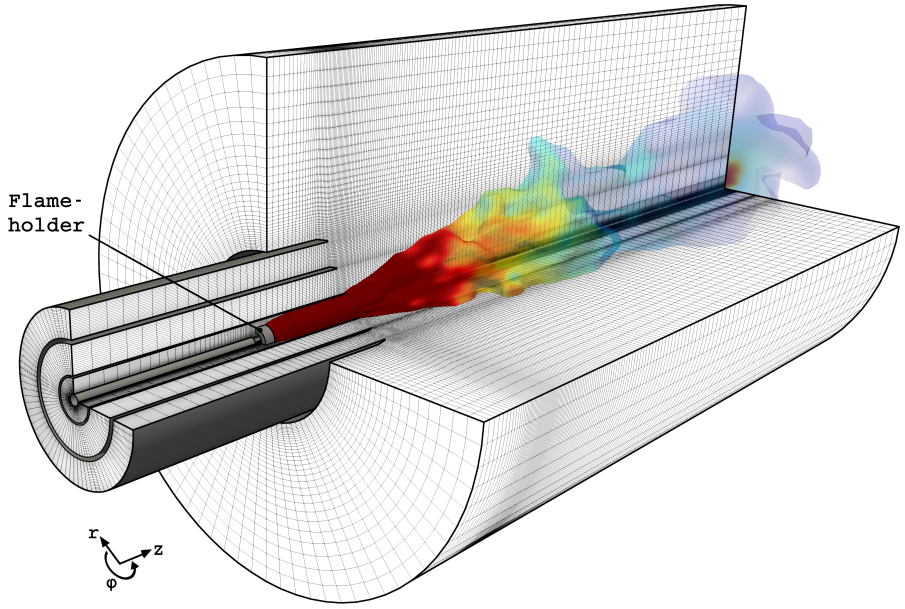

Figure 6.2: Computational domain used for the Darmstadt Stratified Burner simulations. Flame stabilization and stratification are illustrated by a clip of the reaction progress variable $PV > 3 \cdot 10^{-4}$ colored with the equivalence ratio.

tabulation via the Flamelet Generated Manifold method [196]. Regarding the tabulation, a two-dimensional table is employed mapping the thermochemical state onto the mixture fraction Z and reaction progress variable PV in order to account for the physical processes of mixing and reaction, as found in the investigated configuration. The table consists of one-dimensional premixed flamelets as described in Section 3.1.2. The set of equations solved consists therefore of the continuity and momentum equation coupled in a low-Mach manner [165] as well as two additional scalar transport equation for $PV = Y_{\mathrm{CO}_2}$ and mixture fraction Z (Equations 3.98, 3.99, 3.100 and 3.101). The scalar subgrid-fluxes are taken into account via Equation 3.19 using a subgrid-scale Schmidt number $Sc_{sgs} = Sc = 0.7$. The set of coupled PDEs is solved using the previously introduced merged PISO[87]-SIMPLE[137] algorithm described in Section 4.2.2. Thereby, the second-order implicit time-stepping scheme is applied to all fields. The convective momentum fluxes are discretized using the filteredLinear scheme [71] and the convective scalar fluxes are treated using the Minmod flux-limiter scheme [167] (see Section 4.1.1). Regarding the ATF model, a dynamic formulation coupled to a grid-adaptive thickening procedure, described in Section 3.1.3, is used. The proposed formulation for the flame sensor (Equation 3.47) is employed. In order to correct the weakened turbulence flame interaction caused by the thickening of the flame, the efficiency function formulation proposed by Charlette [26] is applied.

6.2.1 Impact of the Spatial Resolution

Before going over to the results and in order to determine the influence of the spatial resolution on the LES results, a systematic grid sensitivity study was carried out for TSF-D-r using three numerical grids with 1.4, 3 and 6 million control volumes, respectively (subsequently denoted as coarse, medium and fine). Figure 6.3 depicts radial profiles at two axial positions z of first and second order statistical moments for the axial velocity and the mixture fraction obtained using the different numerical grids. The origin of the coordinate system is located at the center of the pilot stream on the burner exit plane.

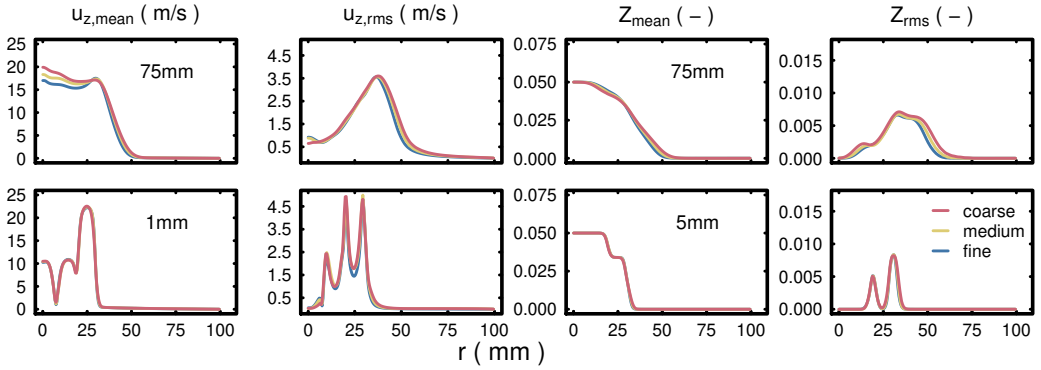

Figure 6.3: Mean and rms values of the axial velocity and the mixture fraction at different axial positions for the three investigated numerical grids.

From Figure 6.3, some differences are perceivable and grid convergence is reached at least for the two highest spatial resolutions. The profiles of mean and rms values obtained from the medium and fine grid are very close to each other. This confirms that both, the medium and fine grids are more appropriate to describe the physics of the Darmstadt stratified burner configuration accurately. Consequently, in order to allow accurate long-term statistics at reasonable computational costs, the medium grid is selected for further analysis. Similar results are obtained for other physical quantities, axial positions and for TSF-A.

6.3 Results

This section is split into two parts: first, time averaged data are presented along radial lines at various axial positions to provide an understanding for the flow field and scalar distribution. In this context, a comparison with experimental data is carried out to certify that the LES-ATF framework is able to reproduce the main features of this configuration. Secondly, the simulation results are used to provide a characterization of the stratification layers and their interaction with the flame.

6.3.1 Evaluation of Temporal Statistics

Figures 6.4 and 6.5 show radial profiles of temporal mean and rms at several axial positions for different quantities. First, the axial and radial velocity profiles displayed in Figure 6.4 are discussed. In the lowest plot, at 1 mm above the pilot exit, the axial velocity features the three distinct jets issuing from the central pilot and the outer two slots. For TSF-A-r, these two slots both have a bulk velocity of $10\,\mathrm{m\,s^{-1}}$, which is in good agreement with the experiment. Likewise, the rms values of the LES are reproducing the experimentally

observed three shears layers reasonably well. As already mentioned, the TSF-D-case differs from the A-case in that the velocity of slot-2 is twice as high. This increase in the averaged axial velocity is well predicted in the simulation. This higher velocity also induces stronger shear layers, as indicated by the higher rms values. For the radial velocity in the lowest plane, the rms values are also reasonably well predicted while the mean component does not fit well. However, it is relatively small in magnitude and deviations can be due to the experimental configuration, i.e. to issues related to the pilot and flameholder centering [183]. Moving to higher axial positions the bulk velocity increases due to the thermal expansion through the flame. For both cases, all trends are well predicted regarding the mean and rms of both velocity components. An exception is the axial velocity above the pilot, which is overestimated by the simulation due to the adiabatic assumptions made. The radial velocity already reveals a geometrical difference between the two cases. The peak present in the mean as well as in the rms values is caused by the presence of the flame. With increasing distance from the burner exit, this peak moves towards higher radial positions due to the spreading of the flame. This is more pronounced for the TSF-A-r while the flame is narrower in TSF-D-r. This phenomenon, caused by the higher bulk velocity in slot-2, is well captured in the simulation.

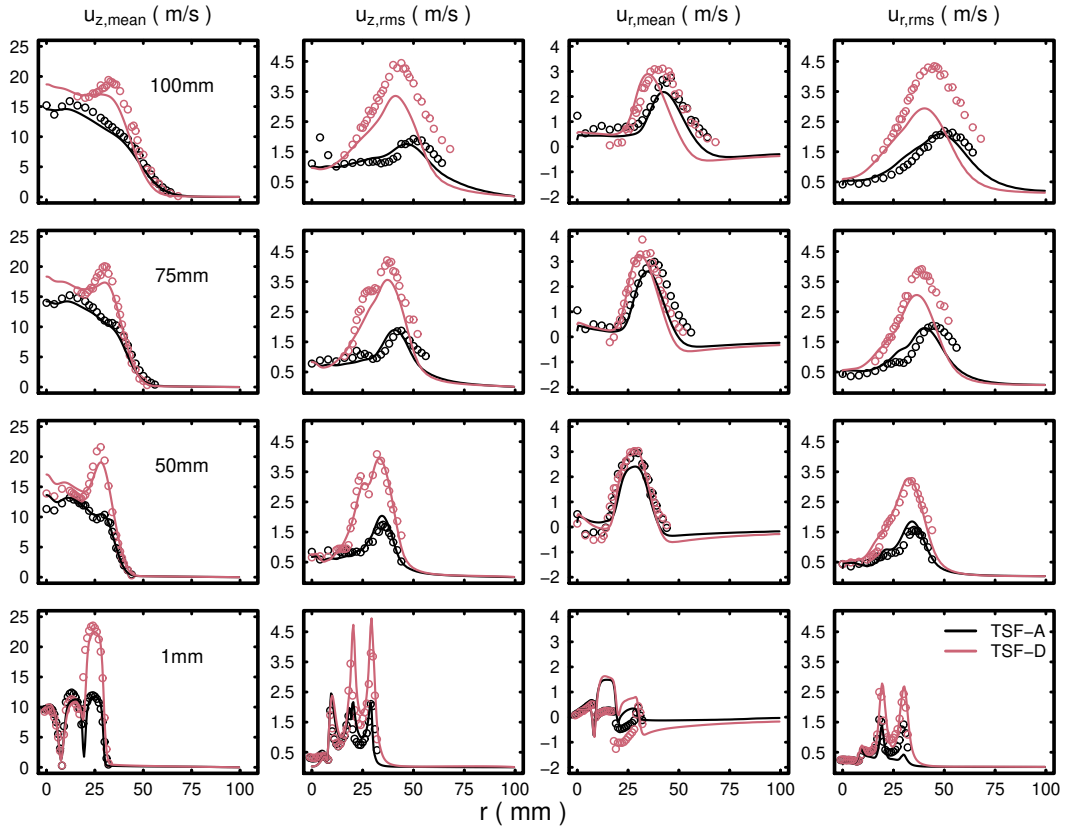

Figure 6.4: Comparison of experimental data with simulation results: Mean and rms value of axial and radial velocity at different axial positions. (—): LES-ATF; ○: experimental measurements.

Next, the scalars shown in Figure 6.5, which were only measured for the TSF-A-r, are discussed. Here, special attention is given to the mixing process, for which further analyses are provided in later parts of this chapter. The mixing process is characterized here by means of the mixture fraction, for which temporal statistics are presented in the

third and fourth columns of Figure 6.5. At the lower positions the two cases behave almost identically: Both feature the first drop in equivalence ratio from 0.9 to 0.6 between slot-1 and slot-2 and the second drop towards pure air in the coflow. In this regard, the mean and variance of mixture fraction agree well with the measurements. One plane further downstream, at 25 mm, the two steps are still distinct and the double peak structure in the rms profiles still pronounced. However, as the axial distance further increases, the two shear layers finally merge into each other yielding one constant slope for the mean. This process is accurately described by the LES. Comparing the cases A and D, differences only become significant at 100 mm, where again the narrower field of case D yields a shift of the profiles towards lower radii. Finally, to represent the flame and the location of hot burnt gases, the first two columns of Figure 6.5 show the time averaged temperature statistics. Compared to the TSF-A-r experiment, the simulation features a slightly stronger flame spreading except for 100 mm. This higher spreading could be caused by an overestimation of the turbulent flame propagation speed (caused for example through a non-optimal exponent β in the efficiency function formulation). However, it is more probable that this radial shift is resulting from the flame attachment on the pilot tube, where the adiabatic assumption causes an overestimation of the reaction rate. The temperature rms values are underestimated, which is however in agreement with the modeling procedure of artificial flame thickening, where the resolved part of the fluctuations reduces naturally. This behavior is more pronounced at higher axial distances from the burner exit due to higher thickening factor values. Similar observations were made by Avdic et al. [5].

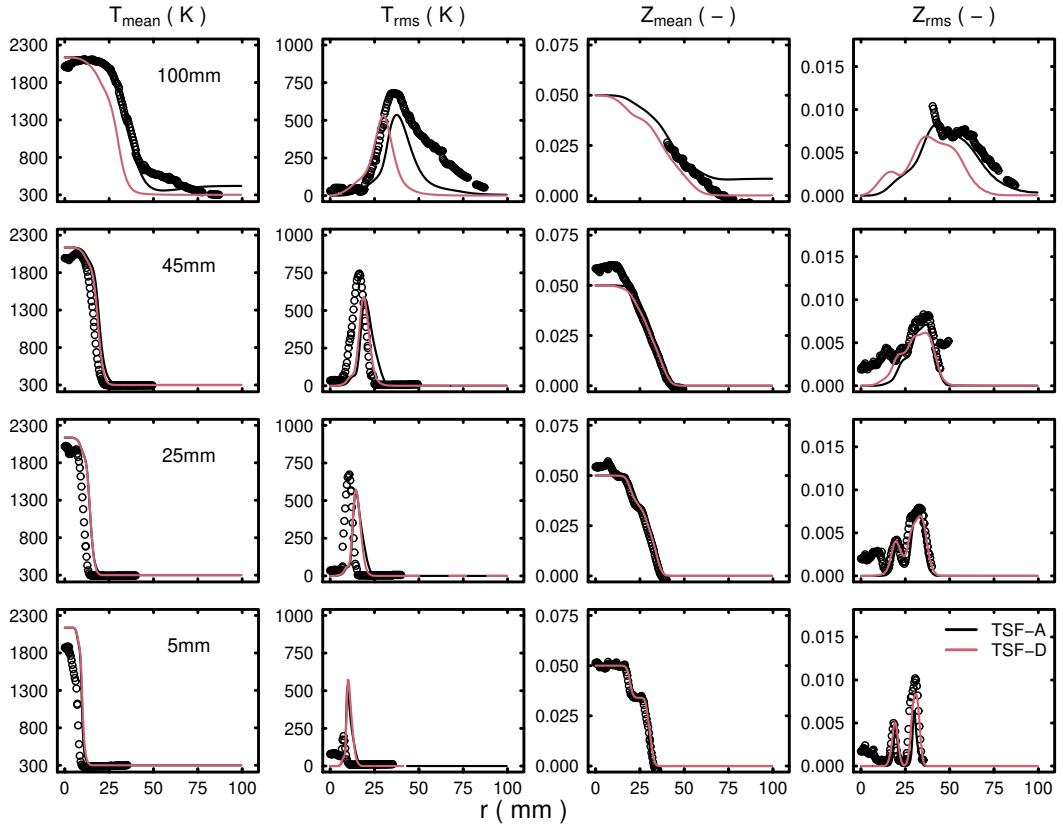

Figure 6.5: Comparison of experimental data (TSF-D-r not available) with simulation results: Mean and rms value of temperature and mixture fraction at different axial positions. (—): LES-ATF; ○: experimental measurements.

6.3.2 Insights into the Stratification Layer and its Interaction with the Flame

A first impression of the stratification is provided by the snapshots shown in Figure 6.6. The two stratification layers are visualized by means of contours of the equivalence ratio gradient. Some patterns are qualitatively observable. These are quantified next through the analysis of probe values given in Figure 6.7. The probes are located at the axial position z = 4 mm downstream of the burner and inside the time averaged stratification layer, i.e. at a temporally averaged equivalence ratio of $\phi = 0.75$ and $\phi = 0.3$. The contours of the equivalence ratio gradient are in agreement with the double peak in the mixture fraction rms profiles discussed in the section above. In the outer layer of TSF-A-r, shown on the left of Figure 6.6, distinct repeating patterns can be identified in Region I. This is not unexpected since this region is characterized by a strong shear between the outer slot and the slow coflow. The emerging vortex shedding yields the large coherent structures observed. The time series (top of Figure 6.7a) of the corresponding probe shows the fluctuation of the mixture fraction varying in between the lean slot-2 conditions and the pure air at frequencies around 350 Hz, as indicated by the spectrum in the lower plot of Figure 6.7a. Regarding this outer layer, TSF-D shows a similar behavior, but differences are also visible. Looking at the contours of equivalence ratio close to the burner exit, the shear layer appears more stable for the case A while the higher velocity in TSF-D-r causes a faster onset of instabilities. Accordingly, the repeating patterns already set in at lower axial position. The corresponding time series (middle row of Figure 6.7a) is a bit more irregular compared to the case A but still has an identifiable repetition. This yields a distinct peak in the spectrum at about 500 Hz, which is higher than in the case A because of the larger velocity. Additionally, the higher velocity in slot 2 also leads to a signal being distributed over a wider range of frequencies for case D.

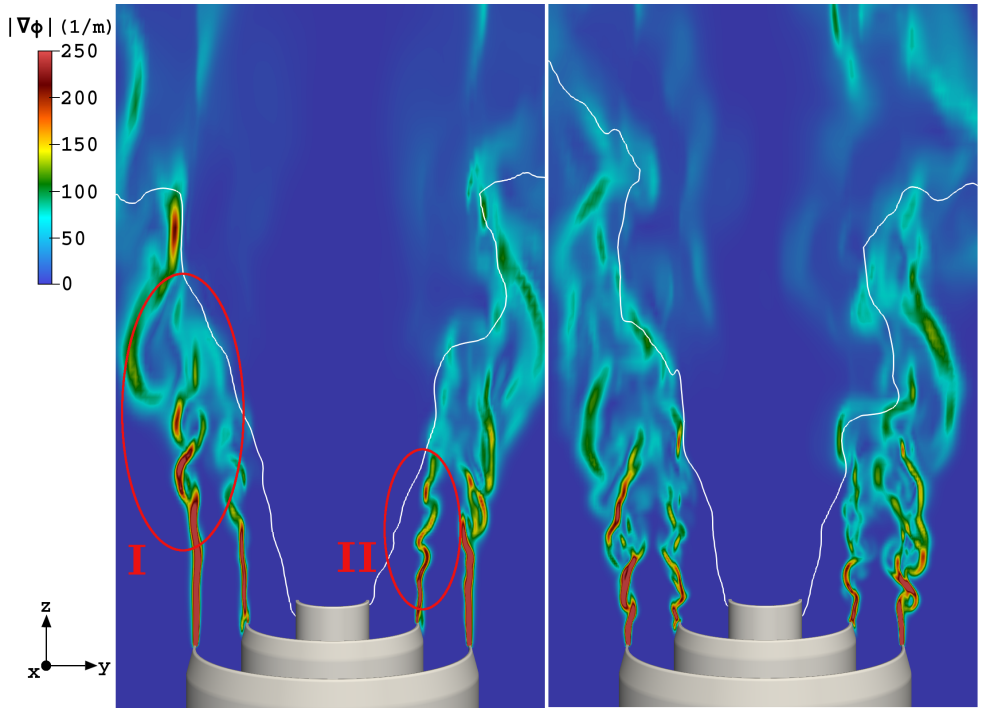

Figure 6.6: Snapshot of equivalence ratio gradients (in m^{-1}) with flame front visualization (white line); left: case TSF-A-r; right: case TSF-D-r.

Going over to the inner shear layer, both cases behave quite differently. Taking a look at region II marked in Figure 6.6 for TSF-A, as for the outer shear layer, the stratification layer remains rather stable in proximity of the burner exit. This is due to the absence of mean shear resulting from identical bulk velocities in slot-1 and slot-2 for this case. Only after a short distance downstream of the exit, the turbulence induces an instability where regular structures similar to a vortex-street can be observed. This is again quantified by the time series in Figure 6.7b and the corresponding spectrum with a peak at about 1050 Hz being above the one of the outer shear layer due to the larger velocity and the scales being smaller, as recognizable in Figure 6.7a. In contrast, for TSF-D, the turbulent intensity and the stronger shear layer in slot-2 causes the mixing layer to quickly destabilize. Furthermore, the mixture fraction signal becomes less regular and as the time series and the spectrum show, no distinct dominating frequency can be identified. This random behavior is characteristic of a fully developed turbulence.

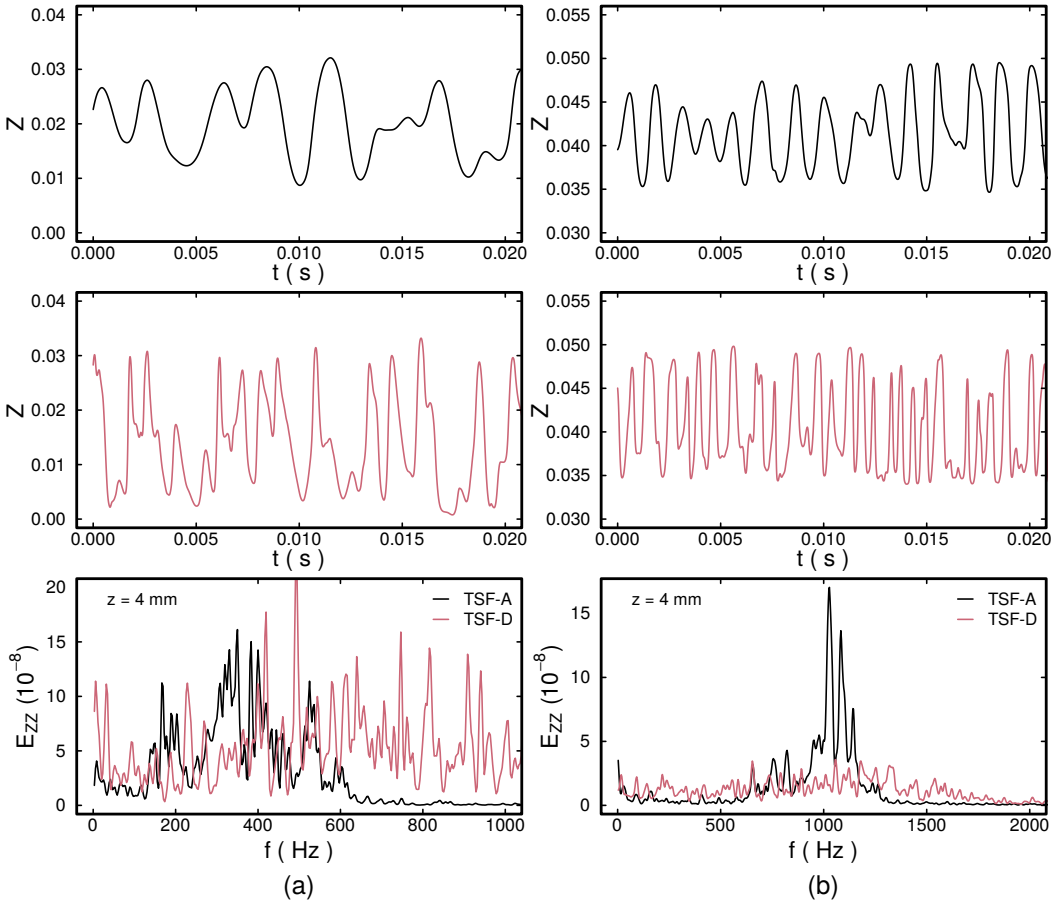

Figure 6.7: Analysis of mixture fraction time series in (a) the outer and (b) the inner shear layers.

So far, the shear layers ahead of the flame have been characterized. It remains to evaluate their effect on the combustion behavior. To analyze this impact, it is important to retain that the mixing and reaction layer behave partially correlated. This means, that simply considering time averaged data, as shown in the previous section, is not sufficient. This is illustrated in Figure 6.8a, which shows the evolution of the equivalence ratio found at the flame surface as function of the distance from the burner exit. The flames are

represented in terms of the normalized progress variables c (see Equation 3.28), which expresses the reaction evolving from an unburnt ($c = 0$) to a fully burnt mixture ($c = 1$). The three dashed lines correspond to the time averaged flame with the values $c = 0.01$ (light-blue), 0.1 (magenta) and 0.5 (red). The solid line in contrast shows the data conditionally averaged, i.e. samples (points in Figure 6.8a) are taken on an instantaneous basis on the flame front at $c = 0.01$ and averaged afterwards (only one layer is shown since the flame is rather thin). The conditional averaging procedure constitutes in axially decomposing the iso-surface of the normalized progress variable c into surface segments. This is performed for each time instant i, so that each segment j at $t = t_i$ has an area representing the resolved flame surface S_j. The temporal average of the equivalence ratio ϕ (or any other scalar quantity) conditioned on the flame surface segment j is then computed through the expression

$$\widehat{\phi}_j = \frac{\sum_i \int_{S_j(t_i)} \phi(t_i) dS}{\sum_i \int_{S_j(t_i)} dS}. \tag{6.1}$$

The conditional averaging was performed over 42 independent instants. The conditioning has an identical effect for both cases: one can see that the time averaged flame perceives leaner conditions earlier than the actual, i.e. conditionally averaged, flame. At lower axial positions, the flame burns in a homogeneous mixture with an equivalence ratio of 0.9, yielding an identical behavior for the conditioned and time averaged flame. However, the actual flame gets delayed in its drop in equivalence ratio. The difference is due to the partially correlated turbulent motion of the mixing and reaction layer caused by the convective part acting on both of them. This hypothesis is confirmed by Figure 6.8b, where the correlation coefficient [13] between reaction progress variable PV and mixture fraction along the temporally averaged stratification layer—as function of the axial distance from the burner exit—is shown. It is observed that the interaction increases with the axial distances for both stratification layers and cases. The high correlations far from the burner exit suggest a complete combustion leading to approximately same contributions for all terms in the scalar transport Equations 3.100 and 3.101. Additionally, the earlier rise of the correlation coefficient for case D indicates that the flame perceives the inner layer equivalence ratio drop earlier then for TSF-A, which is in agreement with Figure 6.8a.

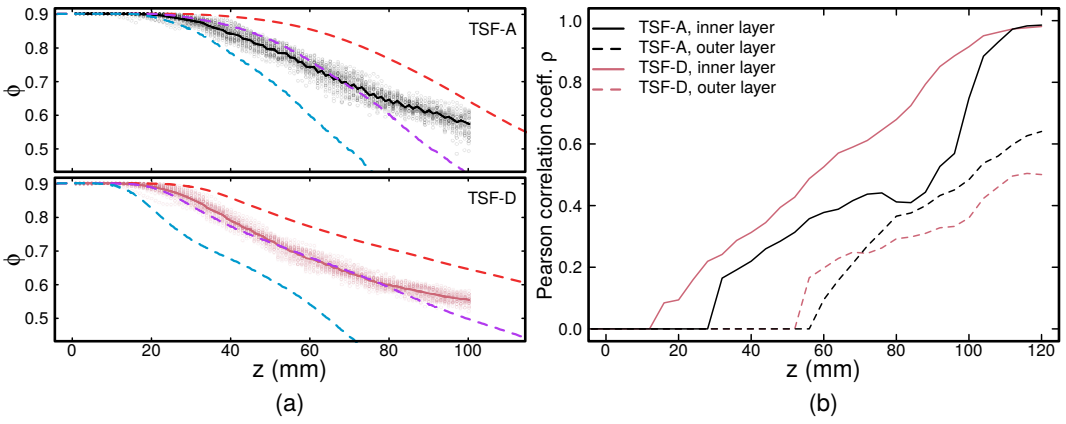

Figure 6.8: (a) Evolution of the equivalence ratio found at the flame as a function of the axial position. Dashed lines mark the time averaged reaction progress ranging from the unburnt (blue) to the burnt (red) values. (b) Correlation coefficient between mixing and reaction layer in the the two stratification layers as function of the axial position.

The partial correlation of the mixing and reaction layer is further illustrated by the time series displayed in Figure 6.9a for TSF-A-r, showing the mixture fraction in the top, and the reaction progress variable in the bottom. It can be perceived that correlated and uncorrelated variations exist. The four larger drops in mixture fraction do clearly have their corresponding drop in the progress variable profiles (red segments in Figure 6.9a). Moreover, the reaction progress also drops twice without the mixture fraction (blue segments), i.e. it burns predominantly in non-stratified regions and fluctuates due to the turbulent flame movement. Finally, a scatter of data taken from a probe inside the inner shear layer of TSF-D-r is presented in Figure 6.9b. One can clearly see the correlation between mixture fraction and reaction progress variable which is caused by the overlap of mixing and reaction layers, in this case with a correlation coefficient of about 0.68.

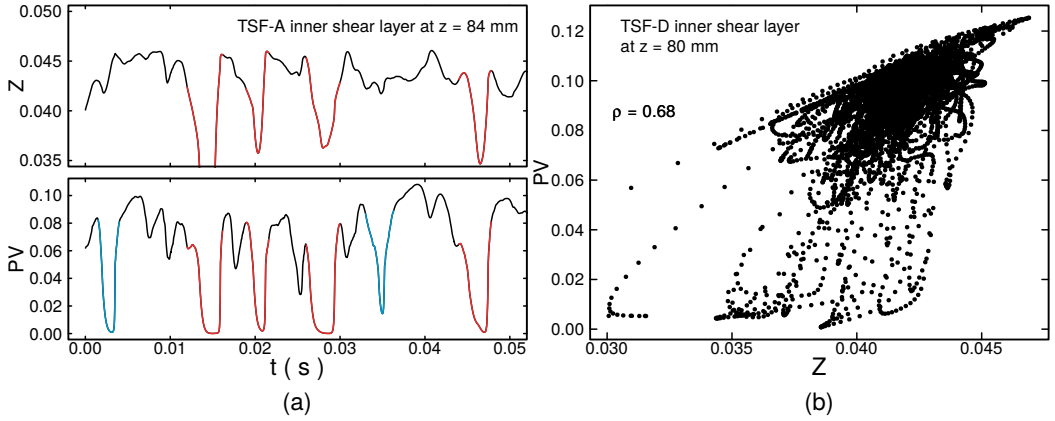

Figure 6.9: (a) Excerpt of a time series of mixture fraction (top) and progress variable (bottom) for TSF-A-r and scatter plot of mixture fraction and progress variable for TSF-D-r.

While these findings illustrates the importance of conditioned evaluation, it should be noted that the significance and strength of the correlation depends on the individual budged contributions (convection, diffusion and source terms) in the progress variable transport equation. At some point, the flame will finally travel through the stratification layer, which will depend on the local mixture composition and the flame surface alignment. This is illustrated in Figure 6.10, where emphasis is placed on the differences between the case A and D with regard to the stratification strength on the reaction layer. This is visualized through the equivalence ratio gradient $|\nabla\phi|$ mapped onto a normalized progress variable iso-surface ($c = 0.01$) of the flame. The initial observation for both cases is that strong local variations of $|\nabla\phi|$ exist. This can be explained with the above discussion of Figure 6.6: at an instantaneous level, even though the gradients reduce before approaching the flame, the mixture is not very homogeneous. Hence, sharp gradients embedded in partially coherent structures are able to approach the flame. Another observation is that both cases burn in homogeneous conditions right after the nozzle exit. This lasts longer for TSF-A than for TSF-D, where the larger momentum of slot-2 pushes the mixing layer towards the flame leading to large $|\nabla\phi|$ values quite early. Looking further downstream for TSF-D, these intense mixture fraction gradients perceived by the flame actually seem to reduce a bit, while the stratified region begins here to show higher equivalence ratio gradient values for case A. These impressions based on a single snapshot are confirmed and quantified in Figure 6.11. It shows the conditionally averaged $|\nabla\phi|$ values. As observed in the snapshot, TSF-D features an increases at lower axial positions compared to TSF-A.

Thereafter, the intensity is then slightly reduced but remains almost constant at a high stratification level. Likewise, as was the impression in the snapshot, TSF-A-r shows a later onset of stratification, but the intensity even surpasses the maximum values of the case D over quite a large region. This shows the significance of the process that carries the mixing layer towards the flame.

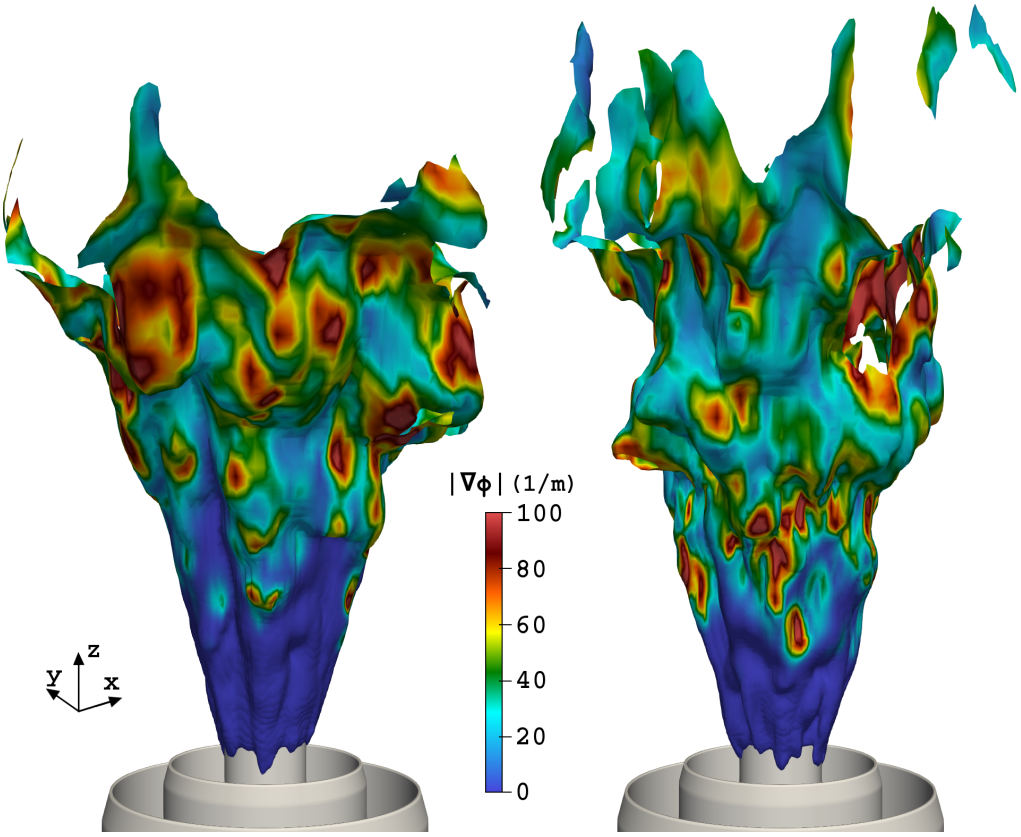

Figure 6.10: Snapshots of the equivalence ratio gradient (in m^{-1}) mapped onto the flame iso-surface for TSF-A-r (left) and TSF-D-r (right).

Finally, to complete this evaluation, Figure 6.12 compares the strengths of the mixing and reaction layer. It is of significance for the physical processes as well as the modeling assumptions. The findings hold for both cases, so only TSF-A-r is considered. For orientation, the right of Figure 6.12 shows the equivalence ratio found at the reaction layer ($c = 0.01$). This value is chosen mainly due to the fact that in this region, the influence of the flame thickening is kept minimal ($F = 1$). This is important as the scalar profiles are strongly smoothened in the thickened flame region and would otherwise discredit the present analysis. The middle shows the ratio of the scalar dissipation rates of progress variable and mixture fraction χ_{PV} and χ_Z, whereas the left plot represents $|\nabla\phi|$ with the mixing layer approaching.

The evaluation of the ratio of the scalar dissipation rates is used to assess whether the assumptions made in the thermochemical lookup-table are justified. For this purpose, it is helpful to consider the species transport equation in composition space for two-dimensional manifolds spanned by mixture fraction and progress variable [127]

$$\frac{\partial Y_k}{\partial \tau} + \frac{\partial Y_k}{\partial PV}\dot{\omega}_{PV} = \chi_{PV}\frac{\partial^2 Y_k}{\partial PV^2} + \chi_Z\frac{\partial^2 Y_k}{\partial Z^2} + 2\chi_{Z,PV}\frac{\partial^2 Y_k}{\partial Z \partial PV} + \dot{\omega}_k. \tag{6.2}$$

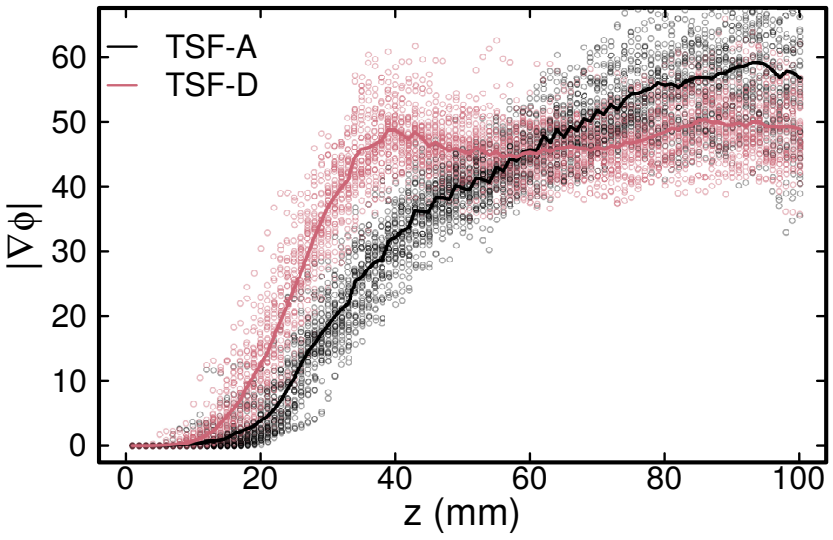

Figure 6.11: Time averaged equivalence ratio gradient (in m^{-1}) conditioned on the flame surface as a function of the axial distance.

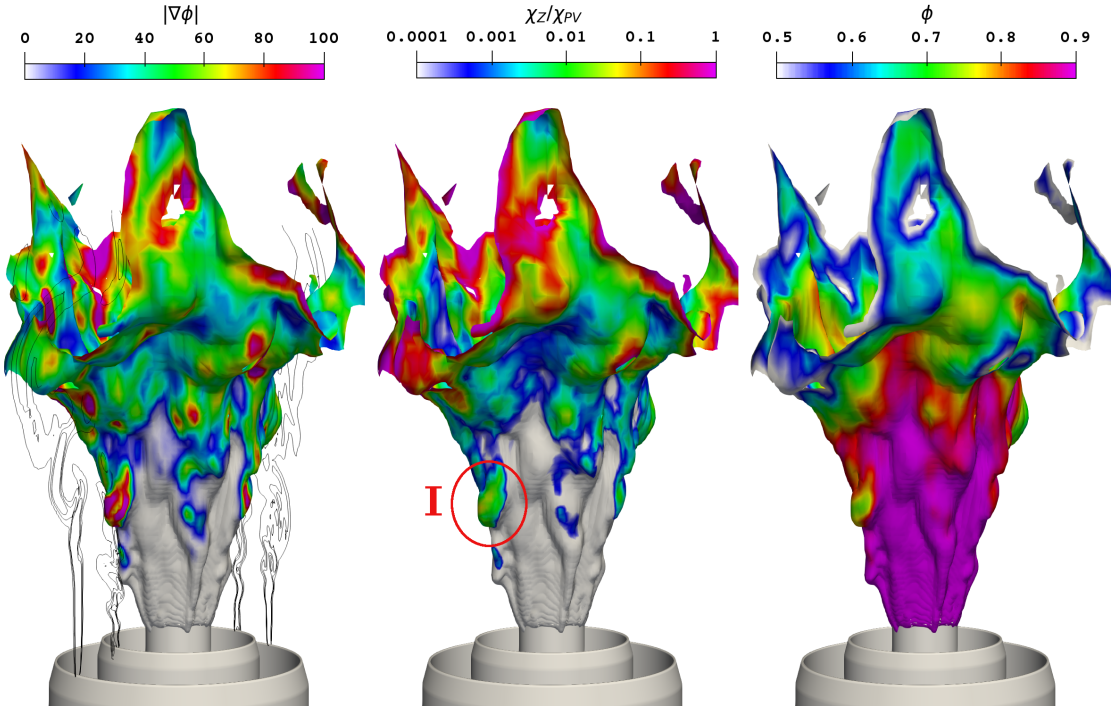

Figure 6.12: Comparison of the mixing and reaction layer for case TSF-A-r.

Thereby, the three dissipation rates χ_{PV}, χ_Z and $\chi_{Z,PV}$ appear in this general formulation. As previously outlined, the adopted tabulation strategy relies on one-dimensional premixed flamelets, which implicitly neglects any cross-flamelet interactions. In other words, each iso-mixture fraction flamelet is being computed independently of its neighboring flamelets. This presumes that the term containing χ_Z and $\chi_{Z,PV}$ can be dismissed in the flamelet precomputations. In regard of the the cross-scalar dissipation term, different works state that its contribution is small compared to the other terms in Equation 6.2 [127, 38]. Its

impact is therefore also assumed to be small for this configuration. The ratio χ_Z/χ_{PV} is therefore used to evaluate the adopted chemistry-tabulation strategy, i.e. to justify the negligence of χ_Z. In this context, a small ratio relates to a thin reaction zone only weakly influenced by mixing gradients, whereas a larger ratio indicates mixing processes taking place at the same scales as the chemical reaction [127].

Looking at the Figure 6.12 middle, a general trend is, that the ratio is indeed small, but increases towards more downstream positions. Herein, two competing effects act: first, χ_Z reduces due to mixing, and second, χ_{PV} also reduces, since the flame broadens in leaner conditions. Apparently the latter dominates, which is in agreement with the previously observed axial evolution of the equivalence ratio gradients found at the flame surface. Interestingly, larger ratios can also reach further upstream as indicated by the event outlined by region I. Even though the ratio is still small (i.e. below 10%) it is noticeably higher than its surrounding. This incident can be explained by the other plots of Figure 6.12. As the equivalence ratio on the right reveals, a lean spot forms which naturally reduces χ_{PV}. Furthermore, as one sees on the left, within this process, a strong equivalence ratio gradient approaches the flame. In contrast to the competing behavior mentioned above, both act towards increasing the ratio of χ_Z/χ_{PV}. Regarding case D (not shown here), the effect is also present but slightly less pronounced, as the higher turbulence enhances mixing, hence further promoting premixed combustion. This is consistent with the lower maximum values of the equivalence ratio gradients found at the flame surface presented in Figure 6.11.

6.4 Conclusions

In this chapter, the previously introduced and implemented ATF modeling framework was validated in the context of gaseous reactive flows. This was achieved by comparing the numerical predictions of time averaged LES with available experimental data. The analysis revealed that the LES is able to reproduce the measured temporal statistics of the flow-field, temperature, and mixture fraction. This represents a crucial step towards the application of the modeling framework to turbulent spray combustion.

Then, as additional purpose of this chapter, a detailed analysis of the mixing and reaction layer was carried out and several interesting findings were provided, thus contributing to a better understanding of the process. First, the mixing layers ahead of the flame were characterized, revealing certain coherent patterns beside turbulent mixing processes. As was shown, these patterns enable large equivalence ratio gradients to approach the flame even at higher axial positions where they only partially have smoothened out. In a next step. the correlation of the displacement of the mixing and the reaction layer was demonstrated by comparing the time-averaged flame with the more appropriate flame-surface-conditioned averages. Based on this, the equivalence ratio gradient actually perceived by the flame was evaluated, suggesting that significant stratifications are interacting with the flame front. At this, the two cases TSF-A and TSF-D showed a different behavior regarding the onset and intensity of stratification. Finally, the evaluation of scalar dissipation rates confirmed the common physical assumptions about their contribution to these types of flames but also revealed processes where χ_Z can possibly approach a similar order of magnitude as χ_{PV}.

It can be summarized that: (1) a higher shear tends to attenuate the level of stratification of the flame; (2) the mixing and reaction layers correlate earlier and stronger with increasing turbulence which can be attributed to the stronger shear; (3) a premixed mode can be promoted with a stronger turbulence.

Chapter 7

Computation of the Sandia Flame D using the Eulerian Stochastic Field Method

In the previous chapter, the prediction ability of the coupled ATF-FGM approach has been demonstrated in a purely gaseous flame. Similarly, the present chapter applies and validates the ESF method by computing the well known Sandia Flame D configuration. The investigated flame is chosen due to the large amount of experimental data available to perform the validation and well defined boundary conditions [182, 10, 11, 8]. The validation data has been used extensively in the context of the International Workshop on Measurement and Computation of Turbulent Flame [9], which resulted in numerous numerical investigations of this flame to demonstrate the suitability of approaches to approximate turbulent combustion [116, 115, 98, 200, 124, 84]. Likewise, the present chapter investigates the performance of the ESF approach coupled to tabulated chemistry for this purely gaseous flame. In that sense, this investigation is the final step before applying the ESF approach to a dilute spray flame.

The first section of this chapter is dedicated to the experimental configuration. Thereafter, the numerical setup is briefly summarized. Then, the simulation results using either 4, 8 or 16 stochastic fields are set aside experimental data and the influence of the number of stochastic fields on the temporal statistics of velocity and various scalars of interest are discussed. Additionally, the results of the simulations with 16 stochastic fields are compared with the experiments in mixture fraction space for temperature and CO_2 mass fraction. Finally, the main outcomes are summarized in the conclusions section.

7.1 Experimental Configuration

The Sandia Flame D denotes a special operating condition of a piloted burner developed at the university of Sydney [119]. The geometry of the burner head is sketched in Figure 7.1a and consists of two concentrically arranged tubes. The circular central stream with a diameter $D = 7.2\,\mathrm{mm}$ is referred to as central—or main—jet. This jet is surrounded by a pilot from which hot burnt gases exit. The burner is placed in a rectangular wind tunnel with the dimensions 30 cm by 30 cm in order to minimize the influence of walls on the flame. The burner is operated using methane as fuel. The mixture exiting the central jet with a bulk velocity of $49.6\,\mathrm{m\,s^{-1}}$ is composed to one part of CH_4 and three parts of air, which results in a mixture fraction of 0.1564. The corresponding jet Reynolds number is 22400. The wind tunnel coflow consists of pure air with a velocity of $0.9\,\mathrm{m\,s^{-1}}$. The

flame-stabilizing pilot is a lean mixture of C_2H_2, H_2, CO_2, N_2 and air with an equivalence ratio $\phi = 0.77$. The mixture has been chosen such that the enthalpy and equilibrium composition are equal to that of a methane-air-flame. The bulk velocity of the burnt gases exiting the pilot is $11.4\,\mathrm{m\,s^{-1}}$. The validation data includes temporal statistics as well as single shot measurements for various scalars, which were obtained using Raman/Rayleigh spectroscopy, laser induced fluorescence (CO-LIF) [10, 11], and temporal velocity statistics using laser Doppler velocimetry performed at the Technical University of Darmstadt [182]. For more information on the experimental setup as well as the experimental data provided, the interested reader is referred to [8].

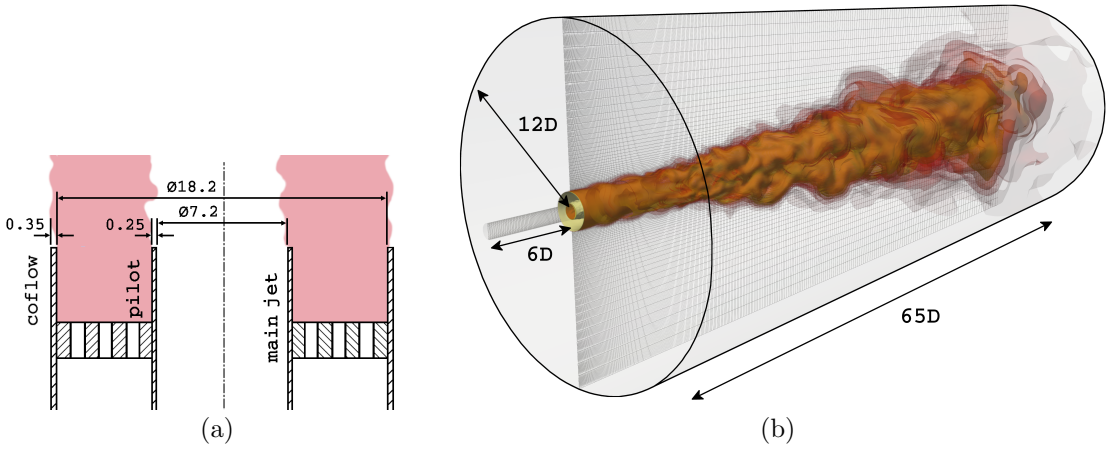

Figure 7.1: (a) Schematic representation of the burner exit (dimensions in mm) and (b) computational domain employed to compute the Sandia Flame D. The dimensions in (b) are all expressed as multiples of the central jet diameter $D = 7.2\,\mathrm{mm}$. The turbulent flame is illustrated by means of temperature iso-surfaces.

7.2 Numerical Setup

As already pointed out, the ESF approach is adopted here. The system of PDEs solved is therefore given by Equations 3.98, 3.99, 3.102 and 3.103. Obviously, all source terms due to the presence of a liquid phase are set to zero. The system of PDEs is formulated in a low-Mach-manner and solved using the merged PISO[87]-SIMPLE[137] algorithm described in Section 4.2.3. The subgrid fluxes in the momentum equation are taken into account using the σ-model [129], whereas the subgrid scalar fluxes are modeled based on the Reynolds analogy (see Equation 3.19). The Schmidt number Sc and the subgrid-scale Schmidt number Sc_{sgs} are both set to 0.7. The diffusion in scalar space in the stochastic field equations is taken into account through the IEM micro-mixing model [199, 60, 39, 133] as introduced in Equation 3.60, where the micro-mixing frequency is computed through Equation 3.61. Regarding the numerical schemes, a second-order implicit backward time integration scheme has been applied to all fields with exception of the stochastic field equations, for which the first order Euler implicit scheme has been used due to the stochastic nature of these equations. The advective momentum fluxes are discretized using the blended scheme with filtering of the high frequency modes described in Section 4.1.1. The convective scalar fluxes are treated using the Minmod flux-limiter scheme [167].

The cylindrical computational domain is shown in Figure 7.1b. It consists of approximately 1.9 million hexahedral control volumes. The mesh ranges 65 central jet diameters

in axial and 12 jet diameters in radial direction. Note that for this study, no influence of the spatial resolution (so-called grid-dependency) study has been performed. As discussed in [115], the spatial resolution is similar to the one employed in [25], where no strong influence of the spatial resolution has been observed. Likewise, the present investigation assumes that the grid-dependency of the results is small. Note that similar observations have been made in [200] by comparing two grids consisting of 1.2 and 5.2 Million cells (even though the dimensions of the computational domain were larger than in the present study). Additionally, as it is shown in the results section of this chapter, the contributions of the subgrid to the temporal statistics appear reasonable in the context of LES.

As can be observed in Figure 7.1b, a considerable part of the main jet upstream of the burner exit is included in the computational domain ($6D$). Similarly to the simulations of the Darmstadt Stratified Burner cases shown in the previous chapter, this is done to allow valuable flow conditions at the burner exit plane. The fully developed turbulent flow assumed for the main jet is generated through a mapping of the velocity profile at the burner exit onto the inflow plane. The weak velocity fluctuations measured in the pilot stream are approximated by superimposing random components to the mean velocity field. The wind-tunnel coflow has been assumed laminar. For the near-wall region, the wall function formulation by Spalding [192] has been applied. At the domain sides and at the outflow, a velocity inlet/outlet condition is used, which emulates any entrainment effect of the jet flame on the surrounding coflow.

The Bilger mixture fraction [14] is used in the lookup-table generation process in order to be consistent with the definition used in the experiments [8]. Accordingly, the Bilger mixture fraction is also transported in the simulations. Note that subsequently, all mentions of the mixture fraction in this chapter refer to the Bilger mixture fraction, which is set to unity in the central jet and zero in the coflow. The pilot flame is simplified to a methane-air flame with the same equivalence ratio as in the experiment ($Z_{Bilger} = 0.27$). For the progress variable, a linear combination of the mass fractions of CO_2, H_2 and H_2O following Equation 3.31, as proposed by [200], is used. Since central jet and coflow are both in an unburnt state, PV is set to zero in both streams. The progress variable value in the pilot has been set such that the experimentally determined temperature of 1880 K is matched.

The simulations are performed using 4, 8, and 16 stochastic fields which are subsequently respectively denoted as ESF(4), ESF(8), and ESF(16). All simulations are initialized using a simulation without any subgrid TCI model and run for approximately 60 ms. Thereafter, the simulations were run for another 300 ms to allow meaningful temporal statistics.

7.3 Results

In this section, the results obtained using the Eulerian stochastic field method are compared with available experimental data. For this purpose, both temporal statistics and results in mixture fraction space at various axial positions are juxtaposed experimental measurements.

7.3.1 Evaluation of Radial Profiles

First, the flow field statistics are considered, which are presented in Figure 7.2. The figure is subdivided into four columns, corresponding to the time averaged axial velocity, its standard deviation, radial velocity and the radial velocity rms, respectively. The comparison

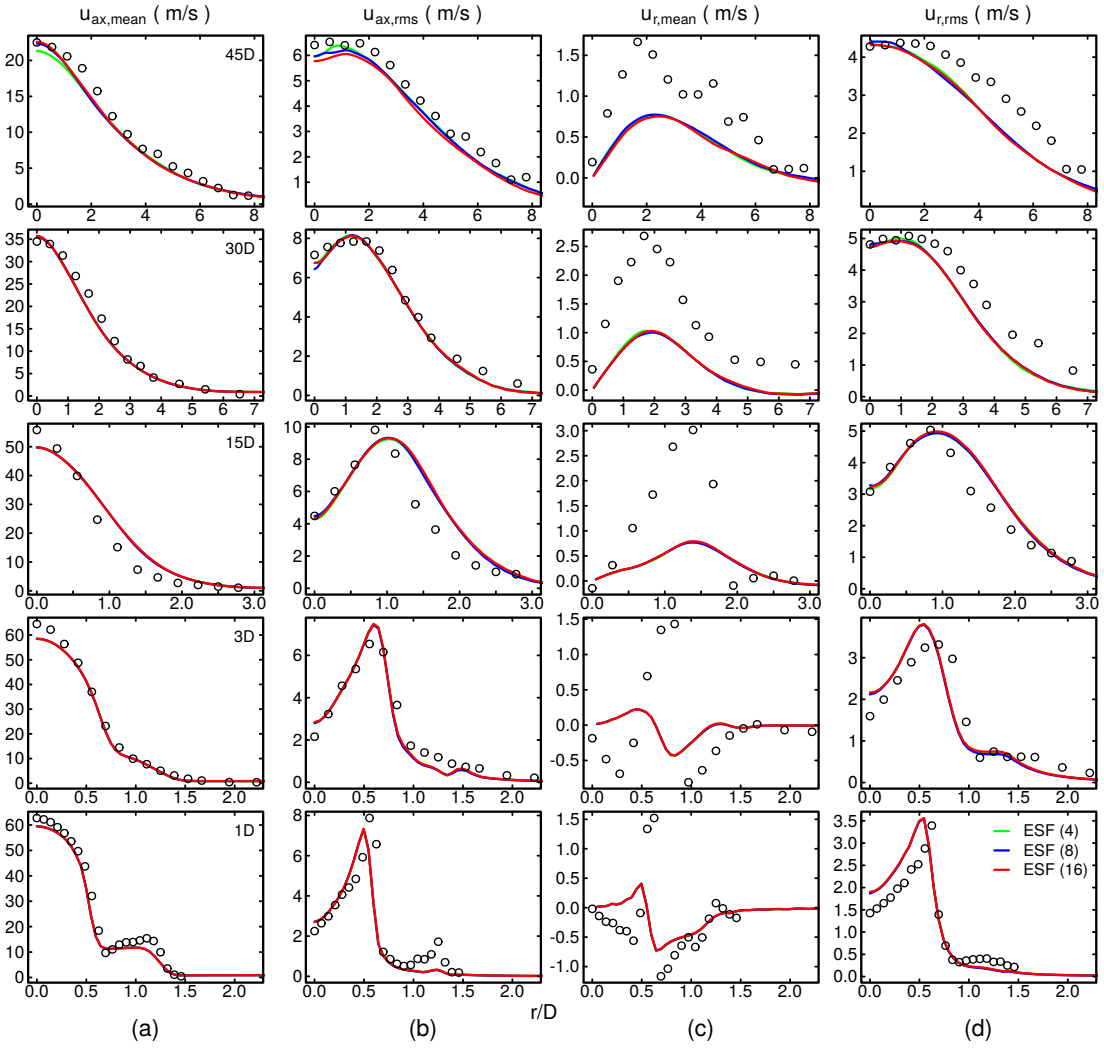

Figure 7.2: Comparison of experimental data with simulation results for the Sandia Flame D: mean and rms values of axial and radial velocities component at different axial positions.

with experimental measurements is performed by means of radial profiles at several axial position, all of which expressed as multiples of the central jet diameter D. Each row of the figure corresponds to one specific position downstream of the burner exit. Starting with the temporal statistics of the axial velocity shown in Figures 7.2a and 7.2b, it can be seen that the experimental trends are well reproduced. Even though the centerline mean axial velocity is slightly underestimated at the lowest axial positions, the rms profile suggest that the shear layer between the fast central jet and the slower pilot stream is well captured. The deviations between simulation and experiment appear to be most significant at 15 diameters downstream of the burner exit, where the simulation predict a broader profile for both mean and rms of the axial velocity component. This discrepancy is probably resulting from the small differences in the velocity profiles at the burner exit plane, which apparently yield a faster spreading of the turbulent jet in the LES. Further downstream, almost no differences between simulations and experiment can be perceived. This is not the case for the radial component of the velocity shown in Figures 7.2c and 7.2d. The discrepancies are especially pronounced for the temporal averages, which seem underpredicted at all axial positions. However, it should be noted that similar deviations

have been observed by many different researchers [116, 25]. Besides noticing these differences in the radial velocity averages, it remains difficult to draw a conclusion on the cause of such discrepancy. In contrast, the standard deviation only seems slightly over-predicted around the centerline at lower axial distances. The results seem to improve as the distance from the burner exit increases. In regard of the impact of the number of stochastic fields adopted, it can be stated that the number of stochastic fields does not seem to have an impact on the flow field predictions, at least in the range considered in this study.

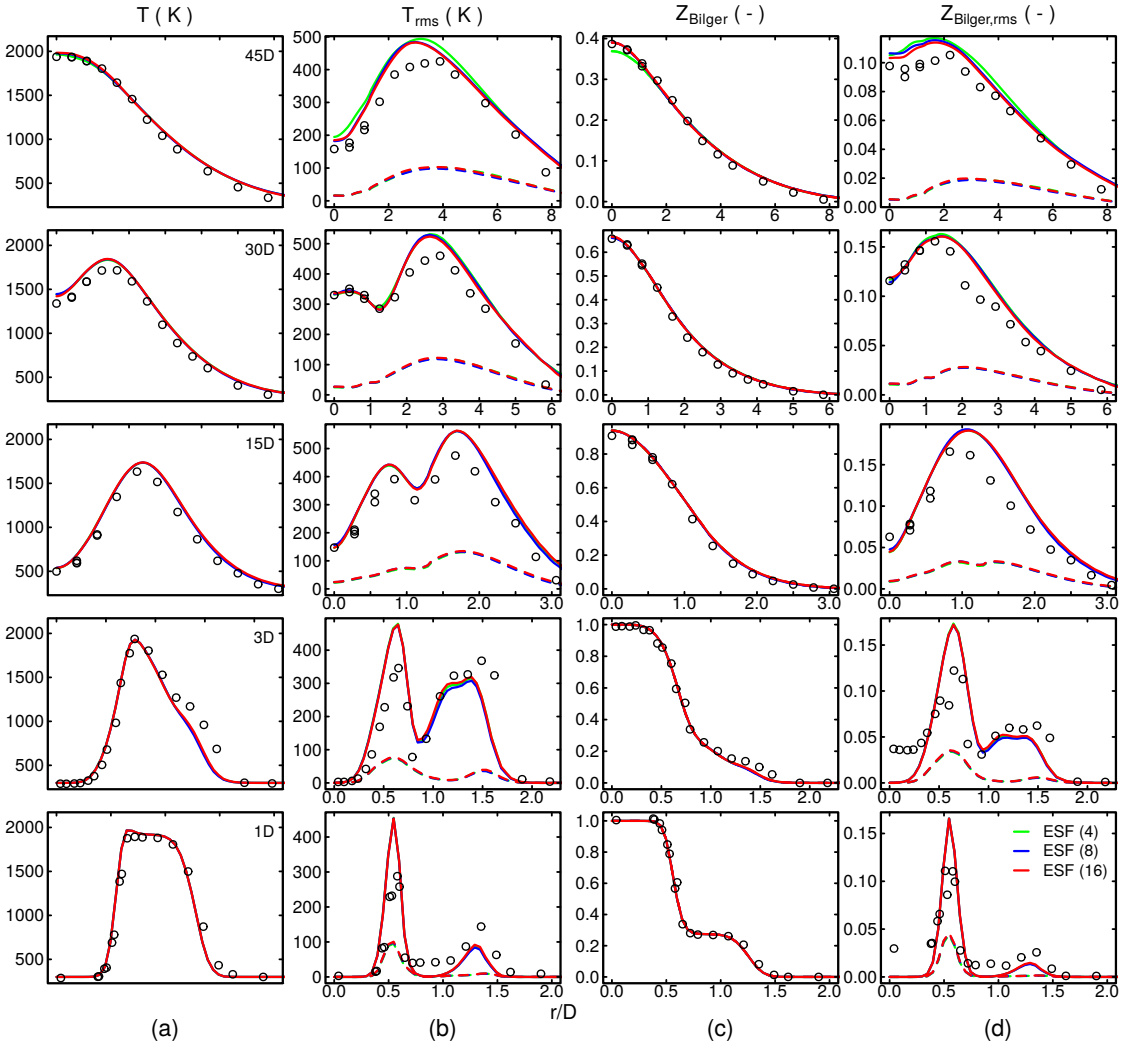

Figure 7.3: Comparison of experimental data with simulation results for the Sandia Flame D: mean and rms values of temperature and Bilger mixture fraction at different axial positions. In (b) and (d), the solid lines represent the total (resolved + subgrid), while dashed lines depict the subgrid contribution to the standard deviation.

Next, the radial profiles of temperature and mixture fraction shown in Figure 7.3 are discussed. Considering the average of temperature and mixture fraction shown in the first and third column, one can observe an excellent agreement of the numerical predictions and the experiments at all axial distances. Going over to the rms profiles, for which the total (resolved and subgrid, solid line) and only subgrid (dashed line) are shown, the ESF results are not far of the measurements. For instance, the double peak in the temperature rms observed in the experiment at $x = 15D$ is well reproduced by the simulations. Considering

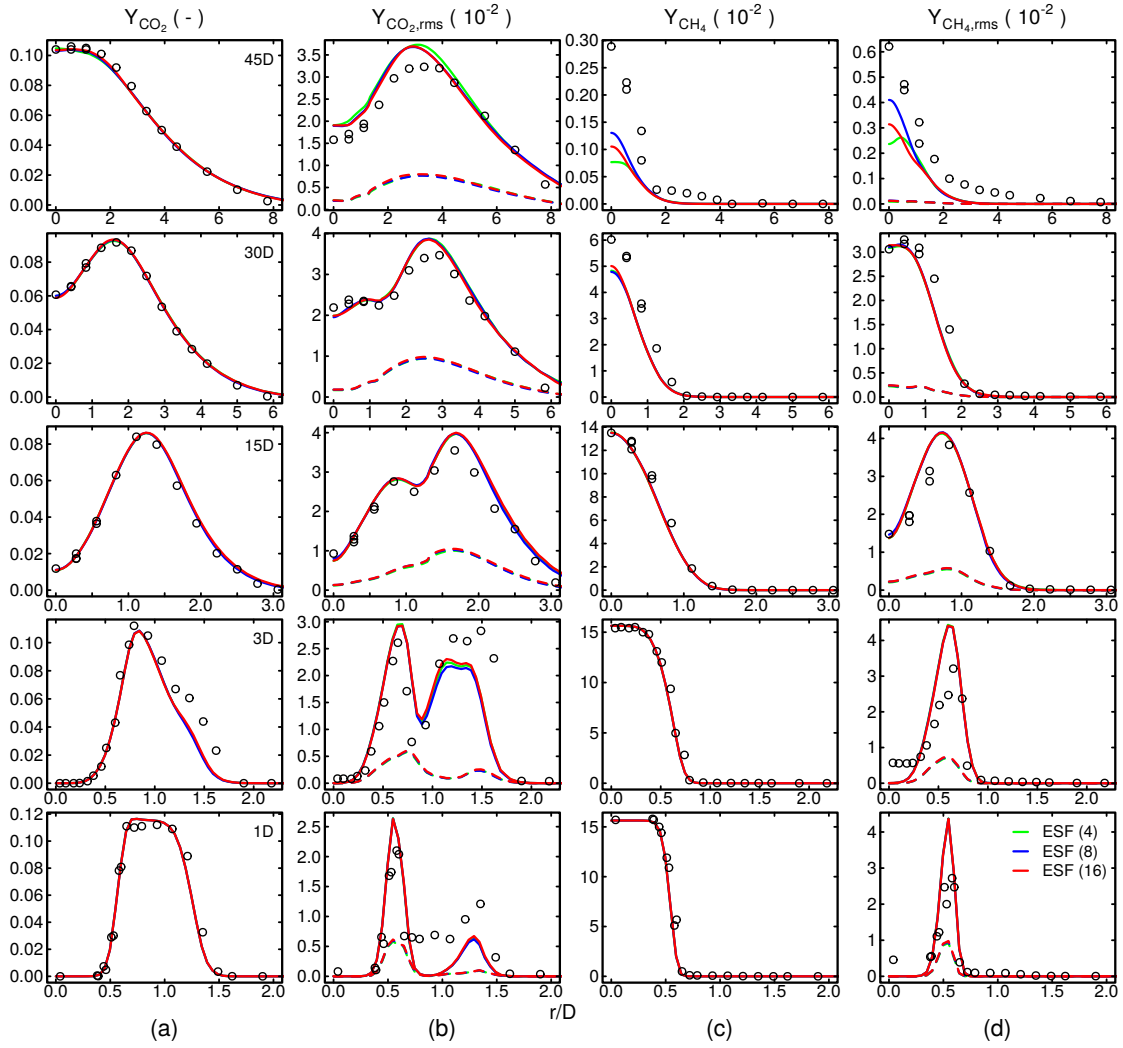

Figure 7.4: Comparison of experimental data with simulation results for the Sandia Flame D: mean and rms values of the CO_2 and CH_4 mass fractions at different axial positions. In (b) and (d), the solid lines represent the total (resolved + subgrid), while dashed lines depict the subgrid contribution to the standard deviation.

the mixture fraction rms profile at the two lowest axial positions, the results suggest that the simulations are underpredicting the centerline rms-measurements. This is unexpected, since the mixture exiting the central jet is supposed to have a constant value $Z_{Bilger} = 1$. Additionally, an interaction of the pilot gases with the inner jet region is highly unexpected at this axial position, which is confirmed by the corresponding temperature mean and rms profiles. To complete the analysis, similar temporal statistics are presented in Figure 7.4 for the CO_2 and the CH_4 mass fractions. Looking at the radial profiles of the temporal averages shown in Figures 7.4a and 7.4c, the ESF results excellently agree with the experimental measurements. Only at the two most downstream positions, small differences can be perceived in the case of methane. However, these deviations appears acceptable considering the overall order of magnitude of the CH_4 mass fraction at these locations. In regard of the standard deviation profiles of the methane mass fraction shown in 7.4d, the same centerline underpredictions as observed for $Z_{Bilger,rms}$ can be perceived. The differences reduce as the distance from the burner exit increases. In the case of CO_2, good

agreement between all simulations and the experiments can be perceived downstream of the position $x = 15D$. It can be observed that in direct proximity of the burner head, the mass fraction rms appears underpredicted, even though the positions of the rms peaks are well predicted. This is probably caused by the simplifying assumptions made in the simulations, mainly due to the turbulent inlet boundary condition which is apparently unable to reproduce the non-uniform flow downstream of the flame-holder placed in the pilot stream. As for the temporal velocity statistics discussed above, the results suggest that the number of stochastic fields is not strongly affecting the first and second moments of the temporal statistics for both, resolved and subgrid components.

7.3.2 Evaluation of Mixture Fraction Conditioned Data

In a second step, the simulation results using 16 stochastic fields are compared with experiments in mixture fraction space. This is done for the temperature in Figure 7.5 and CO_2 mass fraction in Figure 7.6. The comparison is performed at the three axial positions $15D$, $30D$ and $45D$ downstream of the burner exit.

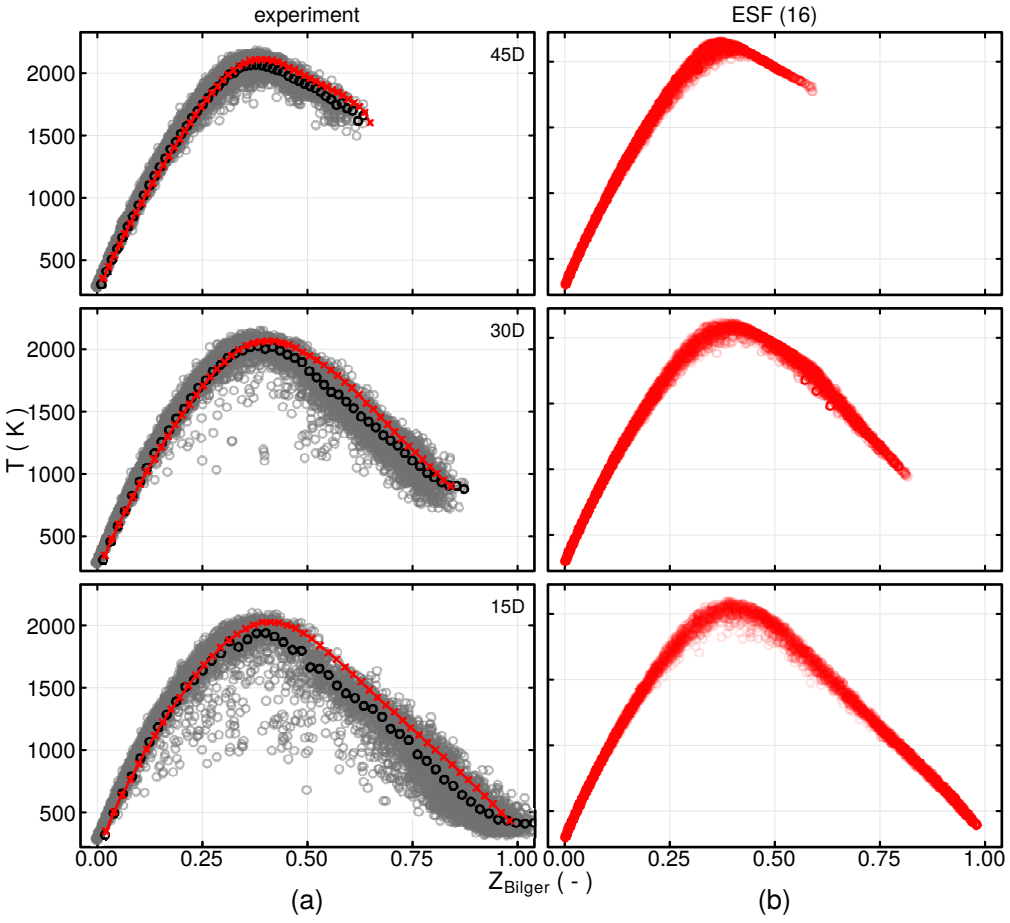

Figure 7.5: Comparison of scatter plots of (a) experimental data with (b) simulation results for the Sandia Flame D obtained using 16 stochastic fields: temperature plotted against mixture fraction at 15, 30 and 45 jet diameters downstream of the burner exit. Additionally, conditional averages for the experiment (black circles) and simulation (red crosses) are shown in (a).

Starting with the temperature, no strong differences can be observed between the experiments and the simulations. Nonetheless, the plots reveal that in the case of the experiment, the temperature is subject to stronger variations in mixture fraction space. This is most pronounced at the lowest axial position considered, where low temperature outliers have been measured, which are not captured by the simulation. This also results in a higher conditional average profile for the simulation in Figure 7.5a. As also discussed in [84], the low temperature events measured indicate local extinction of the flame, which is not taken into account when using a thermochemical lookup-table based on steady state flamelets (as done here). The reason for this is that in the so-called steady flamelet concept, only the stable burning branch is considered [83]. Therefore, the deviations can be attributed to the tabulation strategy. The experimental measurements indicate that such extinction events are less likely to occur at higher distances, which is consistent with the better approximation of the simulation at these positions. The weakness of the present strategy appear less pronounced when considering similar results for the CO_2 mass fraction shown in Figure 7.6. Even though the experimental results feature a broader distribution, the conditional averages obtained from the simulation are in excellent agreement with the experimental data. The only exception is the region $Z_{Bilger} > 0.5$ at the most downstream position where, similarly to [84], minor deviations are perceived.

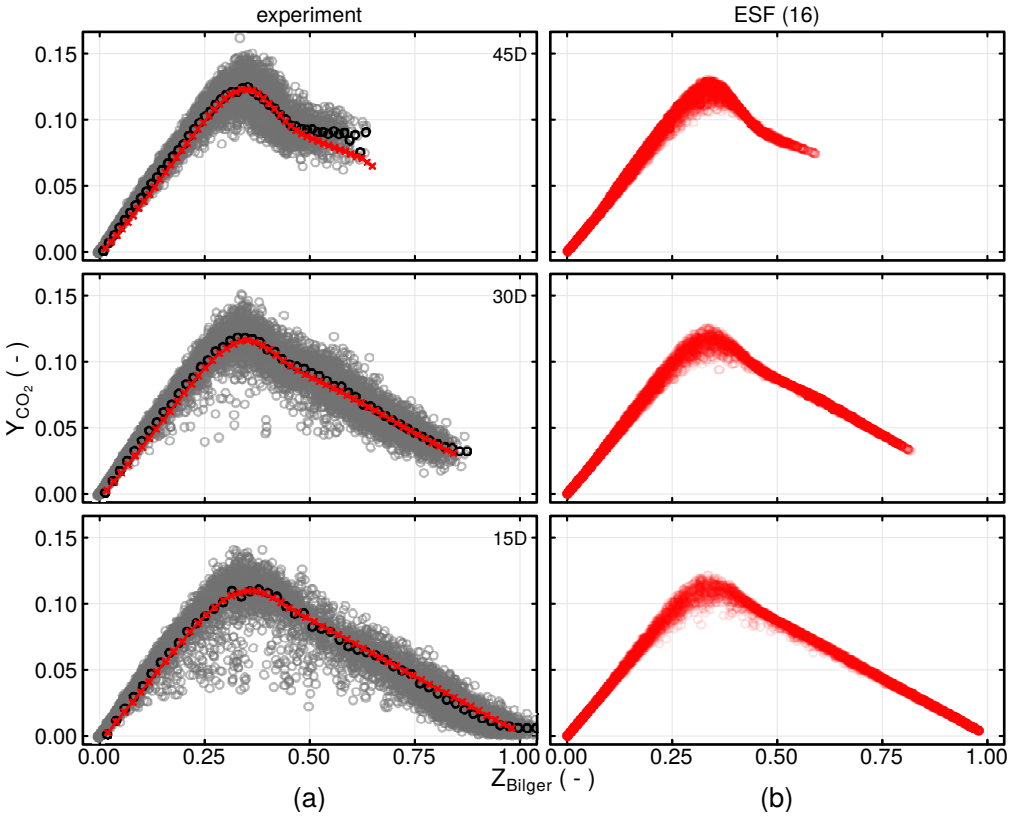

Figure 7.6: Comparison of scatter plots of (a) experimental data with (b) simulation results for the Sandia Flame D obtained using 16 stochastic fields: Y_{CO_2} plotted against mixture fraction at 15, 30 and 45 jet diameters downstream of the burner exit. Additionally, conditional averages for the experiment (black circles) and simulation (red crosses) are shown in (a).

7.4 Summary and Conclusions

The aim of this chapter was to demonstrate that the implemented ESF method is working as expected in the context of LES coupled to tabulated chemistry. For that purpose, the well known Sandia Flame D configuration was chosen due to its well defined boundary conditions and the extensive database available for validation purpose. The results can be summarized as follows: (1) the (temporal) velocity and scalar statistics measured are well captured by the ESF approach. In this regard, it was shown that (2) the simulation results are not sensitive to the number of stochastic fields adopted. (3) The subsequent comparison of mixture fraction conditioned data demonstrated that the thermochemical state accessed at runtime is in good agreement with the experimental data, at least for temperature and the mass fraction of carbon dioxide. However, it has also been shown that the present tabulation strategy reaches its limit in the face of local extinction events. These overall satisfying results justify the further application of the framework to investigate its prediction ability in the context of spray combustion.

PART IV: VALIDATION AND APPLICATION TO TURBULENT REACTIVE MULTIPHASE FLOWS

Chapter 8

Influence of the Thickening Factor Treatment on Predictions of Spray Flame Properties using the ATF Model and Tabulated Chemistry

So far in the present thesis, the ATF-FGM approach has only been applied to LES of purely gaseous combustion. This chapter goes one step further and shows the application of this modeling technique to compute a dilute ethanol spray flame. Additionally, the different strategies to account for the heat and mass transfer between liquid droplets and their carrier phase within the artificially thickened flame approach are analyzed and compared. Both approaches previously introduced in Section 3.2.4, referred to as projection and refraction correction, are compared to state-of-the-art methods in LES of a complex turbulent spray flame. The advantage of both approaches have been clarified in Section 5.2.3 for a simple two-dimensional test-case. However, it remains to be shown how the approach perform in a more complex configuration. The investigated spray flame corresponds to the operating condition EtF6 of the Sydney Spray Burner [70, 69, 120]. It is worth mentioning that this configuration constitutes a test case within the Workshop on Turbulent Combustion of Sprays (TCS, `www.tcs-workshop.org`).

The Sydney Spray Burner was numerically investigated by many different groups [30, 77, 78, 173, 166, 37] as it provides an extensive experimental database for model validation as well as a reduced modeling effort due to the dilute nature of the spray. Chrigui et al. [30] performed LES of the ethanol flames EtF3 and EtF8 using an Euler-Lagrange approach coupled to tabulated chemistry and a presumed PDF-based turbulence combustion interaction model. Rittler et al. [166] validated an approach combining a presumed PDF method, artificial thickening and tabulated chemistry for the cases EtF3, EtF6, and EtF8 and evaluated the impact of the chosen sub-filter distributions. Heye et al. [77] numerically investigated the spray flame EtF1 using LES combined with a Lagrangian Monte-Carlo approach for the flame-turbulence interaction. A valuable contribution is the work by Heye et al. [78], where the authors compared simulations performed by four different research groups for the flames EtF2 and EtF6. The simulations featured—besides diverse numerical treatments and codes—different spray injection strategies, turbulence modeling, evaporation modeling, chemistry treatment and turbulence chemistry interation modeling, including FGM with presumed and transported PDF methods. The authors pointed out that the determining factors are: (1) The inflow conditions chosen for the spray, (2) the evaporation modeling as well as (3) the representation of the complex chemistry and the turbulence-flame interaction model. To mention are also the closely related publications

by Sacomano et al. [171, 172]. In the former, the influence of the evaporative cooling effects was investigated and a flame wrinkling sensitivity study for the spray flame EtF5 was performed, whereas in [172], a dynamic formulation for the flame wrinkling modeling is proposed and validated for the configuration EtF2. An excellent introduction and classification of the different operating conditions of the Sydney Spray Burner can also be found in [70] and [170].

When it comes to the application of the ATF model in LES of turbulent spray combustion, there are few contributions. Work in this field was notably carried out by Cheneau [28] and Cheneau et al. [29], who applied this method in a swirled combustor. These works are based on the contributions of Boileau [21] and Paulhiac [139]. The contribution by Sacomano et al. [175] is also of importance; this involves a numerical investigation of a lean partially prevaporized spray flame. Further applications of this approach can be found in [166, 170, 171, 171, 172]. However, all these contributions generally differ in their strategy for representing the interaction of the droplets with the thickened flame.

The objectives of this chapter, which is based on the results obtained by Dressler et al. [44], is to spread awareness towards the complexities that arise by combining flame thickening approaches with an additional dispersed phase. As is demonstrated subsequently, the treatment of the interaction of droplets and the thickened flame has a significant effect on the overall simulation results. Additionally, the two proposed formulations for the correction of droplet heat and mass transfer which take into account alignment of droplet movement and flame front orientation are set aside state-of-the-art methods.

The rest of this chapter is structured as follows: first, the investigated configuration is introduced. The subsequent section presents a brief summary of the numerical methods adopted. Thereafter, the LES results for the EtF6 spray flame are presented and discussed. Especially, emerging differences caused by the various strategies introduced to treat droplet heat and mass transfer in the presence of a thickened flame are clarified. This is performed in terms of instantaneous contour plots as well as radial profiles of time-averaged quantities of interest for both, the carrier and the dispersed liquid phase. Finally, the achievements are discussed and summarized in the conclusions section.

8.1 Experimental Configuration

The operating condition EtF6 of the well known Sydney Spray Burner [70] is investigated, which is schematically shown in Figure 8.1a. The burner consists of three concentrically arranged streams. The spray is generated using an ultrasonic nebulizer placed almost 21 jet diameters upstream of the burner exit. The droplets are then transported downstream in the central pipe with a diameter $D = 10.5\,\mathrm{mm}$. The central jet is surrounded by an annular pilot consisting of burnt products resulting from a stoichiometric acetylene-hydrogen-air reaction. The burner is centered in a primary coflow with a diameter of 103 mm. The coflow is composed of pure air with an exit bulk velocity of $4.5\,\mathrm{m\,s^{-1}}$. The burner and coflow are placed in a wind tunnel with a cross section of 290 x 290 mm with same composition and velocity as the primary coflow. For the operating condition investigated, two experimental data sets exists, namely A and B (see Table 8.1). Even though both sets delivered similar results, some deviations exist, thus providing an initial estimate of the experimental uncertainties. Additionally, radial velocity measurements are only available for experimental set B [70, 1]. The velocity and droplet size data were obtained through phase Doppler anemometry (PDA) [70], whereas radial temperature measurements were performed at three axial positions using thermocouples [69, 120]. Additionally, qualitative planar OH-LIF, CH_2O-LIF measurements for the carrier phase and Mie-scattering for

droplet visualization are presented in [69]. Further information regarding the burner and the experimental setup can be found in [70, 69, 121].

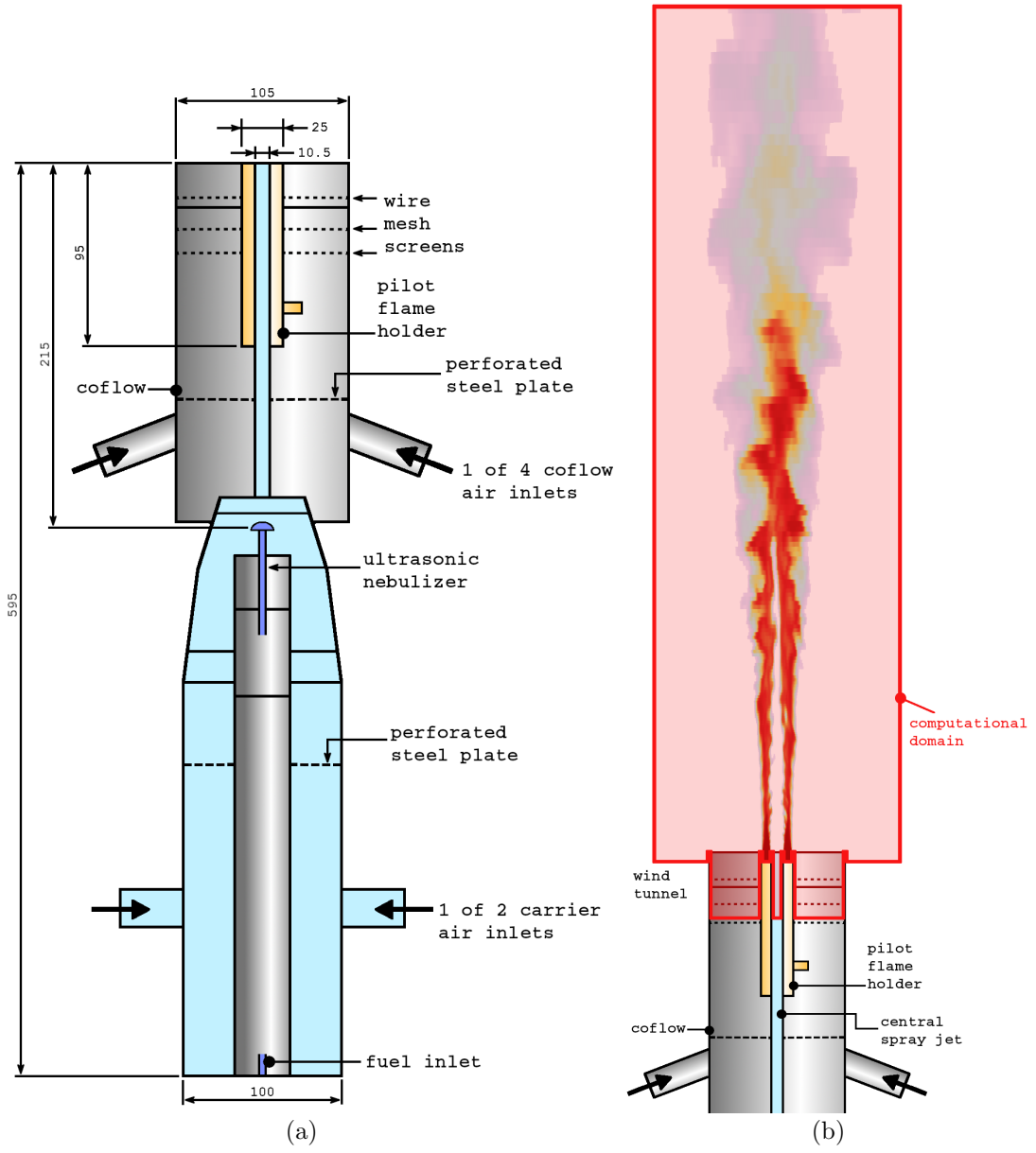

Figure 8.1: (a) Schematic representation of the Sydney Spray Burner geometry [70] and (b) of the computational domain used.

8.2 Numerical Setup

Similar to all studies presented in this work, the investigations are performed using the finite volume open-source C++ code OpenFOAM [92], including the low-Mach number modification described in Section 4.2.1. Dealing with reacting turbulent two-phase flows in the context of ATF and tabulated chemistry, the carrier phase motion is represented by the Favre-filtered transport equation for mass, momentum, reaction progress variable

Operating conditions	EtF6	
	exp. A	exp. B
Bulk jet velocity (m/s)	36	36
Jet Reynolds number	27,400	27,400
Overall equivalence ratio ϕ	1.8	1.8
Carrier mass flow rate (g/min)	225	225
Liquid fuel injection rate (g/min)	45	45
Liquid flow rate at jet exit (g/min)	41.3	41.1
Vapor flow rate at jet exit (g/min)	3.7	3.9
Equivalence ratio at jet exit ϕ_{jet}	0.15	0.2

Table 8.1: Operating conditions for the investigated case [70, 1].

and mixture fraction (Equations 3.98, 3.99, 3.100 and 3.101). The progress variable is defined according to Equation 3.29 as linear combination of the CO, CO_2 and H_2O mass fractions. The combustion modeling is realized by coupling the chemistry tabulation approach based on the FGM method [196] to the artificially thickened flame model [22]. A projection of the thermochemical lookup-table, which is built from one-dimensional freely propagating premixed flamelets assuming a Lewis number of unity, is shown in Figure 3.2. The unresolved turbulent fluxes, which are incorporated through the subgrid scale stress tensor τ_{ij}^{sgs} are modeled using the σ-eddy-viscosity model [129]. The scalar subgrid-fluxes in the mixture fraction and progress variable transport equation are modeled following Equation 3.19, thereby setting the subgrid-scale Schmidt number equal to the Schmidt number ($Sc_{sgs} = Sc = 0.7$). In regard of the ATF model, the mixture-adaptive thickening procedure is adopted and coupled to Equation 3.47 for the flame sensor Ω, whereas the non-dynamic formulation by Charlette [26] is used for the efficiency function. As for the computations of purely gaseous flames, the second-order implicit backward time-stepping scheme has been applied to all field. The convective momentum fluxes are discretized using the blended scheme with filtering of the high frequency modes, whereas the Minmod flux-limiter is used for the convective scalar fluxes [167]. Both are described in Section 4.1.1.

The liquid phase is expressed in a Lagrangian manner as outlined in Section 3.2, where the evolution of computational parcels, each representing a multitude of real droplets having the same properties, is determined by the set of coupled ordinary differential equations for position, velocity, mass and temperature (Equations 3.67, 3.68, 3.94 and 3.95). The effective correction factor F_{eff} in Equations 3.94 and 3.95 is computed depending on the approach to describe the interaction of particles with the thickened flame (see Section 3.2.4). Following the previous investigations related to the evaporation model in Section 5.2.2, the approach by Miller (model M7 in [123]) is used to model heat and mass exchange between liquid and carrier phase.

In contrast to previous works [175, 170, 171], where the carrier gas is simplified as mixture of fuel and air, the strategy proposed in [174] is applied. The mixture surrounding droplets is assumed as compound of 8 species (see Table 8.2). In [174], it is shown that the combination of the 6 major species (CO_2, H_2O, H_2, CO, C_2H_5OH, and air (as a single species)), would be enough to represent the mixture. In that sense, the present approach applies the findings of [174] obtained from laminar flames propagating in droplet mists to turbulent combustion. However, using 8 instead of 6 in the present work results in no significant increase in computational costs. This leads to 8 additional fields that have to be

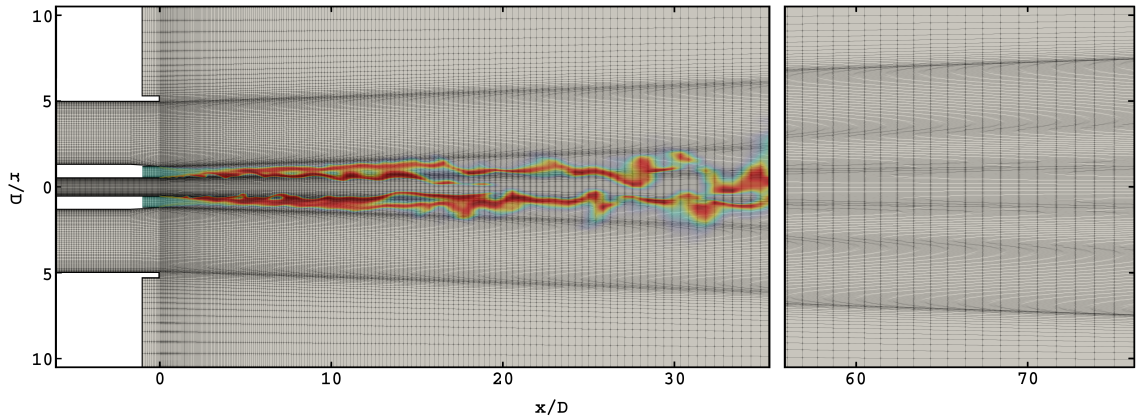

Figure 8.2: Representation of the computational domain used. The flame stabilization through the pilot and combustion reaction are illustrated by the OH mass fraction field.

stored in the thermochemical lookup-table. Note that other authors did already perform detailed mixture description in a turbulent context (e.g. [57, 113]).

species	C_2H_5OH	CO_2	H_2O	CO
	$f(\widetilde{Z}, \widetilde{PV})$	$f(\widetilde{Z}, \widetilde{PV})$	$f(\widetilde{Z}, \widetilde{PV})$	$f(\widetilde{Z}, \widetilde{PV})$
species	OH	O_2	H_2	N_2
	$f(\widetilde{Z}, \widetilde{PV})$	$f(\widetilde{Z}, \widetilde{PV})$	$f(\widetilde{Z}, \widetilde{PV})$	$1 - \sum_{i \neq N_2} Y_i$

Table 8.2: Carrier mixture approximation as perceived by the disperse phase.

To get an initial idea of the dimensions of the computational domain, it is shown in relation to the burner exit in Figure 8.1b. A more detailed representation of the mesh structure is provided in Figure 8.2. The cylindrical computational domain consists of 4.3 million hexahedral control volumes. It ranges 75 jet diameters downstream in axial and 10.5 diameters in radial direction. Therefore, the secondary coflow, i.e. the wind tunnel coflow, is only partially included in the computational domain. A section of 6 jet diameters upstream of the burner exit is included for the central jet to generate valuable conditions at the burner exit plane. Here, a fully developed turbulent flow, attained with a recycling method, is assumed for the central jet which is in agreement with [70, 121]. Figure 8.3a presents an a-priori analysis of the velocity profile at the burner exit plane for EtF6. The fully developed turbulent pipe flow assumed in the simulations has been approximated by a power law profile with an exponent $n = 7$

$$u = u_{bulk} \frac{(n+1)(2n+1)}{2n^2} \left(\frac{D/2 - r}{D/2} \right)^{1/n}. \tag{8.1}$$

Thereby, u_{bulk} refers to the bulk velocity and r the radial distance from the jet center. The gray line in Figure 8.3a indicates that the velocity profile is underestimated when using the bulk velocity specified in Table 8.1. At the same time, a least square fit reveals that a higher bulk velocity is needed to match the experimental profiles. Consequently, the bulk velocity is adjusted to better match the experiment at the burner exit plane (the value used in the simulations can be taken from Figure 8.3a).

The pilot and wind tunnel inflows are considered laminar while random turbulence is applied for the primary coflow. In difference to the experiment [70] and similarly to [30, 37],

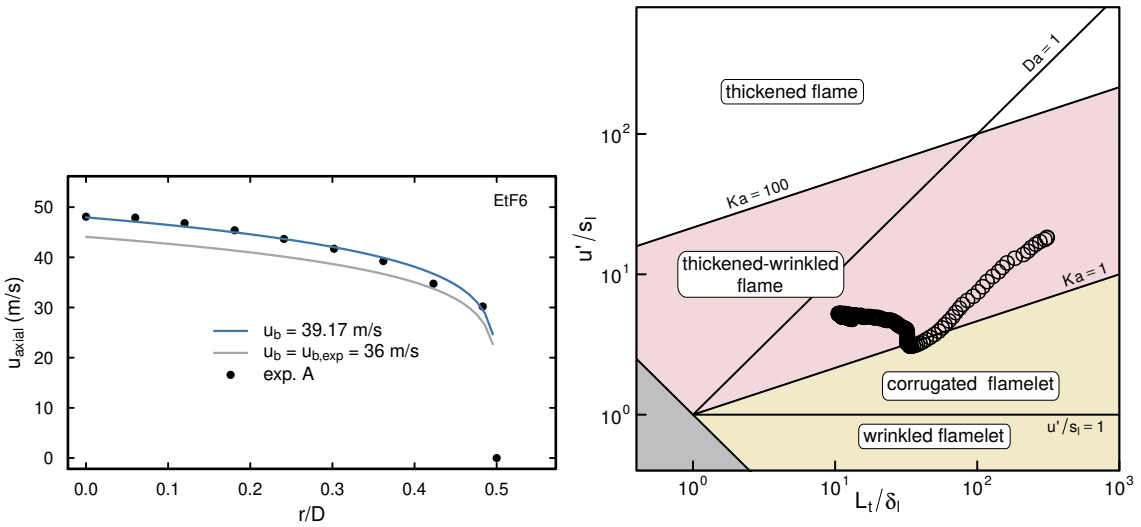

(a) (b)

Figure 8.3: (a) Comparison of power law profiles with experimental velocity data at the burner exit plane (only set A is displayed). (b) Turbulent premixed combustion diagram by Peters [141] alongside EtF6 simulation data.

the present work simplifies the pilot flame as stoichiometric ethanol-air flame. In order to keep the computational cost of the LES reasonable, the near wall regions are modeled through the near wall formulation by Spalding [192]. All further boundary conditions are set to total pressure boundaries, hence enabling the entrainment of the surrounding flow.

The dispersed phase is injected at the axial position $x = 0.3D$ corresponding to the first axial plane measured in the experiments. In this context, a size distribution conditioned on the injection position, obtained from experimental set A [1], is applied. The dispersed phase velocity at injection was simplified to the carrier velocity interpolated at the droplet injection position. It should be noticed that the employed injection strategy assumes an equal mass for all injected parcels. This results in a number of real droplets represented by computational parcels varying from parcel to parcel. The parcel mass at injection is estimated beforehand in order to obtain a computationally affordable number of simultaneously tracked parcels. This number varies from around 2.2 to 2.9 million, depending on the modeling approach employed. By using this strategy, it is also possible to inject parcels representing less than 1 real droplet. This is the case for droplets with larger diameters.

The simulations are first initialized from a non-reacting flow and run for around 0.1 s, which corresponds to approximately 60 jet pipe flow through times, to allow the turbulence in the central jet to develop. Subsequently, the pilot is ignited and simulations are run for another 0.05 s before starting with the liquid injection. Thereafter, the simulations continued running for another 0.1 s before averaging was started. All simulations are averaged over a time period of at least 0.15 s. Additionally, to reduce averaging time, all carrier phase properties shown here are averaged in circumferential direction.

Before looking into the results and their discussion, a critical assessment of the chosen modeling strategy is performed. Some simplifications are made, some more important than others and these shall be discussed. First, since a two-dimensional lookup-table is used, only effects of chemical reaction and mixing are taken into account. Thus, heat losses due to evaporative cooling of the liquid phase are not considered. Beside extending

the thermochemical lookup-table to a third dimension, a possible alternative could be to incorporate the effect of heat losses through linearization of a transported energy variable, as done by Franzelli et al. [57]. Another possibility is to consider the evaporative cooling effect as done by Knudsen et al. [104], which is based on the assumption that all fuel in the fresh mixture originates from droplet evaporation (and based on a Lewis number of unity). By setting the enthalpy of the fresh mixture in the generation of the various flamelets accordingly, it is possible to construct a thermochemical lookup-table that takes liquid evaporation into account. Lately, Sacomano Filho et al. [171] demonstrated that the consideration of evaporative cooling delivers better agreements with experiments than when it is neglected. The impact was investigated for case EtF5 of the Sydney Spray Burner and it was shown that the effect is not pronounced. Nevertheless, in order to focus on the investigated modeling aspects and to avoid the introduction of additional uncertainties, an adiabatic strategy as employed in previous works is used [42, 170, 175, 173, 172]. At that point, it should also be noted that since the employed table consists of purely premixed flamelets, deviations can be expected in diffusion flame mode dominated regions [56, 200]. For the combustion of sprays, this was discussed in [82] with acetone as fuel. It was shown that both regimes, namely premixed and diffusion flames, may coexist for various operating conditions of the investigated Sydney Spray Burner. Another uncertainty is related to the employed efficiency function formulation used to take into account the unresolved flame wrinkling. Here, the common definition by Charlette et al. [26] is adopted due to its broad applicability. However, an adjustment of the exponential factor β may influence simulation results substantially, as demonstrated recently in the sensitivity study by Sacomano Filho et al. [171]. Alternatively, a dynamic formulation as presented in [172] may be applied. To solely focus on the effect of the thickening factor treatment, the coupling of such dynamic modeling of E is not considered.

In view of these simplifications, it should be noted that deviations with experimental data are expected. The comparison with experiments shall, however, guide the present analysis and assist the following interpretation and discussion of the results.

8.2.1 Characterization of the Flame Regime

Going one step ahead of the analysis, the simulation results obtained by Dressler et al. [43] have been used to characterize the flame regime. Thereby the characterization is based on the assumption that the flame burns predominantly in a premixed mode, a simplifying assumption in the context of spray combustion where both, premixed and diffusion type flames can be expected. The present classification should therefore rather be understood as an estimation. The characterization is based on the evaluation of the characteristic turbulent length scale $L_t \approx k^{3/2}/\varepsilon$ [154], where the turbulent kinetic energy and turbulent energy dissipation rate are computed through

$$\langle k \rangle = \frac{1}{2} \left\langle \widetilde{u}_i' \widetilde{u}_i' \right\rangle + \langle k_{sgs} \rangle \qquad \text{and} \qquad \langle \epsilon_k \rangle = - \left\langle \overline{\tau}_{ij}' \frac{\partial \widetilde{u}_i'}{\partial x_i} \right\rangle + \left\langle \epsilon_{k_{sgs}} \right\rangle . \tag{8.2}$$

By using the inertial subrange theory, the unresolved turbulent kinetic energy and its dissipation rate can be calculated as $\langle k_{sgs} \rangle = \langle \nu_{sgs} \rangle^2 \, / \left(\Delta^2 C_K^2 \right)$ and $\left\langle \epsilon_{k_{sgs}} \right\rangle = \langle \nu_{sgs} \rangle^3 \, / (\Delta^4 C_S^4)$, respectively, with $C_K = 0.094$ and $C_S = 0.17$ (see [163, 164]). The turbulent velocity fluctuation is then computed from the total turbulent kinetic energy. The representative length and velocity scale of the combustion process are expressed by the stoichiometric laminar flame thickness $\delta_l = 0.375\,\mathrm{mm}$ and flame speed $s_l = 0.305\,\mathrm{m\,s^{-1}}$. The results are shown in Figure 8.3b. Herein, the previously introduced Peters diagram is complemented

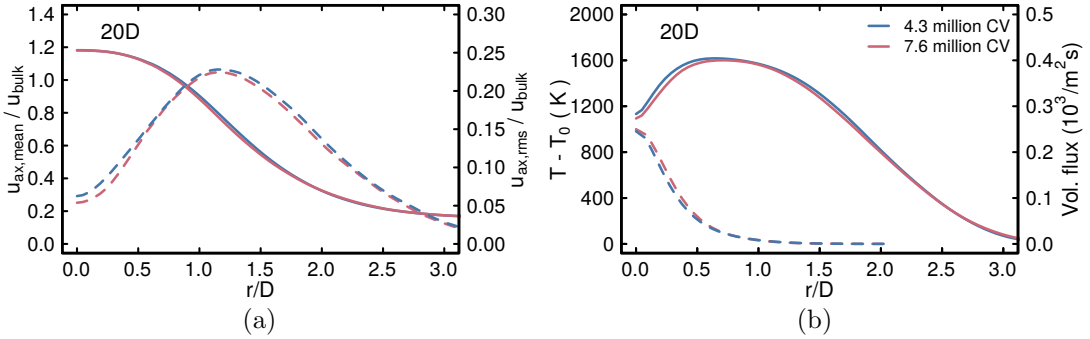

Figure 8.4: Radial profiles of various quantities at the axial distance $x = 20D$ for the two grids considered. (a) Mean (solid line) and rms (dashed line) of carrier axial velocity (b) Carrier temperature (solid line) and liquid volumetric flux (dashed line).

by scattered data obtained from the simulation at the centerline up to 30 jet diameters downstream of the burner exit plane. The turbulent quantities are therefore predominantly evaluated in the fresh gases. The figure shows that the majority of the points fall in the thickened-wrinkled flame regime slightly above the flamelet zone. As pointed out in Section 2.4.4, this does not necessarily discredit the adopted flamelet assumption [148, 197], as in the thickened flame regime, the turbulence seems to mainly affect the preheating zone, leaving the thin reaction zone unaffected. Interestingly, the present results agree well with the analysis based on experimental quantities performed by Sacomano Filho [170] for the flame EtF2, which features the same central jet bulk velocity but a higher liquid mass loading.

8.2.2 Impact of the Spatial Resolution

In order to quantify the impact of the spatial resolution on the results, a systematic grid sensitivity is carried out by using two numerical grids consisting of 4.3 and 7.6 million control volumes. To limit the computational costs, all simulations are averaged over a period of at least 0.1s and spatially averaged in circumferential direction. The projection correction proposed in this work is used for the particle-thickened flame interaction.

From Figure 8.4, some differences are perceivable, but the grid sensitivity does not seem significant when increasing the spatial resolution. This can be deduced from the radial profiles of mean and rms carrier axial velocity (Figure 8.4a) as well as the averaged temperature values (Figure 8.4b) obtained for both grids. Both are very close to each other. Similar conclusions can be drawn regarding the impact of the resolution on the liquid phase statistics, as indicated by the liquid volumetric flux profiles. Equivalent results are also obtained for other physical quantities and axial positions. This confirms that both grids are evenly appropriate to describe the physics of the configuration. Consequently, in order to allow accurate long-term statistics at reasonable computational expenses, the grid with 4.3 million control volumes has been selected for further analysis.

8.3 Results

Up to this point, the impact of the different approaches to represent the interaction of particles with a thickened flame has been only investigated in a generic configuration (see Section 5.2.3). In contrast, the present section clarifies their impact in a complex spray jet flame. First, the influence of the flame sensor formulation is briefly addressed. Thereafter,

the LES results for the EtF6 spray flame are presented and discussed. Especially, emerging differences caused by the various strategies introduced to treat droplet heat and mass transfer in the presence of a thickened flame are clarified. This is performed in terms of instantaneous contour plots as well as radial profiles of quantities of interest for both, the carrier and the dispersed liquid phase.

8.3.1 Influence of the Flame Sensor Formulation

The objective of this section is to briefly discuss (and justify) the choice of the flame sensor formulation. In Figure 8.5, which shows temperature contours with isolines of the flame sensor superimposed with computational parcels, some differences are observed between the formulation used in this work (i.e. Equation 3.47) and a standard formulation commonly used for purely gaseous combustion; the one initially proposed by Durand and Polifke [46] (Equation 3.46). While a different formulation for the flame sensor may impact combustion characteristics for single phase flows, it certainly does influence mixing and reaction processes in the presence of a liquid phase, if a thickening correction is applied [175]. The latter approach, shown on the left of Figure 8.5, detects the flame much earlier than the temperature rise, thus creating a region prior to the flame front, where carrier temperatures are still low, but where artificial thickening is already performed. Taking a look at Equations 3.94 and 3.95, it becomes clear that this circumstance causes a correction of droplet heat and mass transport in low temperature regions. Additionally, since the movement direction of the parcels is predominantly parallel to the flame front, droplets are likely to dwell longer in that region. Both factors are acting towards a reduction of heat and mass transfer between liquid phase and carrier in direct proximity of the flame front. Evidently, this also alters the mixture development of the carrier in flame front parallel direction. Following this line of thought, it can be assumed that the reduction of vapor release in this region influences the flame propagation because of this altered mixture evolution. In contrast to the formulation by [46] and as exhibited on the right of Figure 8.5, the onset of the thickening is much closer to the temperature rise for the definition of Ω used in this work, i.e. Equation 3.47. Hence, by using this formulation, it is likely to substantially reduce the previously described effect.

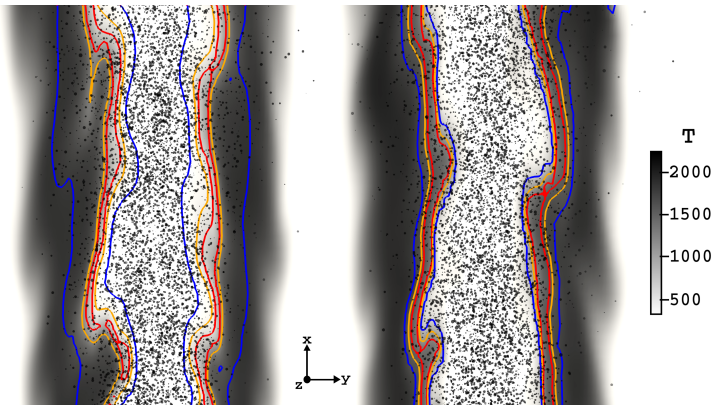

Figure 8.5: Contour plot of temperature with flame sensor isolines (Ω = 0.1 (—), 0.5 (—) and 0.8 (—)) superimposed with computational parcels for EtF6 at the axial position $x/D \approx 10$. Left: flame sensor by Durand and Polifke [46]; right: present formulation (Equation 3.47).

8.3.2 Modeling Assessment in the Turbulent Spray Flame EtF6

The impact of the modeling approaches previously investigated in a simple configuration are now assessed for the EtF6 spray flame. For the sake of clarity, the various approaches summarized in Table 5.4 are displayed again in Table 8.3. Each method addresses the droplet heat and mass transfer in the presence of a thickened flame differently. First, instantaneous contour plots of various scalar fields are shown and differences between the approaches discussed. This discussion is complemented by an analysis of radial profiles of temporal averages and rms values for velocity and scalar fields for both, the carrier and the liquid phase. Note that for all simulations performed, the maximum value of the thickening factor F does not exceed 10.

Modeling approach	Effective thickening factor calculation	Color coding
no correction	$F_{eff}^{none} = 1$	—
standard correction	$F_{eff}^{std} = F$	—
refraction correction	$F_{eff}^{refr} = F$ (+ tracking modification)	—
projection correction	$F_{eff}^{proj} =$ Equation 3.96	—

Table 8.3: Overview of the formulations investigated to represent the correction of heat and mass transfer of droplets interacting with a thickened flame for the EtF6 simulations.

The instantaneous contour plots of temperature, mixture fraction as well as OH and CO mass fraction fields for the standard, projection, and refraction correction are shown in the Figures 8.6, 8.7 and 8.8, respectively. Here, it should be mentioned that the species mass fractions are directly extracted from the thermochemical lookup-table, which may not be rigorous for species with higher chemical timescales [63]. However, the same chemistry treatment for all approaches makes at least a qualitative comparison possible. In direct proximity of the burner exit, no differences between the methods can be observed. In this region, the flame is predominantly found concentric to the main jet and does not propagate towards the centerline as the mixture of the central jet is below the lower flammability limit. As axial distance increases, the mixture evolves towards a flammable one since more fuel vapor is released from the droplets. This aspect summed up with the higher interaction of flame and turbulence allows the propagation of the reaction zone towards the jet centerline for all approaches. At this point, first differences between the various methods become evident. The standard and refraction approaches extend the central non-reacting core up to almost 30 jet diameters, while the projection procedure seems to produce a notably shorter cold core ($\approx 20D$). This disparity also results in what appears to be a shorter flame for the projection approach. A second observation is that all three approaches induce a different distribution of evaporated liquid, shown through the instantaneous contour plots of mixture fraction. First considering Figure 8.7b for the projection correction, some pockets of rich mixtures can be observed at lower axial positions. These richer regions are also present for the standard approach in Figure 8.6. However, they only appear at higher distances from the burner exit and seem less intense. Also noteworthy is the large region with noticeably higher mixture fraction values around $x/D = 25$ for the projection approach, which is narrower and located further downstream in the case of the standard correction. A completely different scenario is observed in Figure 8.8b for the refraction correction. Here, distinct layers of fuel rich mixtures are noticed at lower axial positions. These layers, which are spread over almost 15 jet diameters,

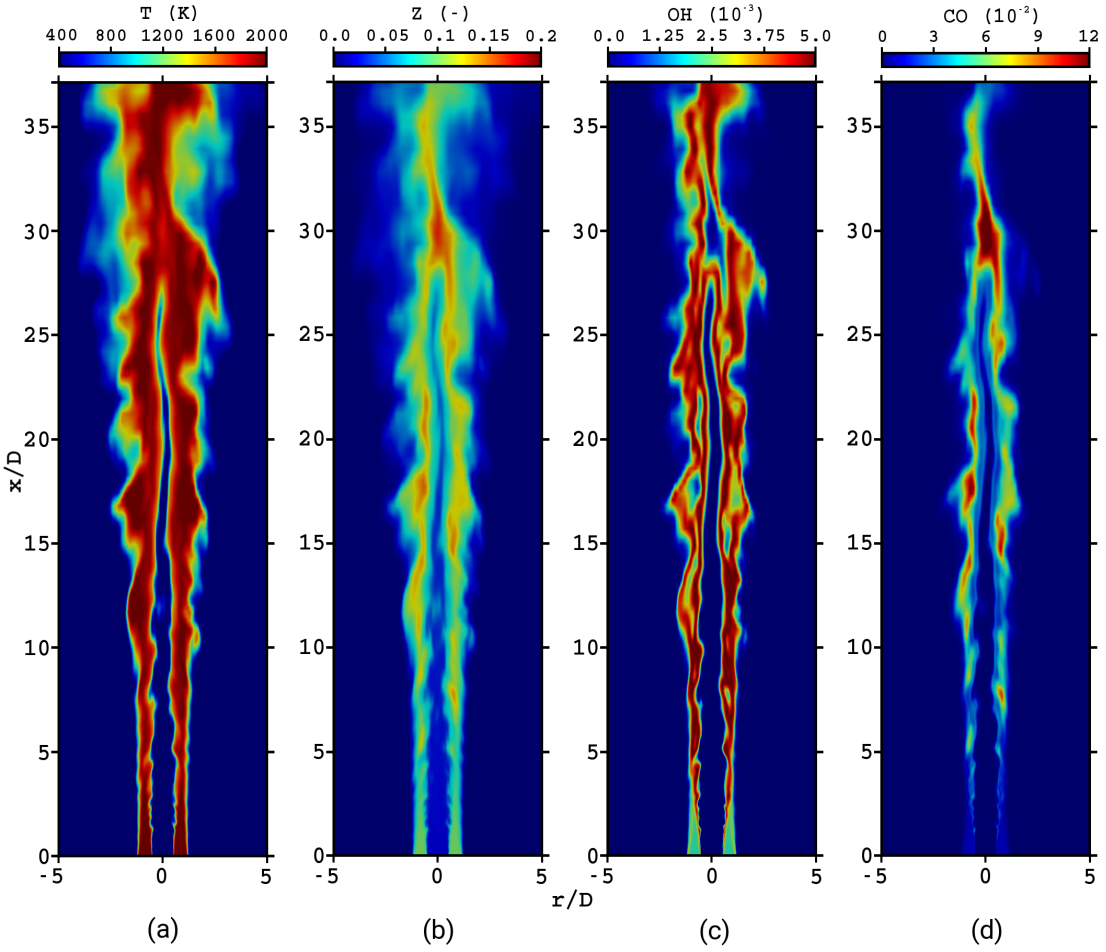

Figure 8.6: Instantaneous contour plots of (a) temperature, (b) mixture fraction, (c) OH and (d) CO using the standard thickening correction.

clearly indicate strong sources of fuel through droplet evaporation in these regions. The corresponding contour plots of CO and OH illustrate that in these richer regions a high concentration of partially oxidized products are present. The rather thin OH zones suggest not only a double flame structure, but also that this method promotes the development of partially-premixed or non-premixed combustion regions at these lower axial positions. This is confirmed by analyzing the volumetric ratio of premixed to non-premixed combustion at lower axial positions ($x < 15D$) which are presented in Table 8.4. This ratio is obtained by evaluating the flame index ξ, conditioned on regions of reactions, i.e. where the progress variable source term $\dot{\omega}_{PV}$ exceeds 10% of its maximal possible value. The flame index follows the definitions used in [207]

$$\xi = \nabla Y_{C_2H_5OH} \cdot \nabla Y_{O_2}. \tag{8.3}$$

Positive values of ξ indicate premixed and negative values non-premixed combustion. A total of 10 independent snapshots were used to allow meaningful statistics. As can be deduced from Table 8.4, while the ratios for the standard and projection approach are almost similar, the refraction correction shifts this ratio in direction of non-premixed combustion. The differences in combustion regime distribution are also present at higher axial positions, where an inverse behavior can be observed. In this region, the premixed

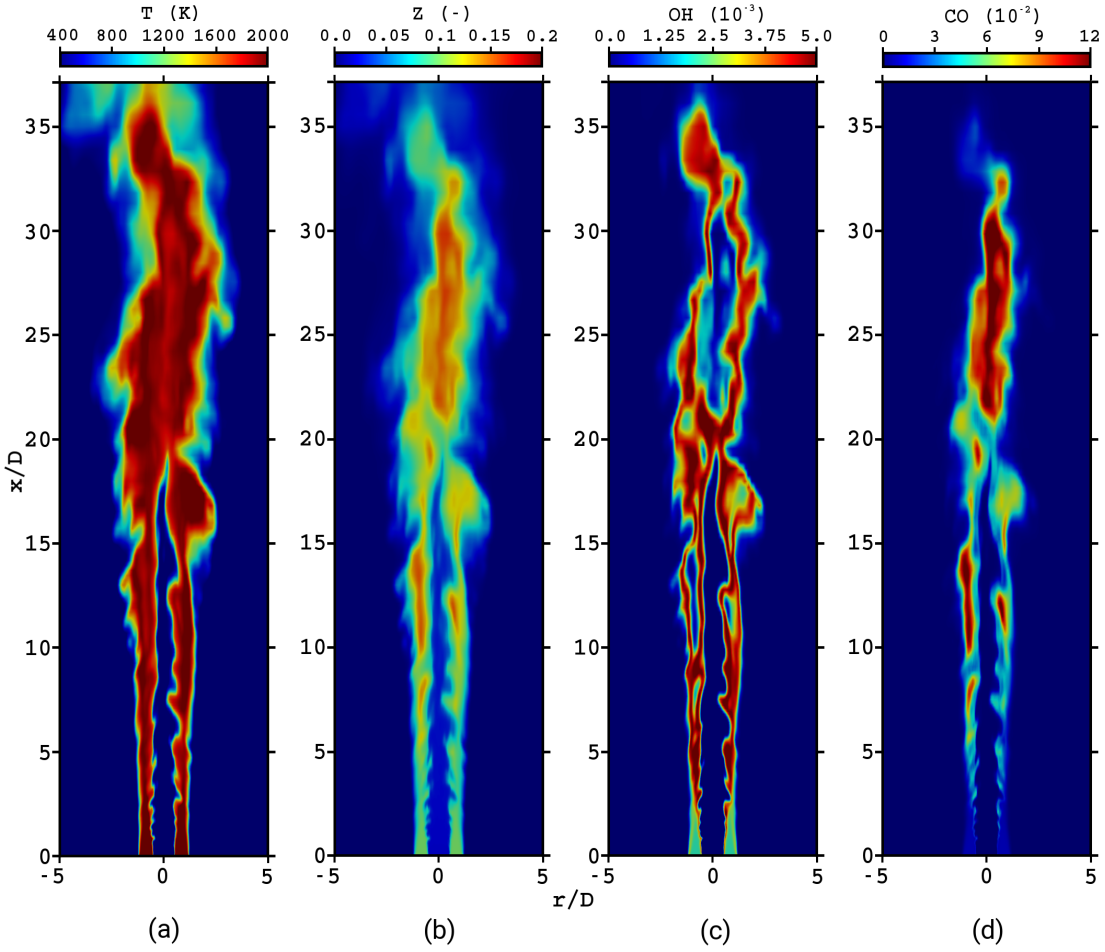

Figure 8.7: Instantaneous contour plots of (a) temperature, (b) mixture fraction, (c) OH and (d) CO using the projection thickening correction.

regime seems still dominant for all correction types, while the refraction approach yields higher volumetric ratios of premixed to non-premixed combustion than the other methods. Going back to the standard and projection approaches shown in Figures 8.6 and 8.7, the OH and CO profiles illustrate some pockets of partially oxidized products evolve behing the flame, suggesting combustion above stoichiometry. This is more evident in Figure 8.7d for the projection approach. A qualitative comparison with OH-LIF measurements (not shown here) found in [1] and [69] (see Figures 7.11-7.13 for this reference) revealed that, beside the reduced flame wrinkling due to the artificial flame thickening, the standard and projection method are evenly able to predict the flame structure at lower axial positions. However, at higher distances, the projection correction better matches the experiments due to the earlier flame propagation towards the jet centerline. Differently, the OH contours observed in Figure 8.8c for the refraction approach barely resemble the experimental results.

By now, it should be clear that the manner in which droplets interact with a thickened flame has a strong influence on the overall flame structure and combustion regime distribution. This divergent behavior of the approaches is consistent with the correction formulations. In the projection approach, the relative movement direction of droplet and thickened flame (i.e. their orientation) is taken into account. Since the main movement direction of the particles is parallel to the flame front, only little or no correction of heat and

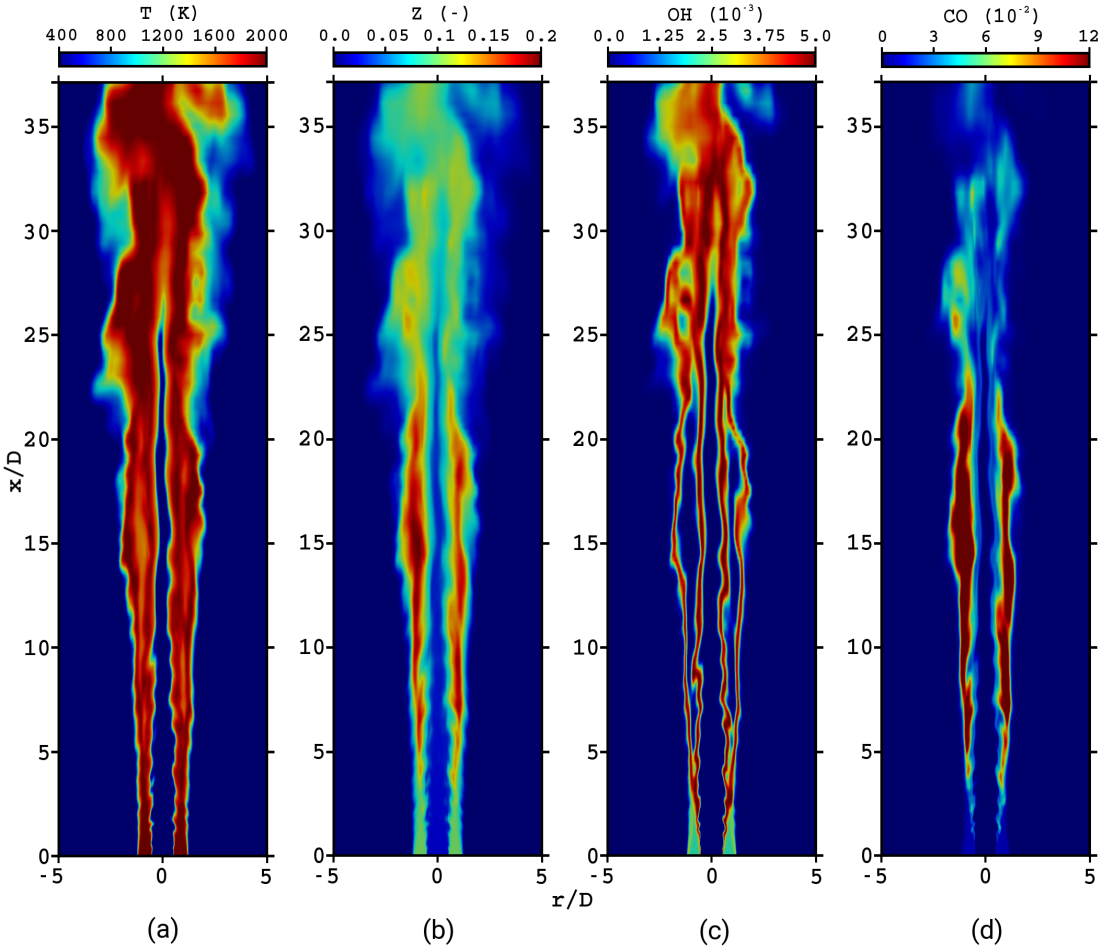

Figure 8.8: Instantaneous contour plots of (a) temperature, (b) mixture fraction, (c) OH and (d) CO using the refraction thickening correction.

mass transfer is applied. This is illustrated in Figure 8.9, which shows on the left-hand-side the instantaneous distribution of computational parcels at the axial plane $x = 5D$ superimposed with isolines of the flame sensor Ω. The parcels are colored with the angle $\gamma = \tan(u_{p,ax}/u_{p,r})$, which represents the angle between radial and axial momentum of the parcels. The right-hand-side shows a probability histogram of the effective correction factor calculated for the parcels at this axial plane (collected over at least 0.15 s). Since the droplets travel mainly in axial direction, the high angles observed in Figure 8.9a are not unexpected. More impressive is however the impact on the computation of the effective thickening factor F_{eff} shown in Figure 8.9b. The high axial velocity of the parcels, combined with a flame front that is predominantly radially oriented, leads to a significant reduction of the effective thickening factor for the projection correction. This promotes faster evaporation and a more intense evolution of the mixture towards flammability at lower axial positions in the case of the projection approach. This is also valid when no thickening correction is applied. In this regard, more details are presented in the next part of this section. Conversely, the standard method does not consider any orientation between parcels/droplets and the thickened flame, leading to correction factors higher than for the projection approach, hence reducing heat and mass transfer for droplets in the thickened flame region. The consequence is, as previously discussed, a mixture changing

$V_{premixed}/V_{diffusion}$	Correction approach		
	standard	projection	refraction
$x < 15D$	9.76	9.31	6.37
$x > 15D$	2.60	2.07	3.53

Table 8.4: Volumetric ratio of premixed ($\xi > 0$) to diffusion flame ($\xi < 0$) regime up- and downstream of the axial positions $x = 15D$ conditioned on regions of reaction, i.e. where $\dot{\omega}_{PV}$ exceeds 10% of its maximal possible value.

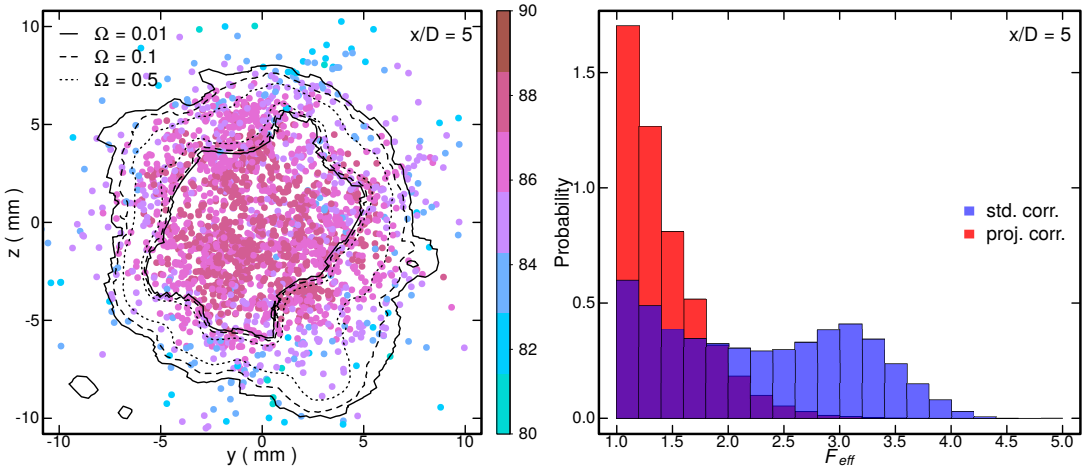

(a) (b)

Figure 8.9: (a) Instantaneous spatial distribution of computational parcels at the axial plane $x = 5D$ superimposed with isolines of the flame sensor Ω. The points, each representing one parcel, are colored with the angle $\gamma = \tan(u_{p,ax}/u_{p,r})$. (b) Probability histogram of the effective correction factor F_{eff} calculated for the parcels at the axial plane $x = 5D$. The shown histograms are conditioned on $F_{eff} > 1.05$.

far less through the longitudinal direction. This is elongating the cold spray core to higher distances from the burner exit and also affects the flame length. At the same time, the differences in the mixture evolution also impact the spatial distribution of partially oxidized products, as the evaporation takes place at higher distances from the burner exit. For the refraction approach, the trajectory correction of the flame front parallel motion causes a considerably richer mixture at lower axial positions compared with the other approaches. This goes hand in hand with the stronger concentration of the vapor release in flame front parallel direction. However, it seems that this approach induces an elongation of the cold central jet core compared with the projection correction. This at first sight unexpected effect is further discussed in the rest of this section.

Next, radial profiles of temporal mean and rms of different carrier phase quantities are presented in Figures 8.10 and 8.11. First, the carrier phase axial and radial mean and rms velocity shown in Figure 8.10 are considered. The simulation results are compared with results from experimental set A and B. It should be mentioned here that the comparison is not fully consistent since experimental carrier data were produced from statistics obtained from droplets with a diameter below 10 µm. In addition radial velocity statistics are only available for experimental set B. All presented fields are normalized with the bulk jet velocity u_{bulk} displayed in Table 8.1. At the lowest measurement plane, $x = 0.3D$ above the burner exit, the distinct peaks of central jet and pilot can be observed for the averaged

axial velocity. As distance from the burner exit increases, these peaks blur quickly into each other leading to the smooth profile observed at the axial position $x = 10D$. Up to that position, the velocity averages are evenly able to reproduce the experimental profiles. However, downstream of that position, first differences between the approaches arise. At $x = 20D$, the refraction approach profile indicates a broader region of higher velocities than the other approaches. The differences are even more pronounced at the last measurement plane, where the centerline values for the standard and refraction approach are noticeably higher than for the two other methods. Considering the standard approach, the reasons for the deviations are twofold: first, since this approach tends to reduce evaporation, liquid penetration will increase and thereby increase momentum exchange with the carrier phase up to higher axial positions. This is especially pronounced at the centerline. Second, as observed in Figure 8.6, the non reactive core may exist up to axial distance slightly below $x = 30D$. A flame front in that region leads to thermal expansion resulting in a higher axial velocity. The combustion reaction taking place at higher axial positions is also responsible for the higher velocities observed for the refraction approach. However, the cause for the observed behavior is different. Here, the trajectory correction coming with this method shifts the residence probability of parcels—at a fixed axial position—towards higher radial positions compared to other approaches. This, combined with the absence of oxidizer, allows the development of the previously mentioned fuel rich layers at lower axial positions (Figure 8.8). The mixing of these oxidizer-lacking-zones with coflow air at higher axial distances from the burner exit promotes combustion reaction yielding thermal expansion and an acceleration of the flow field. In contrast, the projection approach and the one without correction better reproduce the experimental data. In regard of the radial velocity averages, all approaches are in the same order of magnitude as the experiment. However, some differences are also noticeable, which are most pronounced at $x = 10D$, where the peak values of the radial velocity average differ strongly. These higher peak values for the projection approach and the one without correction indicate a stronger combustion reaction in that region, compared with the two other approaches. Looking at rms profiles of axial and radial velocity, one can perceive that, besides centerline values being underestimated at the lowest measurement plane and an overprediction of radial velocity rms at $x = 30D$ for all but the refraction approach, the simulation results reproduce the experimental trends satisfactorily. In fact, all approaches perform evenly with exception of the refraction correction, which generates considerably smaller rms values around the centerline repeatedly. A possible explanation for that is the reduced interaction of droplets with the shear layer that surrounds the main jet stream, which is promoted by the droplet trajectory modification performed for this approach.

Going over to the scalars presented in Figure 8.11, where only the excess temperature $T - T_0$ was measured for experiment A, the impact of the various models becomes more apparent. As has been revealed in the instantaneous contour plots, the mixture evolution apparently depends strongly on the approach to correct heat and mass transfer. This hypothesis is now investigated quantitatively. At the lowest plane $x = 0.3D$, the distinct levels of temperature and mixture fraction corresponding to central jet, stoichiometric pilot flame and primary coflow are clearly visible. This, together with the fluctuations of the turbulent flow, give rise to the two small peaks in the rms profiles of mixture fraction in Figure 8.11c. As the distance from the burner exit increases, the evaporation of the liquid phase leads to an increase of mixture fraction which is expected to be dominant in proximity of the flame front. Here, it should also be mentioned that in view of the adiabatic assumptions made in this work, the overestimation of the maximum temperatures is expected. At $x = 10D$, some differences between the approaches become noticeable.

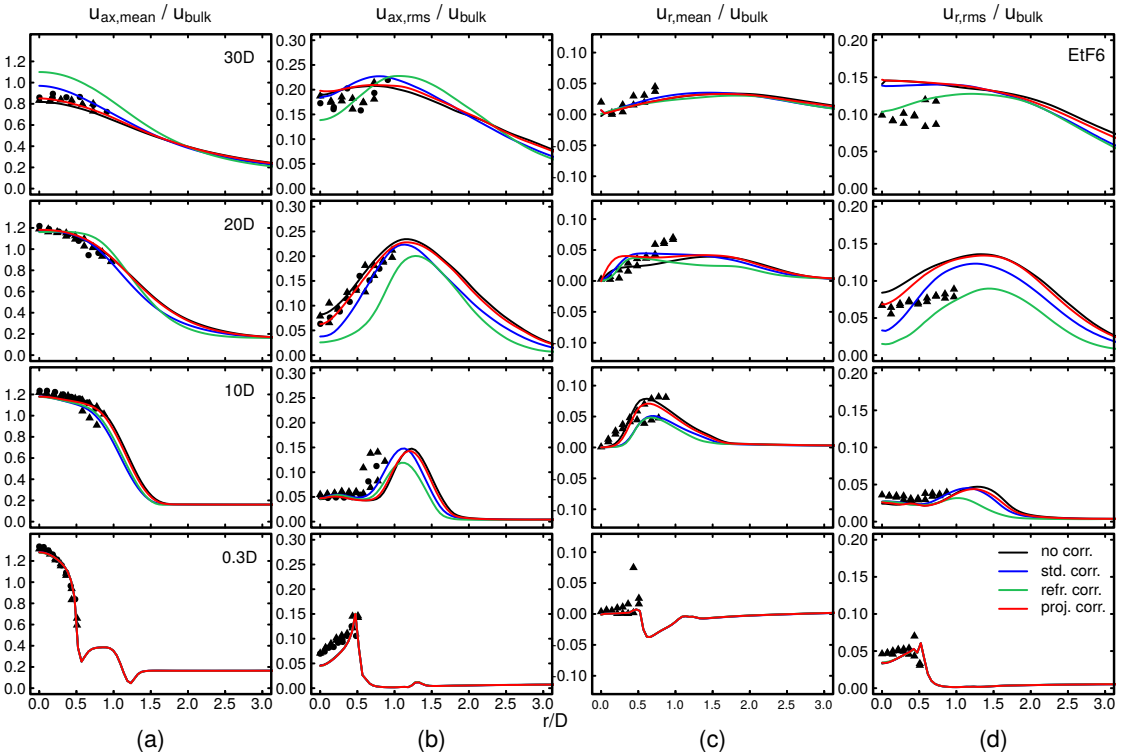

Figure 8.10: Mean and rms of axial and radial carrier velocity components at different axial positions. • and ▲ denote experimental set A and B, respectively.

In regard of the average temperature profile, all simulations tend to underestimate the temperature at the centerline, indicating a longer non-reacting spray-jet core than in the experiments. This attests that flame propagation towards the jet center is underestimated in the simulations at lower axial distances. This is possibly caused by the combined effects of an under prediction of turbulence-flame interaction as discussed at the end of Section 8.2 and the negligence of differential diffusion transport and radiative heat transfer. The consideration of these effects could favor the higher entrance of the flame into the jet core.

In regard of the different approaches, it can not only be observed that the averaged temperature rise takes place at different radial positions, but also that the flame structure varies from approach to approach. This is most evident for the refraction correction, where the double peak present in the average temperature profiles at $x = 10D$ and $x = 20D$ indicates a double flame structure. This confirms the observations from the previous analysis of instantaneous contours (see Figure 8.8 and subsequent discussions). The other approaches better agree with the experimental profiles. At $x = 10D$, the temperature rise, which is closer to the centerline for the projection approach and the one without correction, indicates a different averaged flame position. The lowest radial positions can be observed for the case without thickening correction, as F_{eff} has the smallest value for this approach. This is also confirmed by the averaged and rms mixture fraction profiles. In the case of the mean, a similar behavior as for the averaged temperature can be observed: the projection method and the one without correction yield a mixture fraction rising closer to the centerline due to the different flame position. This is closely connected to the lower values of F_{eff} compared with the other approaches. The indicated effect is also apparent in the variance charts, where undulated profiles with two distinct peaks are visible for all approaches. The most outer peak, corresponding to the pilot-coflow mixing layer, is

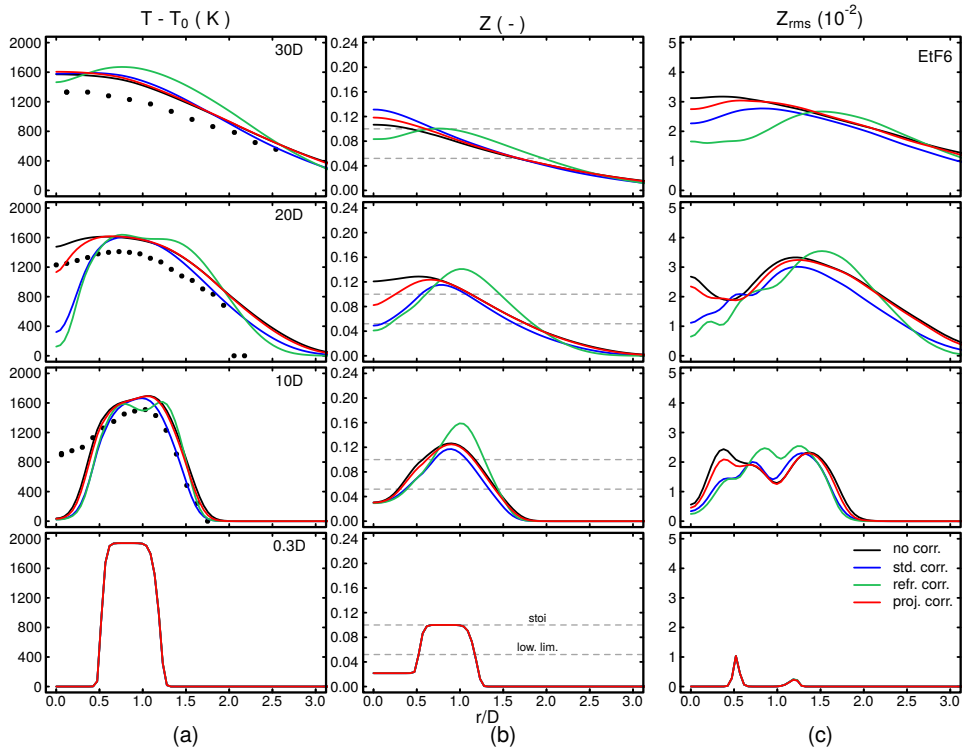

Figure 8.11: Temperature mean, mixture fraction mean and rms at different axial positions. •: experimental set A.

similar for all modeling strategies. In contrast, the most inner peak, which represents a blurring of the jet-pilot mixing layer and the evaporation zone, differs in its strength and position. For the standard and refraction approaches, a small increase of the rms is perceived at lower radii. As the radial distance increases, a peak can be observed around $r = 0.75D$ for the standard approach. Beside being shifted to higher radii, the peak is much more distinct for the refraction correction. Such radial shift is also apparent in the mixture fraction average profile. This is not surprising when considering that the trajectory correction results in higher radial positions of droplets (at a given axial position) compared to the other approaches. This shift clearly affects the strongly connected vapor release and the carrier phase mixture evolution. For the two remaining approaches, namely no-correction and projection correction, the mixture fraction variance peak is much closer to the centerline, suggesting a stronger interaction of the turbulence and evaporated fuel.

The disparities between the approaches reach their maximum at $x/D = 20$. The findings from the instantaneous contour plots analysis are confirmed by the temperature and mixture fraction profiles. It is observed that: (1) for the projection approach and the one without correction, the temperature profile indicates combustion (or hot products) at the centerline, which better matches the experimental measurements. This is not the case for the standard and refraction correction approach suggesting a longer non-reacting cold core. (2) Centerline mixture fractions are shifted towards richer mixtures for the projection method compared to the standard and refraction approach and are highest when no correction is applied. Here, the deviations between the proposed projection method and the one without correction are highest. This is not unexpected, as a large part of the droplets move with a considerable orthogonal component to the flame front, resulting in higher correction factors F_{eff} in this region.

Finally, at the last measurement plane, a considerably higher mixture fraction average can be observed for the standard approach. This is certainly caused by the stronger evaporation rates resulting from a greater spray penetration for this case. Also interesting is the clearly lower mean mixture fraction for the refraction correction which is coupled to the lower centerline temperatures for this method. This observation is attributed to the trajectory correction of the droplet. Since, as a droplet within the central jet travels along its trajectory, the probability to cross a thickened flame region increases with the axial distance the droplet has traveled. This, in turn, increases the probability of the droplet to experience a radial dispersion.

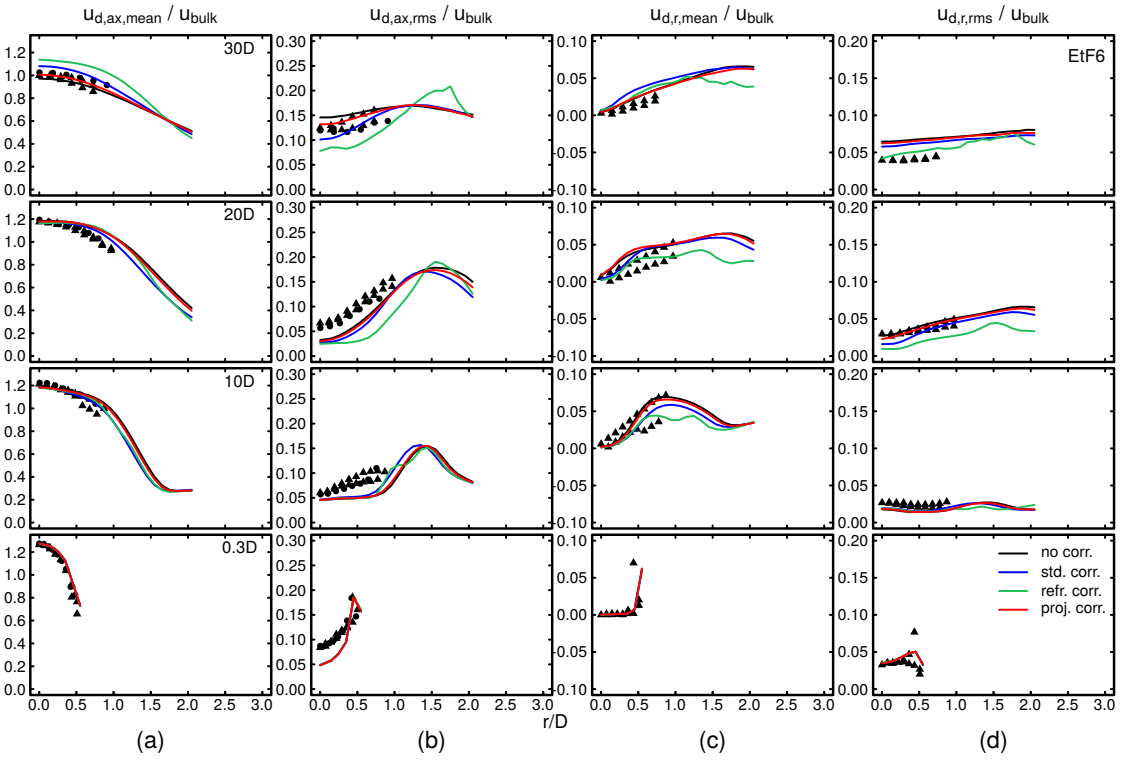

Figure 8.12: Mean and rms of axial and radial liquid phase velocity component at different axial positions. • and ▲ denote experimental set A and B, respectively.

The velocity statistics as well some characteristic scalar properties for the liquid phase are presented in the Figures 8.12 and 8.13. The statistics shown are based on number averages of the real droplets (as each computational parcels represents a specific number of real droplets with the same properties). In regard of the velocity profiles shown in Figure 8.12, a first observation is that all modeling approaches are able to represent the main trends adequately. However, considering the last measurement plane, the standard and refraction approach overestimate axial averages, which is similar to the behavior observed in Figure 8.10a for the carrier phase. The other approaches deliver better results in that region. The similarity of the droplets averaged radial velocity profiles in Figure 8.12c suggests that the radial velocity is not strongly connected to the correction approach. The variance profiles show a similar picture as for the carrier phase velocity profiles, i.e. that the rms of the axial velocity component (Figure 8.12b) are underestimated at the lowest measurement plane. This is resulting from the droplet injection strategy, as computational parcels are injected with the carrier phase velocity interpolated onto the injection position. However, even though all approaches differ from the experimental results, the projection

method and the one without correction seem to deliver smaller offsets than the other approaches. The radial velocity rms profiles also indicate a better agreement with the experiments for the two former approaches, with exception of the last measurement plane.

Radial profiles at different axial positions for liquid phase scalar properties, namely Sauter mean diameter (SMD) D_{32}, mean diameter D_{10}, and liquid volumetric flux are shown in Figure 8.13. Excellent results are obtained for all properties at the lowest measurement plane, which is expected since this is the liquid injection plane in the simulations (see Section 8.2). Taking a look at the characteristic diameters displayed in the first two columns, the simulations have a tendency to underpredict their profiles at all positions and for all approaches with exception of the injection plane. It should be noticed that similar deviations have been observed in the comparative study of Heye et al. [78] for all modeling frameworks compared. The offset goes hand in hand with the simulations predicting longer cold cores (see Figure 8.11) than in the experiment. This is because smaller droplet can exist up to greater axial distances without the presence of a flame or hot products at the centerline. Another possible reason is a mismatch between simulations and experiments for the injection velocity of the liquid phase. Since droplets are injected with the carrier velocity, the velocities of large droplets are likely to be overestimated. This higher injection velocity for large droplets leads to a preferential residence of smaller droplets around the centerline because larger droplets are able to exit the central jet due to their higher inertia. The hypothesis is confirmed by the higher values perceived in the profiles at greater radial positions. This effect and the previously discussed longer non reacting jet core are both acting towards shifting the characteristic diameters around the centerline to smaller values. Nevertheless, one can observe that the projection correction as well as the approach without correction reduce the gap between simulations and experiments. This is most evident at $x = 20D$ for the SMD and at $x = 30D$ for the mean diameter.

The divergent results between the approaches are more pronounced when considering the liquid volumetric flux shown in Figure 8.13c. At $x = 10D$, the profiles are not far apart. However, the slight peak around $r = 1D$ for the refraction approach is remarkable as it does not appear for the other approaches at this radial position. This peak combined with the mixture fraction profile shown in Figure 8.11(b) suggests that the deviation of the particles performed by this approach predominates in lower axial regions. Indeed, the aforementioned peak disappears at higher axial distances. Here, other differences between the correction approaches emerge, which are strongest around $x = 20D$. At this location, the standard approach yields centerline volumetric fluxes almost twice as high than in the experiments or when no thickening correction is performed. The refraction approach is also overestimating the centerline liquid volumetric flux. In between lies the projection approach which seems to slightly overestimate the volumetric flux in that region. The latter discrepancy appears to be consistent with the delayed entrance of the flame in the spray jet, as discussed above for the carrier phase. The differences between the projection approach and the one without correction suggest that droplets are moving with a considerable velocity component in flame front orthogonal direction, yielding higher values for F_{eff}. This in turn affects the evaporation and leads to the differences between the two methods. At the last measurement plane, where $x = 30D$, the standard approach fits the experiments most accurately. However, the previous results as well as the overall order of magnitude for the volumetric flux at this axial positions clearly reduces its significance for interpretation.

To summarize, the above discussion showed that the way in which droplet interacts with a thickened flame has a meaningful impact not only on global flame characteristics, as flame

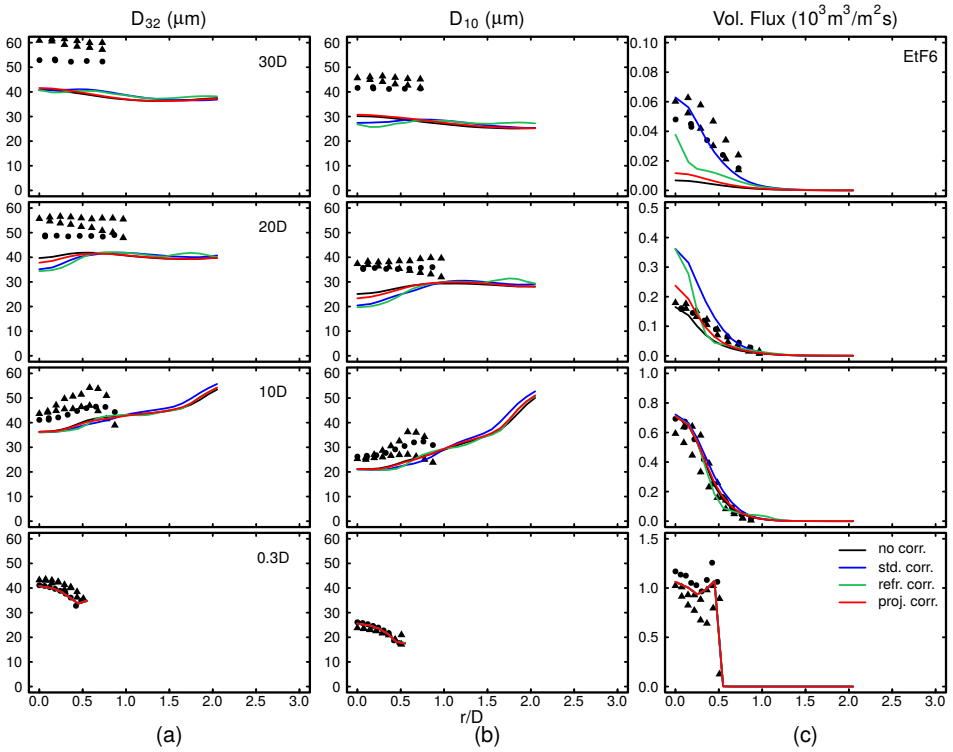

Figure 8.13: Sauter mean diameter, mean diameter and liquid volumetric flux at different axial positions for case EtF6. • and ▲ denote experimental set A and B, respectively.

length or spatial distribution of flame burning modes, but also on the flow dynamics and scalar distribution of the carrier and liquid phase. The differences between the state-of-the-art methods and the introduced correction approaches, namely projection and refraction correction, are evident at numerous axial positions, as indicated by the instantaneous contour plots of carrier scalar fields and the profiles of temporal averages for various fields. The refraction correction, which performed best in the simplified one-way coupled configuration in Section 5.2.3, can by far not be considered adequate when applied to a complex spray flame. Differently, the approach without thickening correction and the projection correction appear to be most promising. The contrast between both approaches is not pronounced, especially when looking at the radial profiles upstream of $x = 20D$. This is expected, since droplet movement is predominantly parallel to the flame front in that region. Differently, around $x = 20D$, the droplet movement orthogonal to the flame front becomes more important, resulting in higher correction factors F_{eff} in that region. This yields the observed deviating results at higher axial positions, which are most evident for mixture fraction averages (Figure 8.11b) and for the liquid volumetric flux (Figure 8.12c).

8.4 Summary and Conclusions

Four different strategies to describe heat and mass transfer of droplets in the presence of an artificially thickened reaction zone were investigated in this chapter. The modeling combined the FGM method with the ATF approach, while the multiphase flow was treated using a two-way coupled Euler-Lagrange framework.

The impact of the various approaches and their prediction ability was evaluated in a turbulent spray flame, the configuration EtF6 of the Sydney spray burner. Here, a differ-

ent behavior than for the two-dimensional test configuration was observed. Interestingly, the refraction approach not only fails to reproduce the experimentally determined flame structure and regime, but delivers also worse carrier and liquid statistics. In retrospective, it becomes clear that these discrepancies are caused by the trajectory correction which yields a radial deflection of the parcels. This is closely connected to the greater mixture fraction values, which occur at higher radial positions for the axial positions $x = 10D$ and $x = 20D$. The projection approach appeared to reproduce the experimental trends and profiles more accurately than the standard approach and the refraction method. To be more specific, the projection approach leads to a better prediction of the flame propagation towards the center of the spray jet, better estimations for the evolution of the disperse liquid phase, shown by means of radial profiles of liquid volumetric fluxes and characteristic diameters at several axial positions, compared with the standard approach used in [175, 28, 29, 100]. The impact on carrier and liquid phase velocity statistics is more important at higher axial distances from the burner exit. The disparities between the proposed projection approach and the one without correction (i.e. $F_{\mathit{eff}} = 1$) are, as expected, most pronounced in regions where flame-normal droplet movement is significant.

It is concluded that: (1) The manner in which the interaction of droplet with a thickened flame is treated does not only strongly affect global flame quantities, for instance the length of the cold central spray core or the flame length, but also the prediction of the flame regime as well as carrier and liquid phase statistics. (2) By taking into account the relative orientation of flame front and droplet movement by means of the novel projection method, the overall consistency of the modeling framework is improved. (3) The present analysis showed that a consideration of a simplified configuration is insufficient to fully uncover the performance of the different approaches. (4) In particular, the projection approach appears most suitable when adopting the ATF technique in a complex spray flame.

Chapter 9

Investigation of a Turbulent Spray Flame Using the Filtered Eulerian Stochastic Field Approach Coupled to Tabulated Chemistry

This chapter contains the results presented by Dressler et al. [43], where the Eulerian Stochastic Fields method, was applied to the spray flame EtF6 investigated in the previous chapter. The ESF approach is applied to represent the turbulence-chemistry interaction in the context of tabulated chemistry. Following a two-way coupled Eulerian-Lagrangian procedure, the spray is treated as a multitude of computational parcels described in a Lagrangian manner, each representing a heap of real spray droplets. The present chapter has two objectives: First, to evaluate the predictive capabilities of the modeling framework by comparing simulation results using 8, 16, and 32 stochastic fields with available experimental data. At the same time, the simulations are compared to the ATF results using the standard correction for droplet heat and mass transfer (extensively discussed in the previous chapter). Second, the dynamics of the subgrid scalar contributions are investigated and the reconstructed probability density distributions are compared to common presumed shapes qualitatively and quantitatively in the context of spray combustion.

In regard of the application of the ESF approach to LES of multiphase combustion, first promising results were attained. More specifically, the approach has been validated for multiphase combustion in a gas turbine combustor [95], a methanol spray flame [94], as well as for spray auto-ignition under EGR conditions [61], and MILD spray combustion [62]. However, all approaches relied on a reduced kinetic mechanism to take into account combustion chemistry. Differently, the present method profits from the recent progress made in tabulated chemistry approaches for spray combustion and combines it with the advanced subgrid closure for the turbulence-chemistry interaction provided by the ESF method.

The remaining of this chapter waives a description the experimental configuration since it is already presented in Chapter 8. The next section is dedicated to the numerical setup, which is directly followed by the results part. The latter comprises similar investigations as shown in the previous chapter, which are complemented by an analysis of the subgrid scalar contributions and an a-posteriori comparison with presumed PDF approaches. This chapter ends with a conclusion.

9.1 Numerical Setup

Within the ESF formalism, the system of PDEs to be solved is given by Equations 3.98, 3.99, 3.102 and 3.103 including non-zero source terms due to the presence of the liquid phase. The system of PDEs is formulated in a low-Mach manner and solved using the merged PISO[87]-SIMPLE[137] algorithm described in Section 4.2.3. As in previous chapters, the subgrid fluxes in the momentum equation are taken into account using the σ-model [129], whereas the subgrid scalar fluxes are modeled based on the Reynolds analogy (see Equation 3.19). The scalar space diffusion in the stochastic field equations is taken into account through the IEM micromixing model [199, 60, 39, 133] as introduced in Equation 3.60, where the micromixing frequency is computed through Equation 3.61. Regarding the numerical schemes, a second-order implicit backward time-stepping scheme has been applied to all fields with exception of the stochastic field equations, for which the first order implicit Euler scheme has been used due to the stochastic nature of these equations. The convective momentum fluxes are discretized using the blended scheme with filtering of the high frequency modes described in Section 4.1.1. The convective scalar fluxes are treated using the Minmod flux-limiter scheme [167].

The computational domain employed in this work is the same as the one described in 8 to allow for a consistent comparison of the simulations. Note that the spatial resolution has been shown to be sufficient in Section 8.2.2. Therefore, no additional grid sensitivity study has been performed. Regarding the boundary conditions the reader is also referred to the previous chapter. The disperse phase evolves according to Equations 3.67, 3.68, 3.73 and 3.74.

9.2 Results

In this part, the main features of the flame are first discussed based on instantaneous and averaged contour plots obtained from the ESF solution before going over to a comparison of the simulation results with available experimental data. Since the ATF model accounts for the turbulence-chemistry-interaction in the context of LES, it is also used together with experiments to appraise the ESF based approach. Thereafter, the evolution of the scalar subgrid fluctuations at a representative position are analyzed using the most detailed simulations, i.e. the one with with 32 stochastic fields. At the same time, the results are used to investigate common presumed PDF shapes.

Carrier Phase Analysis

Figure 9.1 depicts contour plots of the FDF integrated temperature (top) as well as the mixture fraction field (bottom) for the LES with 16 stochastic fields. Each subfigure is divided in its temporal average and instantaneous field, respectively, shown in the upper and lower parts. At lower axial positions, the central spray jet core and the pilot flame are concentrically arranged and the boundaries between both streams are very distinct. In this region, the cold jet core has not reached flammability and therefore hinders the pilot flame from propagating towards the center. Also to mention is the minor wrinkling effect of the shear layer on the flame. As the axial distance from the burner exit increases, the flame wrinkling becomes more intense and large structures are able to propagate towards the centerline. This process seems to be dominated by advection as the mixture around the centerline is still below the flammability limit. The significant mixture fraction increase between $x/D = 10$ and $x/D = 20$, which can be observed for mean and instan-

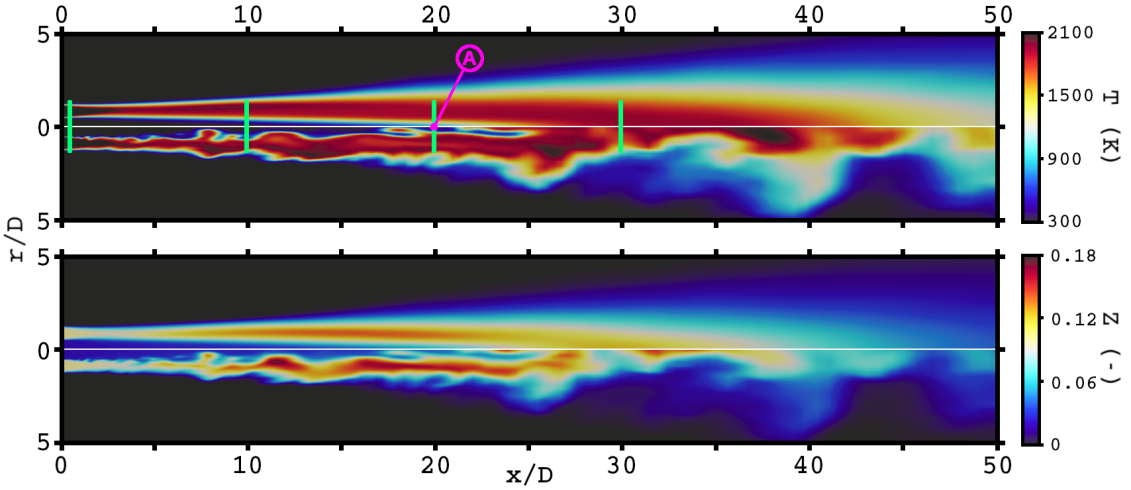

Figure 9.1: Temporal average (upper part) and instantaneous contours (lower part) of both, the FDF integrated temperature (top) and first moment of the mixture fraction FDF (bottom) for the ESF(16) simulation. The vertical green bars denote axial positions at which simulation data are compared with experiments. The magenta colored point exhibits the position of probe A, for which time-series analyses are performed in a later section.

taneous contours, indicates strong evaporation of droplets. Both the higher interaction of turbulence with the flame front and a mixture evolving towards flammability promote the propagation of the reaction zone towards the centerline. This results in a cold spray core which disappears for axial distances $x > 25\,D$. A comparison of the instantaneous contours of temperature with Figures 8.6, 8.7 and 8.8 in the previous chapter already suggests a stronger interaction of turbulence and flame for the transported PDF approach compared to the ATF-based simulations. This is not unexpected as the ATF-induced flame thickening generally damps the flame distortion caused by the turbulent eddies, yielding less spatial displacement of the flame. This impression will be confirmed later in this section by quantitatively comparing temporal rms values of temperature at various positions for the ATF and ESF based approaches.

Next, radial profiles of carrier velocity and scalar temporal statistics are evaluated at the axial positions $x/D = 0.3, 10, 20, 30$, marked with green vertical lines in Figure 9.1. The results of the ESF simulations using 8, 16 and 32 stochastic fields are compared to experimental measurements. The simulation results are also plotted alongside results obtained using the ATF method with standard correction of heat and mass transfer of the droplet (referred to as standard (std) correction in [44] and in Chapter 8). Since the ATF-based simulations were performed using the same framework as their ESF pendant, a comparison of the approaches enables an estimation of the impact of the flame-turbulence interaction treatment for this flame. The simulation results are compared with available measurements for experimental sets A and B. Again, note that the experimentally determined velocity statistics are based on droplet velocities with diameters $< 10\,\mu$m assuming a Stokes number well below unity. First, taking a look at the time-averaged velocity statistics of the carrier phase shown in Figure 9.2, at the lowest axial plane, the three distinct streams corresponding to spray jet, pilot flame, and coflow are visible in the axial velocity profile (Figure 9.2a). As distance from the burner exit increases, these peaks rapidly merge to form one uniform profile which extends through the rest of the domain. The simulation

results agree well with the experimental data except for the most downstream plane, where the axial velocity is overpredicted. A possible reason for this effect could be the adiabatic tabulation strategy employed. Since a two-dimensional lookup-table is used, any cooling effects or heat losses due to the evaporation of the spray are inherently neglected, which is likely to induce higher temperatures than in the experiment. This causes a higher thermal expansion of the carrier phase, which in turn yields higher velocities. Additionally, as will be shown next by means of the scalar statistics shown in Figure 9.3, the simulation tends to overestimate the length of the cold spray core. This is likely to shift the combustion reaction and the associated thermal expansion to higher axial positions. The overestimation of the length of the cold spray core will be the subject of discussion later in this section. Even though underestimating the centerline fluctuations at the lowest axial position, the standard deviation of the axial velocity seems to reproduce the experimental trends well. Similar holds true for the radial velocity statistics except for the radial velocity rms at the most downstream position.

Comparing the different approaches, it is possible to conclude that the flow-field is not strongly affected by the combustion model employed. Both approaches, the ATF model and the ESF based framework are reproducing the measured velocity statistics. Furthermore, it is interesting to note that the presented simulation results are not sensitive to the number of stochastic fields used. This indicates that the use of at least 8 stochastic fields is sufficient to achieve an accurate representation of the flow field.

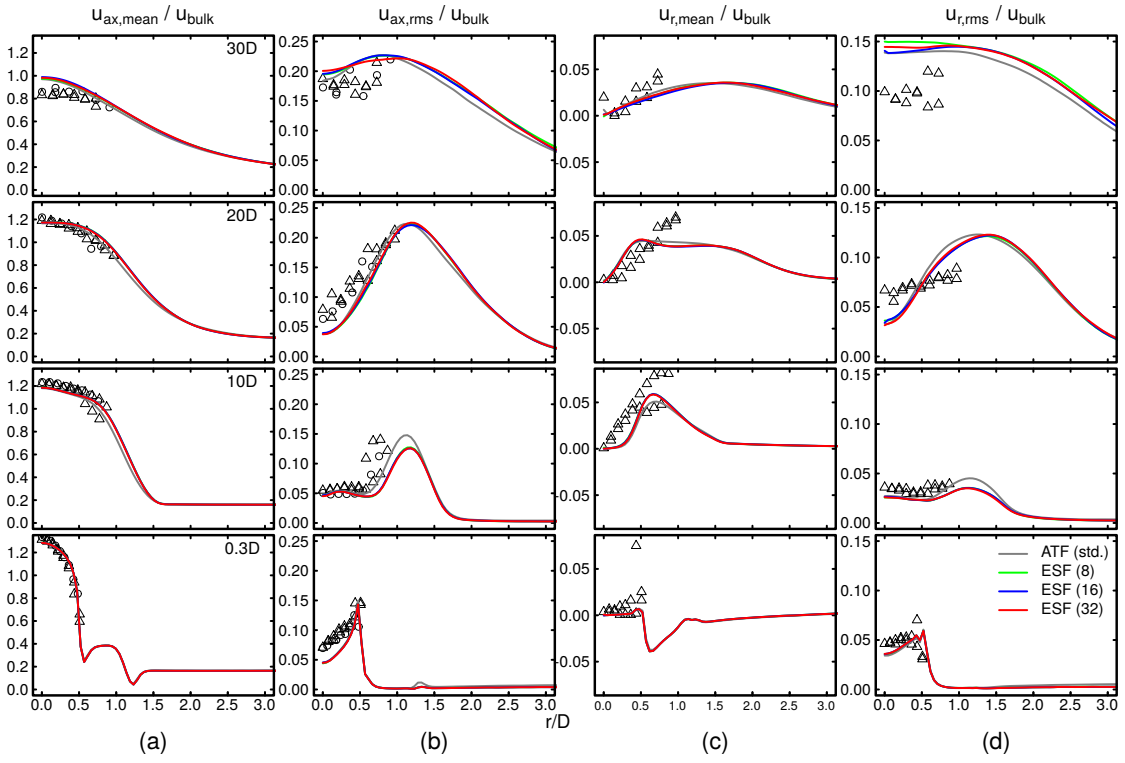

Figure 9.2: Mean and rms of resolved axial and radial velocity components at various axial distances from the burner exit compared with experimental data. Radial velocity statistics are only available for experimental set B. ○ : exp. set A; △ : exp. set B.

Figure 9.3 presents radial profiles of different scalar quantities (temperature and mixture fraction) at the axial positions highlighted in Figure 9.1. Note that for the rms quantities, the time-averaged subgrid contributions obtained from the ESF simulations

are also displayed (dashed lines in Figures 9.3b and 9.3d). At the lowest axial position, the distinct temperature peak corresponding to the hot flue gas of the pilot flame and the differences in mixture fraction between jet, pilot and coflow are clearly visible. Additionally, small peaks are perceivable for temperature and mixture fraction rms, resulting from the interaction with the shear layers. At this position, all approaches perform similarly. Going over to higher axial positions, the flame progresses towards the centerline, as shown by the time-averaged temperature in Figure 9.3a. Simultaneously, the temperature increase induces strong evaporation of liquid droplets, leading to a mixture fraction increase, which can be observed in Figure 9.3c. The uniform profiles of mixture fraction and temperature at the most downstream position confirm that the cold core has disappeared. Going back to the temporal averages of the excess temperature in the very left column of Figure 9.3, large discrepancies between the simulations and the experiments are visible at all measurement planes. First, it can be observed that the peak temperatures are overestimated at all axial positions. Nevertheless, this is consistent with the employed two-dimensional lookup-table, as has been outlined in the previous chapter and in the discussion of the velocity profiles. The impact of the evaporative cooling on the carrier temperature has been investigated by Sacomano Filho et al. [171] for the flame EtF5 of the Sydney Spray Burner. Thereby, it has been shown that the peak carrier temperature is better matched when evaporative cooling is considered. A consideration of the evaporative cooling could be included by using a third table dimension as the enthalpy [170, 171]. Another strategy could be to transport an additional energy variable as performed in [57]. Herein, by assuming a linear behavior between the transported and tabulated energy, an evaporation-corrected temperature can be obtained.

The second point is related to the lower centerline temperatures perceived for all simulations when compared with experimental data. This can be observed in Figure 9.3a at the axial positions $x = 10\,D$ and $x = 20\,D$. The results suggest that all simulations are underpredicting the flame propagation towards the jet center, a matter that has also been observed in the previous chapter for the ATF model and in the LES shown by Heye et al. [78] for the two spray flames EtF2 and EtF6. The reason for the divergent results of experiments and simulation can be devided into three categories: (1) Deviations related to the modeling strategy, (2) uncertainties in the boundary conditions, and (3) uncertainties in the temperature measurements. Regarding the modeling framework, the main shortcomings related to this issue are the neglect of radiative heat transfer and the absence of differential diffusion effects. The former reduces thermal diffusion in the central jet, which in turn yields lower evaporation rates of the spray. This retards the evolution of a burnable mixture and the flame propagation towards the center. The unity Lewis number assumption, which leads to an underestimation of the flame speed, also contributes to a slower flame propagation in the central jet. The uncertainties in the boundary conditions are mainly related to the mixture composition at the burner exit. In this work as well as in previous simulations of various configurations of the Sydney Spray Burner [78, 77, 166, 170, 173, 44, 172], a homogeneous distribution of fuel within the spray pipe is assumed. However, depending on the flow characteristics inside the central jet, the spray dynamics may change, yielding different spatial distributions of the fuel at the burner exit (for instance, due to the development of a liquid film at the pipe walls [121]). As pointed out in the conclusions presented in [78], non-homogeneous mixtures at the burner exit may impact the development and propagation of the flame front significantly. Finally, the temperatures presented in [69, 120] were measured using a R-type thermocouple with a diameter of 0.5 mm. In the doctoral thesis of Gounder [69], it is explicitly stated that the measured temperatures have neither been corrected due to radiation losses, nor modified

due to the cooling effect of droplet impact and liquid film building on the thermocouple surface. Even though the uncertainty is not directly quantifiable, it can be assumed to be rather high.

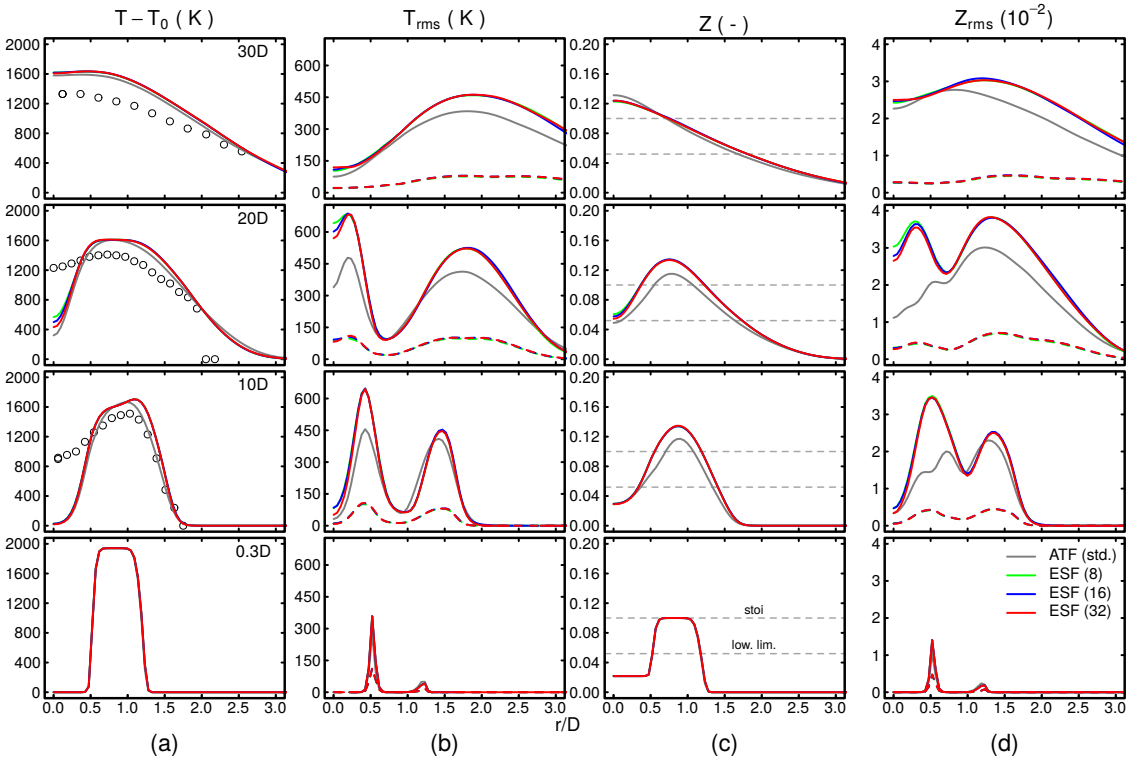

Figure 9.3: Mean excess temperature (a), temperature rms (b), and mixture fraction mean (c) and rms (d) at various axial distances from the burner exit compared with available experimental data. The dashed lines correspond to the unresolved contributions obtained from the LES-ESF simulations. The horizontal grey dotted lines shown in (c) correspond to the lower flammability and stoichiometry, respectively. ○ : exp. set A.

First disparities between the ATF and the ESF approaches arise around $x = 10\,D$ and reach their maximum at $x = 20\,D$. At the latter position, differences are noticed for all scalar quantities shown. The results suggest that the LES-ESF predicts an earlier flame propagation towards the centerline, which is expected since these simulations exceed the lower flammability limit at lower axial positions, as the averaged mixture fraction profiles suggest. The differences between the approaches are even more pronounced when considering the scalar rms profiles shown in Figures 9.3b, 9.3d, and 9.4. Compared to the ATF-based framework, the transported FDF-based method does predict higher rms values at all axial positions for both, temperature and mixture fraction fields. However, it is challenging to evaluate the differences due to the unavailable measurements with respect to the scalar rms values. The results suggest significantly stronger variations across the possible range of values for the ESF simulations, confirming the initial impression of a stronger sensitivity of the flame to turbulent motion indicated by the instantaneous scalar contours shown in Figure 9.1. For instance, the centerline rms of temperature and mixture fraction for the LES-ESF approach are approximately twice as high as the LES-ATF-based modeling strategy. This indicates a higher probability of events that are far away from the temporal mean of the respective fields for the ESF approach. Similar observations were made for simulations of a premixed stratified flame [5]. Regarding the rms values

for the mixture fraction, both approaches do not only differ with respect to the intensity of the scalar fluctuations, but also in the profile shape. This can be observed at the two axial positions $x = 10\,D$ and $x = 20\,D$, where the ESF approach predicts a double peak structure similar to the temperature rms profile. In contrast, the ATF approach produces a triple-peak-like profile with lower maximum values, which is on one hand resulting from a reduced sensitivity of the flame to turbulent motion (or flow perturbations in general) and on the other due to the correction of heat and mass transfer of liquid droplets resulting from the flame thickening. Additionally, one important feature of transported FDF methods is their ability to include subgrid contributions in the scalar fluctuations, shown as dashed lines in Figures 9.3b and 9.3d. As expected for LES, the subgrid contributions to the scalar fluctuations are much smaller than their resolved counterpart. Differently from the carrier velocity statistics, the results suggest a minor dependency of the ESF simulations regarding the number of stochastic fields used. This is most pronounced around $x = 20\,D$ at the centerline, where the ESF(8) simulation predicts the highest centerline temperatures and slightly higher temperature and mixture fraction rms. Considering the corresponding subgrid statistics, the number of stochastic fields appears to have a minor influence. These findings are confirmed by the axial centerline profiles shown in Figure 9.4.

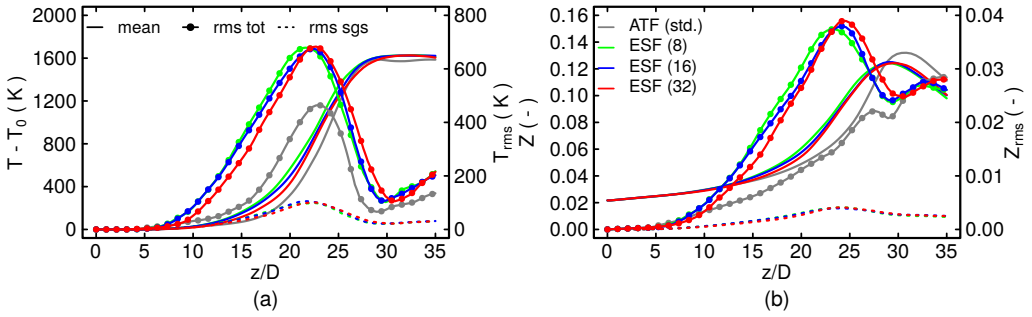

Figure 9.4: Axial evolution of temporal averages and rms of (a) temperature and (b) mixture fraction along the centerline. The solid lines correspond to mean values. The solid lines with dots symbolize the total rms, while the dotted lines represent the unresolved contributions obtained from the LES-ESF simulations.

Dispersed Phase Analysis

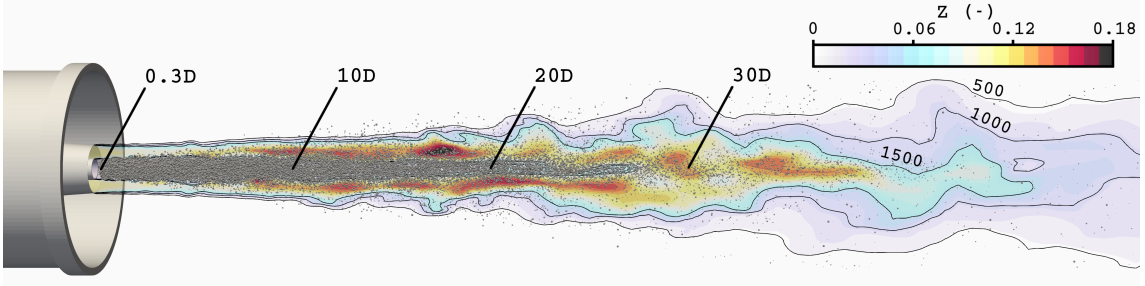

Figure 9.5: Instantaneous contours of mixture fraction superimposed with the Lagrangian parcels and isolines of temperature ($T = 500, 1000, 1500$K) for ESF(32).

A first qualitative impression of the liquid phase is provided in Figure 9.5, which presents instantaneous contours of the mixture fraction superimposed with the Lagrangian parcels

representing the liquid phase. Isolines of temperature are added in order to highlight the hot gases. As shown in the figure and previously outlined in Section 8.2, the parcels are injected $0.3\,D$ downstream of the burner exit plane. Then, parcels are primarily carried by the cold central core, which results in a stronger liquid flux in this region. However, as the axial distance increases, more parcels exit the cold core and interact with the hot pilot gases. This causes the droplets to quickly evaporate, yielding the observed gradual increase in mixture fraction. Downstream of $x = 30\,D$, significantly less parcels can be perceived as even more droplets have evaporated.

Going over to time-averaged droplet statistics, Figure 9.6 presents the Sauter mean diameter D_{32}, the mean diameter D_{10}, and the liquid volumetric flux. At the most upstream plane, all fields agree well with the experimental measurements. Considering Figure 9.6a and 9.6b, a first observation is that the representative diameters tend to be underestimated at higher axial distances from the burner exit. The reason for these deviations in the characteristic diameters are twofold: First, since the flame entrance into the spray jet occurs at higher axial distances (see previous section), small droplets are more likely to be present at higher axial positions. Secondly, by simplifying the injection velocity of the parcels to the gas phase velocity [77], a low Stokes numbers for all droplets injected is being presumed. This yields higher velocities for the large particles than experimentally determined. These higher velocities eventually favor the exit of large droplets from the central jet due to their higher inertia. Both effects are contributing to the lower characteristic diameters observed in the LES. Besides, the longer cold spray core is also responsible for the overprediction of the volumetric flux at $x = 20\,D$ (Figure 9.6c). The differences between ATF and ESF are only visible in the liquid volumetric flux profiles at higher axial positions. These are consistent with previous findings from the carrier phase analysis. As can be observed in Figures 9.3a, the flame enters the central region of the spray jet at lower axial positions for the ESF method. This earlier flame propagation yields stronger evaporation rates of the spray, which become apparent in the lower liquid volumetric fluxes for this approach. As for the carrier phase analysis, only marginal differences between the stochastic fields simulations can be perceived.

To sum up, considering the simplifications made in this work and the uncertainties in the boundary conditions, the observed deviations with the experimental measurements appear reasonable.

Temporal Evolution of the Subgrid Scalar PDF and Comparison with Presumed Shapes

Following the discussion and interpretation of the previous results, an in-depth analysis of the subgrid statistics is performed in the present section. The evaluations are performed for the most detailed simulation, i.e. the LES-ESF with 32 stochastic fields. The most common simplification to bypass the extensive computational costs linked to the transported FDF method is to presume the FDF shape prior to the simulation. Generally, the shape functions are parametrized by the moments of the distribution and it is commonly assumed that the FDF can be represented by its first two moments. This enables the preintegration of the thermochemical lookup-table with the moments of the distribution, which in turn become additional table controlling variables (thus increasing the dimensionality of the lookup-table). Additionally, either transport equations or algebraic closures are required for the moments of the subgrid PDF. However, solving one or two scalar transport equations in contrast to 8, 16 or 32 seems appealing, especially in the context of expensive spray combustion simulations. This motivates the subsequent analysis of the

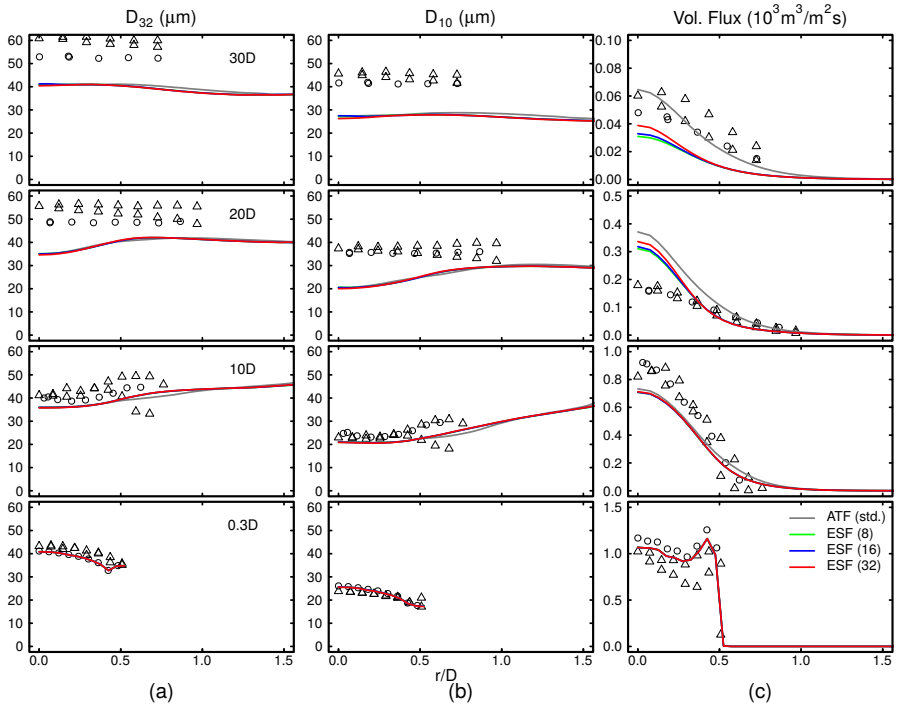

Figure 9.6: (a) Sauter mean diameter D_{32}, (b) mean diameter D_{10} and (c) liquid volumetric flux at various axial distances from the burner exit compared with available experimental data. ○ : exp. set A; △ : exp. set B.

ESF simulations and its comparison with various presumed PDF shapes.

The investigation is based on the time series of the table controlling variables at position A (see Figure 9.1), which is located at the centerline 20 jet diameters downstream of the burner exit plane. This position is chosen based on the high scalar fluctuations observed for temperature and mixture fraction shown in Figure 9.3 and 9.4. Note that the following analysis is performed at a representative position where a significant contribution of the subgrid terms is expected (a similar behavior has been observed at other positions).

Before going over to a detailed analysis of the PDF shapes, a first impression of the dynamics of the subgrid fluctuations is presented in Figure 9.7, which depicts the time series of the mixture fraction and progress variable stochastic fields alongside their respective first moment (red line). Both fields are shown in their normalized form. A first observation is that both, mixture fraction and reaction progress, are subject to strong variations, which is consistent with the high temporal fluctuations of temperature and mixture fraction at the centerline shown in previous figures. Especially, the high fluctuations of the normalized progress variable exhibited in the bottom part of Figure 9.7 indicate rapid changes between unburned (time instant ❶) and burnt states (time instant ❷). Additionally, the paths of the stochastic fields attest strong variations of the width and shape of the subgrid PDF for both mixture fraction and normalized progress variable. Moreover, it is also important to note that the mixture fraction stochastic fields extend over a significantly narrower range than the normalized reaction progress variable. Another remarkable aspect is the apparent strong correlation of mixture fraction and reaction progress variable, as can be deduced from the similar shape of the profiles and which is further attested by a Pearson correlation coefficient [13] for the stochastic fields of 0.87. It seems that the relative contributions of convection and diffusion, which are acting on

both, progress variable and mixture fraction, play a major role at this position.

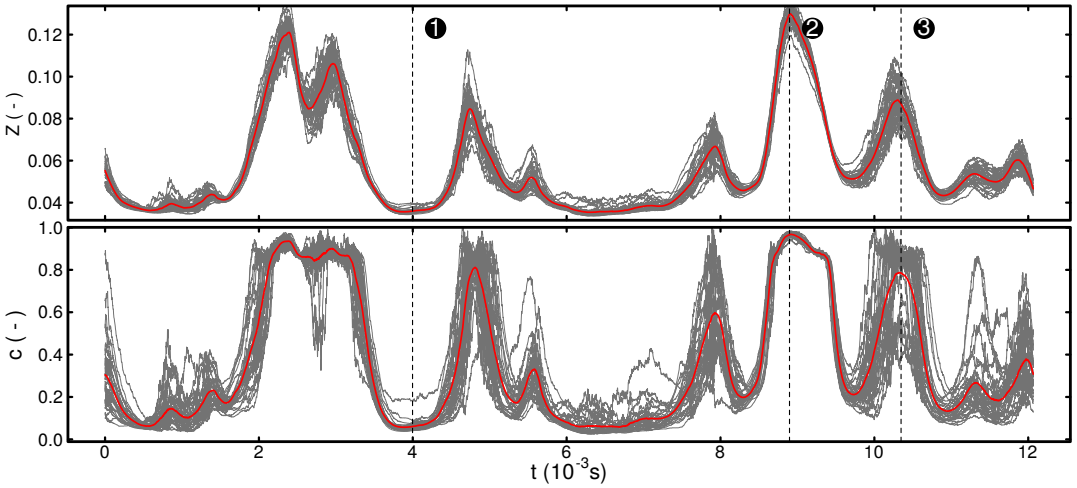

Figure 9.7: Temporal evolution of mixture fraction (top) and normalized progress variable (bottom) stochastic fields (grey lines) alongside their respective first moments, i.e. their arithmetic mean (red lines). The probe is located at the centerline, 20 diameters downstream of the burner exit plane. The position is displayed in Figure 9.1. The vertical dotted lines indicate three representative time instants, which will be discussed subsequently.

The transported stochastic fields can be used to evaluate the shape of the one time (and one point) marginal subgrid PDFs, which is done for the time instants ❶, ❷, and ❸ displayed in Figure 9.7. Note that the FDF shape is approximated by a Kernel Density Estimation (KDE) based on the distribution of the stochastic fields. The KDE of the PDF $\widehat{P}(x)$ is created by superimposing Gaussian density kernels and satisfies the same condition as the real PDF, that is $\widehat{P}(x) \geq 0$ and $\int_0^1 \widehat{P}(x)\mathrm{d}x = 1$. The bandwidth of the Gaussian kernels is here computed using the rule of thumb by Silverman [186]. The KDEs are plotted alongside three widely used presumed PDF shapes in Figure 9.8. The presumed PDF shapes investigated are (1) the δ-shape, (2) a top-hat profile and (3) a β-shape (see Section 3.1.3). Please note that the presumed shapes are all reconstructed using the first and second moments of the runtime-computed FDF obtained directly from the ESF-simulations. The upper row of Figure 9.8 depicts the mixture fraction subgrid FDFs, while the lower is showing the normalized progress variable. Starting with instant ❶ shown in the left column of Figure 9.8, one can clearly see differences between the KDE and the presumed shapes. At this time, the mixture is below the lower flammability limit and both PDFs are narrow. Although the β-shape resembles the KDE most suitably, all presumed shapes present deviations from the KDE. This can not be postulated for time instant ❷, where the rich mixture is almost fully burnt, as can be deduced from a mean normalized progress variable close to unity. Here, the β-shape is not too far off the real FDF KDE for both scalars and seems to perform better than the top-hat approximation. Going over to the time instant ❸ shown in the right column of Figure 9.8, one can observe that the KDE extends over a broader range of values for mixture fraction and normalized progress variable. For the mixture fraction, the ESF simulation predicts a subgrid distribution approximately ranging from the lower flammability limit to stoichiometry, which can be represented by a β-shape. Regarding the normalized progress variable, the distribution of the stochastic fields in Figure 9.7 at that time instant suggest a multi-modal shape, which is confirmed by the KDE shown in Figure 9.8. In this case, all presumed approaches have

difficulties to approximate the ESF-based solution.

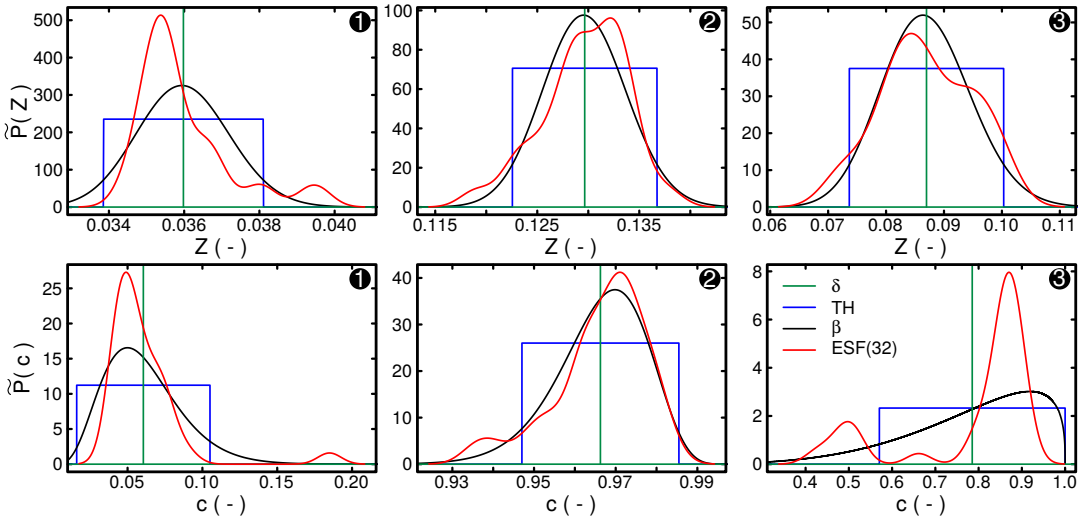

Figure 9.8: Comparison of common presumed subgrid PDF shapes and KDE approximation of the FDF obtained from the ESF simulation with 32 stochastic fields at the various time instants displayed in Figure 9.7 (at probe position A shown in Figure 9.1).

So far, only a qualitative comparison of the presumed PDFs shapes with the stochastic field simulation results has been provided. This analysis is subsequently complemented by a quantitative investigation shown in Figure 9.9. The figure is divided into three parts, where the first one compares the PDF integrated source term $\int_0^1 \int_0^1 \dot{\omega}_{PV} \widetilde{P}(Z,c)\mathrm{d}c\mathrm{d}Z$ obtained from the ESF simulation with 32 stochastic fields with its preintegrated equivalents resulting from various presumed shapes. The comparison is performed over the same time period shown in Figure 9.7. The second part exhibits the absolute difference $|\Delta\widetilde{\dot{\omega}}_{PV}|$ between the simulation results and the a-posteriori evaluated integrated source terms. Finally, the Hellinger distance H^2, which is a measure for the distance between two probability density functions, is evaluated for the marginal scalar PDFs using β and top-hat presumed shapes. Note that in order to estimate the differences between probability distributions, different approaches can be applied. For instance, Ihme and Pitsch [83] applied the Kullback-Leibler-divergence or maximum entropy principle in order to derive a statistically most likely distribution (SMLD) based on DNS data. In this work, the Hellinger distance is used, which is a symmetric measure to evaluate the similarity of two probability density function $P(x)$ and $Q(x)$ [34]

$$H^2(P,Q) = 1 - \int \sqrt{P(x)Q(x)}\mathrm{d}x \tag{9.1}$$

and is bounded between zero and one, where zero indicates identical distributions and one maximum distance between P and Q.

First, considering the first row of Figure 9.9, the non zero values in the profile of the reaction progress variable source term indicate regions of chemical reactions which are caused by the flame front approaching and/or crossing the probe location. In between those regions are zones where the source term is zero, which is consistent with the previously discussed temporal profiles of the stochastic fields. More precisely, the zones are mostly characterized by mixture fraction values below the lower flammability limit. The various PDF integrated source terms resulting from the presumed shapes are plotted alongside the closed source term obtained from the stochastic fields simulation. Thereby, statistical

independence of Z and c is implicitly assumed for the presumed PDF method and the same shape function is set for progress variable and mixture fraction. This yields three presumed joint PDF representations: (1) a double δ-, (2) a double top-hat- and (3) a double β-distribution.

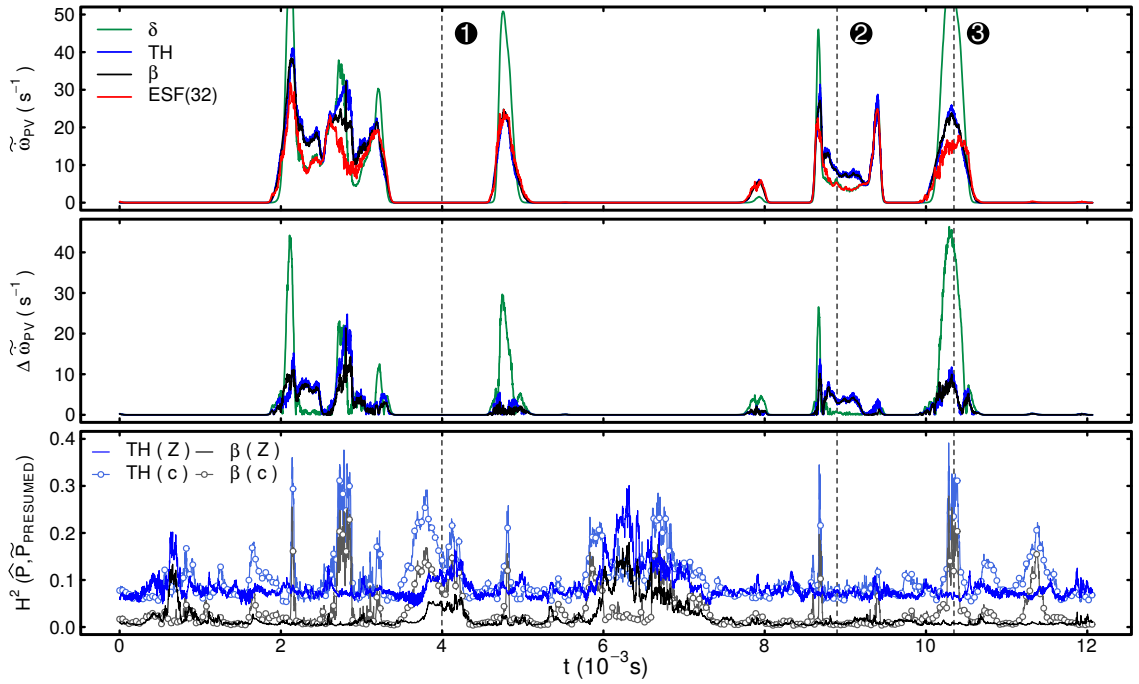

Figure 9.9: Top: Temporal evolution of the PDF-integrated progress variable source term $\widetilde{\dot{\omega}}_{PV}$ at the location of Probe A for the ESF simulations alongside results obtained from three presumed PDF shapes. Center: Absolute difference between the presumed approaches and the ESF(32) simulation results. Bottom: Hellinger distance between the stochastic fields FDF-KDE and the presumed shapes. Vertical dotted lines: time instants discussed previously.

As shown in the upper two rows of Figure 9.9, the value of the progress variable source term may vary considerably depending on which shape of the scalar subgrid PDF is assumed. Moreover, the results suggest that neglecting subgrid-scale interactions, as performed by assuming a double δ-shape, yields at most times considerably higher values of the source term compared with the ESF. The two other presumed approaches, that is the top-hat- and β-shape deliver considerably lower deviations and are at some points able to reproduce the results from the stochastic fields reasonably well (see for instance the source term peak around 5 ms). From these profiles, it is also possible to infer that the double top-hat- and double β-function presumed shapes perform almost evenly. This is especially noteworthy since the top-hat-function considerably facilitates the storage and the retrieval of the thermochemical state in the lookup-table compared to its β-counterpart (see for instance [134, 166]). Nonetheless, the integrated source term profiles corresponding to these presumed shapes also reveal substantial deviations from the ESF solution, as can be noticed exemplarily around time instant ❸, where both approaches are approximately 50% off the ESF results.

Finally, the temporal evolution of the Hellinger distance is shown in the bottom row of Figure 9.9 to quantify the differences between the presumed PDF shapes and the ESF results. A value of zero denotes identical functions and one indicates the maximum distance

between both probability density functions compared. The Hellinger distance is computed by comparing the marginal PDFs obtained from the ESF simulation with their respective presumed shape. A first observation is that the top-hat shape produces higher distances over the whole time range considered for both Z and c, which is expected considering the qualitative comparison shown in Figure 9.8. A second finding is that the subgrid probability density function of mixture fraction appears to be approximated more accurately than its normalized progress variable equivalent. This can be deduced from the higher distances obtained for the normalized progress variable. Going back to the actual source term differences shown in the plot above (Figure 9.9, center row), one can see a correlation with the Hellinger norm. For instance, the rise in $|\Delta\widetilde{\dot{\omega}}_{PV}|$ around 3 ms and at time instant ❸ clearly have their corresponding peaks in the H^2-profiles for the presumed FDFs of c. This finding, combined with a lower Hellinger distance for the mixture fraction presumed PDFs, confirms that the mismatch of the source terms is mainly caused by a deviation in the normalized progress variable presumed PDF shapes. Moreover, a comparison of the two lower plots of Figure 9.9 also reveals regions where the Hellinger distance attests high deviations in the PDF shape for both scalars, but no deviations between the presumed and transported PDF integrated source term are found. The most striking examples for such a scenario can be found in the time range from 6 ms to 8 ms and at time instant ❶. As previously outlined, in these ranges, the mixture fraction is below the lower flammability limit and the thermochemical state does not feature any strong nonlinearity across the table controlling variables. In these regions, predicting the correct shape of the subgrid-PDF has no impact on the closure of the reaction source term. This leads to the conclusion that deviations in PDF shapes cannot be exclusively used to evaluate the prediction ability of the a presumed PDF approach. On the other side, the sole comparison of certain PDF-integrated quantities also appears reductionistic due to the neglect of error compensation effects and due to the fact that each quantity varies differently across the thermochemical lookup-table. In this context, it is important to mention that in difference to the analysis presented in this work, presumed PDF approaches usually rely on closures in order to obtain the required moments of the marginal PDFs, which may introduce additional uncertainties. It seems that only a combination of both previously mentioned approaches, i.e. comparing the subgrid PDF integrated values and a direct comparison of the PDFs themselves with a suitable norm, can reveal the whole picture, thus helping to evaluate the prediction ability of presumed PDF shapes.

9.3 Summary and Conclusions

A novel strategy to perform simulations of turbulent spray combustion has been proposed in this chapter. The modeling framework is based on the Eulerian Stochastic Fields method coupled to the FGM tabulation strategy, while the multiphase flow is treated using a two-way coupled Euler-Lagrange approach. The predictive capability was demonstrated for the EtF6 operating condition of the Sydney spray burner. The results were compared with experimental measurements and previous simulations obtained using the Artificially Thickened Flame model with standard correction of droplet heat and mass transfer. It was demonstrated that the approach is able to reproduce the temporal statistics of the flow field reasonably well. Regarding the scalar statistics of the carrier phase, an underestimation of the flame propagation towards the jet centerline was revealed, which agrees with the previous observations made in Chapter 8 as well as in [44] and [78]. Nonetheless, as can be seen from the centerline evolution of the carrier scalars shown in Figure 9.4, the LES-ESF simulations predict an earlier propagation of the flame towards the center of

the spray jet, which shows better agreement with the experiments than the ATF results considered. The temporal scalar fluctuations indicate a much stronger flame-turbulence interaction for the ESF-based approach. The liquid phase statistics are in excellent agreement with the experimental measurements at lower axial positions but differ at higher distances from the burner exit, which is consistent with the evolution of the carrier temperature. Besides, it was shown that the ESF results are not strongly influenced by the number of stochastic fields employed in the range investigated, which confirms the previous investigations performed in Chapter 7 as well as other contributions for purely gaseous combustion [126, 75].

In a next step, the ESF simulation with 32 stochastic fields were used to characterize the evolution of the subgrid contributions at a representative position. Thereby, the time series shown for the two table controlling variables of mixture fraction and progress variable (in its normalized form) revealed strong variations of the subgrid FDF width and shape, which were confirmed by reconstructing the marginal subgrid FDFs at various time instants. Additionally, these one time, one point FDFs obtained from the ESF simulations were compared qualitatively with common presumed density function shapes. Thereafter, this analysis was complemented by a comparison of the PDF integrated source term of the progress variable. It was shown that the closed reaction progress variable source term value is strongly connected to the presumed FDF shape. The highest deviations between source term obtained from the transported and presumed FDF were observed for a double δ distribution and the smallest deviations for a double β-shaped FDF. Next, the temporal evolution of the Hellinger distance revealed a clear correlation with $|\Delta\widetilde{\omega}_{PV}|$, which is the absolute difference between computed and presumed FDF integrated source term. The profiles also suggest that the difference in source term value is mainly caused by a deviation in the normalized progress variable presumed PDF shapes. The analysis also unveiled regions where the Hellinger distance attests high deviations in the PDF shape for both scalars, but no deviations between the presumed and transported FDF integrated source term are found. This leads to the conclusion that quantifying the similarity of presumed and transported PDF shape is not sufficient to evaluate the prediction ability of a presumed PDF shape. On the other side, a quantification solely based on integral values for certain quantities also appears incomplete. For instance, comparing a different quantity than the progress variable source term may favor one or another presumed shape, depending on the operating condition and the respective subgrid fluctuations. The analysis demonstrates that a combination of both evaluation methods improves its informative quintessence. Nevertheless, a complete evaluation of the presumed PDF function performance and accuracy should include results obtained from simulations conducted with this approach. Furthermore, while the considered position unveiled various possible subgrid PDF shapes, many more scenarios exist. In order to make the present investigations more general, it remains to be shown whether the results can be transfered to other operating conditions or configurations. These aspects and the incorporation of subgrid effects on the disperse phase will be subject of future works.

PART V: CONCLUSIONS AND OUTLOOK

Chapter 10

Conclusions and Outlook

The foundation of the present research activities was to develop a framework to simulate turbulent multiphase combustion, in particular spray combustion, while consistently considering the interaction processes between turbulence, chemistry and droplets. For this purpose, two advanced combustion models, namely the artificially thickened flame model and the Eulerian stochastic field formalism, have been considered, implemented, adapted and further developed. The starting point was to demonstrate the expected behavior by means of simple test-cases. Thereafter, the methodologies were applied to single phase turbulent combustion. It was shown that the modeling framework is able to reproduce experimental measurements with great accuracy. The final step in this ladder of gradually increasing complexity was to couple the respective frameworks with an additional liquid phase, described by means of Lagrangian particles. The simulations were performed for the configuration EtF6 of the Sydney Spray Burner.

For the liquid phase treatment, two novel approaches to represent the interaction of droplets with a thickened flame were proposed and evaluated. By taking into account the relative orientation of flame front and droplet movement using the novel projection correction method, the overall consistency of the modeling framework was improved. Additionally, it was shown that the manner in which the interaction of droplet with a thickened flame is treated, strongly affects global flame quantities, for instance the length of the cold central spray core or the flame length, as well as the temporal carrier and liquid phase statistics.

Additionally, a novel modeling framework to compute turbulent spray combustion based on the Eulerian Stochastic Fields method coupled to the FGM tabulation strategy was proposed. Its predictive capability was demonstrated and the results were used to characterize the evolution of the subgrid contributions at a representative position. Furthermore, the comparison of the ESF-results with various presumed probability function shapes (qualitatively and quantitatively) revealed that the adopted ESF method can be a valuable tool to evaluate presumed PDF approaches.

The modeling framework implemented builds an excellent foundation for future investigations. For instance, parts of the framework have already been used to investigate the effect of hydrogen addition in stratified premixed combustion using the ATF approach [203]. Another promising research area is the numerical prediction of soot formation, which is performed as part of the ESTiMatE project [2]. Since it is well known that the initial formation of soot from its precursors occurs at very small scales, the advanced closure for the turbulence-chemistry interaction provided by the ESF appears promising to model such phenomena.

Many possible paths can be taken to further improve the modeling strategy. Regarding the tabulated chemistry approach adopted, the inclusion of evaporative cooling effects caused by the droplets in the carrier phase (or heat losses in general) is desired. This was, for instance, performed in Sacomano Filho et al. [171], who demonstrated that the consideration of evaporative cooling delivers better agreements with experiments in comparison to its neglect. Another possible improvement is the inclusion of differential diffusion effects within the tabulated chemistry framework in the context of ESF, similarly to the work by Hansinger et al. [74], where a reduced chemical mechanism was used.

In view of the high memory demand connected to high-dimensional thermochemical lookup-tables, the consideration of artificial neural networks (ANN) as a replacement for such tables seems appealing. This idea is not new and was for instance put into practice by Christo et al. [31] and Balsco et al. [19]. However, the idea regained importance as the development of suitable software libraries to easily embed such neural networks in own applications became available [52, 85, 73].

To further improve the understanding of spray combustion and its modeling, high-quality experimental data will be needed. The standards for such experiments are high. They must provide detailed boundary conditions for both, the carrier phase and the spray, which is a complex endeavor in itself. Additionally, detailed measurements of the velocity and scalar fields should be made available alongside detailed information regarding the evolution of the disperse liquid phase. This is a non-trivial problem which involves the usage of multiple measurement techniques. Regarding quantitative scalar field measurements, the main problem is the presence of the liquid phase, which induces strong reflection and refraction of the excitation light source towards the sensors, hence prohibiting any useful signal detection. First measurements of the species concentration, temperature and mixture fraction performed by Dunn et al. [45] for the Sydney Needle Burner configuration (an extension of the Sydney Spray Burner investigated in this work) are promising and could help to identify potential strengths and weaknesses of the developed modeling framework. Future progress in the field of spray combustion simulations is therefore also tightly coupled to the progress made in experimental measurements.

Bibliography

[1] Clean Combustion Research Group Database, University of Sydney. `http://web.aeromech.usyd.edu.au/thermofluids/database.php`, 2019. Online; accessed: 2019-07-23.

[2] ESTiMatE (Emissions SooT ModEl) - project. `https://estimate-project.eu/`, 2020. Online; accessed: 2021-04-22.

[3] B. Abramzon and W. A. Sirignano. Droplet vaporization model for spray combustion calculations. *International journal of heat and mass transfer*, 32(9):1605–1618, 1989.

[4] K. Aschmoneit. *Numerische Beschreibung technischer Verbrennungssysteme (in German).* PhD thesis, Technische Universität Darmstadt, 2013.

[5] A. Avdić, G. Kuenne, F. di Mare, and J. Janicka. LES combustion modeling using the eulerian stochastic field method coupled with tabulated chemistry. *Combustion and Flame*, 175:201–219, 2017.

[6] A. Avdić, G. Kuenne, A. Ketelheun, A. Sadiki, S. Jakirlić, and J. Janicka. High performance computing of the darmstadt stratified burner by means of large eddy simulation and a joint ATF-FGM approach. *Computing and Visualization in Science*, 16(2):77–88, 2013.

[7] J. H. Bae, J. Y. Yoo, and H. Choi. Direct numerical simulation of turbulent supercritical flows with heat transfer. *Physics of fluids*, 17(10):105104, 2005.

[8] R. S. Barlow. Sandia/TUD piloted CH4/air jet flames. `https://www.sandia.gov/TNF/DataArch/FlameD.html`. Online; accessed 06.04.2021.

[9] R. S. Barlow. TNF workshop. `https://tnfworkshop.org/`. Online; accessed 06.04.2021.

[10] R. S. Barlow and J. H. Frank. Effects of turbulence on species mass fractions in methane/air jet flames. In *Symposium (International) on Combustion*, volume 27, pages 1087–1095. Elsevier, 1998.

[11] R. S. Barlow, J. H. Frank, A. N. Karpetis, and J.-Y. Chen. Piloted methane/air jet flames: Transport effects and aspects of scalar structure. *Combustion and flame*, 143:433–449, 2005.

[12] J. Bellan and M. Summerfield. Theoretical examination of assumptions commonly used for the gas phase surrounding a burning droplet. *Combustion and Flame*, 33:107–122, 1978.

[13] J. Benesty, J. Chen, Y. Huang, and I. Cohen. Pearson correlation coefficient. In *Noise reduction in speech processing*, pages 1–4. Springer, 2009.

[14] R. W. Bilger. The structure of turbulent nonpremixed flames. *Symposium (International) on Combustion*, 22(1):475–488, jan 1989.

[15] M. Bini and W. P. Jones. Particle acceleration in turbulent flows: A class of nonlinear stochastic models for intermittency. *Physics of Fluids*, 19(3):035104, 2007.

[16] M. Bini and W. P. Jones. Large eddy simulation of an evaporating acetone spray. *International Journal of Heat and Fluid Flow*, 30(3):471–480, 2009.

[17] S. Binti Saharin. *Vaporization and autoignition characteristics of ethanol and 1-propanol droplets: influence of water.* PhD thesis, Université de Bourgogne, 2013.

[18] S. Binti Saharin, B. Lefort, C. Morin, C. Chauveau, L. Le Moyne, and R. Kafafy. Vaporization characteristics of ethanol and 1-propanol droplets at high temperatures. *Atomization and Sprays*, 22(3):207–226, 2012.

[19] J. A. Blasco, N. Fueyo, C. Dopazo, and J. Ballester. Modelling the temporal evolution of a reduced combustion chemical system with an artificial neural network. *Combustion and Flame*, 113(1-2):38–52, 1998.

[20] B. Böhm, J.H. Frank, and A.s Dreizler. Temperature and mixing field measurements in stratified lean premixed turbulent flames. *Proceedings of the Combustion Institute*, 33(1):1583–1590, 2011.

[21] M. Boileau. *SGE de l'allumage diphasique des foyers aeronautiques (in French)*. PhD thesis, Institut National Polytechnique de Toulouse, France, 2007.

[22] T.D. Butler and P. j. O'Rourke. A numerical method for two dimensional unsteady reacting flows. *Symposium (International) on Combustion*, 16(1):1503–1515, jan 1977.

[23] V. Bykov and U. Maas. The extension of the ILDM concept to reaction–diffusion manifolds. *Combustion Theory and Modelling*, 11(6):839–862, nov 2007.

[24] D. Carrington. Wide range of cars emit more pollution in realistic driving tests, data shows. `https://www.theguardian.com/environment/2015/sep/30/wide-range-of-cars-emit-more-pollution-in-real-driving-conditions-tests-show`, 2015. Online; accessed: 2021-04-27.

[25] F. Cavalcanti Miranda. *Large Eddy Simulation of Turbulent Reacting Flows With Radiative Heat Transfer*. PhD thesis, Technical University of Darmstadt, Germany, 2019.

[26] F. Charlette, C. Meneveau, and D. Veynante. A power-law flame wrinkling model for LES of premixed turbulent combustion part I: non-dynamic formulation and initial tests. *Combustion and Flame*, 131(1-2):159–180, 2002.

[27] F. Charlette, C. Meneveau, and D. Veynante. A power-law flame wrinkling model for LES of premixed turbulent combustion part II: dynamic formulation. *Combustion and Flame*, 131(1-2):181–197, 2002.

[28] B. Cheneau. *Etudes numerique de combustion dans un bruleur diphasique turbulent a deux etages (in french)*. PhD thesis, Universite de Paris-Saclay, 2019.

[29] B. Cheneau, A. Vié, and S. Ducruix. Characterization of the hysteresis cycle in a two-stage liquid-fueled swirled burner through numerical simulation. *Proceedings of the Combustion Institute*, 37(4):5245–5253, 2019.

[30] M. Chrigui, A. R. Masri, A. Sadiki, and J. Janicka. Large eddy simulation of a polydisperse ethanol spray flame. *Flow, turbulence and combustion*, 90(4):813–832, 2013.

[31] F. C. Christo, A. R. Masri, E. M. Nebot, and S. B. Pope. An integrated PDF/neural network approach for simulating turbulent reacting systems. In *Symposium (International) on Combustion*, volume 26, pages 43–48. Elsevier, 1996.

[32] O. Colin, F. Ducros, D. Veynante, and T. Poinsot. A thickened flame model for large eddy simulations of turbulent premixed combustion. *Physics of fluids*, 12(7):1843–1863, 2000.

[33] R Courant, K. Friedrichs, and H. Lewy. Über die partiellen differenzengleichungen der mathematischen physik (in german). *Mathematische Annalen*, 100(1):32–74, 1928.

[34] H. Cramér. *Mathematical methods of statistics*. Princeton university press, 1999.

[35] C. T. Crowe, M. P. Sharma, and D. E. Stock. The particle-source-in cell (PSI-CELL) model for gas-droplet flows. *J. Fluids Eng.*, 99(2):325–332, 1977.

[36] T. E. Daubert and R. P. Danner. *Data compilation tables of properties of pure compounds*. Design Institute for Physical Property Data, American Institute of Chemical Engineers, 1985.

[37] S. De, K. N. Lakshmisha, and R. W. Bilger. Modeling of nonreacting and reacting turbulent spray jets using a fully stochastic separated flow approach. *Combustion and Flame*, 158(10):1992–2008, 2011.

[38] P. Domingo, L. Vervisch, and J. Réveillon. DNS analysis of partially premixed combustion in spray and gaseous turbulent flame-bases stabilized in hot air. *Combustion and Flame*, 140(3):172–195, 2005.

[39] C. Dopazo and E. E. O'Brien. Functional formulation of nonisothermal turbulent reactive flows. *The Physics of Fluids*, 17(11):1968–1975, 1974.

[40] C. G. Downing. The evaporation of drops of pure liquids at elevated temperatures: Rates of evaporation and wet-bulb temperatures. *AIChE Journal*, 12(4):760–766, 1966.

[41] A. Dreizler, H. Pitsch, C. Schulz, and J. Janicka. Positionspapier: Energiewende verlässlich, machbar, technologieoffen (in german). Technical report, 2020.

[42] L. Dressler, F. Ries, G. Kuenne, J. Janicka, and A. Sadiki. Analysis of shear effects on mixing and reaction layers in premixed turbulent stratified flames using LES coupled to tabulated chemistry. *Combustion Science and Technology*, 2019.

[43] L. Dressler, F. L. Sacomano Filho, F. Ries, H. Nicolai, J. Janicka, and A. Sadiki. Numerical prediction of turbulent spray flame characteristics using the filtered eulerian stochastic field approach coupled to tabulated chemistry. *Fluids*, 6(2), 2021.

[44] L. Dressler, F. L. Sacomano Filho, A. Sadiki, and J. Janicka. Influence of thickening factor treatment on predictions of spray flame properties using the ATF model and tabulated chemistry. *Flow Turbulence and Combustion*, 106, 2021.

[45] M. J. Dunn, A. R. W. Macfarlane, R. S. Barlow, D. Geyer, K. Dieter, and A. R. Masri. Spontaneous raman–LIF–CO–OH measurements of species concentration in turbulent spray flames. *Proceedings of the Combustion Institute*, 2021.

[46] L. Durand and W. Polifke. Implementation of the thickened flame model for large eddy simulation of turbulent premixed combustion in a commercial solver. In *Volume 2: Turbo Expo 2007*. ASME, 2007.

[47] S. Elghobashi. On predicting particle-laden turbulent flows. *Applied scientific research*, 52(4):309–329, 1994.

[48] European Commission. The european green deal, COM(2019) 640 final. Technical report, European Union, 2019.

[49] J. H. Ferziger, M. Perić, and R. L. Street. *Computational methods for fluid dynamics*, volume 3. Springer, 2002.

[50] B. Fiorina, O. Gicquel, L. Vervisch, S. Carpentier, and N. Darabiha. Approximating the chemical structure of partially premixed and diffusion counterflow flames using FPI flamelet tabulation. *Combustion and flame*, 140(3):147–160, 2005.

[51] B. Fiorina, R. Vicquelin, P. Auzillon, N. Darabiha, O. Gicquel, and D. Veynante. A filtered tabulated chemistry model for LES of premixed combustion. *Combustion and Flame*, 157(3):465–475, 2010.

[52] F. Flemming, A. Sadiki, and J. Janicka. LES using artificial neural networks for chemistry representation. *Progress in Computational Fluid Dynamics, An International Journal*, 5(7):375–385, 2005.

[53] J. Floyd, A. M. Kempf, A. Kronenburg, and R. H. Ram. A simple model for the filtered density function for passive scalar combustion LES. *Combustion Theory and Modelling*, 13(4):559–588, 2009.

[54] O. R. Fox. *Computational Models for Turbulent Reacting Flows*. Cambridge series in chemical engineering. Cambridge University Press, illustrated edition edition, 2003.

[55] R. O. Fox. The fokker–planck closure for turbulent molecular mixing: Passive scalars. *Physics of Fluids A: Fluid Dynamics*, 4(6):1230–1244, 1992.

[56] B. Franzelli, B. Fiorina, and N. Darabiha. A tabulated chemistry method for spray combustion. *Proceedings of the Combustion Institute*, 34(1):1659–1666, jan 2013.

[57] B. Franzelli, A. Vié, M. Boileau, B. Fiorina, and N. Darabiha. Large eddy simulation of swirled spray flame using detailed and tabulated chemical descriptions. *Flow, Turbulence and Combustion*, 98(2):633–661, sep 2016.

[58] D. Fredrich, W. P. Jones, and A. J. Marquis. Application of the eulerian subgrid probability density function method in the large eddy simulation of a partially premixed swirl flame. *Combustion Science and Technology*, 191(1):137–150, 2019.

[59] D. Fredrich, W. P. Jones, and A. J. Marquis. The stochastic fields method applied to a partially premixed swirl flame with wall heat transfer. *Combustion and Flame*, 205:446–456, 2019.

[60] V. A. Frost. Model of a turbulent, diffusion-controlled flame jet. *Fluid Mechanics Soviet Research*, 4:124–133, 1975.

[61] S. Gallot-Lavallée and W. P. Jones. Large eddy simulation of spray auto-ignition under EGR conditions. *Flow, Turbulence and Combustion*, 96(2):513–534, 2016.

[62] S. Gallot-Lavallée, W. P. Jones, and A. J. Marquis. Large eddy simulation of an ethanol spray flame under mild combustion with the stochastic fields method. *Proceedings of the Combustion Institute*, 36(2):2577–2584, 2017.

[63] S. Ganter, A. Heinrich, T. Meier, G. Kuenne, C. Jainski, M. C. Rißmann, Dreizler A., and J. Janicka. Numerical analysis of laminar methane–air side-wall-quenching. *Combustion and Flame*, 186:299–310, dec 2017.

[64] A. Garmory. *Micromixing effects in atmospheric reacting flows*. PhD thesis, University of Cambridge, 2008.

[65] H.-W. Ge. *Probability density function modeling of turbulent non-reactive and reactive spray flows*. PhD thesis, Ruprecht-Karls-Univesität Heidelberg, 2006.

[66] M. Germano, U. Piomelli, P. Moin, and W. H. Cabot. A dynamic subgrid-scale eddy viscosity model. *Physics of Fluids A: Fluid Dynamics*, 3(7):1760–1765, 1991.

[67] O. Gicquel, N. Darabiha, and D. Thévenin. Laminar premixed hydrogen/air counterflow flame simulations using flame prolongation of ILDM with differential diffusion. *Proceedings of the Combustion Institute*, 28(2):1901–1908, jan 2000.

[68] D. G. Goodwin, R. L. Speth, H. K. Moffat, and B. W. Weber. Cantera: An object-oriented software toolkit for chemical kinetics, thermodynamics, and transport processes. `https://www.cantera.org`, 2021. Version 2.5.1.

[69] J. D. Gounder. *An experimental investigation of non-reacting and reacting spray jets*. PhD thesis, School of Aerospace, Mechanical and Mechatronic Engineering, University of Sydney, 2009.

[70] J. D. Gounder, A. Kourmatzis, and A. R. Masri. Turbulent piloted dilute spray flames: Flow fields and droplet dynamics. *Combustion and flame*, 159(11):3372–3397, 2012.

[71] C. J. Greenshields. OpenFOAM programmer's guide. 2015.

[72] F. Hahn. *Zur Vorhersage technischer Verbrennungssysteme im Hinblick auf flüssige Brennstoffe (in German)*. PhD thesis, Technische Universität Darmstadt, 2009.

[73] M. Hansinger, Y. Ge, and M. Pfitzner. Deep residual networks for flamelet/progress variable tabulation with application to a piloted flame with inhomogeneous inlet. *Combustion Science and Technology*, 0(0):1–27, 2020.

[74] M. Hansinger, M. Pfitzner, and V. Sabelnikov. LES of oxy-fuel jet flames using the eulerian stochastic fields method with differential diffusion. *Proceedings of the Combustion Institute*, 2020.

[75] M. Hansinger, T. Zirwes, J. Zips, M. Pfitzner, F. Zhang, P. Habisreuther, and H. Bockhorn. The eulerian stochastic fields method applied to large eddy simulations of a piloted flame with inhomogeneous inlet. *Flow, Turbulence and Combustion*, pages 1–31, 2020.

[76] D. C. Haworth. Progress in probability density function methods for turbulent reacting flows. *Progress in Energy and Combustion Science*, 36(2):168–259, 2010.

[77] C. Heye, V. Raman, and A. R. Masri. LES/probability density function approach for the simulation of an ethanol spray flame. *Proceedings of the Combustion Institute*, 34(1):1633–1641, 2013.

[78] C. R. Heye, A. Kourmatzis, V. Raman, and A. R. Masri. A comparative study of the simulation of turbulent ethanol spray flames. In *Experiments and numerical simulations of turbulent combustion of diluted sprays*, pages 31–54. Springer, 2014.

[79] C. W. Hirt and B. D. Nichols. Volume of fluid (VOF) method for the dynamics of free boundaries. *Journal of computational physics*, 39(1):201–225, 1981.

[80] C. Hollmann and E. Gutheil. Modeling of turbulent spray diffusion flames including detailed chemistry. In *Symposium (international) on combustion*, volume 26, pages 1731–1738. Elsevier, 1996.

[81] A. Hosseinzadeh, T. Schmitt, A. Sadiki, and J. Janicka. Application of the dynamic F-TACLES combustion model to a lean premixed turbulent flame. *Flow, Turbulence and Combustion*, 95(2):481–500, 2015.

[82] Y. Hu and R. Kurose. Nonpremixed and premixed flamelets LES of partially premixed spray flames using a two-phase transport equation of progress variable. *Combustion and Flame*, 188:227–242, feb 2018.

[83] M. Ihme and H. Pitsch. Prediction of extinction and reignition in nonpremixed turbulent flames using a flamelet/progress variable model: 1. a priori study and presumed PDF closure. *Combustion and Flame*, 155(1):70 – 89, 2008.

[84] M. Ihme and H. Pitsch. Prediction of extinction and reignition in nonpremixed turbulent flames using a flamelet/progress variable model: 2. application in LES of sandia flames D and E. *Combustion and flame*, 155(1-2):90–107, 2008.

[85] M. Ihme, C. Schmitt, and H. Pitsch. Optimal artificial neural networks and tabulation methods for chemistry representation in LES of a bluff-body swirl-stabilized flame. *Proceedings of the Combustion Institute*, 32(1):1527–1535, 2009.

[86] H. G. Im, T. S. Lund, and J. H. Ferziger. Large eddy simulation of turbulent front propagation with dynamic subgrid models. *Physics of Fluids*, 9(12):3826–3833, 1997.

[87] R. I. Issa. Solution of the implicitly discretised fluid flow equations by operator-splitting. *Journal of computational physics*, 62(1):40–65, 1986.

[88] F. A. Jaberi, P. J. Colucci, S. James, P. Givi, and S. B. Pope. Filtered mass density function for large-eddy simulation of turbulent reacting flows. *Journal of Fluid Mechanics*, 401:85–121, 1999.

[89] S. James, J. Zhu, and M. S. Anand. Large eddy simulations of turbulent flames using the filtered density function model. *Proceedings of the Combustion Institute*, 31(2):1737–1745, 2007.

[90] J. Janicka and A. Sadiki. Large eddy simulation of turbulent combustion systems. *Proceedings of the Combustion Institute*, 30(1):537–547, jan 2005.

[91] H. Jasak. *Error analysis and estimation for the finite volume method with applications to fluid flows.* PhD thesis, Imperial College London (University of London), 1996.

[92] H. Jasak, A. Jemcov, and Z. Tukovic. OpenFOAM: A C++ library for complex physics simulations. In *International workshop on coupled methods in numerical dynamics*, pages 1–20. IUC Dubrovnik Croatia, 2007.

[93] P. Jenny, D. Roekaerts, and N. Beishuizen. Modeling of turbulent dilute spray combustion. *Progress in Energy and Combustion Science*, 38(6):846–887, 2012.

[94] W. P. Jones, A. J. Marquis, and D. Noh. LES of a methanol spray flame with a stochastic sub-grid model. *Proceedings of the Combustion Institute*, 35(2):1685–1691, 2015.

[95] W. P. Jones, A. J. Marquis, and K. Vogiatzaki. Large-eddy simulation of spray combustion in a gas turbine combustor. *Combustion and flame*, 161(1):222–239, 2014.

[96] W. P. Jones and S. Navarro-Martinez. Numerical study of n-heptane auto-ignition using LES-PDF methods. *Flow, turbulence and combustion*, 83(3):407–423, 2009.

[97] W. P. Jones, S. Navarro-Martinez, and O. Röhl. Large eddy simulation of hydrogen auto-ignition with a probability density function method. *Proceedings of the Combustion Institute*, 31(2):1765–1771, 2007.

[98] W. P. Jones and V. N. Prasad. Large eddy simulation of the sandia flame series (d–f) using the eulerian stochastic field method. *Combustion and Flame*, 157(9):1621–1636, 2010.

[99] D. Jou, J. Casas-Vázquez, and G. Lebon. *Classical and Rational Formulations of Non-equilibrium Thermodynamics*, pages 3–40. Springer Berlin Heidelberg, Berlin, Heidelberg, 1996.

[100] J. C. G. Kadavelil. *Numerische Beschreibung reaktiver Zweiphasenströmungen für technische Anwendungen (in German).* PhD thesis, Technische Universität Darmstadt, 2017.

[101] A. R. Kerstein, W. T. Ashurst, and F. A. Williams. Field equation for interface propagation in an unsteady homogeneous flow field. *Physical Review A*, 37(7):2728, 1988.

[102] M. Klein. *Towards LES as an Engineering Tool.* habilitation, Technical University of Darmstadt, 2008.

[103] P. E. Kloeden and E. Platen. *Numerical solution of stochastic differential equations*. Springer Science & Business Media, 1992.

[104] Ed. Knudsen, Shashank, and H. Pitsch. Modeling partially premixed combustion behavior in multiphase LES. *Combustion and Flame*, 162(1):159–180, 2015.

[105] A. N. Kolmogorov. The local structure of turbulence in incompressible viscous fluid for very large reynolds numbers. *Cr Acad. Sci. URSS*, 30:301–305, 1941.

[106] G. Kuenne, A. Ketelheun, and J. Janicka. LES modeling of premixed combustion using a thickened flame approach coupled with FGM tabulated chemistry. *Combustion and Flame*, 158(9):1750–1767, 2011.

[107] G. Kuenne, F. Seffrin, F. Fuest, T. Stahler, A. Ketelheun, D. Geyer, J. Janicka, and A. Dreizler. Experimental and numerical analysis of a lean premixed stratified burner using 1D raman/rayleigh scattering and large eddy simulation. *Combustion and Flame*, 159(8):2669–2689, 2012.

[108] G. Künne. *Large Eddy Simulation of Premixed Combustion Using Artificial Flame Thickening Coupled with Tabulated Chemistry.* PhD thesis, Technical University of Darmstadt, 2012.

[109] K. K. Kuo and R. Acharya. *Fundamentals of turbulent and multiphase combustion*. John Wiley & Sons, 2012.

[110] A Lefebvre. Atomization and sprays, 1989.

[111] J.-P. Legier, T. Poinsot, and D. Veynante. Dynamically thickened flame LES model for premixed and non-premixed turbulent combustion. In *Proceedings of the summer program*, volume 12. Center for Turbulence Research Stanford, CA, 2000.

[112] J. L. Lumley. *Stochastic tools in turbulence*. Dover Publications Inc., 2007.

[113] L. Ma, B. Naud, and D. Roekaerts. Transported PDF modeling of ethanol spray in hot-diluted coflow flame. *Flow, Turbulence and Combustion*, 96(2):469–502, jun 2015.

[114] U. Maas and S. B. Pope. Simplifying chemical kinetics: Intrinsic low-dimensional manifolds in composition space. *Combustion and Flame*, 88(3-4):239–264, mar 1992.

[115] R. Mahmoud. *Development and Application of an Eulerian Density Function Methodology coupled to Flamelet Progress Variable Approach for the Simulation of Oxyfuel Combustion*. PhD thesis, Université Paris-Saclay, France & Technical University of Darmstadt, Germany, 2020.

[116] R. Mahmoud, M. Jangi, F. Ries, B. Fiorina, J. Janicka, and A. Sadiki. Combustion characteristics of a non-premixed oxy-flame applying a hybrid filtered eulerian stochastic field/flamelet progress variable approach. *Applied Sciences*, 9(7):1320, 2019.

[117] D. L. Marchisio and R. O. Fox. *Computational models for polydisperse particulate and multiphase systems*. Cambridge University Press, 2013.

[118] N. M. Marinov. A detailed chemical kinetic model for high temperature ethanol oxidation. *International Journal of Chemical Kinetics*, 31(3):183–220, 1999.

[119] A. R. Masri, R. W. Dibble, and R. S. Barlow. The structure of turbulent nonpremixed flames revealed by raman-rayleigh-LIF measurements. *Progress in Energy and Combustion Science*, 22(4):307–362, 1996.

[120] A. R. Masri and J. D. Gounder. Turbulent spray flames of acetone and ethanol approaching extinction. *Combustion Science and Technology*, 182(4-6):702–715, 2010.

[121] A. R. Masri and J. D. Gounder. Details and complexities of boundary conditions in turbulent piloted dilute spray jets and flames. In *Experiments and numerical simulations of diluted spray turbulent combustion*, pages 41–68. Springer, 2011.

[122] B. J. McBride, S. Gordon, and M. A. Reno. Coefficients for calculating thermodynamic and transport properties of individual species. NASA Technical Memorandum 4513, National Aeronautics and Space Administration, 1993.

[123] R. S. Miller, K. Harstad, and J. Bellan. Evaluation of equilibrium and non-equilibrium evaporation models for many-droplet gas-liquid flow simulations. *International Journal of Multiphase Flow*, 24(6):1025–1055, 1998.

[124] H. Müller, F. Ferraro, and M. Pfitzner. Implementation of a steady laminar flamelet model for non-premixed combustion in LES and RANS simulations. In *8th International OpenFOAM Workshop*, pages 1–12, 2013.

[125] M. Muradoglu, P. Jenny, S. B. Pope, and D. A. Caughey. A consistent hybrid finite-volume/particle method for the PDF equations of turbulent reactive flows. *Journal of Computational Physics*, 154(2):342–371, 1999.

[126] R. Mustata, L. Valino, C. Jimenez, W. P. Jones, and S. Bondi. A probability density function eulerian monte carlo field method for large eddy simulations: Applications to a turbulent piloted methane/air diffusion flame (sandia d). *Combustion and Flame*, 145:88–104, 2006.

[127] P.D. Nguyen, L. Vervisch, V. Subramanian, and P. Domingo. Multidimensional flamelet-generated manifolds for partially premixed combustion. *Combustion and Flame*, 157(1):43–61, 2010.

[128] F. Nicoud and F. Ducros. Subgrid-scale stress modelling based on the square of the velocity gradient tensor. *Flow, turbulence and Combustion*, 62(3):183–200, 1999.

[129] F. Nicoud, H. B. Toda, O. Cabrit, S. Bose, and J. Lee. Using singular values to build a subgrid-scale model for large eddy simulations. *Physics of fluids*, 23(8):085106, 2011.

[130] N. Nordin. *Complex chemistry modeling of diesel spray combustion.* PhD thesis, Chalmers University of Technology Sweden, 2001.

[131] W. L. Oberkampf and F. G. Blottner. Issues in computational fluid dynamics code verification and validation. *AIAA journal*, 36(5):687–695, 1998.

[132] W. L. Oberkampf, T. G. Trucano, and C. Hirsch. Verification, validation, and predictive capability in computational engineering and physics. *Appl. Mech. Rev.*, 57(5):345–384, 2004.

[133] E. E. O'brien. The probability density function (PDF) approach to reacting turbulent flows. In *Turbulent reacting flows*, pages 185–218. Springer, 1980.

[134] C. Olbricht, O. T. Stein, J. Janicka, J. A. Van Oijen, S. Wysocki, and A. M. Kempf. LES of lifted flames in a gas turbine model combustor using top-hat filtered PFGM chemistry. *Fuel*, 96:100–107, 2012.

[135] P. J. O'Rourke and F. V. Bracco. Two scaling transformations for the numerical computation of multidimensional unsteady laminar flames. *Journal of Computational Physics*, 33(2):185–203, 1979.

[136] S. V. Patankar. *Numerical heat transfer and fluid flow.* Taylor & Francis, 2018.

[137] S. V. Patankar and D. B. Spalding. A calculation procedure for heat, mass and momentum transfer in three-dimensional parabolic flows. In *Numerical Prediction of Flow, Heat Transfer, Turbulence and Combustion*, pages 54–73. Elsevier, 1983.

[138] V. C. Patel and M. R. Head. Some observations on skin friction and velocity profiles in fully developed pipe and channel flows. *Journal of Fluid Mechanics*, 38(1):181–201, 1969.

[139] D. Paulhiac. *Modelisation de la combustion d'un spray dans un bruleur aeronautique (in French).* PhD thesis, Institut National Politechnique de Toulouse, France, 2015.

[140] C. Pera, J. Réveillon, L. Vervisch, and P. Domingo. Modeling subgrid scale mixture fraction variance in LES of evaporating spray. *Combustion and Flame*, 146(4):635–648, 2006.

[141] N. Peters. The turbulent burning velocity for large-scale and small-scale turbulence. *Journal of Fluid Mechanics*, 384:107–132, 1999.

[142] N. Peters. *Turbulent Combustion.* Cambridge University Press, 2000.

[143] M. A. Picciani. *Investigation of numerical resolution requirements of the Eulerian Stochastic Fields and the Thickened Stochastic Field approach.* PhD thesis, University of Southampton, 2018.

[144] C. D. Pierce and P. Moin. Progress-variable approach for large-eddy simulation of non-premixed turbulent combustion. *Journal of Fluid Mechanics*, 504:73–97, apr 2004.

[145] H. Pitsch. A consistent level set formulation for large-eddy simulation of premixed turbulent combustion. *Combustion and Flame*, 143(4):587–598, 2005.

[146] H. Pitsch. Large eddy simulation of turbulent combustion. *Annual Review of Fluid Mechanics*, 38(1):453–482, jan 2006.

[147] H. Pitsch and L. Duchamp de Lageneste. Large-eddy simulation of premixed turbulent combustion using a level-set approach. *Proceedings of the Combustion Institute*, 29(2):2001–2008, jan 2002.

[148] T. Poinsot and D. Veynante. *Theoretical and Numerical Combustion.* RT Edwards, Inc., 2012.

[149] B. E. Poling, J. M. Prausnitz, and J. P. O'connell. *Properties of gases and liquids.* McGraw-Hill Education, 2001.

[150] M. Pollack, F. Ferraro, J. Janicka, and H. Hasse. Evaluation of quadrature-based moment methods in turbulent premixed combustion. *Proceedings of the Combustion Institute*, 2020.

[151] S. B. Pope. The statistical theory of turbulent flames. *Philosophical Transactions of the Royal Society of London. Series A, Mathematical and Physical Sciences*, 291(1384):529–568, 1979.

[152] S. B Pope. A monte carlo method for the PDF equations of turbulent reactive flow. *Combustion Science and Technology*, 25(5-6):159–174, 1981.

[153] S. B. Pope. PDF methods for turbulent reactive flows. *Progress in Energy and Combustion Science*, 11(2):119–192, jan 1985.

[154] S.. B Pope. *Turbulent Flows*. Cambridge University Press, 2000.

[155] L. Prandtl. Über die ausgebildete turbulenz. (on fully developed turbulence. in german). *ZAMM*, 5:136–139, 1925.

[156] V. N. Prasad. *Large eddy simulation of partially premixed turbulent combustion*. PhD thesis, Imperial College London (University of London), 2011.

[157] V. Raman and H. Pitsch. A consistent LES/filtered-density function formulation for the simulation of turbulent flames with detailed chemistry. *Proceedings of the Combustion Institute*, 31(2):1711–1719, 2007.

[158] V. Raman, H. Pitsch, and R. O. Fox. Hybrid large-eddy simulation/lagrangian filtered-density-function approach for simulating turbulent combustion. *Combustion and Flame*, 143(1-2):56–78, 2005.

[159] W. E. Ranz and W. R. Marshall. Evaporation from drops, part I & II. *Chem. Eng. Prog*, 48:141–146;173–80, 1952.

[160] R. P. Rhodes. A probability distribution function for turbulent flows. In *Turbulent mixing in nonreactive and reactive flows*, pages 235–241. Springer, 1975.

[161] L. F. Richardson. *Weather prediction by numerical process*. Cambridge University Press, 1922.

[162] L. Riedel. Eine neue universelle damfdruck-formel (a new universal vapor pressure equation). *Chem. Ing. Tech*, 26:83, 1954.

[163] F. Ries. *Numerical Modeling and Prediction of Irreversibilities in Sub- and Supercritical Turbulent Near-Wall Flows*. PhD thesis, Technical University of Darmstadt, Germany, 2018.

[164] F. Ries, K. Nishad, J. Janicka, and A. Sadiki. Entropy generation analysis and thermodynamic optimization of jet impingement cooling using large eddy simulation. *Entropy*, 19:129, 2019.

[165] F. Ries, P. Obando, I. Shevchuck, J. Janicka, and A. Sadiki. Numerical analysis of turbulent flow dynamics and heat transport in a round jet at supercritical conditions. *International Journal of Heat and Fluid Flow*, 66:172–184, 2017.

[166] A. Rittler, F. Proch, and A. M. Kempf. LES of the sydney piloted spray flame series with the PFGM/ATF approach and different sub-filter models. *Combustion and Flame*, 162(4):1575–1598, 2015.

[167] P. L. Roe. Characteristic-based schemes for the euler equations. *Annual review of fluid mechanics*, 18(1):337–365, 1986.

[168] V. Sabel'nikov and O. Soulard. *Eulerian (Field) Monte Carlo Methods for Solving PDF Transport Equations in Turbulent Reacting Flows*, chapter 4, pages 75–119. American Cancer Society, 2010.

[169] V. A. Sabel'nikov and O. Soulard. Rapidly decorrelating velocity-field model as a tool for solving one-point fokker-planck equations for probability density functions of turbulent reactive scalars. *Physical Review E*, 72(1):016301, 2005.

[170] F. L. Sacomano Filho. *Novel approach toward the consistent simulation of turbulent spray flames using tabulated chemistry*. PhD thesis, Technische Universität Darmstadt, 2017.

[171] F. L. Sacomano Filho, L. Dressler, A. Hosseinzadeh, A. Sadiki, and G. C. Krieger Filho. Investigations of evaporative cooling and turbulence flame interaction modeling in ethanol turbulent spray combustion using tabulated chemistry. *Fluids*, 4:187, oct 2019.

[172] F. L. Sacomano Filho, A. Hosseinzadeh, A. Sadiki, and J. Janicka. On the interaction between turbulence and ethanol spray combustion using a dynamic wrinkling model coupled with tabulated chemistry. *Combustion and Flame*, 215:203–220, 2020.

[173] F. L. Sacomano Filho, J. Kadavelil, M. Staufer, A. Sadiki, and J. Janicka. Analysis of LES-based combustion models applied to an acetone turbulent spray flame. *Combustion Science and Technology*, 191(1):54–67, 2018.

[174] F. L. Sacomano Filho, G. C. Krieger Filho, J. A. van Oijen, A. Sadiki, and J. Janicka. A novel strategy to accurately represent the carrier gas properties of droplets evaporating in a combustion environment. *International Journal of Heat and Mass Transfer*, 137:1141–1153, 2019.

[175] F. L. Sacomano Filho, G. Kuenne, M. Chrigui, A. Sadiki, and J. Janicka. A consistent artificially thickened flame approach for spray combustion using LES and the FGM chemistry reduction method: Validation in lean partially pre-vaporized flames. *Combustion and Flame*, 184:68–89, 2017.

[176] P. Sagaut. *Large eddy simulation for incompressible flows: an introduction*. Springer Science & Business Media, 2006.

[177] K. Salari and P. Knupp. Code verification by the method of manufactured solutions. Technical report, Sandia National Labs., Albuquerque, NM (US); Sandia National Laboratories, 2000.

[178] Q. Schiermeier. The science behind the volkswagen emissions scandal. *Nature News*, 2015.

[179] L. Schiller and Z. Naumann. Über die grundlegenden berechnungen bei der schwerkraftaufbereitung (in german). *Ver. Deut. Ing.*, 77:318–321, 1933.

[180] H. Schlichting and K. Gersten. *Boundary-Layer Theory*. Springer, 2017.

[181] T. Schmitt, A. Sadiki, B. Fiorina, and D. Veynante. Impact of dynamic wrinkling model on the prediction accuracy using the f-tacles combustion model in swirling premixed turbulent flames. *Proceedings of the Combustion Institute*, 34(1):1261–1268, 2013.

[182] C. Schneider, A. Dreizler, J. Janicka, and E. P. Hassel. Flow field measurements of stable and locally extinguishing hydrocarbon-fuelled jet flames. *Combustion and Flame*, 135(1-2):185–190, 2003.

[183] F. Seffrin, F. Fuest, D. Geyer, and A. Dreizler. Flow field studies of a new series of turbulent premixed stratified flames. *Combustion and Flame*, 157(2):384–396, 2010.

[184] J. A Sethian and P. Smereka. Level set methods for fluid interfaces. *Annual review of fluid mechanics*, 35(1):341–372, 2003.

[185] L. Shunn, F. Ham, and P. Moin. Verification of variable-density flow solvers using manufactured solutions. *Journal of Computational Physics*, 231(9):3801–3827, 2012.

[186] B. W. Silverman. *Density estimation for statistics and data analysis*. Routledge, 2018.

[187] J. Smagorinsky. General circulation experiments with the primitive equations: I. the basic experiment. *Monthly weather review*, 91(3):99–164, 1963.

[188] G. P. Smith, D. M Golden, M . Frenklach, N . W. Moriarty, B. Eiteneer, M. Goldenberg, C. T. Bowman, R. K. Hanson, S. Song, W. C. Jr. William C. Gardiner, V. V. Lissianski, and Z. Qin. GRI-Mech 3.0. `http://www.me.berkeley.edu/gri_mech/`, 2019. Online; accessed: 2021-01-15.

[189] M. D. Smooke. *Reduced kinetic mechanisms and asymptotic approximations for methane-air flames: a topical volume*. Springer, 1991.

[190] B. Somers. *The simulation of flat flames with detailed and reduced chemical models*. PhD thesis, Gastec NV NL, 1994.

[191] M. Sommerfeld, B. van Wachem, and R. Oliemans. *Best practice guidelines for computational fluid dynamics of dispersed multiphase flows*. Ercoftac, 2008.

[192] D. B. Spalding. A single formula for the "law of the wall". *Journal of Applied Mechanics*, 28(3):455–458, 1961.

[193] S. Subramaniam and S. B. Pope. A mixing model for turbulent reactive flows based on euclidean minimum spanning trees. *Combustion and Flame*, 115(4):487–514, 1998.

[194] L. Valiño. A field monte carlo formulation for calculating the probability density function of a single scalar in a turbulent flow. *Flow, turbulence and combustion*, 60(2):157–172, 1998.

[195] L. Valiño, R. Mustata, and K. B. Letaief. Consistent behavior of eulerian monte carlo fields at low reynolds numbers. *Flow, Turbulence and Combustion*, 96(2):503–512, 2016.

[196] J. A. Van Oijen and L. P. H. De Goey. Modelling of premixed laminar flames using flamelet-generated manifolds. *Combustion Science and Technology*, 161(1):113–137, 2000.

[197] J. A. Van Oijen, A. Donini, R. J. M. Bastiaans, J. H. M. ten Thije Boonkkamp, and L. P. H. De Goey. State-of-the-art in premixed combustion modeling using flamelet generated manifolds. *Progress in Energy and Combustion Science*, 57:30–74, 2016.

[198] H. K. Versteeg and W. Malalasekera. *An introduction to computational fluid dynamics: the finite volume method*. Pearson education, 2007.

[199] J. Villermaux and L. Falk. A generalized mixing model for initial contacting of reactive fluids. *Chemical Engineering Science*, 49(24):5127–5140, 1994.

[200] A.W. Vreman, B.A. Albrecht, J.A. van Oijen, L.P.H. de Goey, and R.J.M. Bastiaans. Premixed and nonpremixed generated manifolds in large-eddy simulation of sandia flame D and F. *Combustion and Flame*, 153(3):394–416, may 2008.

[201] J. Warnatz, U. Maas, and R. Dibble. *Combustion*. Springer, 2006.

[202] H. G. Weller, G. Tabor, H. Jasak, and C. Fureby. A tensorial approach to computational continuum mechanics using object-oriented techniques. *Computers in Physics*, 12(6):620, 1998.

[203] X. Wen, L. Dressler, A. Dreizler, A. Sadiki, J. Janicka, and C. Hasse. Flamelet les of turbulent premixed/stratified flames with H2 addition. *Combustion and Flame*, 230:111428, 2021.

[204] C. R. Wilke. A viscosity equation for gas mixtures. *The journal of chemical physics*, 18(4):517–519, 1950.

[205] F. A. Williams. *Combustion theory*. Westview Press Inc, 1985.

[206] S. C. Wong and A. C. Lin. Internal temperature distributions of droplets vaporizing in high-temperature convective flows. *Journal of fluid mechanics*, 237:671–687, 1992.

[207] H. Yamashita, M. Shimada, and T. Takeno. A numerical study on flame stability at the transition point of jet diffusion flames. In *Symposium (International) on Combustion*, volume 26, pages 27–34. Elsevier, 1996.

[208] M. C. Yuen and L. W. Chen. On drag of evaporating liquid droplets. *Combustion Science and Technology*, 1976.